East European Journal of Physics. 4. 469-483 (2025)
DOI:10.26565/2312-4334-2025-4-48 ISSN 2312-4334

DFT-BASED STUDY OF TlX AND BX (X= N, P, As) COMPOUNDS: A COMPARATIVE INSIGHT INTO STRUCTURAL, ELECTRONIC, AND OPTICAL BEHAVIOR

Abed Zoulikha*, Lachabi Abdelhadi, Abdelali Laid
Applied Materials Laboratory, Research Center, Sidi Bel Abbes University, 22000, Algeria
**Corresponding Author E-mail: zoulikhaabed3@gmail.com*
E-mail co-authors: lachebia@yahoo.fr; laidabdelali@gmail.com
Received July 28, 2025; revised October 17, 2025; accepted November 1, 2025

This work presents a detailed theoretical investigation of the structural, electronic, and optical properties of thallium-based (TlX) and boron-based (BX) compounds, where X = N, P, As, within the zinc-blende crystal structure. First-principles calculations were performed using density functional theory (DFT) within the generalized gradient approximation (GGA). The obtained results reveal that Tl-based compounds exhibit lower total energies compared to BX compounds, indicating higher structural stability. In terms of electronic behavior, BX compounds maintain their semiconducting nature. In contrast, TlX compounds show metallic or near-metallic characteristics due to the absence of an energy gap at the Fermi level. Furthermore, optical investigations demonstrate that TlX compounds possess higher static refractive indices and stronger absorption features in the low-energy region. These findings highlight the potential of Tl-based compounds for future applications in optoelectronic and photonic devices. Overall, this comparative study provides valuable insights for the design of advanced materials for electronic and energy-related technologies.
Keywords: *Thallium compounds; Boron compounds; First-principles calculations; Density functional theory (DFT); Electronic properties; Band structure; Semiconductors; TlX; BX*
PACS: 84.60.Jt;78.20.Bh;89.30.Cc;42.60.Lh

1. INTRODUCTION

In recent years, the investigation of the structural, electronic, and optical properties of III-V semiconductors has attracted considerable attention due to their potential applications in advanced electronic and optoelectronic devices. Among these compounds, boron-based (B-V) and thallium-based (Tl-V) materials have emerged as promising candidates thanks to their unique electronic band structures, wide-ranging energy gaps, and favorable optical characteristics. These compounds have been extensively studied through both experimental techniques and first-principles calculations, especially those based on density functional theory (DFT), which remains a reliable and widely used approach for predicting the fundamental properties of materials at the atomic scale. It is evident that there has been a significant interest in using first-principles calculations [2, 11, 12, 14], including density functional theory (DFT) [9, 13], to investigate the structural and electronic properties of III-V semiconductors and superlattice structures. The physical properties of B-V and Tl-V compounds have been the subject of extensive theoretical and experimental research. In this context, several relevant studies can be mentioned, such as the work of *Akshay* [1], who focused on the structural and electronic properties of BN compounds, as well as the theoretical studies of *Yousra Megdoud* [6], which were dedicated to the structural and electronic investigation of BX compounds where X = N, P, As. Furthermore, *Nawel Saidi* [3] has conducted an in-depth study on Tl-V compounds, emphasizing the influence of structural aspects on their electronic behavior. Within this scientific context, the present work is devoted to a comprehensive first-principles investigation of the structural, electronic, and optical properties of boron-based (BX with X = N, P, As) and thallium-based (TlX with X = N, P, As) compounds in the zinc blende phase. In all calculations carried out in this study, the density functional theory (DFT) framework has been adopted, employing the generalized gradient approximation (GGA) to describe the exchange-correlation effects accurately.

The aim is to provide a systematic and comprehensive comparison between thallium-based (TlX) and boron-based (BX) compounds, where X = N, P, As, focusing on their structural stability, electronic band structures, density of states, and optical response. The novelty of this study lies in its unified theoretical approach, as most previous investigations have considered each compound separately, without drawing a direct comparison between these two families.

By adopting this comparative perspective, the present work seeks to highlight both the key differences and possible similarities, thereby evaluating their suitability for future optoelectronic applications.

2. METHOD

The theoretical calculations in this study were performed using the WIEN2k Software package [8], which empioys the (FP-LAPW) technique under the theoretical framework of density functional theory (DFT). This method is considered one of the most accurate for studying the structural and electronic properties of crystalline solids, as it imposes no shape approximation on the potential or electron density, making it particularly well-suited for systems containing heavy atoms such as thallium. The generalized Gradient Approximation (GGA) in the Perdew-Burke-Erzerhof (PBW) form was adopted to describe the exchange-correlation interactions between electrons [5]. This functional has proven effective in accurately modeling the ground state properties of semiconductors and complexes compounds.

Cite as: A. Zoulikha, L. Abdelhadi, A. Laid, East Eur. J. Phys. 4, 469 (2025), https://doi.org/10.26565/2312-4334-2025-4-48

(i) Crystal Structure setup: the made compounds TlX and BX were modeled in the zinc blend (ZB) structure, which belongs to the F-43m (No.216) space group. This cubic arrangement is widely observed in III-V semiconductors [10]. In this structure, the thallium and boron atoms occupy the positions of a face-centered cubic (FCC) lattice, while the group V atoms (N, As, P) are shifted by (0.25, 0.25, 0.25) within the unit cell, thus occupying the tetrahedral sites of the FCC lattice.

(ii) ***Numerical parameters:*** To avoid overlap between atomic spheres, the muffin-tin radii ($_{RMT}$) were carefully chosen for each atom, the product $_{RMT}$ x $_{Kmaa}$ = 7.0. The Brillouin Zone (BZ) was sampled using a Monkhorst-Pack k-point mesh [10] of at least 11x11x11 to guarantee convergence of total energy and electronic properties.
A total of 56 k-points were employed for the integration over the irreducible part of the Brillouin zone. The convergence of the total energy with respect to ensure the accuracy of the calculations.

(iii) ***Structural optimization:*** The optimal lattice constant was obtained by evaluating the total energy as a function of the unit cell volume. The resulting energy-volume data were then fitted using the *Murnaghan equation of state* [7] to identify the minimum energy and the corresponding equilibrium structural parameters. All subsequent calculations were carried out using this optimized geometry.

$$E(V) - E(V_0) = \frac{B_0 V}{B_0'}\left[\frac{(V_0|V)^{B_0'}}{B_0'-1} + 1\right] - \frac{B_0 V_0}{B_0'-1}, \quad (1)$$

$$B_0 = V\frac{\partial^2 E}{\partial V^2} = \frac{4}{9a}\frac{\partial^2 E}{\partial a^2} \quad (2)$$

Where B_0 is the bulk modulus given by the relation (1-b) at zero pressure (P=0), V_0 is the equilibrium volume, E (V_0) is the energy corresponding to equilibrium volume, B_0' is the pressure derivative of the bulk modulus at P=0 and, a is lattice constant.

(iv) Electronic Properties: with the optimized structure; self-consistent field (SCF) calculations were performed to obtain the band structure along high-symmetry directions in the Brillouin zone, as well as the total and partial density of states (DOS). These results provided insights into the nature of the band gap (direct or indirect), its magnitude, and the orbital contributions from different atomic states near the valence and conduction bands [4].

(v) Optical Properties: the optical properties were evaluated using the optics module of WIEN2K, which computes the complex dielectric function based on the electronic structure. From the real and imaginary parts of the dielectric function, various optical constants were extracted, including the refractive index, absorption coefficient, reflectivity, and energy loss function [4]. These quantities are essential for materials in optoelectronic and photonic application.

In this work, different muffin-tin radii were chosen for each atom in order to improve the accuracy of the calculations within the WIEN2K framework [8]. These values were selected to avoid overlap between spheres and to ensure numerical stability during the DFT simulation. The Table 1 summarizes the selected muffin-tin radii for each atomic species, along with their corresponding electronic configuration to properly define valence states.

Table 1. Atomic muffin-tin radii and corresponding electronic configurations

Element	*Rmt (a.u.)*	*Z*	*Full Electronic Configuration*	*Valence Electrons Treated in DFT*
Tl	2.50	81	[Xe] $4f^{14}$ $5d^{10}$ $6s^2$ $6p^1$	$5d^{10}$ $6s^2$ $6p^1$
B	1.60	5	$1s^2$ $2s^2$ $2p^1$	$2s^2$ $2p^1$
N	1.55	7	$1s^2$ $2s^2$ $2p^3$	$2s^2$ $2p^3$
P	1.85	15	[Ne] $3s^2$ $3p^3$	$3s^2$ $3p^3$
As	1.90	33	[Ar] $3d^{10}$ $4s^2$ $4p^3$	$3d^{10}$ $4s^2$ $4p^3$

3. ANALYSIS AND INTERPRETATION OF RESULTS

3.1. Structural parameters

Figure 1 illustrates the crystal structures of the TlX and BX compounds where X = N, P, As. All these compounds crystallize in the zinc-blende (B3) structure. This structure belongs to the face-centered cubic (FCC) system and consists of two interpenetrating cubic sublattices displaced by one quarter of the body diagonal of the unit cell.

In the primitive cell, the B and X atoms in the BX compounds, as well as the Tl and X atoms in the TlX compounds occupy the Cartesian positions (0, 0, 0) and (a/4, a/4, a/4) respectively, where a denotes the conventional cubic lattice parameter. Each unit cell contains four boron atoms and each boron atom is surrounded by four X atoms arranged in a tetrahedral configuration. Thus, the unit cell contains sixteen X atoms distributed around the boron atoms.

A similar arrangement is observed for the TlX compounds where each thallium atom is coordinated to four X atoms in the same tetrahedral geometry. This atomic arrangement gives these compounds a high degree of crystalline symmetry belonging to the space group (F-43m) which is characteristic of the zinc-blende structure.

The lattice constant (a), equilibrium volume (V_0), bulk modulus (B_0), its pressure derivative (B_0'), and the total ground-state energy (E) were calculated using density functional theory (DFT) within the generalized gradient approximation (GGA), for BX and TlX compounds (X = N, P, As) in the zinc-blende (ZB) structure. The results are summarized in the Table 2 and 3.

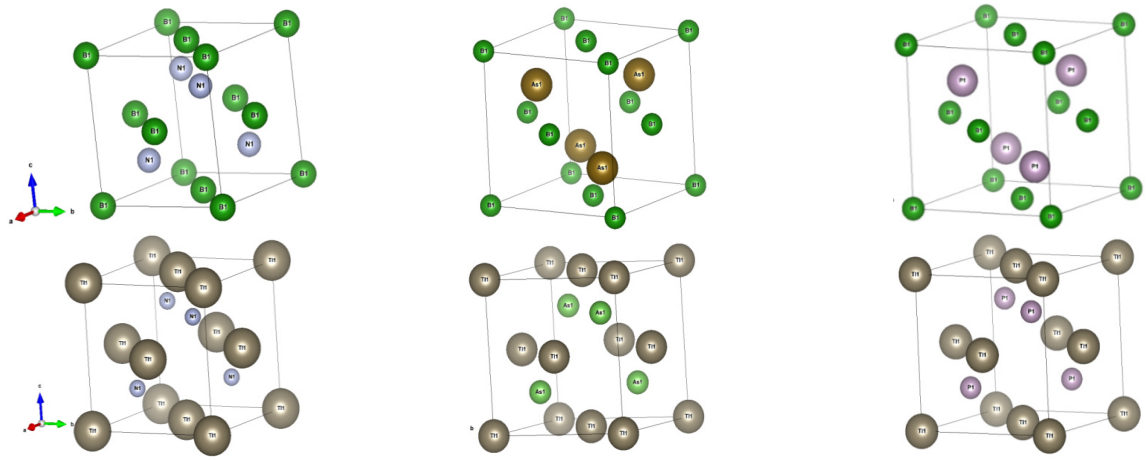

Figure 1. Optimized crystal structures of BX and of TlX compounds obtained from our calculations using the GGA approximation

Table 2. Values of lattice parameter a (Å), bulk modulus (B_0), pressure derivative of the bulk modulus (B0') equilibrium volume (V_0), and total energy of TlX compounds:

		a (Bohr)	a (Å)	B_0 (GPa)	B_0'	V_0 (Ry)	E (Ry)
TlN	Calculations	9.9803	5.2814	89.3550	4.9537	248.5287	-40687.222951
	Other calculatios	- -	5.2723 [15] 5.297 [16] 5.267 [20]	94.06 [15] 89.723 [16] 101.5 [20]	4.3038 [15] 5.026 [16] 3.9 [20]	- -	-40687.232557 [15] -
TlP	calculations	11.5659	6.1208	45.9402	4.9292	386.869	-41262.006475
	Other calculatios	- -	6.135 [16] 5.96 [19] 6.124 [3]	44.981 [16] 57 [19] 46.75 [3]	4.8771 [16] - -	- - -	- - -
TlAs	calculations	12.0088	6.3548	38.1483	4.8986	432.9475	-45099.985275
	Other calculatios	- -	6.374 [16] 6.170 [21]	37.196 [16] 50.2 [21]	4.910 [16] -	- -	- -

Table 3. Values of lattice parameter a (Å), bulk modulus (B_0), pressure derivative of the bulk modulus (B0') equilibrium volume (V_0) and total energy of BX compounds

		a (bohr)	a (Å)	B_0 (GPa)	B_0'	V_0 (Ry)	E (Ry)
BN	calculations	6.855	3.6280	373.1226	3.7538	80.5613	-159.394567
	experimental		3.615 [22]	369 [22]	4 [22]	-	-
	Other calculatios	- -	3.530 [17] 3.606 [18]	417.44 [17] 367 [18]	3.78 [17] -	- -	- -
BP	calculations	8.5986	4.5502	161.5866	3.6769	158.9336	-733.960301
	experimental		4.538[23]				
	Other calculatios	-	4.558[18] 4.425[17]	166[18] 182.81[17]	- 3.77[17]	- -	- -
BAs	calculations	9.0947	4.8127	130.9268	4.0777	188.0645	-4571.898798
	experimental		4.777 [24]	-	-	-	-
	Other calculatios	- -	4.668[17] 4.777 [18]	154.30[17] 145 [18]	3.87[17] -	- -	- -

The obtained data, illustrated in Figures 2 and 3 and supported by the results shown in Tables 2 and 3, clearly demonstrate a significant contrast in the structural stability and total energy between thallium-based compounds (TlX) and boron-based compounds (BX), where X = N, P, As. Thallium compounds exhibit much more negative total energies, which indicates higher thermodynamic and dynamical stability. For instance, the total energy of TlN is about −40637.22 Ry, while that of TlP and TlAs reaches −43461.54 Ry and −45099.98 Ry respectively, compared to the boron-based compounds BN (−159.39 Ry), BP (−4414.99 Ry), and BAs (−4571.89 Ry), confirming the superior energetic stability of Tl-based materials.

Regarding mechanical properties, the calculated equilibrium volume (Vo) and bulk modulus (Bo) reveal fundamental structural differences between the two families. TlX compounds are characterized by larger equilibrium volumes and lower bulk moduli, indicating relatively softer crystal structures. For example, TlP has a Vo of 271.37 a.u³ and Bo of 33.14 GPa, while TlAs displays an even larger Vo (296.76 a.u³) and a lower Bo (28.21 GPa). In contrast, BX compounds are more compact and mechanically robust, particularly BN, which shows the smallest Vo (80.56 a.u³) and the highest Bo (373.12 GPa), pointing to high mechanical hardness and strong covalent bonding.

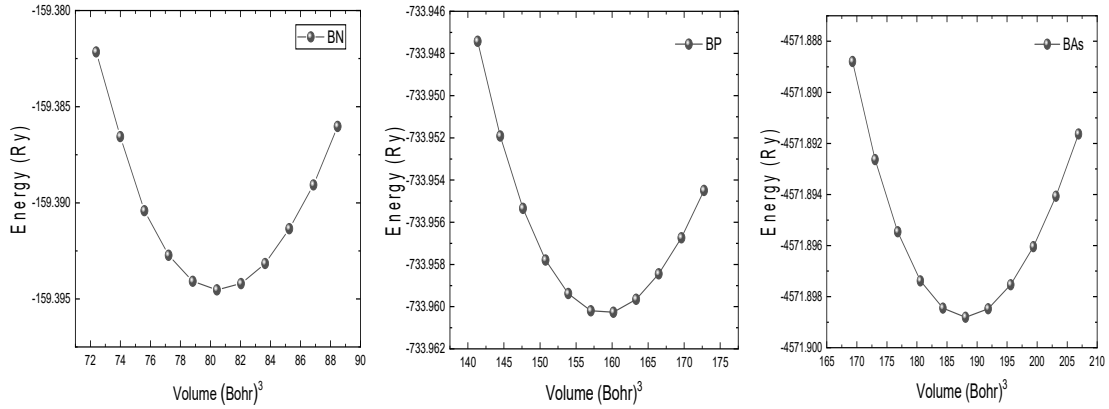

Figure 2. Variation of total energy as a function of atomic volume for BX compounds in the zinc blend structure

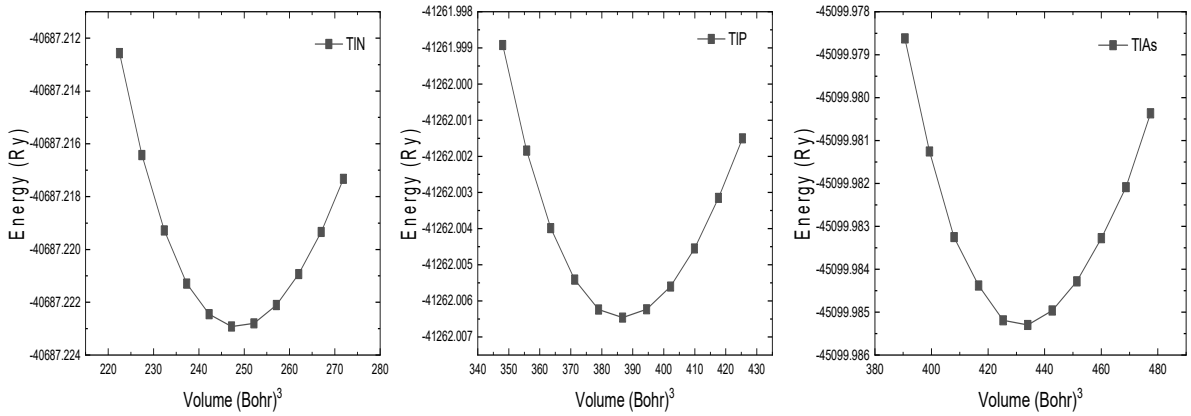

Figure 3. Variation of total energy as a function of atomic volume for TlX compounds in the zinc blend structure

Based on these results, one can conclude that TlX compounds exhibit clear advantages in terms of total energy and thermal stability, making them suitable for optoelectronic applications requiring flexibility and robustness. Conversely, BX compounds—especially BN—are more appropriate for extreme conditions that demand high mechanical performance. This complementary contrast in physical properties paves the way for future hybrid applications that exploit the strengths of both compound families.

Our results are in good agreement with previous theoretical studies, confirming their reliability, however there is no experimental result available for the III-V compounds.

3.2. Electronic parameters

Figures 4 to 7 present the calculated electronic band structures and density of states for BX and TlX compounds in the zinc blende structures. The analysis begins with the boron-based compounds, which exhibit wide band gaps, followed by the thallium-based compounds, whose electronic behavior is influenced by relativistic effects. These results help identify the nature and origin of the band gaps, as will be discussed in the following sections.

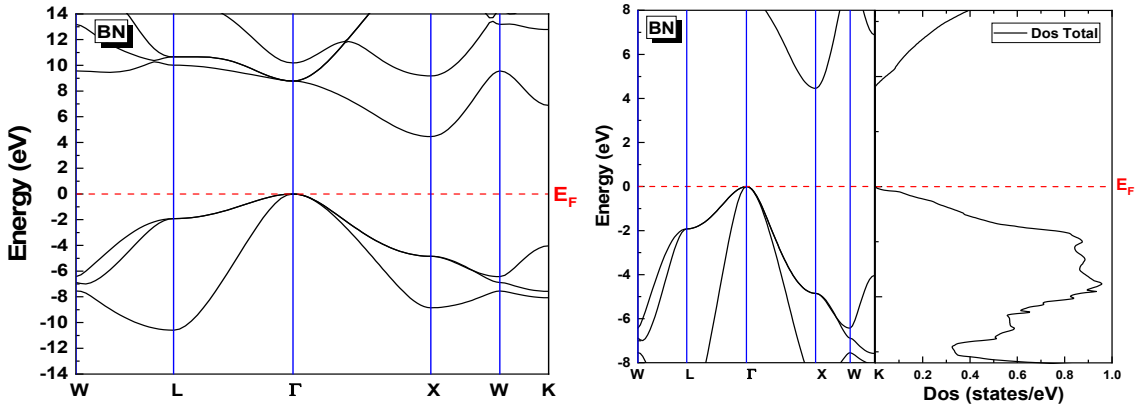

Figure 4. Calculated band structure and total density of states of BX (X=N, P, As) compound

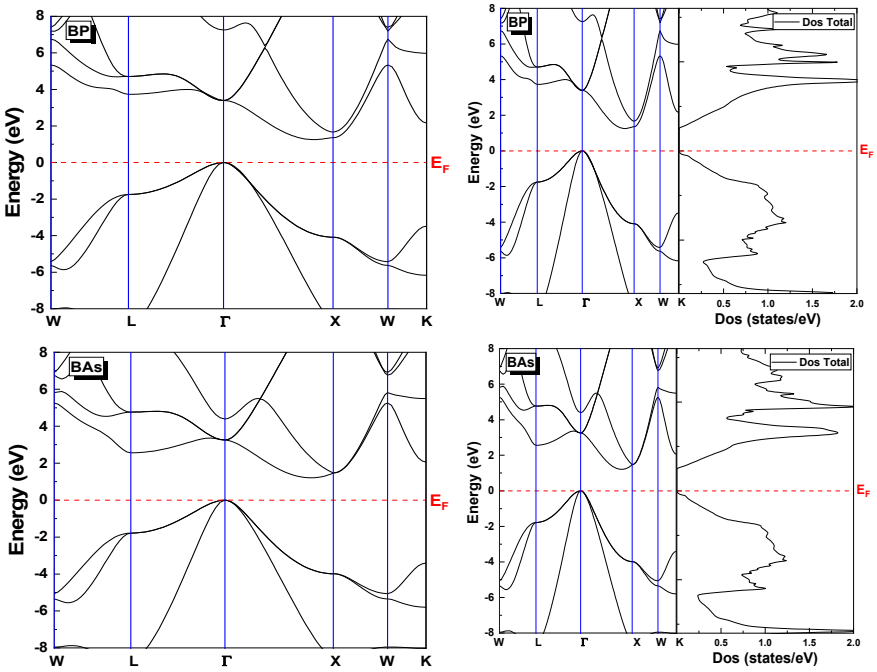

Figure 4. Calculated band structure and total density of states of BX (X=N, P, As) compound (*continued*)

The results are given in Table 3 show that BX (X= N, P, and As) are an indirect gap semiconductor with the minimum of conduction band at Γ, X point.

Table 3. Band gaps of BN, BP, and Bas in the zinc blende structure (all energies are in eV)

compounds	calculations	Other calculations	*Nature of the band gap*
BN	4.4593	4.85 [25], 4.35 [46]	(Γ===X) : *indirect*
BP	1.25317	1.24 [26], 1.14 [27]	(Γ===X) : *indirect*
BAs	1.20819	1.21 [26], 1.23 [30], 1.25 [18], 1.36 [42]	(Γ===X) : *indirect*

The electronic band structure calculations reveal that boron-based compounds BX (X = N, P, As) crystallizing in the zinc blende structure exhibit indirect band gaps. Among these materials, BN possesses the widest band gap, followed by BP and finally BAs with the smallest gap. This decreasing trend in the band gap values is mainly attributed to the increasing atomic number of the group V element. These findings are consistent with recent DFT studies reported in the literature [6. 29]. To gain deeper insights into the electronic structure, the total and partial density of states for BN, BP, and Bas were calculated and illustrated in Figure 5 using the GGA approximation.

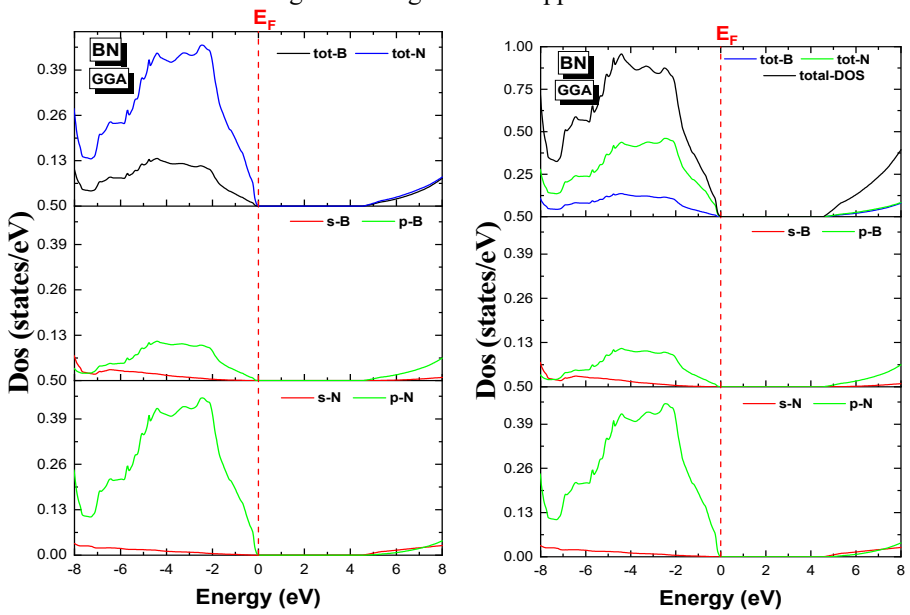

Figure 5. Total and partial densities of states of BX (X=N, P, As). Compound within GGA approximation

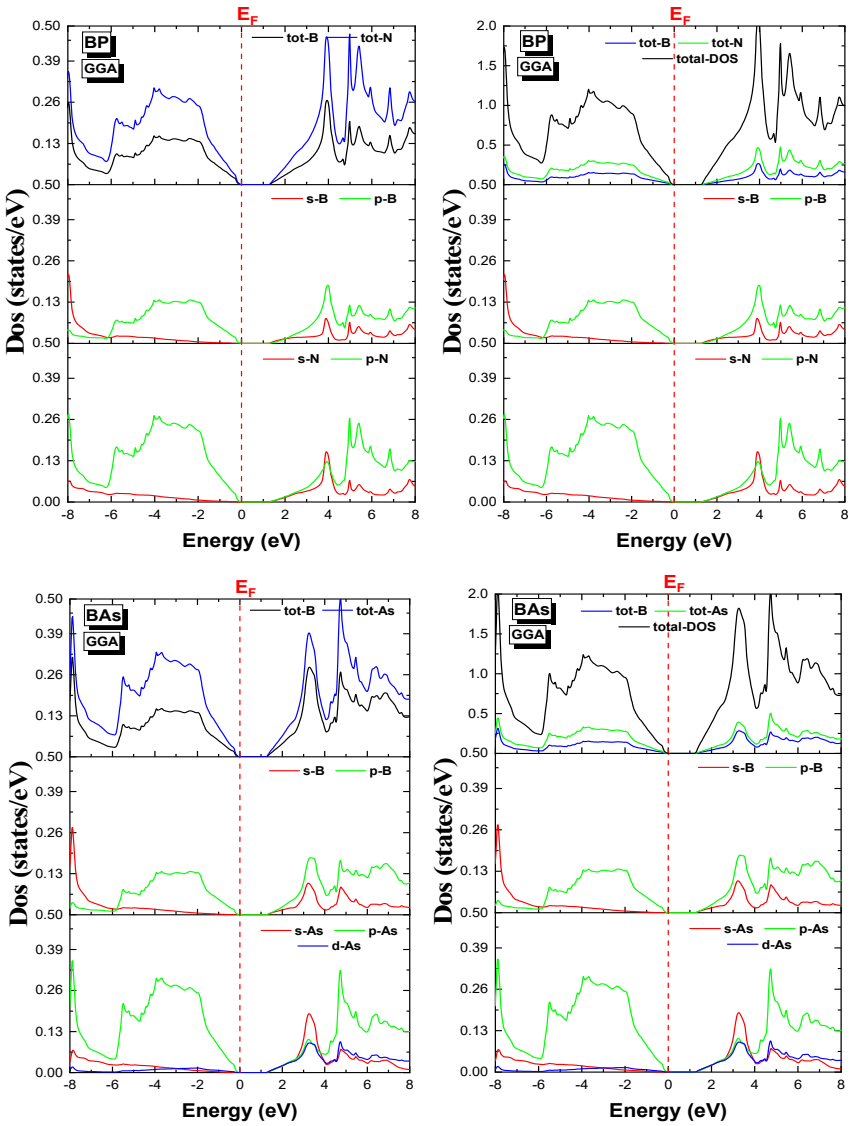

Figure 5. Total and partial densities of states of BX (X=N, P, As). Compound within GGA approximation (*continued*)

Figure 5 presents the total and partial density of states for the BN, BP, and Bas compounds in the Zinc blende structure. For BN, the valence band region, spanning from -8 eV to 0 eV, is strongly dominated by the p orbitals of the nitrogen atom (N-p), with a smaller contribution from the p orbitals of boron (B-p). This indicates a significant ionic character in the B-N bond, driven by the high electronegativity difference between the constituent atoms. In contrast, the conduction band (5-8eV) shows only weak contributions from al orbitals, suggesting a relatively low density of available states for electronic conduction in this energy range.

For BP, both B-p and P-p orbitals contribute significantly within the same valence band range (-8 to 0 eV), while the conduction band (1.25-8 eV) displays distributed contributions from multiple orbitals. This reflects a more covalent and delocalized nature of bonding compared to BN. As for Bas, the valence band is characterized by overlapping contributions from p orbitals of both boron and arsenic (B-p and As-p) within the -8 eV to 0 eV range, whereas the d orbitals of arsenic (As-d) exhibit nearly negligible participation. In the conduction band region (1.2-8eV), the electronic density remains distributed across the same previously mentioned orbitals, indicating similar bonding characteristics to BP but with a different electronic distribution profile.

After completing the analysis of the structural properties of the BX compounds (BN, BP, BAs), we now move on to the study of the TlX compounds (TlN, TlP, TlAs), in order to highlight the fundamental differences between these two families of materials. Unlike the BX compounds, which exhibit typical characteristics of light-element semiconductors, such as small lattice constants and wide band gaps, the structural properties of the TlX compounds clearly reflect the influence of the heavier thallium atom, resulting in noticeably different behavior. These structural differences are expected to have a direct impact on the electronic and optical properties of these materials.

Therefore, it is important to provide a detailed and precise analysis of the TlX compounds in order to clarify how the incorporation of thallium affects the crystal structure and distinguishes them from their boron-based counterparts.

The bands structure of TlX compounds for ZB phase is show in Fig. 6. Electronic structure calculations based on the GGA approximation reveal that the TlN, TlP, and TlAs compounds, crystallizing in the zinc blende (ZB) structure, exhibit a metallic or semi-metallic character, as indicated by the intersection of the Fermi level (EF) with the conduction band. These results confirm the absence of an energy band gap, with a calculated band gap value of 0 eV for all three materials. These findings are consistent with previous theoretical studies, which have also reported a zero-gap behavior in TlX compounds within the same crystal structure, using both GGA and more advanced functional such as mBJ and HSE 06 [3, 30, 31].

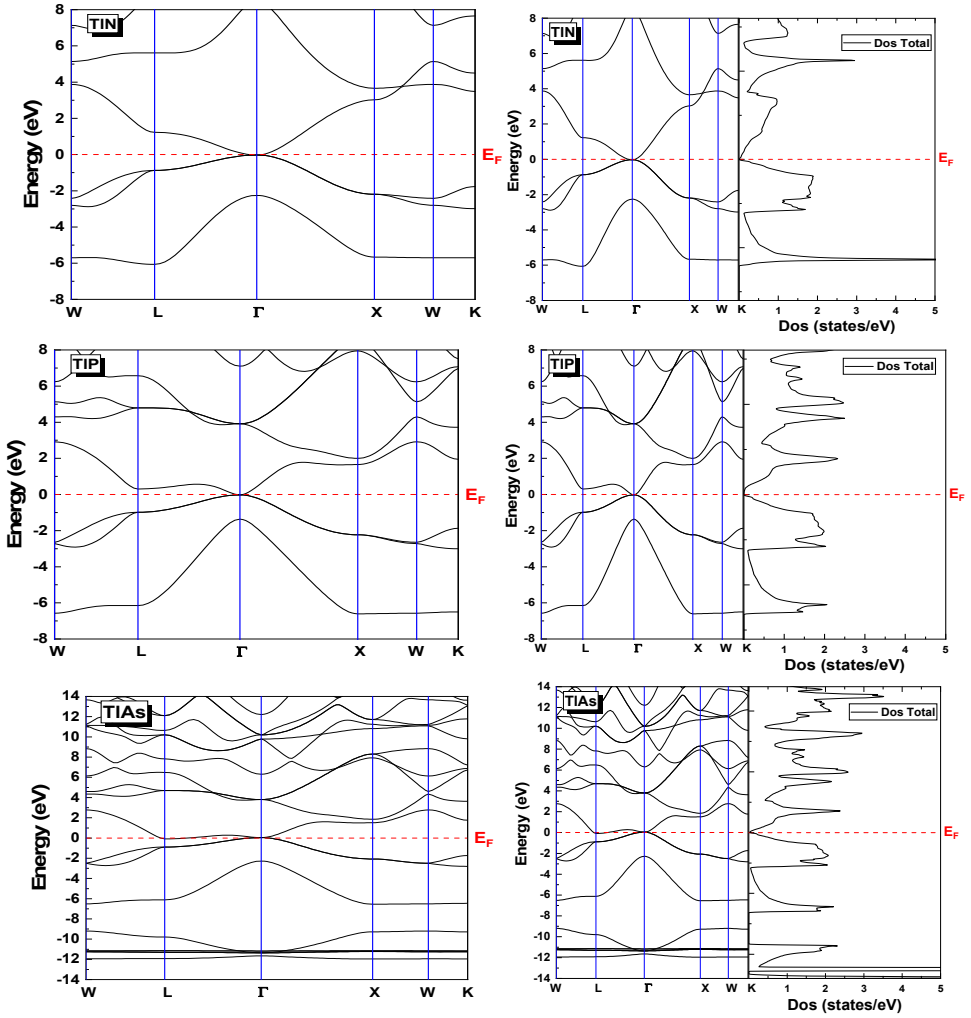

Figure 6. Calculated band structure and total density of states of TlX (X=N, P, As). Compound

To explore the electronic structures in greater detail, the total and partial density of states for TlN, TlP, and TlAs were calculated within the GGA approximation, as illustrated in Figure 7.

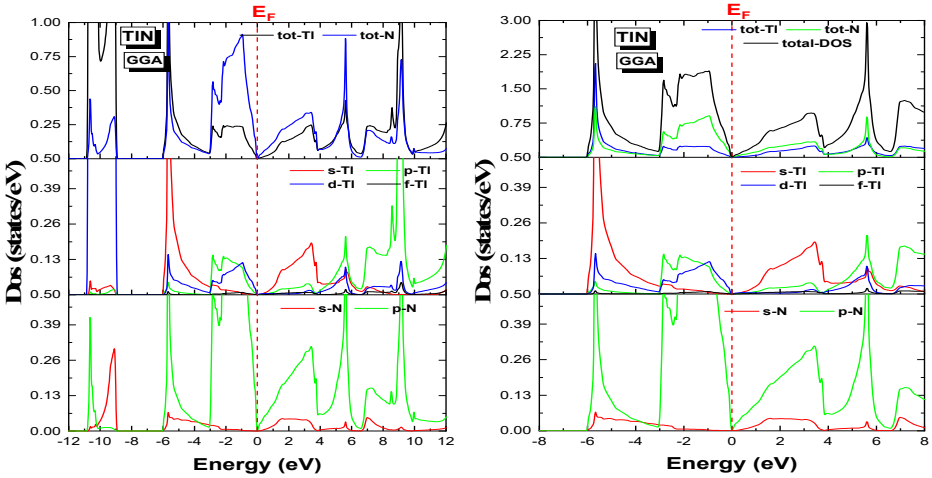

Figure 7. total and partial densities of states of TlX (X=N, P, As). Compound within GGA approximation

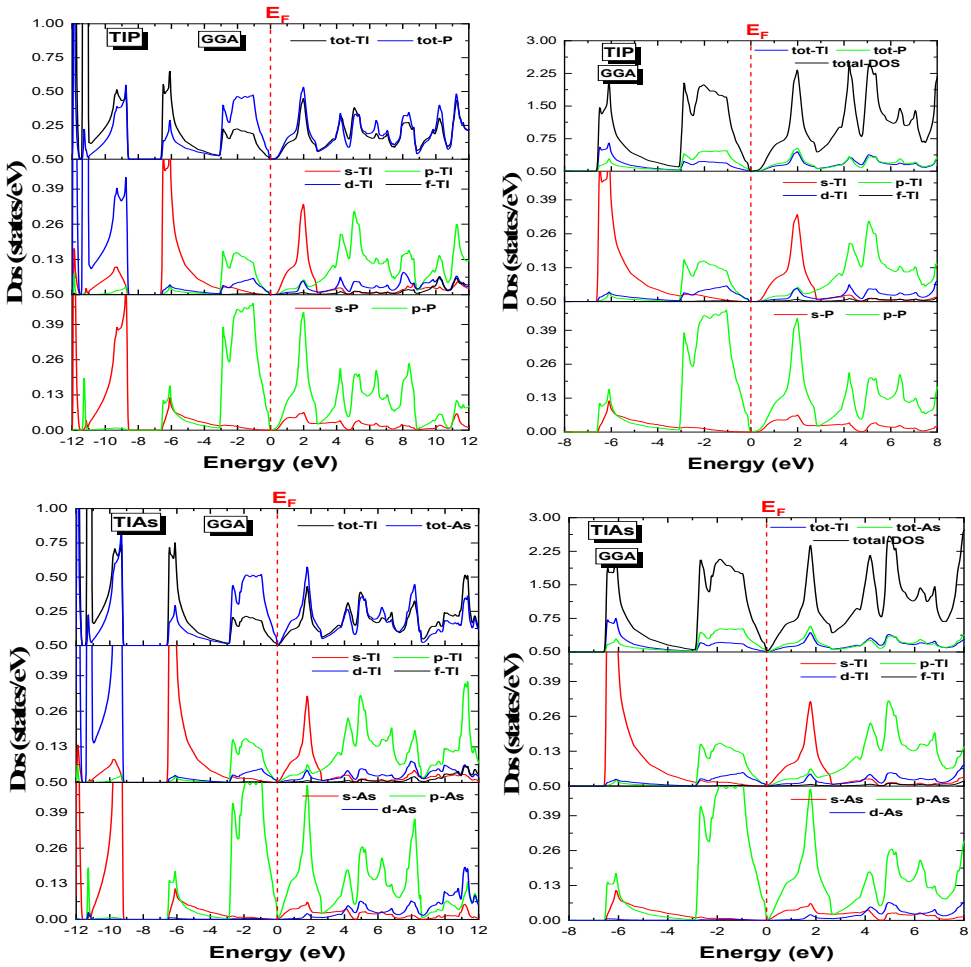

Figure 7. total and partial densities of states of TlX (X=N, P, As). Compound within GGA approximation (*continued*)

A detailed inspection of the partial densty of states for the TlX compounds reveals a clear distinction in the orbital contributions across the valence and conduction bands, which is essential for understanding their electronic behavior and bonding nature.

In the case of thallium nitride, the valence band can be divided into two main regions:

(i) The lower valence band, spanning from approximately -11 to -9 eV is primarily dominated by the Tl-d, N-s, and N-p states. This indicates strong hybridization between thallium and nitrogen deep core levels, reflecting a notable covalent character.

(ii) The upper valence region, from -6 eV to 0 eV, the dominant contributions arise from the Tl-s and N-s orbitals, with a moderate participation of Tl-d and N-s states.

As for the conduction band, starting just above the Fermi level (0 eV) and extending up to 12 eV, it is mainly composed of Tl-p, Tl-s and N-p orbitals. A minor yet noticeable contribution from the Tl-f states is also observed at higher energies, suggesting possible f-character at conduction states in excited conditions.

For TlP the the PDOS profile shows:

(i) A deep valence band segment between-12eV and -9.5 eV,where Tl-d and P-s states dominate, while Tl-s and P-p exhibit weaker contributions.

(ii) In the valence band range from -7eV to 0eV, there is a pronounced mixing for Tl-6p, Tl-s, P-s, and P-p states, with a slight presence of Tl-d this highlights the significant hybridization between thallium and phosphorus s-and p-orbitals near the Fermi level.

In the conduction band, contribution mainly stem from Tl-p, Tl-s, P-s, while Tl-d and Tl-f states appear marginal, indicating limited involvement of deeper core orbitals in the conduction process.

Finally, the PDOS spectrum of thallium arsenide closely resembles that of TlP:

(i) The lower valence band region (-12eV to-9eV) is predominantly characterized by As-s and Tl-d states, marking the interaction between deeper core levels of the two atoms.

(ii) Moving to the upper valence range (-6.5eV to 0eV), significant contributions from Tl-s and As-p are noted, with secondary inputs from Tl-p and As-s

So, in the conduction band (0 to ~8eV), the most pronounced contributions arise from Tl-s, T-p and As-4p, reflecting strong s-p hybridization, essential for the conduction mechanism. Additionally modest involvement of Tl-d, Tl-f, and As-d orbitals is identified at higher energy levels.

The analysis of the electronic band structures alongside the total and partial density of states for TlN, TlP, and TlAs demonstrates that the valence and conduction bands either intersect or come into direct contact at the Fermi level. This particular feature suggests the absence of a real band gap, placing these materials within the category of semi-metallic systems. Such behavior is typically associated with weak orbital hybridization and the influence of relativistic effects linked to the heavy.

So, these differences in the electronic distribution are directly reflected in the physical properties of the compounds. While the BX compounds retain a tunable semiconducting behavior, the TlX compounds appear unsuitable for conventional electronic applications, but they may be exploited in systems with metallic or semi-metallic character.

3.3. Optical parameters

Optical properties play a crucial role in evaluating the potential of materials for electronic and optoelectronic applications, such as detectors and photonic devices. These properties are derived from the energy-dependent dielectric function. In the following, we analyze key optical parameters including reflectivity *R(ω)*, absorption coefficient *α(ω),* energy loss function *L(ω*, and *ε1(ω) and ε2(ω* the real and imaginary parts of the refractive index *n(ω)*. These optical properties were investigated for the studied compounds within the photon energy range of 0 to 14 eV.

The complex dielectric function is used to describe the linear response of a material under an external electromagnetic field. It distinguishes between the contributions of intra-band and inter-band transitions and is represented by its real (ε_1) and imaginary (ε_2) parts [32]. Generally, the $\varepsilon_1(\omega)$ is closely related to the polarization, while $\varepsilon_2(\omega)$ is closely related to the absorption properties [38]:

$$\varepsilon(\omega) = \varepsilon_1(\omega) + i\varepsilon_2(\omega) \tag{3}$$

The imaginary component of the dielectric function at low photon energies is evaluated through electronic structure computations, relying on the joint density of states and the transition matrix elements between filed and empty electronic states. Subsequently, the real part is derived using the Kramers-Kronig transformation [33].

As previously mentioned, this work provides a detailed presentation and analysis of the main optical properties, such as the refractive index and the absorption coefficient, which are determined according to relations (4) and (5), respectively.

$$n(\omega) = \left[\frac{\varepsilon_1(\omega)}{2} + \frac{\sqrt{\varepsilon_1^2(\omega)+\varepsilon_2^2(\omega)}}{2}\right]^{1/2} \tag{4}$$

$$\alpha(\omega) = \frac{4\pi}{\lambda} k(\omega) \tag{5}$$

In these relations, k represents the extinction coefficient, while λ refers to the wavelength of light in vacuum. Further details on the methodology used to calculate these optical properties can be found in the works of Ambrosch-Draxl and Sofo [34, 35, 36].

The calculated Real and Imaginary Parts of the Dielectric Function $\varepsilon_1(\omega)$ and $\varepsilon_2(\omega)$, Refractive Index n(ω), Energy Loss Function L(ω), Reflectivity R(ω), and Absorption Coefficient α(ω) of BX(X=N, P, As) shown in Fig. 8.

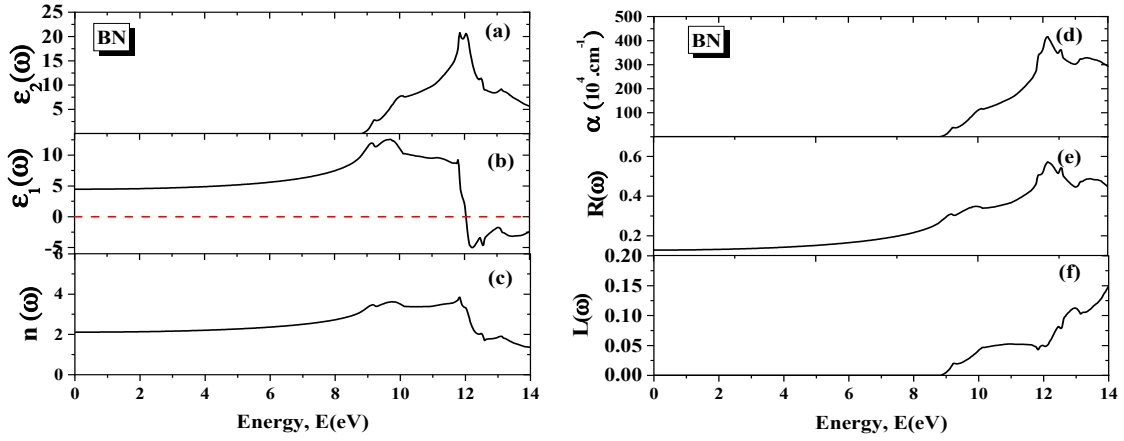

Figure 8. Real and Imaginary Parts of the Dielectric Function $\varepsilon_1(\omega)$ and $\varepsilon_2(\omega)$, Refractive Index n(ω), Energy Loss Function L(ω), Reflectivity R(ω), and Absorption Coefficient α(ω) of BX(X=N, P, As)

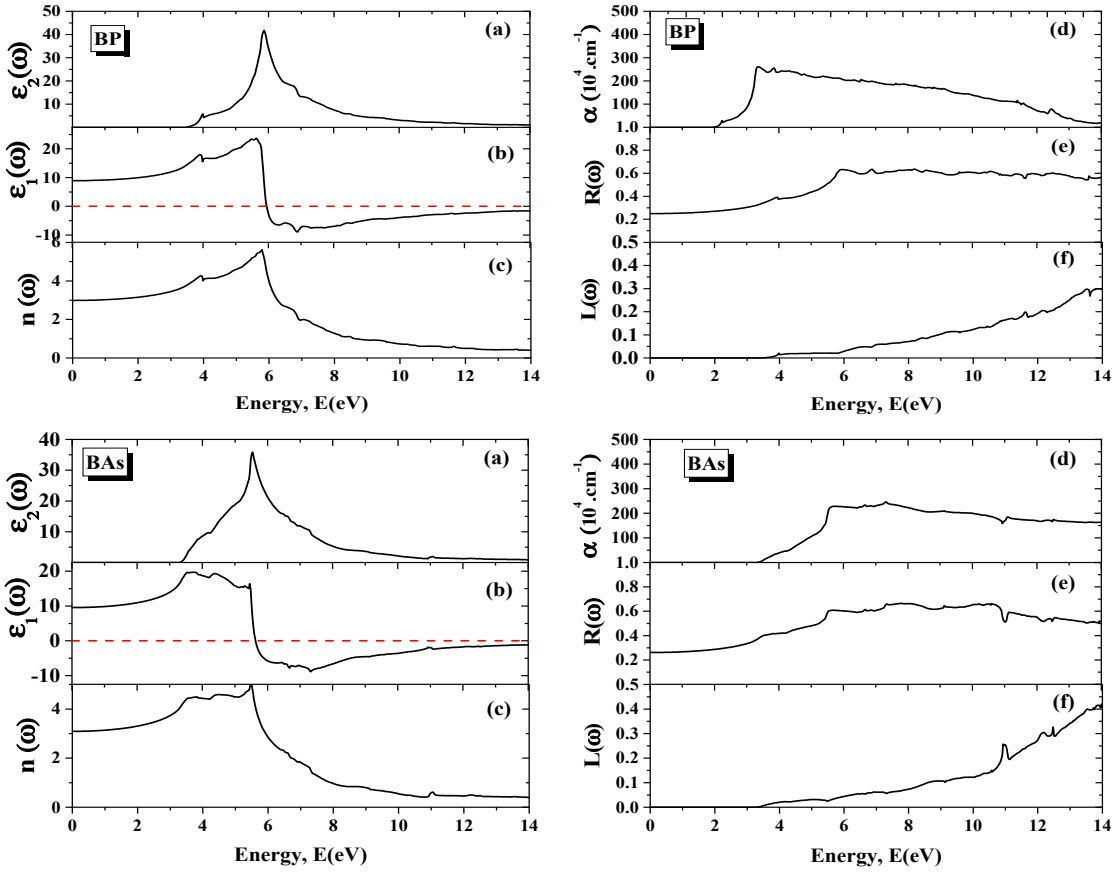

Figure 8. Real and Imaginary Parts of the Dielectric Function ε1(ω) and ε2(ω), Refractive Index n(ω), Energy Loss Function L(ω), Reflectivity R(ω), and Absorption Coefficient α(ω) of BX(X=N, P, As) (*continued*)

Imaginary Part ε2(ω): For BN compound, it is observed that the absorption starts in the ultraviolet region, around 9 eV, which clearly indicates the presence of a wide energy gap. Moreover, the low values of the imaginary part of the dielectric function (ε2) up to this energy confirm the transparency of the material in the infrared, visible, and near-ultraviolet ranges. Beyond this point, ε2 gradually increases, reaching its maximum around 12 eV, reflecting sharp and intense electronic transitions in the deep ultraviolet region. These results are in good agreement with the work reported by Artús et al. [45].

For both BP and BAs compounds, it is observed that the onset of optical absorption starts at an energy value of approximately 3.5 eV for each, indicating that their energy gaps are smaller compared to BN. Moreover, two prominent absorption peaks are recorded for both compounds within the energy range of 5 to 6 eV, with the maximum absorption intensity reaching around 40 for BP and about 35 for BAs. Beyond these peaks, a gradual decrease in absorption is observed until it becomes almost negligible in the deep ultraviolet region for both compounds.

Real Part ε1 (ω): For the BN compound in the energy range between 0 and 6 eV (from the infrared to the near-ultraviolet region), the real part ε1 remains approximately constant. Subsequently, this value increases gradually, reaching a maximum of about 12.5 at energy of approximately 10 eV, which corresponds to the deep ultraviolet region. Beyond this point, ε1 decreases significantly and becomes negative at higher photon energies, indicating the occurrence of plasmonic response in this energy range. For the BP and BAs compounds At 0 eV, the imaginary part ε2 is around 9 for BP and approximately 10 for BAs. These values remain nearly constant in both the infrared and visible regions. As the photon energy increases, ε2 starts to rise gradually until two pronounced peaks appear in the near-ultraviolet region:

(i) A pronounced peak around 25 is observed for BP within the energy range of 5-6 eV.

(ii) Another peak around 20 for BAs, located in the energy range between 3 and 4 eV.

Refractive Index n(ω): For BN, the static refractive index is n(0) = 2.1. This value remains almost constant up to (≈ 9 eV), beyond which it increases, reaching its maximum peak at around 12 eV. After this point, the refractive index decreases rapidly. In the case of BP, the static refractive index is n(0) = 3. This value remains nearly unchanged in the low-energy region up to about 4 eV, where the first peak appears with a refractive index of 4. Subsequently, the highest peak emerges at around 5.7 eV with a maximum value of n = 5.5, followed by a continuous decrease. For BAs, the static refractive index is n (0) = 3.1. A distinct peak appears at around 5.5 eV. These results are in good agreement with the work reported by Artús et al. [45]

Absorption Coefficient α(ω): The curves illustrating the variation of the absorption coefficient as a function of photon energy reveal the following behavior: For BN, no absorption is observed up to approximately 9 eV in the ultraviolet (UV) region. Beyond this energy, the absorption gradually increases, reaching its maximum peak around 12 eV in the deep UV region. For BP, the absorption remains negligible up to about 2 eV. It then increases progressively, reaching a maximum value of approximately 250 at around 3.2 eV, followed by a decrease.

For BAs, the absorption is absent in both the infrared and visible regions. It starts to increase at higher photon energies, reaching a maximum value of approximately 250, and then gradually decreases thereafter.

Reflectivity R(ω): The optical reflectivity of the compounds BN, BP, and BAs exhibits distinct behaviors for each material. For BN, at the zero-energy limit, the reflectivity is approximately 0.06% in the infrared region, and it gradually increases with photon energy, reaching about 0.5% in the deep ultraviolet region. For BP, the reflectivity at zero energy is R(0) = 0.25%. Nearly equal peaks of about 0.65% are observed within the energy range between 6 and 14 eV.

For BAs, the zero-energy reflectivity is approximately R(0) = 0.28%. It gradually increases beyond 5.5 eV, reaching values between 0.5% and 0.7%. The absence of absorption in the infrared region, along with the low reflectivity values, highlights the potential of these materials for use as cold, anti-reflective coatings in optical fiber technologies.

Energy Loss Function L(ω): Based on the analysis of the electron energy loss function (EELF) data, it is observed that the maximum peak for BN appears at approximately 14 eV. In contrast, for the compounds BP and BAs, the main peaks of the energy loss function are located within the energy range of 13.5 to 14 eV, indicating a similar optical behavior in this energy interval, which is typically associated with the plasmon excitation energies of these materials.

It is worth mentioning that some of the obtained results are in good agreement with several recent studies, which reinforces the validity of the reliability of the achieved findings [39, 40, 41, 42]. In this section, we will analyze the optical calculation results of thallium compounds So that the calculated Real and Imaginary Parts of the Dielectric Function $\varepsilon_1(\omega)$ and $\varepsilon_2(\omega)$, Refractive Index n(ω), Energy Loss Function L(ω), Reflectivity R(ω), and Absorption Coefficient α(ω) of TX(X=N, P, As) shown in Figure. 9.

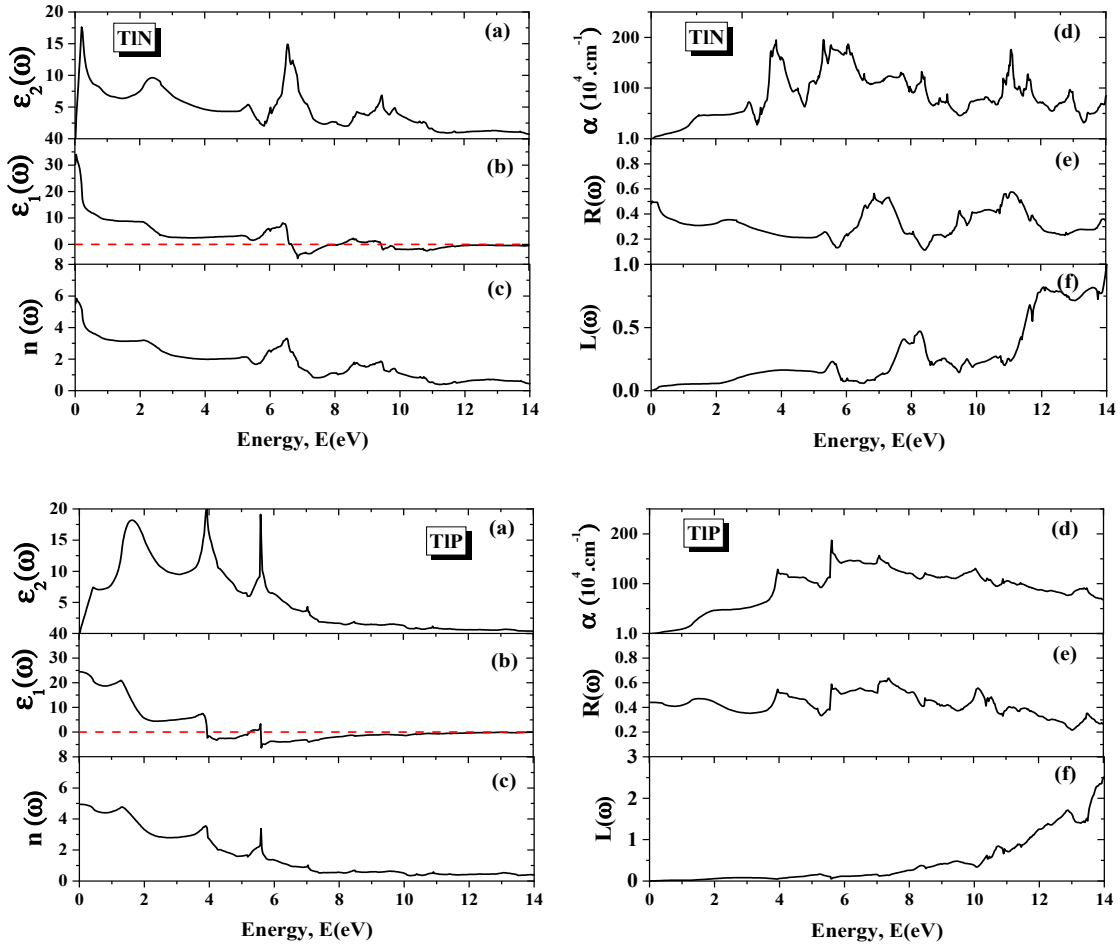

Figure 9. Real and Imaginary Parts of the Dielectric Function $\varepsilon_1(\omega)$ and $\varepsilon_2(\omega)$, Refractive Index n(ω), Energy Loss Function L(ω), Reflectivity R(ω), and Absorption Coefficient α(ω) of TX(X=N, P, As) and TlX(X=N, P, As)

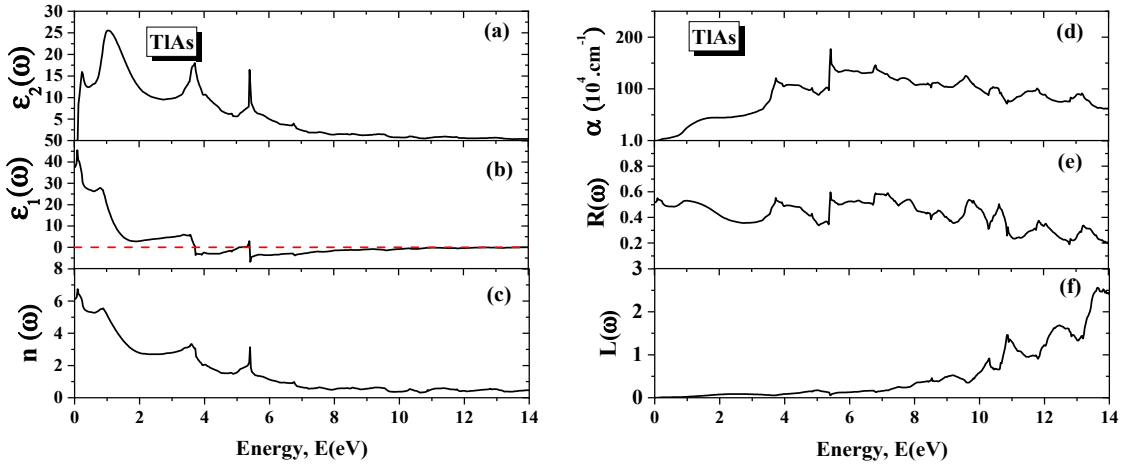

Figure 9. Real and Imaginary Parts of the Dielectric Function $\varepsilon_1(\omega)$ and $\varepsilon_2(\omega)$, Refractive Index $n(\omega)$, Energy Loss Function $L(\omega)$, Reflectivity $R(\omega)$, and Absorption Coefficient $\alpha(\omega)$ of TX(X=N, P, As) and TlX(X=N, P, As) (*continued*)

Imaginary Part $\varepsilon_2(\omega)$: The thallium compounds exhibit remarkable optical activity in the low-energy range. For TlN, distinct peaks are observed up to approximately 10 eV, with the most intense peak occurring below 1 eV, which corresponds to the infrared region. As for TlP and TlAs, noticeable peaks appear up to around 6 eV, after which the intensity gradually decreases.

Real Part $\varepsilon_1(\omega)$: The real part of the dielectric function $\varepsilon 1(\omega)$ is considered a key factor in understanding the optical behavior of this class of compounds, as it reflects the material's ability to polarize under the influence of external electromagnetic fields.

According to the obtained results, the highest values of $\varepsilon 1$ are recorded at 0 eV, which corresponds to the infrared region, indicating a strong capacity of these materials to store electric energy in this energy range. Among the studied compounds, the highest static dielectric constant was observed for TlAs, with $\varepsilon_1(0) = 45$, followed by TlN with a value of approximately $\varepsilon_1(0) = 35$, and finally TlP with $\varepsilon_1(0) = 25$. These results highlight the differences in polarization ability among the compounds, where TlAs exhibits a stronger polarizability compared to TlN and TlP, which is reflected in their distinct electromagnetic responses at low frequencies

Index n(ω): In this study, the refractive index at zero photon energy is extracted from the optical spectra as follows: $n(0) = 6.7$ for TlN, $n(0) = 5$ for TlAs, and $n(0) = 5$ for TlP. These values highlight the relatively high refractive indices of the thallium-based compounds in comparison with boron-based compounds, especially in the low-energy region. With increasing photon energy, the refractive index decreases progressively to reach values as low as 0.5 beyond 10 eV, indicating a weak refractive response at high energies.4. These results are in good agreement with the findings reported in 2023, which confirmed that materials with small or negligible band gaps generally exhibit high refractive index values at low photon energies, followed by a gradual decrease as the photon energy increases, according to the Wemple–DiDomenico model [44].

Absorption Coefficient α(ω): The optical absorption of the studied compounds starts within the infrared region and gradually increases, exhibiting pronounced peaks in the energy range between 3.5 and 6.5 eV. Additionally, for TlN, a distinct absorption peak appears around 13 eV, indicating active electronic transitions within these energy regions. For the compounds TlP and TlAs, two sharp peaks are observed near 6 eV for each, followed by a gradual decrease in the absorption coefficient. This behavior reflects a reduction in the density of electronic transitions in this energy range [43].

Reflectivity R(ω): The initial reflectivity values for the three compounds are approximately similar, with about 0.5 for TlN, 0.45 for TlP, and 0.51 for TlAs at zero photon energy. For TlN, two distinct reflectivity peaks are observed: the first located around 7 eV, and the second between 10 and 12 eV. In contrast, TlP and TlAs exhibit less pronounced and more gradually diminishing peaks as the photon energy increases. Notably, unlike TlP and TlAs, the reflectivity of TlN decreases between 11 and 12.5 eV, but shows a slight increase beyond this range.

Energy Loss Function L(ω): The energy loss function exhibits a low initial peak for all the compounds (TlN, TlP, and TlAs), followed by a clear increase starting from around 8 eV. A prominent and well-defined main peak is identified for each compound at approximately 14 eV, indicating strong energy loss behavior in this energy region.

4. CONCLUSIONS

In this study, the structural, electronic, and optical properties of thallium-based compounds TlX (X = N, P, As) and boron-based compounds BX (X = N, P, As) in the zinc-blende structure were systematically investigated using density functional theory (DFT) within the GGA approximation. The obtained results reveal that boron compounds exhibit a typical semiconductor behavior with well-defined energy gaps, while thallium compounds exhibit a nearly metallic

behavior with a vanishing energy gap. From the optical perspective, all compounds show a decreasing trend in the refractive index as photon energy increases, starting from relatively high values at low energies, which indicates a weak optical response at high photon energies. Furthermore, the analyses of the absorption spectra and dielectric functions highlighted the presence of significant electronic transitions at specific energy ranges for each compound, reflecting the density of available electronic states. These findings clearly demonstrate the distinct electronic and optical behaviors between thallium-based and boron-based compounds, underscoring their potential relevance for advanced electronic and optoelectronic applications. Moreover, the observed trends are largely consistent with recent theoretical studies cited throughout this work.

Acknowledgments

I would like to express my sincere gratitude to my supervisor, Professor Lachebi Abdelhadi, for his continuous support, valuable guidance, and insightful remarks that significantly contributed to the successful completion of this work. I would also like to extend my heartfelt thanks to my colleague, El Aid Abdelali, for his constant encouragement and fruitful collaboration throughout the preparation of this research.

ORCID

Abed Zoulikha, https://orcid.org/0009-0007-4824-1099; **Abdelali Laid**, https://orcid.org/0009-0009-9173-3835

REFERENCES

[1] A.M, Satawara, G.A. Shaikh, S.K. Gupta, and P.N. Gajjar, "Structural, electronic and optical properties of hexagonal boron-nitride (h-BN) monolayer: An Ab-initio study," Material Today: Proceedings, **47**(10), 529-532 (2020). https://doi.org/10.1016/j.matpr.2020.10.589

[2] D. Allali, B. Abdelmajid, S.E. Saber, D. Bahri, F. Zerarga, R. Amari, M. Radjai, *et al*. "Afirst-principles investigation on the structural, electronic and optical characteristics of tetragonal compounds XAgO (X = Li, Na, K, Rb)," Computational Condensed Matter. **38**, e00876 (2024). https://doi.org/10.1016/j.cocom.2023.e00876

[3] N. Saidi-Houat, A. Zaoui, and M. Ferhat, "Structural Stability of Thallium–V Compounds," Journal of Physics: Condensed Matter, **19**(10), 106221 (2007). https://doi.org/10.1088/0953-8984/19/10/106221

[4] C. Ambrosch-Draxi, and J.O. Sofo, "Linear optical properties of solids within the full- potential linearized augmented plane wave method," Computer Physics Communications, **175**, 1-14 (2006). https://doi.org/10.1016/j.cpc.2006.03.005

[5] J.P. Perdew, K. Burke, and M. Ernzerhof, "Generalized Gradient Approximation Made Simple," Physical Review Letters, **77**, 3865–3868 (1996). https://doi.org/10.1103/PhysRevLett.77.3865

[6] Y. Megdoud, Y. Benkrima, L. Tairi, R. Meneceur, S. Ghemid, and H. Meradji, Functional materials, **31**(2), 232-251 (2024). https://doi.org/10.15407/fm31.02.232

[7] F.D. Murnaghan, "The compressibility of media under extreme pressures," Proceedings of the national Academy of Sciences, **30**(9), 244-247 (1944). https://doi.org/10.1073/pnas.30.9.244

[8] P. Blaha, K. Schwarz, G.K.H. Madsen, D. Kvasnicka, and J. Luitz, *WIEN2K: An Augmented Plane Wave plus Local Orbitals Program for Calculating Crystal Properties,* (J. Techniche Universtät Wien,Wien. Austria, 2001).

[9] Alleg Abdelakader, Benamara Ahmed, Moulay Noureddine, Berrahal Mokhtar, Zoukel Abdelhalim; Mansour Omar, Bensaid Djillali, Azzaz Yahia, Y. Al-Douri, Solid State Communications 380, 115435 (2024). https://doi.org/10.1016/j.ssc.2024.115435

[10] H.J. Monkhorst, and J.D. Pack, "Special points for Brillouin-zone integrations," Phys. Rev. B, **13**, 5188-5192 (1976). https://doi.org/10.1103/PhysRevB.13.5188

[11] H. Allaf, M. Radjai, D. Allali, A. Bouhemadou, S.S. Essaoud, S.B. Omran, R. Khenata, and Y. Al-Douri, "Ab initio predictions of pressure-dependent structural, elastic, and thermodynamic properties of $CaLiX_3$ (X = Cl, Br, and I) halide perovskites," Computational Condensed Matter, **37**, E00850 (2023). https://doi.org/10.1016/j.cocom.2023.e00850

[12] D. Allali, R. Amari, A. Bouhemadou, A. Boukhari, B. Deghfel, S.S. Essaoud, S. Bin-Omran, *et al*. "*Ab initio* investigation of structural, elastic, and thermodynamic characteristics of tetragonal XAgO compounds (X = Li, Na, K, Rb)," Physica Scripta, **98**, 115905 (2023). https://doi.org/10.1088/1402-4896/acfbfe

[13] J.I. Al-Hawarin, A.-A. Abu-Yamin, Abd Al-Aziz A. Abu-Saleh, I.A.M. Saraireh, M.H. Almatarneh, M. Hasan, O.M. Atrooz, *et al*. "Synthesis, Characterization, and DFT Calculations of a New Sulfamethoxazole Schiff Base and Its Metal Complexes," Materials, **16**(14), 5160 (2023). https://doi.org/10.1088/1402-4896/acfbf

[14] R. Samia, A. Yahia, B. Ahmed, B. Mokhtar, M. Noureddine, L. Mohamed, B. Djillali, *et al*. "Electronic, elastic and piezoelectric properties calculations of perovskites materials type BiXO3(X = Al, Sc): DFT and DFPT investigations," Chemical Physics, **573**, 111998 (2023). https://doi.org/10.1016/j.chemphys.2023.111998

[15] M. Farzan, S.M. Elahi, H. Salehi, and M.R. Abolhassani, "A Comparison of the~Structural, Electronic, Optical and Elastic Properties of Wurtzite, Zinc-Blende and Rock Salt TlN: A DFTStudy," Acta Phys. Pol. A, **130**(3), 758–768 (2016). https://doi.org/10.12693/APhysPolA.130.758

[16] A. El Hassasna, and A. Bechiri, "Electronic and Elastic Properties of TlX (X = N, P, As and Sb) in Zinc-Blende Structure," Solid State Phenom. **297**, 82–94 (2019). https://doi.org/10.4028/www.scientific.net/SSP.297.82

[17] K. Bencherif, A. Yakoubi, and H. Mebtouche, "Structural and Electronic Properties of the BN, BP and BAs in the Different Phases of Zinc-Blende, NaCl and CsCl," Acta Phys. Pol. A, **131**(1), 209–212 (2017). https://doi.org/10.12693/aphyspola.131.209

[18] R.M. Wentzcovitch, M.L. Cohen, and P.K. Lam, "Theoretical study of BN, BP, and BAs at high pressures," Phys. Rev. B, **36**(11), 6058 (1987). https://doi.org/10.1103/PhysRevB.36.6058

[19] M. Van Shilfgaarde, A.-B. Chen, S.S.A. Krishnamurthy and A. Sher, "InTlP – a proposed infrared detector material," Appl. Phys. Lett. **65**, 2714–2716 (1994). https://doi.org/10.1063/1.112567

[20] N. Saidi-Houat, A. Zaoui, and M. Ferhat, "Ab initio study of the fundamental properties of novel III-V nitride Alloys $Ga_{1-x}Tl_xN$," Materials Science and Engineering B, **162**, 26-31 (2009). https://doi.org/10.1016/j.mseb.2009.01.031

[21] H.M. Mazouz, A. Belabbes, A. Zaoui, and M. Ferhat, "First-principles study of lattice dynamics in thallium-V compounds," Superlatices and Microstructures, **48**, 560-5568 (2010). https://dx.doi.org/10.1016/j.spmi.2010.09.012

[22] B.B. Bouiadjra, N. Mehnane, and N. Oukli, "First principles calculation of structural, electronic and optical properties of (001) and (110) growth axis (InN)/(GaN)n superlattices," Revista Mexicana de Fisica, **67**(1), 7-17 (2021). https://doi.org/10.31349/RevMexFis.67.7

[23] R. Riane, Z. Boussahla, S.F. Matar, and A. Zaoui, "Structural and Electronic Properties of Zinc Blende-type Nitrides $B_xAl_{1-x}N$," Z. Naturforsch. **63**(9), 1069-1076 (2008). https://doi.org/10.1515/znb-2008-0909

[24] S. Adachi, *Properties of Group IV, III–V and II–VI Semiconductors*, (John Wiley & Sons, 2005). https://doi.org/10.1002/0470090340

[25] A. Said, M. Debbichi, and M. Said, "Theoretical study of electronic and optical properties of BN, GaN and $B_xGa_{1-x}N$ in zinc blende and wurtzite structures," Optik, **127**(20), 9212–9221 (2016). https://doi.org/10.1016/j.ijleo.2016.06.103

[26] H. Meradji, S. Drablia, S. Ghemid, H. Belkhir, B. Bouhafs, and A. Tadjer, "First-principles elastic constants and electronic structure of BP, BAs, and BSb," Phys. Status Solidi B, **241**(13), 2881–2885 (2004). https://doi.org/10.1002/pssb.200302064

[27] P. Rodriguez-Hernandez, M. Gonzalez-Diaz, and A. Munoz, Phys. Rev. B, **51**, 14705 (1995). https://doi.org/10.1103/physrevb.51.14705

[28] A. Zaoui, M. Ferhat, B. Khelifa, J.P. Dufour, and H. Aourag, "Correlation between the Ionicity Character and the Charge Density in Semiconductors," Phys. Stat. Sol. (b), **185**, 163-169 (1994). https://doi.org/10.1002/pssb.2221850112

[29] H. Belghoul, M. Oukli, F. Moulay, K. Ghlam, and H. Abid, "First-principles calculations to investigate structural, electronic and optical properties of BN by inserting an ultrathin XY(X = B, Al and Y= Bi, P, N) layer to form short-period (XY)1/(BN)1 superlattice," Optoelectronics and Advanced Materials," **18**(7-8), 363-382 (2024).

[30] S.E. Gulebaglan, E.K. Dogan, M. Aycibin, M.N. Secuk, B. Erdinc, and H. Akkus. "Structural and electronic properties of zincblende phase of $Tl_xGa_{1-x}As_yP_{1-y}$ quaternary alloys: First-principles study," Cent. Eur. J. Phys. **11**(12), 1680-1685 (2013). https://doi.org/10.2478/s11534-013-0314-1

[31] S.Q. Wang. H.Q. Ye, "," Phys. Rev. B, **66**, 235111 (2002). https://doi.org/10.1103/PhysRevB.66.235111

[32] Y. Al-Douri, B. Merabet, H. Abid, and R. Khenata, "First-principles calculations to investigate optical properties of ByAlxIn1−x−yN alloys for optoelectronic devices," Superlattice and Microstructures, **51**, 404-411 (2012). https://doi.org/10.1016/j.spmi.2012.01.004

[33] S. Alnujaim, A. Bouhemadou, M. Chegaar, A. Guechi, S. Bin-Omran, R. Khenata, Y. Al-douri, W. Yang. and H. Lu, "Density functional theory screening of some fundamental physical properties of Cs2InSbCl6 and Cs2InBiCl6 double perovskites," The European Physical Journal B, **95**, 114 (2022). https://doi.org/10.1140/epjb/s10051-022-00381-2

[34] M. Merabet, S. Benalia, L. Djoudi, O. Cheref, N. Bettahar, D. Rached, R. Belacel, Chinese Journal of Physics 60, 462 (2019). https://doi.org/10.1016/j.cjph.2019.05.026.

[35] C. Ambrosch-Draxl, and J.O. Sofo, "Linear optical properties of solids within the full-potential linearized augmented planewave method," Computer Physics Communications, **175**, 1-14 (2006). https://doi.org/10.1016/j.cpc.2006.03.005

[36] D.P. Rai, Sandeep, A. Shankar, A.P. Sakhya, T.P. Sinba, P. Grima-Gallardo, H. Cabrera, R. Khenata, *et al*. "Electronic, optical and thermoelectric properties of bulk and surface (001) CuInTe2: A first principles study," Journal of Alloys and Compounds, **699**, 1003-1011 (2017). https://doi.org/10.1016/j.jallcom.2016.12.443

[37] A. El Hassasna, and A. Bechiri, "Electronic and Elastic Properties of TlX (X= N, P, As and Sb) in zinc-Blende Structure," Solid State Phenomena, **297**, 82-94 (2019). https://doi.org/10.4028/www.scientific.net/SSP.297.82

[38] S. Ding, H. Zhang, R. Dou, W. Liu, D. Sun, and Q. Zhang, "Theoretical and Experimental studies of electronic, optical and luminescent properties for Tl-based garnet materials," J. Solid State Chem. **263**, 123-130 (2018). https://doi.org/10.1016/J.JSSC.2018.04.028

[39] B. Song, *et al*. "Optical Properties of cubic boron arsenide," Applied Physics Letters, **116**, 141903 (2020). https://doi.org/10.1063/5.0004666

[40] X. Huang, Q. Cao, M. Wan, and H.-Z. Song, "Electronic and optical properties of BP, InSe mono layer and BP/InSe Heterojunction with promising photo electronic performance," Materials, **15**, 6214 (2022). https://doi.org/10.3390/ma15186214

[41] M.M. Nobahari, "Electro-optical properties of strained mono layer boron phosphide," Scientific-Reports, **13**, 9849 (2023). https://doi.org/10.1038/s41598-023-37099-9

[42] E. da Silva Barboz, A.A. Dias, L. Graco, S.S. Carara, D. Da Costa, and T.A.S. Pereira. "Electronic, excitonic, and optical properties of zinc blende boron arsenide tuned by hydrostatic pressure," ACS Omega, **9**, 47710-47718 (2024). https://doi.org/10.1021/ACSOMEGA.4C07598

[43] C. Zhang, S. Mahadevan; J. Yuan, J.K. Wai, H.Y. Gao, W. Liu, H. Zhong, *et al*. "Unraveling Urbach Tail Effects in High-Performance Organic Photovoltaics: Dynamic vs Static Disorder," ACS Energy Lett. **7**(6), 1971-1979 (2022). https://doi.org/10.1021/acsenergylett.2c00816

[44] A. Lamichhane, "Energy–Gap–Refractive Index Relations in Semiconductors—Using Wemple–DiDomenico Model to Unify Moss, Ravindra, and Herve–Vandamme Relationships," Solids, **4**(4), 316–326 (2023). https://doi.org/10.3390/solids4040020

[45] L. Artús. M. Feneberg, C. Attaccalite, J.H. Edgar, J. Li, R. Goldhahn, and R. Cuscó, "Ellipsometry Study of Hexagonal Boron Nitride Using Synchrotron Radiation: Transparency Window in the Far-UVC," Adv. Photonics Res. **2**(4), 2000101 (2021). https://doi.org/10.1002/adpr.202000101

[46] A. Zaoui, and F. El Haj Hassan, "Full potential linearized augmented plane wave calculations of structural and electronic properties of BN, BP, BAs and BSb," J. Phys. Condens. Matter, **13**, 253 (2001). https://doi.org/10.1088/0953-8984/13/2/303

ДОСЛІДЖЕННЯ СПОЛУК TlX ТА BX (X= N, P, As) НА ОСНОВІ DFT: ПОРІВНЯЛЬНИЙ ОГЛЯД СТРУКТУРНОЇ, ЕЛЕКТРОННОЇ ТА ОПТИЧНОЇ ПОВЕДІНКИ

Абед Зуліха, Лачабі Абдельхаді, Абделалі Лаїд

Лабораторія прикладних матеріалів, дослідницький центр, Університет Сіді-Бель-Аббес, 22000, Алжир

У цій роботі представлено детальне теоретичне дослідження структурних, електронних та оптичних властивостей сполук на основі талію (TlX) та бору (BX), де X = N, P, As, у кристалічній структурі цинкової суміші. Розрахунки з перших принципів були виконані з використанням теорії функціоналу густини (DFT) в узагальненому градієнтному наближенні (GGA). Отримані результати показують, що сполуки на основі Tl демонструють нижчі загальні енергії порівняно зі сполуками BX, що вказує на вищу структурну стабільність. З точки зору електронної поведінки, сполуки BX зберігають свою напівпровідникову природу. На відміну від цього, сполуки TlX демонструють металеві або майже металеві характеристики через відсутність енергетичної щілини на рівні Фермі. Крім того, оптичні дослідження показують, що сполуки TlX мають вищі статичні показники заломлення та сильніші характеристики поглинання в області низьких енергій. Ці результати підкреслюють потенціал сполук на основі Tl для майбутнього застосування в оптоелектронних та фотонних пристроях. Загалом, це порівняльне дослідження надає цінні знання для розробки передових матеріалів для електронних та енергетичних технологій.

Ключові слова: *сполуки талію; сполуки бору; розрахунки з перших принципів; теорія функціоналу густини (DFT); електронні властивості; зонна структура; напівпровідники; TlX; BX*

East European Journal of Physics. 4. 484-495 (2025)
DOI:10.26565/2312-4334-2025-4-49 ISSN 2312-4334

PHASE TRANSFORMATIONS AND STRUCTURAL TRANSFORMATIONS OF MANGANESE SILICIDES IN THE Si-MN SYSTEM

Sh.B. Utamuradova, Sh.Kh. Daliev, J.J. Khamdamov, Kh.J. Matchonov*, A.Kh. Khaitbaev
Institute of Semiconductor Physics and Microelectronics, National University of Uzbekistan,
20 Yangi Almazar st., Tashkent, Uzbekistan
**Corresponding Author e-mail: husniddin94_04@bk.ru*
Received August 31, 2025; revised October 8, 2025; accepted October 12, 2025

A comprehensive investigation of thermally induced phase transformations in the silicon-manganese (Si–Mn) system was conducted. The study utilized X-ray diffraction (XRD), Raman spectroscopy (including chemical Raman mapping), scanning electron microscopy with energy-dispersive X-ray spectroscopy (SEM–EDS), deep-level transient spectroscopy (DLTS), and thermodynamic CALPHAD modeling. The sequence of transformations has been reliably reconstructed as follows: (i) interstitial incorporation of Mn and partial amorphization of the near-surface Si layer; (ii) nucleation and growth of MnSi (B20 structure, $P2_13$); (iii) stabilization of the higher silicide phase Mn_4Si_7 under Si-rich conditions; (iv) at T ≫ 900 °C, a partial reverse transformation to MnSi. DLTS analysis revealed three electrically active deep-level centers with activation energies of Ec–0.53 eV, Ec–0.43 eV, and Ec–0.20 eV ($\sigma_n \approx 10^{-16}$–$10^{-15}$ cm²), which correlate with the MnSi → Mn_4Si_7 transition and interface traps at the "silicide/Si" boundary. CALPHAD modeling confirmed negative Gibbs free energies of formation (ΔGf) and identified thermodynamic stability windows for MnSi (600–750 °C) and Mn_4Si_7 (800–950 °C). The resulting process map provides the technological parameters for synthesizing CMOS-compatible Si–Mn structures.
Keywords: *Silicon; Manganese; Manganese Silicides; MnSi; Mn_4Si_7; Phase transformations; XRD; Raman; SEM–EDS; DLTS; CALPHAD; Gibbs free energy*
PACS: 68.37.Hk, 33.20.Fb

INTRODUCTION

Doping silicon with transition metals is a strategically important direction in the engineering of functional semiconductor materials, aimed at broadening the spectrum of its electronic, magnetic, and thermal properties. Among the wide range of 3D-elements, manganese attracts particular attention due to its ability to form stable silicide phases, as well as to induce spin-dependent conductivity and weak ferromagnetism in the Si matrix [1-5]. The silicon-manganese (Si–Mn) system is a complex binary system characterized by a rich phase diagram with numerous intermetallic compounds of variable composition. The most studied and practically significant phases are MnSi (cubic B20 structure), Mn_4Si_7 (tetragonal), and more silicon-rich compounds such as $Mn_{11}Si_{19}$ [6-9].

These silicides are distinguished by their high thermal and chemical stability, low specific thermal conductivity, and pronounced anisotropic magnetotransport properties, including the spin-filtering effect and the anomalous Hall effect [10-14]. This combination of properties makes them candidates for applications in the fields of spintronics, thermoelectric converters, and CMOS-compatible nanoelectronic platforms [15-18].

Despite the existence of a significant body of experimental and theoretical data on the Si–Mn system, several key issues remain unresolved. The mechanisms and temperature thresholds of phase transitions during thermal processing have not been fully established. The localization of manganese atoms in the early stages of annealing (including interstitial and cluster states) is unclear. The formation conditions of the Mn_4Si_7 phase and its possible transformation back to MnSi upon further heating are insufficiently studied, as is the influence of non-stoichiometry and internal stresses on the stability of silicide phases.

A particular challenge is the reliable identification of the early stages of silicide formation at low temperatures, where Mn may still exist in a disordered form or as a dissolved atom in a-Si. Such states are difficult to distinguish using XRD methods but can be partially detected using highly sensitive vibrational spectroscopies (in particular, Raman) [18-21]. Furthermore, the use of a thermodynamic approach to analyzing phase equilibria, based on the CALPHAD (CALculation of PHAse Diagrams) methodology, is of critical importance. This approach allows for the prediction of silicide stability based on the Gibbs free energy of formation and the modeling of binary phase diagrams [21-25]. A comprehensive investigation of thermally induced phase transformations in the Si–Mn system, involving both experimental methods (XRD, Raman, XPS) and computational modeling (CALPHAD), is necessary to construct a complete picture of the phase evolution. This not only contributes to a deeper understanding of the fundamental processes of doping and diffusion in semiconductors but also opens up possibilities for the predictable synthesis of functional nanostructures with desired properties.

Thus, the investigation of phase formation and phase stability of manganese silicides in doped silicon films as a function of annealing conditions is a relevant task at the intersection of solid-state physics, materials science, and applied nanotechnology.

Cite as: Sh.B. Utamuradova, Sh.Kh. Daliev, J.J. Khamdamov, Kh.J. Matchonov, A.Kh. Khaitbaev, East Eur. J. Phys. 4, 484 (2025), https://doi.org/10.26565/2312-4334-2025-4-49

MATERIALS AND METHODS

The starting materials were single-crystalline p-type and n-type silicon wafers with resistivities ranging from 5 to 35 Ω·cm. Doping with high-purity (≥ 99.999%) metallic manganese was performed by thermal vacuum evaporation in a high vacuum environment ($P \leq 10^{-7}$–10^{-8} Torr), maintained by an oil-free turbomolecular pumping system. Manganese doping was carried out through high-temperature annealing in sealed vacuum quartz ampules at temperatures ranging from 600 to 1200 °C for durations of 0.5 to 10 hours. Upon completion of the heat treatment, the samples were subjected to either rapid quenching or slow furnace cooling. These different thermal trajectories allowed for the simulation of both near-equilibrium and metastable conditions for crystallization and phase transformation, which significantly influence the morphology of the silicide phases and the distribution of Mn within the Si matrix [25, 26].

Vibrational properties were investigated by micro-Raman spectroscopy using a SENTERRA II spectrometer (Bruker Optik GmbH, Germany). A green laser with a wavelength of λ = 532 nm and adjustable power up to 25 mW was used for excitation. Spectra were recorded in the range of 50–4265 cm^{-1} with an exposure time of 100–120 s. The spectral resolution was 4.0 cm^{-1}, ensuring the differentiation of silicide vibrational modes and Si phonon lines. To eliminate thermal shifts, a dual-channel registration of Stokes and anti-Stokes components was employed, with the actual temperature calculated using a modified Boltzmann formula [18]. The wavelength accuracy was calibrated against NIST standards (mono-Si and acetaminophen). Laser-induced heating was monitored by the ratio of the Stokes/anti-Stokes components, using the modified Boltzmann formula:

$$\frac{I_{\text{anti-Stokes}}}{I_{\text{Stokes}}} = \exp\left(-\frac{h\nu}{kT}\right)$$

The phase composition was investigated using X-ray diffraction (XRD) with a MiniFlex II instrument (Rigaku, Japan), operating at CuKα radiation (λ = 1.5406 Å). Scans were performed in the 2θ range of 3°–60° with a step size of 0.02° and a dwell time of 2 seconds per point. Phase identification was performed using the ICDD PDF-4+ database, with analysis of interplanar spacings, relative intensities, and indexing of reflections according to known structures of manganese silicides (MnSi, Mn_4Si_7, etc.) [27-30].

To study the surface morphology, microstructure, and distribution of dopant elements in the silicon samples, scanning electron microscopy (SEM) combined with energy-dispersive X-ray spectroscopy (EDS) was employed. The measurements were conducted on a ZEISS GeminiSEM 300 electron microscope (Carl Zeiss AG, Germany) equipped with an integrated EDS detector. The instrument's operating mode included an accelerating voltage of 20 kV, which provided a sufficient penetration depth for analyzing near-surface structures, and a low residual pressure in the sample chamber of approximately 10^{-3} mmHg, which eliminated the effects of contamination and plasma ionization.

DLTS measurements were performed on Schottky barrier diode structures. The top electrode was made of Au, with contact areas on the order of several square millimeters. Temperature dependencies were recorded in a liquid nitrogen cryostat with controlled heating over a working temperature interval of 80–360 K, with a setpoint stability of ±0.2 K.

RESULTS AND DISCUSSION

Figure 1 shows the DLTS spectra for an n-Si<Mn> sample, obtained at a rate window of $e = 60\ s^{-1}$. Three distinct peaks are observed in the spectra at approximately T ≈ 130–150 K, 220–240 K, and 300–320 K. An Arrhenius analysis was performed for the electron emission channel using the equation: $e^n = \sigma_n v_{th} N_c \cdot \exp[-(E_c - E_t)/kT]$, where $v_{th} \propto T^{1/2}$, $N_c \propto T^{3/2}$. From this analysis, three electrically active deep levels were identified.

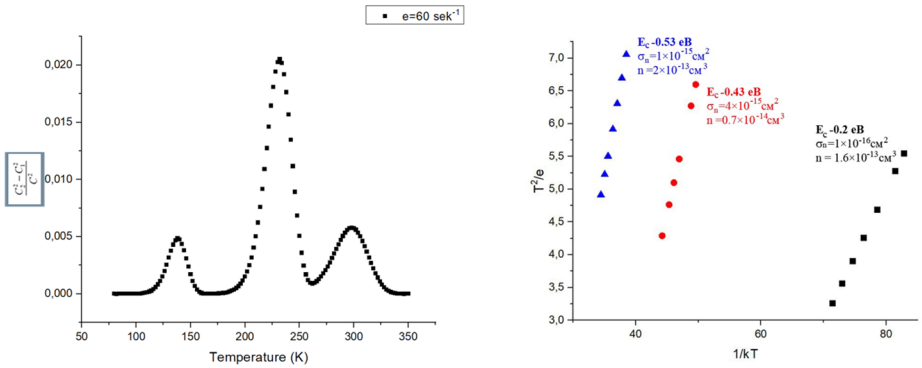

Figure 1. DLTS spectra and Arrhenius plots for the deep levels in n-Si<Mn>.

All three defects are electron traps with capture cross-sections on the order of 10^{-16}–10^{-15} cm^2. The most dominant recombination center is the E_2 level (having the largest values of σ_n and N_t).

Structural data and CALPHAD modeling indicate that heat treatment induces the nucleation and growth of MnSi nanophases, and upon further silicon saturation, leads to the MnSi → Mn_4Si_7 transformation. This transformation is accompanied by the redistribution of Mn, an increase in elastic stresses, and the formation of a well-defined "silicide/Si" interface. During this process: (i) the E_1 level (E_c−0.53 eV) correlates with Mn-related complexes in the shell of the MnSi

precipitates; (ii) the E_2 level (E_c−0.43 eV) reaches its maximum contribution during the formation of the higher silicide phase Mn_4Si_7 and the growth of misfit dislocations; (iii) the shallow E_3 level (E_c−0.20 eV) reflects the presence of interface traps at the “silicide/Si” boundary, the contribution of which increases with the coarsening of the precipitates.

The obtained experimental data provide evidence of a stepwise phase transformation in the Si–Mn system, governed by thermodynamic and diffusion factors. The phase transformation was confirmed by both X-ray diffraction analysis and Raman spectroscopy, which reflects structural changes at the level of chemical bonds and lattice symmetry (Fig. 2).

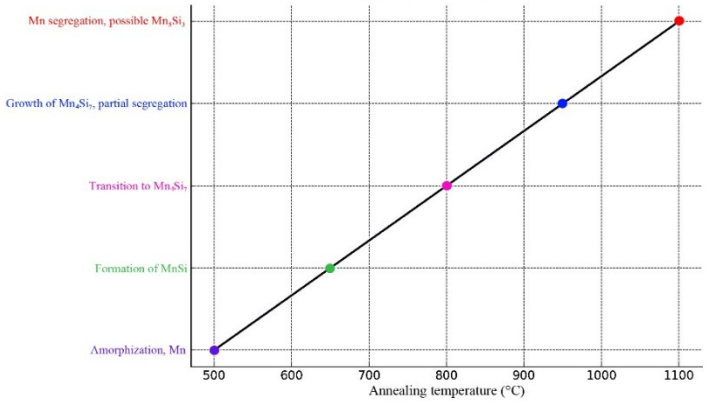

Figure 2. Stages of phase transformations in the Si–Mn system.

X-ray diffraction studies allowed for the tracking of the thermodynamically driven evolution of the phase composition in the Si–Mn system as a function of the annealing temperature. In the initial stage of heat treatment ($T \leq 600$°C), the diffractograms predominantly show broad and poorly resolved diffraction maxima, which indicates a low degree of crystallinity, a significant number of lattice defects, and partial amorphization of the upper layer (see Fig. 3). The appearance of broad maxima in the 2θ range of ≈ 28–29° may be associated with an expansion of the lattice parameter of crystalline Si as a result of the incorporation of Mn atoms into interstitial positions [31].

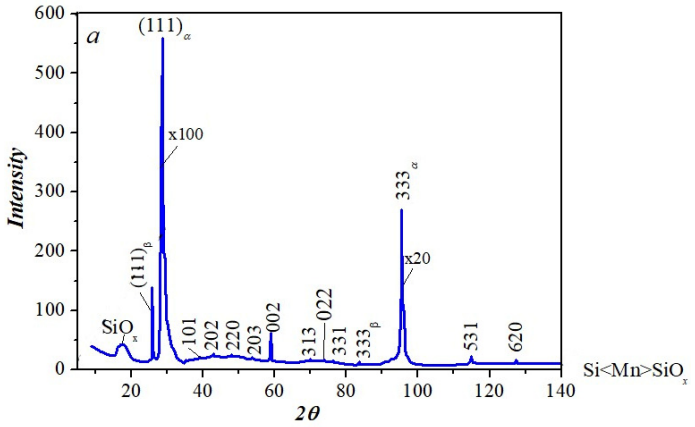

Figure 3. X-ray diffraction pattern of the Si<Mn> sample after thermal annealing and subsequent oxidation (Si<Mn>→SiO_x).

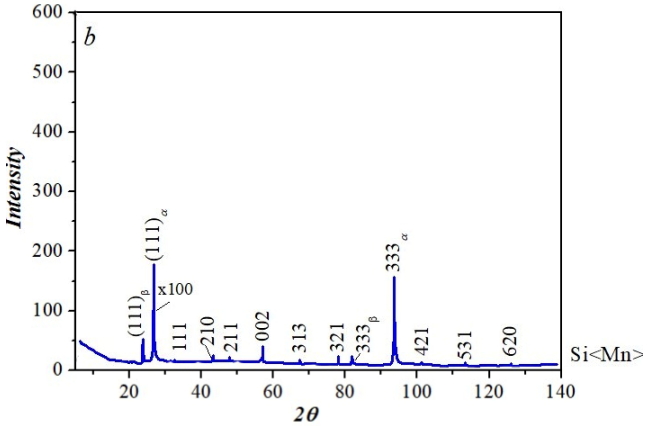

Figure 4. X-ray diffraction pattern of the Si<Mn> sample after thermal annealing (T = 900–1000 °C).

In the image (Fig. 4), diffraction peaks corresponding to crystalline silicon (Si) and the silicide phases Mn_4Si_7 and MnSi are clearly visible. Reflections (111)α, (333)α, as well as peaks from a β-phase are noted, indicating the development of a multicomponent crystalline structure. The increase in intensity and narrowing of the peaks indicate the coarsening of domains and an increase in the degree of crystallinity following high-temperature thermal treatment.

With an increase in temperature to 600–700 °C, well-defined diffraction peaks characteristic of the intermetallic compound MnSi are formed. The most intense reflections are observed at 2θ ≈ 31.6°, 36.1°, 47.3°, and 55.5°, which corresponds to a cubic structure (space group $P2_13$) according to the ICDD PDF database #01-072-0566 [32]. Concurrently, the silicon peaks, particularly (111)α and (220)α, are preserved; however, their noticeable broadening indicates residual stresses and partial lattice restructuring (Fig. 4).

In the image (Fig. 4), diffraction peaks of silicon (α-phase, e.g., (111)α) are clearly visible, as are signals corresponding to a β-phase and an oxide component (SiO_x) near 2θ ≈ 20°. The presence of multiple reflections—(101), (202), (313), (333) β—indicates the formation of a multiphase structure involving manganese silicides and their reaction products with oxygen. The increased intensity of reflections in the range 2θ ≈ 26–35° is consistent with the formation of a thin SiO_2-like layer on the surface.

In the temperature range of 800–900°C, an intensification of signals related to the Mn_4Si_7 phase is observed in the system. Its diffraction peaks are recorded in the interval 2θ = 27°–45°, including the characteristic reflections (210), (211), (002), and (313). This structure is tetragonal and thermodynamically more stable at moderate Mn concentrations [33]. The increase in intensity and the narrowing of the peak widths (as determined by the Scherrer formula) testify to an increase in crystallinity and the growth of grain domains to ~30 nm. Simultaneously, a decrease in the intensity of the MnSi lines is observed, which confirms its transformation into the more thermodynamically stable Mn_4Si_7 phase.

$$2\ MnSi + 5\ Si \rightarrow Mn_4Si_7$$

At an annealing temperature exceeding 900 °C, a further narrowing of the diffraction peaks is observed, indicating the growth of crystallites to ~40–45 nm. In individual samples, weak signals characteristic of Mn-rich phases, including Mn_5Si_3, are detected, which appear as additional lines at 2θ ≈ 43.2° and 46.8°. This may be evidence of local Mn segregation during thermodynamic overheating and a partial disruption of phase equilibrium (Fig. 5) [34].

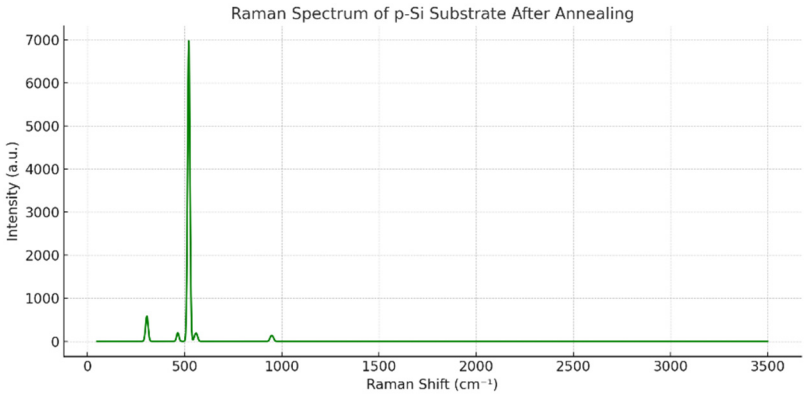

Figure 5. Raman spectrum of the p-Si substrate after annealing at 1200°C

The XRD data are consistent with the results of CALPHAD modeling and are complemented by Raman spectroscopy, which allows for a reliable reconstruction of the phase evolution of the Si–Mn system over a wide temperature range.

Raman spectroscopy is an effective method for analyzing the crystallinity, phase composition, and structural changes in silicon films doped with transition metals, particularly manganese. In crystalline silicon (c-Si), a characteristic Raman scattering line is observed at ~521 cm^{-1}, corresponding to the transverse optical (TO) phonon mode at the center of the Brillouin zone (Γ point) [35, 36]. For amorphous silicon (a-Si), this peak is broadened and shifted to the 480–500 cm^{-1} region as a consequence of lattice disorder [37].

The main peak (Fig. 6) at 521.6 cm^{-1} corresponds to crystalline silicon (the TO mode at the Γ point). The weak band near 303 cm^{-1} is due to two-phonon scattering (2TA), and the remaining peaks (554–954 cm^{-1}) may be related to second-order vibrations or traces of impurity phases. This spectrum serves as a reference for analyzing the doped films.

The doping of Si with manganese and subsequent thermal annealing promote the formation of silicide phases, such as MnSi and Mn_4Si_7, which possess their own characteristic phonon modes that can be detected in Raman spectra. For instance, crystalline MnSi (B20 structure) is characterized by modes at ~194 and ~316 cm^{-1} [35, 38], while for Mn_4Si_7, peaks in the range of 270–330 cm^{-1} are typical [39].

The intense line (Fig. 6) at 521 cm^{-1} corresponds to crystalline silicon, whereas the additional peaks at ~181, 286, 302, and 320 cm^{-1} indicate the presence of the silicide phases MnSi and Mn_4Si_7.

In the initial state (before heat treatment), the spectra of silicon films with Mn content up to 20 at.% exhibit a broad band in the 460–500 cm^{-1} interval, which indicates an amorphous or nanocrystalline structure. After annealing at 600 °C,

a narrow line appears around 521 cm^{-1}, characteristic of c-Si, along with additional peaks in the 275–320 cm^{-1} region, which is evidence of the formation of Mn_4Si_7 and $MnSi_{1.7}$ phases [39–41].

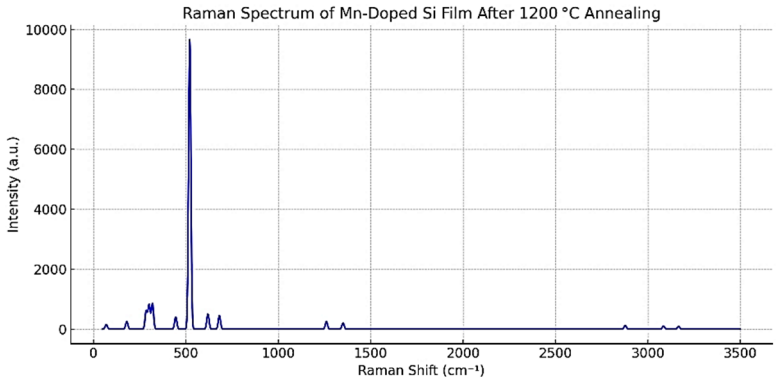

Figure 6. Raman spectrum of a silicon film doped with manganese (~20 at.%) after annealing at 1200 °C (1 h, inert atmosphere)

Increasing the annealing temperature to 900–1000 °C results in an enhancement of the intensity and a narrowing of the c-Si line, indicating the growth and ordering of Si crystallites. At the same time, the additional silicide peaks become more distinct (285, 305, and 335 cm^{-1}), reflecting the phase segregation and crystallization of Mn_4Si_7. At 1100–1200 °C, a partial transformation of the higher silicide phase into the thermodynamically more stable MnSi is observed. This is confirmed by the appearance of lines characteristic of B20-MnSi (~190 and ~316 cm^{-1}).

The shift of the silicide Raman lines compared to literature values is attributed to tensile stresses arising from differences in thermal expansion coefficients, as well as to deviations from stoichiometric composition (an excess of Mn leads to a softening of phonon modes) [36, 41]. The observed redshifts of 5–13 cm^{-1} and line broadenings of up to 15–20 cm^{-1} indicate the presence of internal defects and a size effect. Upon further heat treatment, stress relaxation is observed, accompanied by a shift of the peaks toward their tabulated values and a decrease in their width to ~8–10 cm^{-1} [38, 41].

Overall, Raman spectroscopy has enabled the stepwise tracing of the phase composition evolution in the silicon-manganese system. The formation of the Mn_4Si_7 silicide phase in the early stages of annealing, followed by a transition to MnSi at high temperatures, is consistent with X-ray diffraction data and literature sources [38–42].

In addition to point spectral analysis, visualization of the phase and chemical component distribution was performed on a p-Si<Mn> sample annealed at 1200 °C, using chemical Raman mapping techniques (Fig. 7). This methodology allows for the simultaneous acquisition of spatial and spectroscopic information with high resolution, which is critically important for studying heterogeneous nanostructures and local phase transformations [43–45].

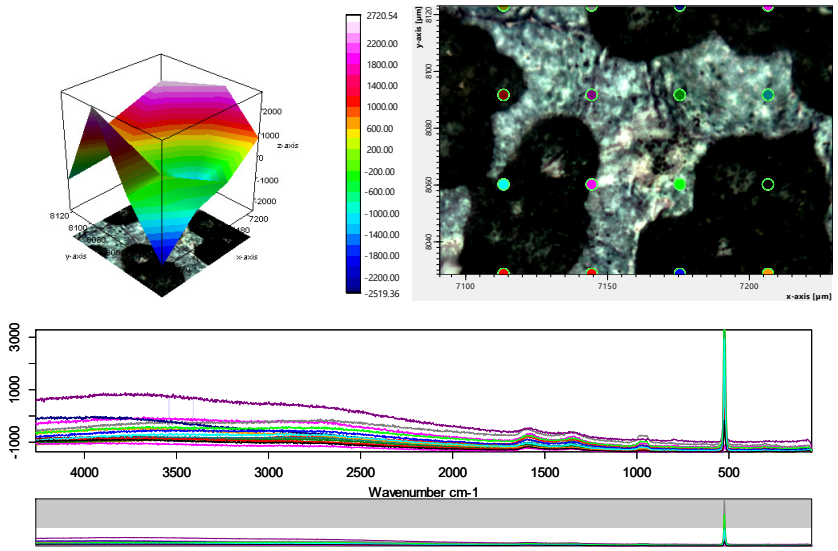

Figure 7. Chemical Raman image of the p-Si<Mn> sample after annealing at 1200 °C: signal intensity distribution (color scale, 3D), phase contrast map (top right), and integrated spectra from selected regions (bottom)

Analysis of the spectra at various points on the surface revealed an inhomogeneous distribution of band intensities in the 250–400 cm^{-1} and 520–525 cm^{-1} ranges, which is interpreted as the result of the formation of MnSi and Mn_4Si_7 phases against a background of crystalline silicon. The main Si peak (521 cm^{-1}) exhibits significant variability in intensity and shape, which is attributed to local lattice deformation and variations in manganese concentration across individual zones.

The three-dimensional reconstruction of the Raman signal intensity (upper left part of the figure) shows pronounced peaks in the range of 2000–2700 arbitrary units, corresponding to regions with a high concentration of silicide phases. The distribution map (top right) illustrates the segregation of Mn-rich areas, consistent with EDS (Energy Dispersive X-ray Spectroscopy) and XRD data. This confirms the existence of phase inhomogeneity, which forms as a consequence of Mn redistribution during high-temperature annealing and its limited solubility in the Si lattice.

Thus, chemical mapping allows for the visualization of the Mn silicide formation mechanism at the micro-level, confirming both the phase and structural evolution previously identified by XRD and point Raman spectroscopy methods.

To verify the elemental composition and evaluate the extent of manganese diffusion into the silicon substrate, energy-dispersive X-ray spectroscopy (EDX) analysis was performed on samples prepared by the thermal annealing of Mn nanofilms on a Si/SiO_2 substrate.

For the morphological and elemental analysis of the p-Si<Mn> samples, scanning electron microscopy (SEM) was used in combination with energy-dispersive spectroscopy (EDS). The investigations were conducted on a ZEISS GeminiSEM 300 microscope at an accelerating voltage of 20 kV and a chamber pressure of approximately 10^{-3} mm Hg. The analysis was performed on several areas of the surface to assess the uniformity of element distribution and the nature of the micro- and nanophases formed as a result of annealing.

The SEM images (Fig. 6a) show a homogeneous, granular structure with inclusions of varying contrast, indicating the presence of phases with different atomic masses. The elemental distribution obtained from EDS mapping (Fig. 8b–d) confirms the localization of manganese (Mn-K) predominantly in the form of separate domains and inclusions, uniformly distributed across the sample surface. Silicon (Si-K) demonstrates a continuous distribution, corresponding to the primary matrix material. Carbon signals (C-K) are interpreted as residual contaminants, possibly from the diffusion process or from interaction with the environment.

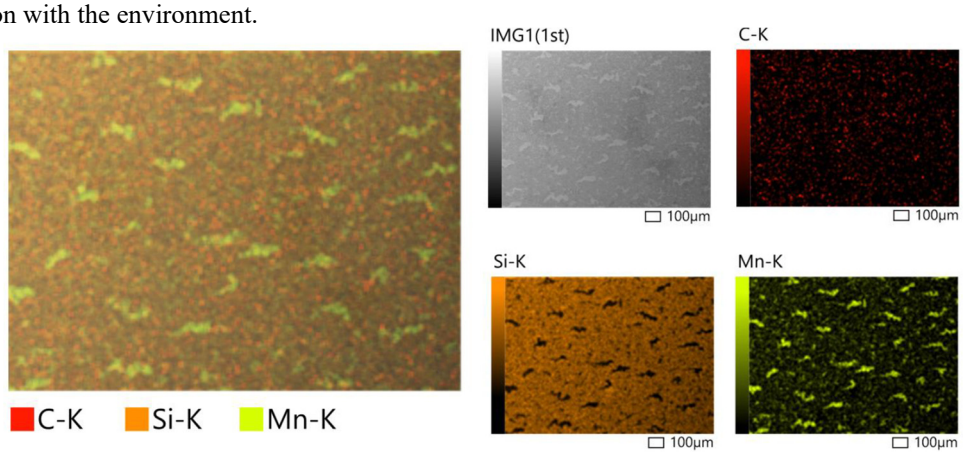

Figure 8. SEM and EDS images of the p-Si<Mn> sample surface. a) SEM micrograph at ×1000 magnification, obtained at 20 kV; b) Carbon (C-K) distribution map; c) Silicon (Si-K) distribution map; d) Manganese (Mn-K) distribution map; e) Combined EDS map of C-K, Si-K, and Mn-K distribution (in pseudo-colors: red – C, orange – Si, yellow-green – Mn). The scale bar is 100 μm

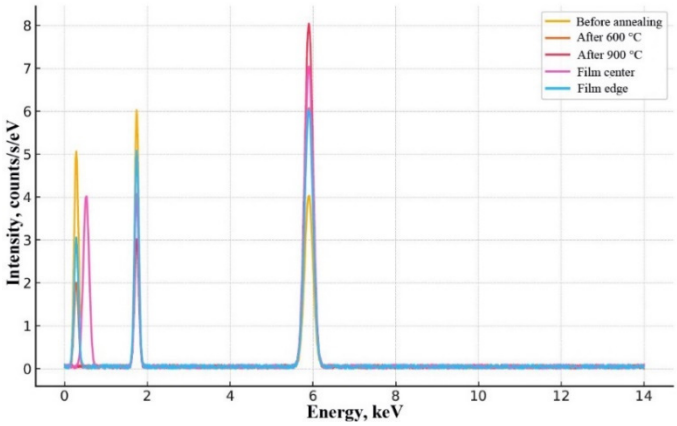

Figure 9. Comparative EDX spectra of the modified structures after annealing at 600 °C and 900 °C. The increase in the Mn Kα and Si Kα intensities, alongside a decrease in the O Kα intensity, indicates a phase transformation and the possible formation of manganese silicides

The spectra (Fig. 9) demonstrate the presence of intense peaks for Mn Kα (~5.9 keV), Si Kα (~1.74 keV), O Kα (~0.52 keV), and a weak peak for C Kα (~0.28 keV). This indicates the presence of the main component (manganese) as well as elements corresponding to the substrate and surface contaminants. A comparison of the spectra reveals that as the annealing temperature increases to 900°C, an increase in the Mn signal intensity and a relative decrease in the oxygen

signal are observed. This suggests that manganese not only diffuses into the oxide layer but also reacts with silicon, forming phases such as MnSi, Mn_4Si_7, and their derivatives.

The qualitative and quantitative analysis of the EDX spectra (Table 1) indicates a predominance of manganese (47.2 wt.%), silicon (28.5 wt.%), and oxygen (21.0 wt.%). The high oxygen content in the structure points to the presence of oxide compounds, such as MnO, Mn_2O_3, or transitional manganese silicates ($MnSi_xO_\gamma$), which is supported by literature data [46–49].

Table 1. Elemental composition of the investigated structures based on EDX analysis results

Element	Line	Mass % (wt.%)	Atomic % (at.%)
Mn	Kα	47.2	22.6
Si	Kα	28.5	38.4
O	Kα	21.0	35.2
C	Kα	3.3	3.8

At a temperature of 600°C, the initial stage of formation of the intermetallic phase MnSi can be expected, which is stable in the 550–750°C range and is characterized by a B20-type structure ($P2_13$) [49, 50]. Increasing the temperature to 900°C promotes the diffusion of Mn through the oxide layer and the formation of Mn_4Si_7 phases (Nowotny chimney ladder type structure), which possess thermoelectric properties and are stable at 800–950 °C [51, 52]. The appearance of adjacent phases, including $Mn_{11}Si_{19}$ and $Mn_{15}Si_{26}$, is also possible during local overheating [53].

The EDS mapping results are consistent with the X-ray diffraction analysis data and indicate the heterophase nature of the Mn distribution in the Si crystal lattice. It is noted that the morphology and composition of the resulting nanocomposites significantly depend on the heat treatment conditions, particularly the annealing duration and cooling rate.

Thus, the obtained EDX data confirm not only the presence of manganese on the Si/SiO_2 surface but also indicate a phase evolution of the composition with increasing annealing temperature. These results are consistent with the predictions of the Mn–Si system phase diagram and CALPHAD modeling [54].

The correlation of X-ray diffraction (XRD) analysis and Raman spectroscopy provides a comprehensive characterization of the phase composition and structural evolution in the Si–Mn system during annealing. XRD reveals the formation of crystalline phases and changes in lattice parameters, whereas Raman spectra reflect local ordering, the presence of defects, and stress fields.

Table 2. Structured scheme of phase evolution

Annealing Temperature	Phase Processes	Structural Signatures
≤ 600 °C	Matrix amorphization, interstitial incorporation of Mn, and formation of small clusters.	Broad, low-intensity XRD maxima; dome-shaped Raman lines at 480–500 cm^{-1}, absence of c-Si (521 cm^{-1}) [44-45].
600–700 °C	Nucleation of initial MnSi silicides (B20 structure).	Appearance of weak B20-MnSi reflections (XRD); Raman lines at 285–300 cm^{-1} corresponding to T-phonons of MnSi [46].
800–900 °C	Growth and ordering of Mn_4Si_7 ($MnSi_{1.7}$) phases, suppression of MnSi.	Intensification and narrowing of Mn_4Si_7 XRD peaks; Raman triplet at ~275/300/320 cm^{-1} - characteristic of the higher silicide phase [46,45].
> 900 °C	Crystallite coalescence, Mn segregation, partial transition of $Mn_4Si_7 \rightarrow$ MnSi.	Narrowing of XRD lines; stabilization of Raman lines at ~190 and ~316 cm^{-1} (E- and T-modes of B20-MnSi); decrease in FWHM and approach of frequencies to bulk values [45,46].

Thermodynamic calculations were performed within the framework of the CALPHAD approach, which revealed that at moderate temperatures and with an excess of silicon, Mn_4Si_7 is the preferred phase. However, with an increase in temperature and Mn concentration, the near-stoichiometric MnSi phase is stabilized [57]. This phase dynamic is confirmed by experiments with Mn silicides on Si substrates: observations of XRD and Raman modes indicate a transition from $MnSi_{1.7}$ to B20-MnSi with increasing temperature and annealing time [57-59].

For example, in the work by Li et al. (2022), it was shown that in MnSi films on Si(100), both $MnSi_{1.7}$ and MnSi are formed during annealing, with Raman spectral peaks at ~190 and ~316 cm^{-1} being clearly identified at temperatures ≥ 900°C [60]. Ferri et al. (2009) also reported Raman lines at ~320 cm^{-1}, associating them with polycrystalline Mn_4Si_7 inclusions [61].

The resulting phase formation scheme demonstrates consistency between the experimental XRD and Raman results, CALPHAD calculations, and literature data, thereby confirming the thermodynamic correlation of the phase composition and the kinetics of its formation.

The sequence of phase transformations with increasing annealing temperature is presented (Fig. 10): from the incorporation of Mn into amorphous silicon to the coexistence and eventual predominance of the MnSi phase. The table at the bottom of the illustration links the thermodynamically expected phases with their spectral signatures.

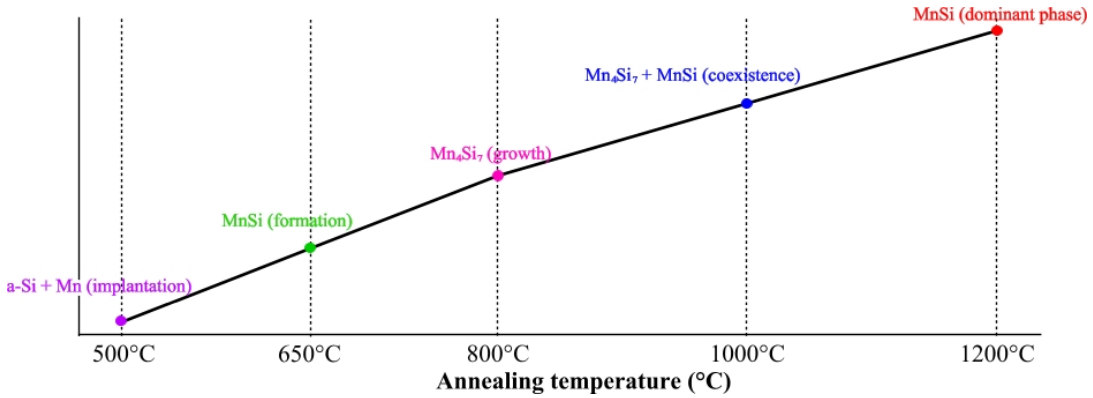

Annealing Temperature	Phase	Raman/XRD Features
≤ 600 °C	a-Si + Mn	Broad Raman bands, amorphous structure
600–700 °C	MnSi	Appearance of Raman peak ~285 cm^{-1}
800–900 °C	Mn_4Si_7	Growth of Raman lines ~275–320 cm^{-1}
> 900 °C	Mn_4Si_7 → MnSi	Narrowing of Raman bands, stabilization of Si lines

Figure 10. A scheme of phase formation in the Si–Mn system during thermal processing, based on the combined data from Raman spectroscopy and X-ray diffraction.

Thus, the comprehensive analysis of the structural (XRD) and vibrational (Raman) characteristics of the doped silicon films has not only allowed for the establishment of the sequence of phase transformations in the Si–Mn system but also for the identification of fundamental correlations between phase stability, the crystal chemistry of the silicides, and the thermal processing parameters. The formation of the Mn_4Si_7 phase at intermediate stages, accompanied by its partial transformation into B20-MnSi at elevated temperatures, confirms the existence of a thermodynamically driven segregation of components, as well as kinetic limitations associated with the diffusion of Mn in the Si matrix.

The observed shifts, broadenings, and stabilization of the Raman lines provide additional information about stresses, non-stoichiometry, and relaxation processes in the formed phases. The concordance of the experimental spectral and diffraction data with CALPHAD model calculations and literature sources on Si–Me type systems (in particular, Si–Mn, Si–Fe, Si–Co) serves as a reliable basis for generalizing the observed regularities. These results expand the understanding of phase engineering in multicomponent silicon systems and have applied significance for the design of nanostructured materials with controlled electronic and thermoelectric properties [62–64].

The CALPHAD (CALculation of PHAse Diagrams) methodology is a standardized thermodynamic approach widely used to describe phase equilibria in multicomponent systems. The method is based on the construction and parameterization of the Gibbs free energy of the phases (G) as a function of temperature, pressure, and composition, using both experimental data and results from *ab initio* calculations and statistical thermodynamics (including methods like DFT, Monte Carlo, CVM, etc.) [62].

As applied to the Mn–Si system, CALPHAD modeling has enabled a quantitative description of the phase stability and thermodynamic boundaries for the formation of the key intermetallic compounds—MnSi and Mn_4Si_7. Based on the optimized Thermo-Calc database (TCHEA, SSOL) and the work of [63], the dependences of the change in the Gibbs energy of formation (ΔGf) on temperature were calculated for the most significant phases. The summary results of the thermodynamic calculations are presented in Table 3.

Table 3. Thermodynamic parameters of phase stability in the Mn–Si system

Phase	Stability Range	Minimum ΔGf (kJ/mol)	Crystallography (PDF)	Stoichiometry
MnSi	600–750 °C	≈ –12	B20 (ICDD 01-072-0566)	Mn:Si ≈ 1:1
Mn_4Si_7	800–950 °C	≈ –15	Tetragonal (PDF 01-089-4880)	Mn:Si ≈ 4:7

As shown in the thermodynamic calculations (see Fig. 4), both phases exhibit a negative Gibbs free energy of formation within the relevant temperature ranges, confirming that their formation is energetically feasible. Specifically, the MnSi phase, which has a B20-type structure ($P2_13$), demonstrates stability at relatively low temperatures (600-750°C), where diffusion processes are limited. Still, the reactive intercalation of Mn into the Si environment is already possible. This is confirmed by experimental data, including the diffraction peaks at $2\theta \approx 31.6°$, 36.1°, and 47.3° [64].

The Mn_4Si_7 phase, which is a higher silicide structure, forms at a higher temperature range (800–950 °C). Here, enhanced diffusion and a change in the chemical potential of the components lead to a redistribution of the composition toward Si-rich silicides. The modeling predicts a local minimum for ΔG_f of around –15 kJ/mol, making this phase thermodynamically favorable under these conditions. However, the thermodynamic stability window for Mn_4Si_7 is narrow, and with a further increase in temperature, a partial decomposition of this phase is observed, with the formation of MnSi—which is more stable in the presence of excess manganese and reduced silicon activity [65].

These results are in complete agreement with the X-ray diffraction and Raman analysis data, which show that the phase sequence is MnSi → Mn_4Si_7 → MnSi (reverse), depending on the temperature regime. The behavior of the Gibbs free energy also explains the observed partial disappearance of the Mn_4Si_7 Raman bands at temperatures above 1000°C, where the dominance of MnSi is re-established.

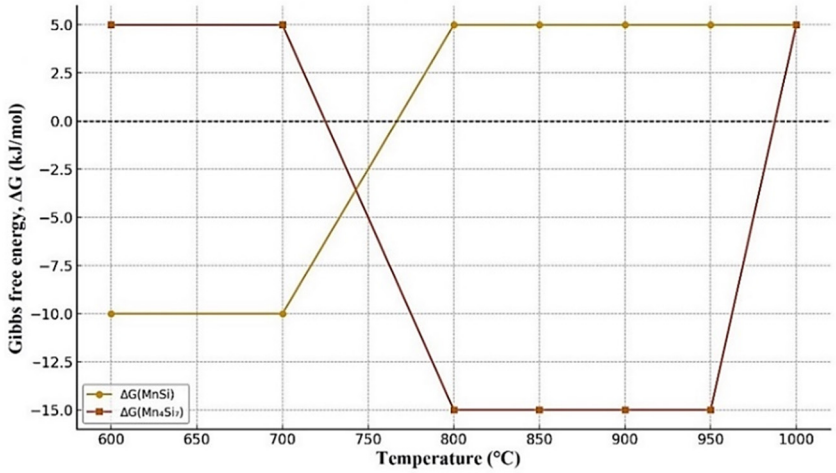

Figure 10. Temperature dependence of the Gibbs free energy of formation, ΔG(T), for the MnSi and Mn_4Si_7 phases, calculated using the CALPHAD method

The negative values of ΔGf confirm the thermodynamic feasibility of the phases. It is evident that MnSi is stable at 600–750°C, while Mn_4Si_7 is stable at 800–950°C. Thus, the thermodynamic analysis confirms the experimental observations and indicates the critical temperature intervals in which the MnSi → Mn_4Si_7 phase transition occurs. The CALPHAD model provides a reliable thermodynamic basis for describing and predicting the phase evolution in the Mn–Si system under thermal influence. It effectively complements experimental methods (XRD, Raman) and serves as a tool for designing new functional silicide structures with controlled properties. This is of fundamental importance for the targeted synthesis of stable silicide structures with desired properties in micro- and nanoelectronics.

CONCLUSIONS

The conducted research has enabled the establishment of a clear sequence of phase formation in the Si–Mn system during thermal processing, as confirmed by both experimental methods (X-ray diffraction and Raman spectroscopy) and thermodynamic modeling (CALPHAD). It was found that the phase evolution includes four key stages:

1. ≤ 600°C – Amorphization of the Si matrix with the incorporation of Mn and the formation of clusters, confirmed by a broad amorphous Raman line.
2. 600–750°C – Formation of the intermetallic phase MnSi (B20); XRD reveals weak reflections, and Raman detects modes at ~190 and ~316 cm^{-1}, which is consistent with the data from Li et al. (2022) [1].
3. 800–950°C – Growth of the higher silicide phase Mn_4Si_7; XRD peaks become more intense and narrower, and a triplet at ~275, 300, 320 cm^{-1} appears in the Raman spectra, as described by Ferri et al. (2009) [60].
4. > 950°C – Partial transformation of Mn_4Si_7 → MnSi, with crystallite coalescence and stabilization of spectral lines observed; the integrity of this data is confirmed in the work by Kim et al. (2008) [10].

CALPHAD modeling (Dupin et al., 2013) [6] showed negative Gibbs free energy values (ΔG < 0) for both phases within their respective temperature ranges, confirming their thermodynamic stability. The comprehensive correlation between experimental observations and modeling shows that MnSi is preferred at 600–750°C, whereas Mn_4Si_7 is stable in the 800–950°C range, and that a further increase in temperature shifts the system back toward MnSi due to a change in the chemical potential of manganese.

Thus, the obtained data provide a reliable experimental-theoretical scheme for phase formation in the Si–Mn system and shed light on the fundamental mechanisms of silicide growth and transformation. This has applied significance for the design of functional silicon-containing materials with a controlled phase architecture, especially in the fields of micro- and nanoelectronics.

ORCID

Sharifa B. Utamuradova, https://orcid.org/0000-0002-1718-1122; **Jonibek J. Khamdamov,** https://orcid.org/0000-0003-2728-3832
Khusniddin J. Matchonov, https://orcid.org/0000-0002-8697-5591; **Shakhrukh Kh. Daliev,** https://orcid.org/0000-0001-7853-2777

REFERENCES

[1] K.S. Daliev, Sh.B. Utamuradova, J.J. Khamdamov, M.B. Bekmuratov, O.N. Yusupov, Sh.B. Norkulov, and Kh.J. Matchonov, "Defect Formation in MIS Structures Based on Silicon with an Impurity of Ytterbium," East Eur. J. Phys. (4), 301-304 (2024). https://doi.org/10.26565/2312-4334-2024-4-33

[2] F.A. Ferri, *et al*. "Evidence of magnetic vortices formation in Mn-based sub-micrometre structures embedded in Si–Mn films," J. Phys. D: Appl. Phys. **42**, 105005 (2009). https://doi.org/10.1088/0022-3727/42/13/132002
[3] K.P. Abdurakhmanov, Kh.S. Daliev, Sh.B. Utamuradova, and N.Kh. Ochilova, "On defect formation in silicon with impurities of manganese and zinc," Applied Solar Energy (English translation of Geliotekhnika), **34**(2), 73–75 (1998).
[4] Sh.B. Utamuradova, A.V. Stanchik, and D.A. Rakhmanov, "X-ray structural investigations of n-Si<Pt> irradiated with protons," East Eur. J. Phys. (2), 201-205 (2023). https://doi.org/10.26565/2312-4334-2023-2-21
[5] Kh.S. Daliev, Sh.B. Utamuradova, Z.E. Bahronkulov, A.Kh. Khaitbaev, J.J. Hamdamov, East Eur. J. Phys. (4), 193 (2023). https://doi.org/10.26565/2312-4334-2023-4-23
[6] N. Dupin, B. Sundman, U.R. Kattner, *et al*. "Implementation of an effective bond energy formalism in the multicomponent CALPHAD approach," Calphad, **43**, 18–31 (2013). https://doi.org/10.6028/jres.123.020
[7] Sh.B. Utamuradova, and D.A. Rakhmanov, "Effect of holmium impurity on the processes of radiation defect formation in n-Si<Pt>," Physics AUC, **32**, 132-136 (2022). https://cis01.central.ucv.ro/pauc/vol/2022_32/15_PAUC_2022_132_136.pdf
[8] Sh.B. Utamuradova, A.V. Stanchik, D.A. Rakhmanov, A.S. Doroshkevich, and K.M. Fayzullaev, "X-ray structural analysis of n-Si<Cr>, irradiated with alpha particles," New materials, compounds and applications, **6**(3), 214 – 219 (2022).
[9] K.P. Abdurakhmanov, Sh.B. Utamuradova, Kh.S. Daliev, S.G. Tadjy-Aglaeva, and R.M. Érgashev, "Defect-formation processes in silicon doped with manganese and germanium," Semiconductors, **32**(6), 606–607 (1998).
[10] S. Utamuradova, S. Daliev, J. Khamdamov, K. Matchonov, M. Karimov, and K. Utemuratova, East Eur. J. Phys. (1), 276 (2025), https://doi.org/10.26565/2312-4334-2025-1-32
[11] Z. Li, *et al*. "On Curie temperature of B20–MnSi films with $MnSi_{1.7}$ admixture," Scientific Reports, **12**, 16388 (2022). https://doi.org/10.1038/s41598-022-20483-2
[12] Kh.S. Daliev, Sh.B. Utamuradova, Sh.Kh. Daliev, J.J. Khamdamov, and Sh.B. Norkulov, "The effect of dysprosium atoms introduced during the growth phase on the formation of radiation defects in silicon crystals," East Eur. J. Phys. (3), 343-347 (2025). https://doi.org/10.26565/2312-4334-2025-3-33
[13] S. Shtrikman, *et al*. "Phase Equilibria in the Mn–Si System," J. Less-Common Met. **20**, 61–71 (1970).
[14] Sh.B. Utamuradova, Kh.S. Daliev, E.K. Kalandarov, and Sh.Kh. Daliev, "Features of the behavior of lanthanum and hafnium atoms in silicon," Technical Physics Letters, **32**(6), 469–470 (2006). https://doi.org/10.1134/s1063785006060034
[15] K.S. Daliev, Sh.B. Utamuradova, A. Khaitbaev, J.J. Khamdamov, Sh.B. Norkulov, and M.B. Bekmuratov, "Defective Structure of Silicon Doped with Dysprosium," East Eur. J. Phys. (2), 283-287 (2024). https://doi.org/10.26565/2312-4334-2024-2-30
[16] K.S. Daliev, Sh.B. Utamuradova, J.J. Khamdamov, Sh.B. Norkulov, and M.B. Bekmuratov, "Study of Defect Structure of Silicon Doped with Dysprosium Using X-Ray Phase Analysis and Raman Spectroscopy," East Eur. J. Phys. (4), 311-321 (2024). https://doi.org/10.26565/2312-4334-2024-4-35
[17] Kh.S. Daliev, Sh.B. Utamuradova, A.I. Khaitbaeva, J.J. Khamdamov, J.Sh. Zarifbaev, and B.Sh. Alikulov, "Defect Structure of Silicon Doped with Erbium," East Eur. J. Phys. (2), 288 (2024). https://doi.org/10.26565/2312-4334-2024-2-31
[18] Y. Ishikawa, *et al*. "Magnetic properties of MnSi with B20 structure," Phys. Rev. B, **31**, 5884 (1985). https://doi.org/10.1103/physrevb.31.5884
[19] K.S. Daliev, Sh.B. Utamuradova, J.J. Khamdamov, M.B. Bekmuratov, Sh.B. Norkulov, and U.M. Yuldoshev, "Changes in the Structure and Properties of Silicon During Ytterbium Doping: The Results of o Comprehensive Analysis," East Eur. J. Phys. (4), 240-249 (2024). https://doi.org/10.26565/2312-4334-2024-4-24
[20] Ismaïla Kounta, *et al*. "Competitive actions of MnSi in the epitaxial growth of Mn5Si3 thin films on Si(111)," PHYSICAL REVIEW MATERIALS 7, 024416 (2023).
[21] A.Y. Boboev, I.M. Soliev, N.Y. Yunusaliyev, M.M. Xotamov, East European Journal of Physics, (3), 408–412 (2025), https://doi.org/10.26565/2312-4334-2025-3-42
[22] S. Sugahara, and M. Tanaka, "A spin metal–oxide–semiconductor field-effect transistor using half-metallic-ferromagnet contacts for spin injection and detection," Appl. Phys. Lett. **84**, 2307 (2004). https://doi.org/10.1063/1.1689403
[23] B.D. Igamov, *et al*. "Electrophysical and Thermoelectric Properties And Crystal Structure Of The Formed Mn4Si7 Thin Vacuum Coating" Advanced Physical Research Vol.7, No.2, 2025, pp. 212-221 https://doi.org/10.62476/apr.72212
[24] Kh.S. Daliev, Sh.B. Utamuradova, J.J. Khamdamov, Z.E. Bahronkulov, East Eur. J. Phys. 2, 304 (2024), https://doi.org/10.26565/2312-4334-2024-2-34
[25] Sh.B. Utamuradova, A.V. Stanchik, K.M. Fayzullaev, and B.A. Bakirov, "Raman scattering of light by silicon single crystals doped with chromium atoms," Applied Physics, (2), 33–38 (2022). https://doi.org/10.51368/1996-0948-2022-2-33-38
[26] Sh.B. Utamuradova, D.A. Rakhmanov, A.S. Doroshkevich, *et al*. "Impedance spectroscopy of p-Si<Pt>, p-Si<Cr> irradiated with protons," Advanced Physical Research, **5**(1), 5–11 (2023).
[27] M.K. Karimov, Kh.J. Matchonov, K.U. Otaboeva, M.U. Otaboev, "Computer Simulation of Scattering Xe+ Ions from InP(001)⟨110⟩ Surface at Grazing Incidence", e-J. Surf. Sci. Nanotechnol. 17, 179−183 (2019), https://doi.org/10.1380/ejssnt.2019.179
[28] S.I. Novikov, *et al*. "Formation of manganese silicides in silicon films by high-temperature annealing," Semiconductors, **54**, 1105–1110 (2020).
[29] Bruker Optik GmbH. SENTERRA II User Manual (2018).
[30] ICDD PDF-4+ Database. International Centre for Diffraction Data (Release 2023).
[31] Sh.B. Utamuradova, Kh.J. Matchonov, J.J. Khamdamov, and Kh.Y. Utemuratova, "X-ray diffraction study of the phase state of silicon single crystals doped with manganese," New Materials, Compounds and Applications, **7**(2), 93-99 (2023). http://jomardpublishing.com/UploadFiles/Files/journals/NMCA/v7n2/Utamuradova_et_al.pdf
[32] S.B. Utamuradova, S.K. Daliev, A.K. Khaitbaev, J.J. Khamdamov, Kh.J. Matchonov, and X.Y. Utemuratova, "Research of the Impact of Silicon Doping with Holmium on its Structure and Properties Using Raman Scattering Spectroscopy Methods," East European Journal of Physics, (2), 274-278 (2024). https://doi.org/10.26565/2312-4334-2024-2-28

[33] L.J. Zhang, Y. Du, H.H. Xu, *et al*. "Thermodynamic description of the Mn-Si-Zn system," Sci. China Tech. Sci. **55**, 475–483 (2012). https://doi.org/10.1007/s11431-011-4676-6
[34] A. Nicholas Grundy, Bengt Hallstedt, and Ludwig J. Gauckler, "Assessment of the Mn-O system," Journal of Phase Equilibria, **24**(1), 21–39 (2003). https://link.springer.com/article/10.1007/s11669-003-0004-6
[35] Z. Li, *et al*. "On Curie temperature of B20-MnSi films" Scientific Reports, **12**, 16388 (2022). https://doi.org/10.1038/s41598-022-20483-2
[36] E. Anastassakis, A. Cantarero, and M. Cardona, "Lattice dynamics of silicon and germanium," Phys. Rev. B, **41**, 7529 (1990). https://doi.org/10.1103/PhysRevB.41.7529
[37] D.E. Aspnes, *et al*. "Optical properties of amorphous silicon and silicon dioxide," J. Appl. Phys. **60**, 754 (1986). https://doi.org/10.1063/1.337713
[38] Z. Li, *et al*. "B20–MnSi films grown on Si(100) substrates with magnetic skyrmion signature," Materials Today Physics, **21**, 100541 (2021). https://doi.org/10.1016/j.mtphys.2021.100541
[39] F.A. Ferri, *et al*. "Evidence of magnetic vortices formation in Mn-based sub-micrometre structures embedded in Si–Mn films," J. Phys. D: Appl. Phys. **42**, 105005 (2009). https://doi.org/10.1088/0022-3727/42/10/105005
[40] B.D. Igamov, *et al*. "Electrophysical and Thermoelectric Properties and Crystal Structure of the Formed Mn_4Si_7 Thin Vacuum Coating," Advanced Physical Research, **7**(2), 212–221 (2025). https://doi.org/10.14704/nq.2025.07.02.407
[41] Y.-W. Kim, *et al*. "Formation of Mn-silicide thin films on Si substrate: structural and transport properties," Thin Solid Films, **516**, 7053–7058 (2008). https://doi.org/10.1016/j.tsf.2007.12.070
[42] T. Goto, *et al*. "High-temperature thermoelectric properties of MnSi1.7 films prepared by reactive deposition epitaxy," Journal of Alloys and Compounds, **509**, 3076–3080 (2011). https://doi.org/10.1016/j.jallcom.2010.11.101
[43] E. Smith, and G. Dent, *Modern Raman Spectroscopy: A Practical Approach*, (John Wiley & Sons, 2005).
[44] A. Misra, and M.C. Bhatnagar, "Raman Imaging in Semiconductor Materials," Materials Today: Proceedings, **49**(5), 1751–1756 (2022). https://doi.org/10.1016/j.matpr.2021.09.313
[45] Q. Ruan, *et al*. "Chemical Imaging of Silicon-Based Heterostructures Using Confocal Raman Microscopy," J. Raman Spectrosc. **50**(12), 1733–1740 (2019). https://doi.org/10.1002/jrs.5678
[46] J.S. Lee, Y.T. Kim, and H.G. Kim, "Characterization of Mn–Si thin films and their application to thermoelectric devices," Mater. Sci. Eng. B, **147**(2), 103–108 (2008). https://doi.org/10.1016/j.mseb.2007.09.017
[47] H. Flandorfer, "Binary manganese silicides," J. Alloys Compd. **489**(1), 57–60 (2010). https://doi.org/10.1016/j.jallcom.2009.09.103
[48] S.M. Sze, and K.K. Ng, *Physics of Semiconductor Devices*, (Wiley-Interscience, 2006).
[49] G. Ottaviani, and A. Modelli, "Formation of manganese silicides on Si(100): Structure and kinetics," J. Appl. Phys. **70**(7), 4029-4036 (1991). https://doi.org/10.1063/1.349637
[50] A.B. Gordienko, *et al*., "Mn silicide phases formation by ion beam synthesis," Phys. Status Solidi A, 203(14), 3452–3457 (2006). https://doi.org/10.1002/pssa.200622189
[51] X. Zhang, and Y. Shiraki, "Silicide formation in Mn/Si systems studied by RHEED and AES," Appl. Surf. Sci. **99**(4), 345–352 (1996). https://doi.org/10.1016/0169-4332(96)00358-7
[52] Y. Kurosaki, S. Yabuuchi, A. Nishide, N. Fukatani, and J. Hayakawa, "Thermoelectric Properties of Texture-controlled MnSi 1.7 -based Composite Thin Films," Int. J. Metall. Mater. Eng. **3**, 130 (2017). http://dx.doi.org/10.15344/2455-2372/2017/130
[53] W. Jeitschko, "Silicides and germanides of manganese: phase equilibria and structures," J. Solid State Chem. **6**, 363–370 (1973). https://doi.org/10.1016/S0022-4596(73)80089-2
[54] P. Franke, and D. Neuschütz, "Mn–Si (Manganese–Silicon)," in: *Binary Systems. Part 4: Binary Systems from Mn–Ni to Y–Zr*, (SpringerMaterials, 2006). https://materials.springer.com/isp/phase-diagram/docs/sm_0544667
[55] Z. Li, *et al*. "On Curie temperature of B20-MnSi films with $MnSi_{1.7}$ admixture," Scientific Reports, **12**, 16388 (2022). https://doi.org/10.1038/s41598-022-20483-2
[56] D.E. Aspnes, *et al*. "Optical properties of amorphous silicon: Raman signatures of disorder," J. Appl. Phys. **60**, 754–767 (1986). https://doi.org/10.1063/1.337426
[57] F.A. Ferri, *et al*. "Raman identification of Mn_4Si_7 in Si–Mn films: phase evolution under annealing," J. Phys. D: Appl. Phys. **42**, 105005 (2009). https://doi.org/10.1088/0022-3727/42/13/132002
[58] A.Y. Boboev, N.Y. Yunusaliyev, Kh.A. Makhmudov, F.A. Abdulkhaev, G.G. Tojiboyev, M.O. G'ofurjonova, "Surface Morphology and Roughness of Sulfur-Doped ZnO Thin Films: Analysis Based on Atomic Force Microscopy," East European Journal of Physics, (3), 319–324 (2025), https://doi.org/10.26565/2312-4334-2025-3-30
[59] E. Karhu, *et al*. "Structure and magnetic properties of MnSi epitaxial thin films," Phys. Rev. B 82, 184417 (2010). https://doi.org/10.1103/PhysRevB.82.184417
[60] F.A. Ferri, *et al*. "Evidence of magnetic vortices formation in Mn-based sub-micrometre structures embedded in Si–Mn films," Journal of Physics D: Applied Physics, **42**, 132002 (2009). https://doi.org/10.1088/0022-3727/42/13/132002
[61] A.Y. Boboev, B.M. Ergashev, N.Y. Yunusaliyev, J.S. Madaminjonov, "Electrophysical Nature of Defects in Silicon Caused by Implanted Platinum Atoms," East European Journal of Physics, (2), 431–435 (2025), https://doi.org/10.26565/2312-4334-2025-2-53
[62] N. Saunders, and A.P. Miodownik, CA*LPHAD (Calculation of Phase Diagrams): A Comprehensive Guide*, (Elsevier, 1998).
[63] A.Y. Boboev, Kh.A. Makhmudov, N.Y. Yunusaliyeva, M.O. G'ofurjonova, F.A. Abdulkhaev, G.G. Tojiboyeva, "Simulation of Radiation-Induced Structural and Optical Modifications in ZnO:S/SI Thin Film Structures," East European Journal of Physics, (3), 382–387 (2025), https://doi.org/10.26565/2312-4334-2025-3-39
[64] ICDD PDF-4+ Database, Card No. 01-072-0566 (MnSi, B20 structure).
[65] ICDD PDF-4+ Database, Card No. 01-089-4880 (Mn_4Si_7, Tetragonal).

ФАЗОВІ ПЕРЕТВОРЕННЯ ТА СТРУКТУРНІ ПЕРЕТВОРЕННЯ СИЛІЦИДІВ МАРГАНЦЮ В СИСТЕМІ Si-Mn

Ш.Б. Утамурадова, Ш.Х. Далієв, Дж.Дж. Хамдамов, Х.Дж. Матчонов, А.Х. Хайтбаєв

Інститут фізики напівпровідників та мікроелектроніки Національного університету Узбекистану, вул. Янги Алмазара, 20, Ташкент, Узбекистан

Було проведено комплексне дослідження термічно індукованих фазових перетворень у системі кремній-марганець (Si–Mn). У дослідженні використовувалися рентгенівська дифракція (XRD), раманівська спектроскопія (включаючи хімічне раманівське картування), скануюча електронна мікроскопія з енергодисперсійною рентгенівською спектроскопією (SEM-EDS), глибокорівнева перехідна спектроскопія (DLTS) та термодинамічне моделювання CALPHAD. Послідовність перетворень була надійно реконструйована наступним чином: (i) міжвузлове включення Mn та часткова аморфізація приповерхневого шару Si; (ii) зародження та ріст MnSi (структура B20, $P2_13$); (iii) стабілізація вищої силіцидної фази Mn_4Si_7 в умовах, збагачених Si; (iv) при $T \gg 900$ °C, часткове зворотне перетворення до MnSi. Аналіз DLTS виявив три електрично активні центри глибокого рівня з енергіями активації E_c–0,53 еВ, E_c–0,43 еВ та E_c–0,20 еВ ($\sigma_n \approx 10^{-16}$–$10^{-15}$ см²), які корелюють з переходом MnSi → Mn_4Si_7 та інтерфейсними пастками на межі «силіцид/Si». Моделювання CALPHAD підтвердило негативні вільні енергії Гіббса утворення (ΔG_f) та визначило термодинамічні вікна стабільності для MnSi (600-750°C) та Mn_4Si_7 (800–950°C). Отримана карта процесу забезпечує технологічні параметри для синтезу CMOS-сумісних структур Si–Mn.

Ключові слова: *кремній; марганець; силіциди марганцю; MnSi; Mn_4Si_7; фазові перетворення; рентгенівська дифракція; раманівська спектроскопія; CEM-EDS; DLTS; CALPHAD; вільна енергія Гіббса*

EAST EUROPEAN JOURNAL OF PHYSICS. 4. 496-505 (2025)
DOI:10.26565/2312-4334-2025-4-50 ISSN 2312-4334

ANALYSING THE STRUCTURAL, ELECTRONIC AND OPTICAL PROPERTIES OF Ca_3PCl_3 PEROVSKITE FOR ITS APPLICABILITY IN GREEN ENERGY AND OPTOELECTRONIC APPLICATIONS

Chakshu Malan[1], Krishna Kumar Mishra[1]*, Rajnish Sharma[2]
[1]*Chitkara University Institute of Engineering and Technology, Chitkara University, Rajpura, Punjab-140401, India*
[2]*School of Engineering and Technology Chitkara University, Solan, Himachal Pradesh- 174103, India*
**Corresponding Author e-mail: krishna.mishra@chitkara.edu.in*
Received August 18, 2025; accepted October 6, 2025

The objective of this research is to provide a detailed examination of ways to improve the efficiency of perovskite Ca_3PCl_3 in optoelectronic and solar cell applications. The substance known as Ca_3PCl_3 is classified in the same category as perovskites that are composed of inorganic metal halides. In the scope of this study, the density functional theory (DFT), that are the base principle, was used to examine the optical, electrical, and structural characteristics. The generalized gradient approximation (GGA), the Perdew Burke–Ernzerhof functionals, and the linear combination of atomic orbital calculator are the tools that are utilized to gain an understanding of the characteristics of the Ca_3PCl_3 perovskite. The key point includes the material's direct band gap, which is measured to be 20.35eV at the Γ-point. It has also been found that the dielectric function and absorption spectra change depending on the photon's energy. It has been reported that the extinction coefficient is 3.6963×10^4 and the refractive index is 1.4410. Therefore, studying Ca_3PCl_3's optical properties is crucial for considering this material for future use in photovoltaic and optoelectronic devices.
Keywords: *Structural properties; Optical properties; Electrical properties; Layer separation*
PACS: 71.20.−b, 77.22.−d, 78.20.Ci

1. INTRODUCTION

The significance of solar energy as a green, sustainable as well as enduring primary energy source is unquestionable. In comparison to conventional energy sources, solar photovoltaic technology clearly emerges as the superior choice. Photovoltaic cells efficiently convert light energy into electrical energy with minimal losses. Because of its widespread availability of irradiance absorption and allowable band gap for semiconductor devices, industrial photovoltaic systems are of major type. Additionally, their manufacturing process is very cost-effective. Perovskite compounds have garnered a lot of attention throughout the past few years as potential substitutions for traditional photovoltaic solar materials from a variety of fields. Silicon (Si), cerium titanate (CdTe), gallium arsenide (GaAs), and copper indium gallate selenide (CIGS) are all examples of such materials [1-4]. Having the capacity to absorb light across a wide range of wavelengths is absolutely necessary in order to create semiconductor devices that have the appropriate energy gap [5-7]. The operational characteristics of inorganic metal halide perovskites, Considerable attention has been created by their semiconducting solid-state nature, high absorption coefficients, and low reflection rates. [8-10].

During the last thirteen years, there has been a significant increase in the power conversion efficiency (PCE), which has risen from 3.8% to 26.1% [11-13]. Nevertheless, the extensive utilization of these potential attributes is made difficult by a lack of consistency. The perovskites' stability is extremely susceptible to moisture, air, light and temperature, making them particularly sensitive in real-world situations [14]. In the year 1839, Gustav Rose made the discovery of perovskite substance, which was subsequently called after the notable Russian mineralogist Lev Perovski. The term "perovskites" does not refer to the complex oxides of calcium and titanium ($CaTiO_3$) in particular rather, it refers to a group of chemicals that have the chemical formula ABX_3, where X represents an anion whereas A and B represent cations of varying sizes, typically, A is cation of a bigger metal as compared to B [15-21]. Ions of transition metals usually occupy the B-site, while ions of rare earth or alkaline earth elements usually occupy the A-site. Particularly perovskite oxides are referred to by the symbol ABX_3[22-24]. Furthermore, the development of solar cell technology has been greatly aided by ABX_3 cubic perovskites, which are characterized by high symmetry space group Pm-3m. The reason for this is that parity facilitates transitions in close proximity to the band edge, hence enhancing their light absorption capabilities and increasing their charge mobility. By adjusting the bandgaps of these materials, it becomes possible to have more versatility in capturing solar energy across a wider range of wavelengths, hence enhancing the structural advantages. Whereas Ca_3PCl_3, which is a perovskite compound, is advantageous in a number of ways, this material is well-suited for many technical uses, especially in the fields of photovoltaics and optoelectronics. Because it is suitable for large-scale manufacturing utilizing scalable fabrication techniques, Ca_3PCl_3, demonstrates a tremendous potential for the creation of solar cells and optoelectronic devices that are both high-performance and cost-effective. Optoelectronic devices facilitate the development of connections between the structure, mechanism, characteristics, and performance of materials. These electrical devices are available in a wide variety of combinations. Efforts are currently underway to develop computational techniques that can improve the discovery of materials suitable for high-performance optoelectronic devices [25-30]. Furthermore, apart from the ongoing investigation

Cite as: C. Malan, K.K. Mishra, R. Sharma, East Eur. J. Phys. 4, 496 (2025), https://doi.org/10.26565/2312-4334-2025-4-50

into innovative perovskite halide materials for possible application in solar cells and other optoelectronic devices, these materials can also be modified to possess flexibility and lightness, which provides a major benefit [31-35].

The selection of materials that are used in the production of flexible electronic devices has a significant impact on the performance, durability and flexibility of these devices within the industry. Combining a number of different materials makes it possible to create a technical gadget that may be used in a variety of contexts. As a result of its unique nature, which demonstrates great performance and technological priority, the halide perovskite is defined by its high level of cost-effectiveness and efficiency [36-42].

The aim is to address the discovered significant research gaps by concentrating on the different qualities. Possible results of this study include expanding our knowledge of perovskite material behaviour and encouraging the creation of new compositions that provide an environmentally friendly and practical substitute for current solar power systems, both of which aim to overcome the current limitations of perovskite solar cells.

Our methodological approach included calculating the density of states and band structure (DOS), and we have computed the elastic constants as well. The compound's stability was determined by using the Born-Huang inequality equations. Additionally, the mechanical constants, such as Young's modulus, shear modulus, and bulk modulus, were computed by employing the equations that relate to each of these constants. These equations offer extremely helpful information regarding the elasticity of the material as well as its capacity to withstand deformations.

Throughout the entirety of the work, there are four separate sections that have been incorporated. Within the introduction part, there is a description of the objectives and scope of our research. Presented in the second section is an explanation that is both clear and simple to understand of the computational methods that were applied. In the third section, our findings are reported and analyzed in detail. Each of the significant results and the consequences of those findings are detailed out in great detail in the fourth section. Based on the findings of the investigation, it offers a complete analysis and draws conclusions.

2. COMPUTATIONAL DETAILS

The primary objective of this research is to enhance the quality of Ca_3PCl_3 material that is used in the production of new perovskites. During the process of improving the bandgap, we explored its possible applications in the conversion of solar energy and in optoelectronic devices. In order to carry out the analysis, we use Quantum ATK software program to do computations based on the Density Functional Theory (DFT). Using the Materials Project database, we first gathered information about the A_3BX_3 type crystal, which contains 7 atoms per unit cell.

For the purpose of determining the structural properties of the novel perovskite Ca_3PCl_3, calculations were carried out with the assistance of the exchange–correlation generalized gradient approximation (GGA) and the Perdew–Burke–Ernzerhof (PBE) functionals for linear combination of atomic orbitals (LCAO) calculator [43-45]. Quantum ATK Tool, version- 2023.12 was utilized in order to carry out these calculations.

The band structure and partial density of states of Ca_3PCl_3 both are analysed in Brillouin zone using computational methods. In order to get accurate computations, the Brillouin zone was partitioned into a grid of points using a K mesh of order (5×5×5), with a density mesh cutoff of 60 Hartree. A convergence tolerance of 0.0001 was consistently maintained throughout the whole procedure. The process of optimization was modified by employing the Fermi–Dirac occupation approach over 9 self-consistent field phases. Both the Fast Fourier Transform (FFT) method and the Poisson solver have been applied. For the identification of eigen values, a medium pseudopotential was used. For calcium, PseudoDozo [z=10], PseudoDozo [z=5] for phosphorous and for chlorine it is PseudoDozo [z=7]. By this technique, researchers are able to get a deeper understanding of the material's potential that uses in a variety of fields, including semiconductor devices and catalysis, among others.

3 RESULTS AND DISCUSSION

3.1 Structural Properties:

Perovskites are a group of materials characterised by their distinctive crystal structure, which can be expressed by the formula ABX_3. Ca_3PCl_3 belongs to the same chemical family with a Pm-3m cubic face and is formed of 7 atoms as its basic building block. Figure 1(a) displays the crystallographic structure of Ca_3PCl_3, which forms in the Pm-3m space group, is indicated schematically.

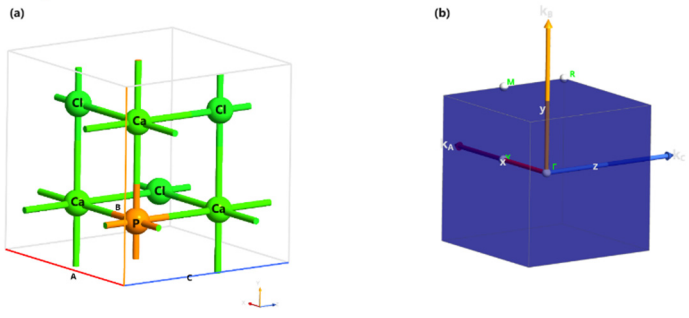

Figure 1. (a) The ideal framework of Ca_3PCl_3 perovskite and (b) k-path of Brillouin zone

Within the unit cell, the Cl atom is positioned at the edge of the face, The phosphorus atom is precisely located at the centre of the crystal, and the Ca atom is located at the vertex of the crystal. The k-path that is represented within the Brillouin zone (BZ) of the atomic structure is shown in Figure 1(b). Due to the high symmetry points (Γ-X-M-Γ-R-X-R-M), the Brillouin Zone occupies a position of great significance. The bond length of Ca-P and Ca-Cl in Ca_3PCl_3 perovskite material is 3.0005 Å. The behaviour of electrons at high-symmetry k-points is an important bit of information that is needed in order to have a thorough understanding of the conductivity, energy bandgap and electrical properties of the material.

To determine the minimum energy of the ground state and maintain the stability of the lattice, the lattice constant that leads to the lowest energy in the actual environment is of most significance. Lattice constant of Ca_3PCl_3 perovskite is 6.001Å as shown in Table 1. The rise in ion radius has been found to have a direct association with the modification of lattice constant, unit cell volume and density that has been discovered. Our optimization of the geometry turned out to be reliable with the comparison that had previously studied. The findings of our investigation indicated that the conclusions were in agreement with the findings of further theoretical studies that had been conducted. According to Apurba et.al [46] and Rasidul et.al [47], in their research they find the value of approximate to 6.00 Å as the lattice constant of Ca_3PCl_3. With the help of the comparison, we were able to show that the approaches that we use to optimize geometry are accurate.

Table 1. Positioning of Ca_3PCl_3 lattice parameters

Material		Lattice constant (Å)	Lattice type	Unit cell volume	Space Group	Density
Ca_3PCl_3	Present study	6.001	Simple cubic	216.1Å^3	Pm-3m (221)	1.979 g/cm^3
	Others study	5.69 [46]	Simple cubic	-	Pm-3m (221)	-
		5.725 [47]	Simple cubic	-	Pm-3m (221)	-

In addition, by analysing their mechanical characteristics by examining the elastic properties of system. Fundamental elastic constants that are C_{11}, C_{22} and C_{44}, can be used to evaluate the mechanical properties of perovskite [48-49]. According to the findings of our research, the values of C_{11}, C_{12}, and C_{44} are 44.78, 11.25 and 15.82 respectively as shown in Table 2. The Born-Huang stability criteria have become known as the necessary conditions for a cubic structure to be stable, $C_{44} > 0$, $C_{11}-C_{12} > 0$ and $C_{11} + 2C_{12} > 0$. Furthermore, the elastic constants were used to establish the material properties, such as the Bulk modulus, shear modulus and Young's modulus, in order to determining the ductility and brittleness of a material [50-53]. On the other hand, poisons ratio that is calculated is 0.2008 which measures the number of dimensional changes that occur when a material is subjected to a load. Mechanical properties make this material perfect for flexible electronics. Solar cells and data storage systems that need regular performance satisfying the needs of modern applications that require strength and flexibility.

Table 2. The calculated values of elastic constants of the Ca_3PCl_3 compound

Material	C_{11}	C_{12}	C_{44}	Bulk modulus (B)	Shear modulus (G)	Young's modulus (Y)
Ca_3PCl_3	44.78	11.25	15.82	22.4245	16.2002	40.2578

2.2 Electronics Properties

3.2.1 Band Structure

A substance's electronic properties are those that pertain to creation and flow of electrons inside its molecular structure [54]. Understanding the electronic band structure allows one to predict the electron behaviour in materials, light absorption and electrical conductivity. The band structure and the electron density of states are the two types of properties that are associated with electrical devices [55].

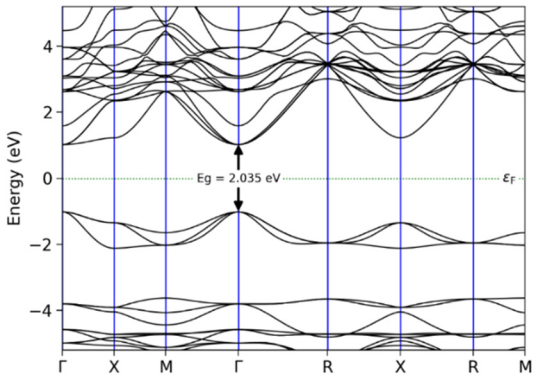

Figure 2. The electronic band structures of Ca_3PCl_3 perovskite

A representation of the energy band structure of Ca_3PCl_3 with BZ points (Γ-X-M-Γ-R-X-R-M) is presented in Fig. 2, encompassing a range of -5 to 5 electron volts. In Table 3, Ca_3PCl_3 has been shown to have a direct band gap of 2.035 eV,

while the CBE is 1.0189 eV and the VBE is -1.0163 eV from measurements that were taken. It is at the Γ-point, which is the central point within the Brillouin zone, that the conduction band and the valence band exhibit their lowest and highest energy points, respectively. This characteristic is preferable for optoelectronic devices, as it indicates the potential for effective charge carrier mobility.

Materials with a bandgap lower than 3.1 electron volts hold great potential for the development of devices that utilize visible light. Across the energy range of 1.2-12.3 eV, the perovskite exhibits considerable differences in its optical features, which makes it suitable for use, such as light-emitting diodes (LEDs) or photodetectors that are designed to detect ultraviolet light, as well as solar cells that are purpose-built to detect visible light [56]. Based on the calculations, Ca_3PCl_3 has a direct band gap, making it a perfect material for use in optoelectronic devices.

Table 3. Electrical Properties of Ca_3PCl_3 Perovskite

Material	Direct Bandgap (eV)		CBE (eV)	VBE (eV)	Layer separation (Å)
Ca_3PCl_3	Present study	2.035	1.0189	-1.0163	6.00
	Pervious study	2.208[46]	-	-	-
		2.109[47]	-	-	-

3.2.2 Complex Band Structure

A material's transport characteristics can be derived from its complex band structure, which also allows in identifying the charge carriers that contribute to tunnelling currents within the band gap. There are two different sorts of modes that are included in the complex band structure (CB), these modes are a propagating mode and a decaying mode, as shown in Fig. 3. It is possible to make use of the value of the wave vector (k) that has been provided for any of the two different sorts of modes. Within the same directional spectrum, decaying modes are described by a complex Bloch phase factor, whereas propagating modes are characterized by a real Bloch phase factor in the direction opposite to the C axis.

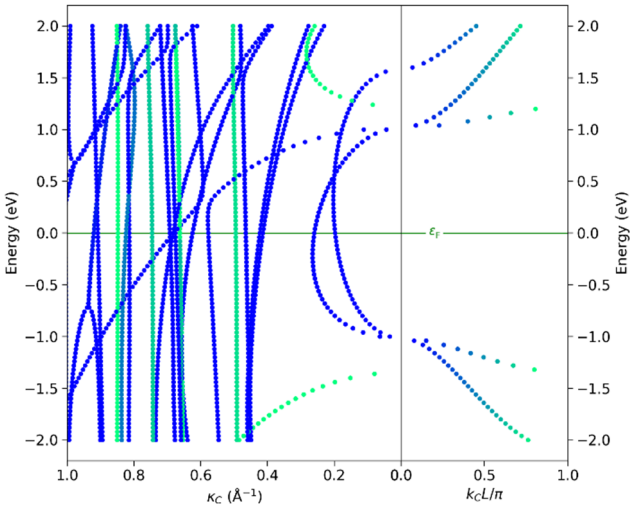

Figure 3. Complex band structure of novel perovskite Ca_3PCl_3

In the field of optoelectronics, our investigation of the CBS aims to throw provide light on the potential applications of these materials. The real values of k_c represent the conventional Bloch states, which are observed on the right side of the diagram. Conversely, complex k_c values are associated with states that are in proximity to the material's surface. With a layer separation of 6.00 Å, the presence of Ca_3PCl_3 is shown by the CBS. Therefore, this study's findings show that the novel Ca_3PCl_3 perovskite halide is a great material to employ in the production of optoelectronic devices.

3.2.3 Density of State

When it comes to the perovskite halide Ca_3PCl_3, the density of states (DOS) is all about how the electronic states are ordered throughout the material's different energy levels. This is related to the composition of the substance. By utilising density of states, one can find out considerable amount of information about the electrical structure and characteristics of the materials. Crystal structure, bandgap and electron density between atoms are three important variables that define the DOS.

Fig. 4 shows the distribution of density of states for Ca_3PCl_3. It covers an energy range from -5 to 5 eV. The energy spectrum is fully occupied by the hybrid states of phosphorous (P) and calcium (Ca) in conjunction with chlorine (Cl). Density of states identifies peaks at -4.7 eV, -3.8 eV and -1.9 eV within the valence band (left side) and 4.4 eV, 3.4 eV and 3.3eV in the conduction band (right side). In optoelectronic applications, direct bandgap semiconductors are frequently chosen because of their exceptional efficiency in optoelectronic conversions and solar cells, this paper details the electrical properties of Ca_3PCl_3, offering insight into its potential usage.

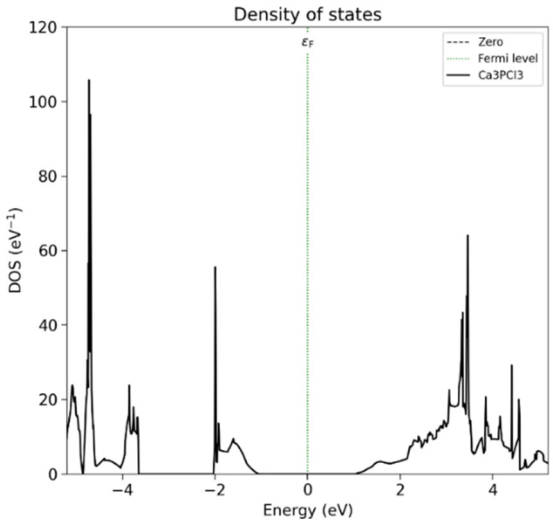

Figure 4. Total density of states of novel perovskite Ca_3PCl_3

3.2.4 Projected Density of States

Projected density of states (PDOS) of Ca_3PCl_3 provides information about the distribution of electronic states among the calcium, phosphorus and chlorine atoms. It gives information regarding the electrical configuration of the compound as well as the bonding characteristics that are important when knowing its properties in various applications. This illustrates the way in which orbitals from each individual atom contribute to the overall density of states of the complex [57-58].

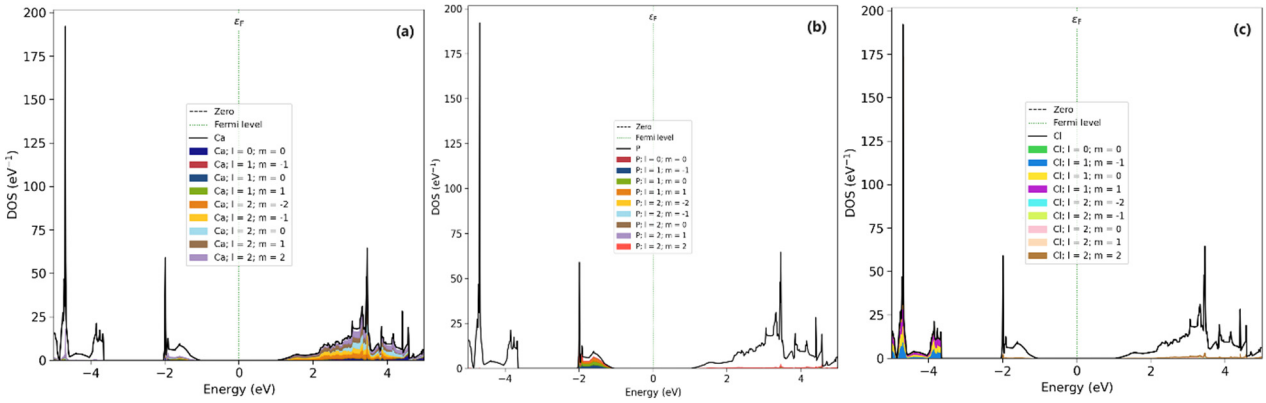

Figure 5. Projected density of states of Ca_3PCl_3 perovskite

The calculation of a PDOS takes place using an energy range from (-5 to 5 eV). Figure 5 (a-c) shows the PDOS of particular atoms of Ca_3PCl_3. According to the results of our research, the p-orbital densities of phosphorus (P) and chlorine (Cl) have a significant impact on the behaviour of the valence band (VB) also the calcium d-orbital has an effect on the conduction band (CB). The presence of these energy levels allows for a diverse variety of electron states to make contributions to the valence band.

3.2.5 Electron Density

The electron density distribution forms a cloud around the atoms during the bonding process. As the density of this cloud increases, it represents the probability of an electron being found in a certain location. For stronger bonding interactions, a higher density is preferred. When attempting to identify the electronic properties of a material, it is necessary to investigate the electronic charge density of the material [59-61]. Presented in Figure 6(a) is a two-dimensional representation of the crystallographic plane. Each colour on the bottom-right scale bar represents a different strength of the electron density.

An illustration of a viewpoint that appears to be comparable to that of a bird's eye view may be obtained from Figure 6(b). It is much simpler to understand the manner in which the charges are dispersed surrounding the atoms in different amounts within the structure. The three dimension image of charge distribution can be seen in Fig. 6(c), from this one can acquire a comprehensive understanding of the distributing of charges around atoms with different levels of intensity.

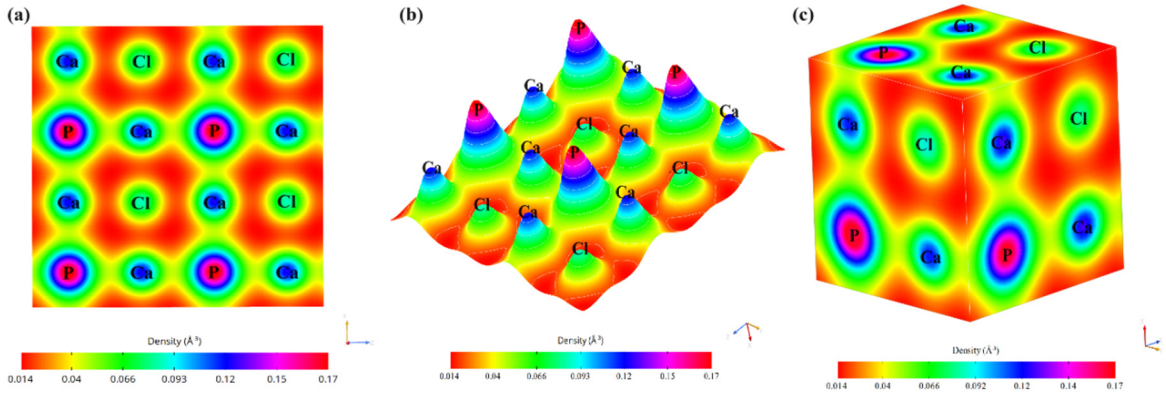

Figure 6. The charge density distribution of Ca_3PCl_3 can be visually represented in three different ways: (a) a two-dimensional depiction, (b) a top-down perspective resembling a bird's eye view, and (c) a three-dimensional view

3.3 Optical Properties

These properties of Ca_3PCl_3 make it highly suitable for extensive application in the field of optoelectronics. Thorough testing is necessary to ascertain the suitability of materials for application in solar cell and optoelectronic devices [62]. Several optical properties, including as the absorption coefficient, conductivity, dielectric functions, reflectivity, extension coefficient and refractive index, are included in the of this study and shown in Table 4. A material's optical qualities are affected by its light-reactivity and light-adjustment capabilities, which are in turn affected by its interaction with light. In the following equation of the dielectric function, the real and imaginary parts are denoted by the symbols (Re(ε)) as well as (Im(ε)), respectively.

$$\varepsilon = \mathrm{Re}\,(\varepsilon) + \mathrm{Im}\,(\varepsilon) \tag{1}$$

Where absorption coefficient indicates that it has improved capacity to absorb light of varying wavelengths as compared to other compounds. The real and imaginary dielectric functions can be used to calculate absorption coefficient. The absorption coefficient of a perovskite made of Ca_3PCl_3 has been shown in Figure 7(a).

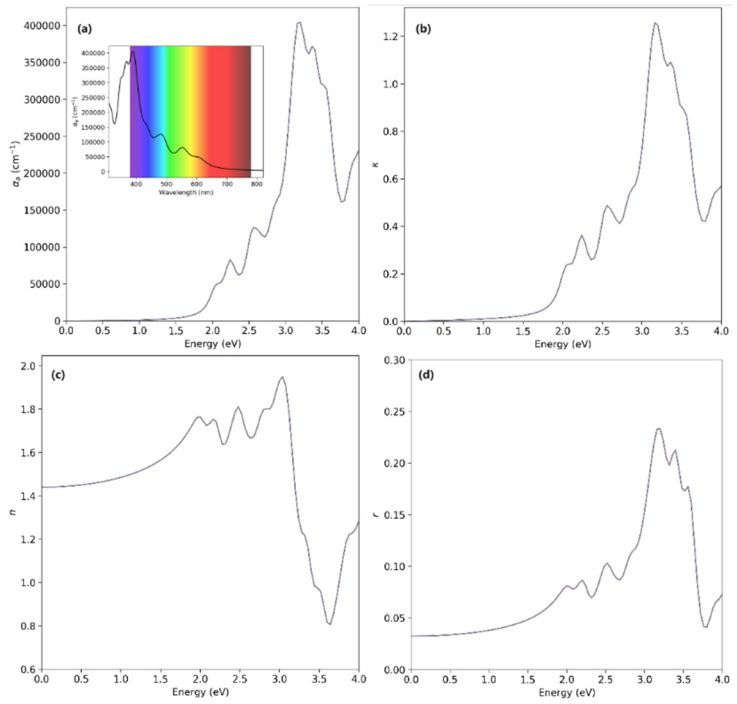

Figure 7. The real coefficients of optical constants Ca_3PCl_3: (a) absorption coefficient (α), (b) extinction coefficient (k), (c) refractive index (n) and (d) reflectivity (r)

From the observed value, the highest absorption peak is observed at 3.2 eV, corresponding to 404615 cm^{-1}. This, in turn, would raise the competitiveness of these materials in the market for solar components. Whereas, the extinction coefficient is a measure of the reduction in electromagnetic radiation within a substance, determined by measuring the imaginary part of the refractive index. On the other hand, the real component denotes the velocity at which EM waves travel through the substance. The material Ca_3PCl_3 exhibits a low κ value of 0 eV, suggesting its minimum absorption at low energies (3.6963×10^{-5}) as shown in Fig. 7(b). The refractive index (η) is a quantitative measure used to determine the

stability of a material in different device applications by measuring the changes in the speed of light within the material. This specific parameter is an aspect of the complex interaction that occurs between light and a material. In Fig 7(c), the material's refractive index, indicating a substantial level of light interaction within this energy range during its propagation. When developing antireflective layers for solar cells, it is feasible to utilize materials with a high refractive index [63]. The calculated value of refractive index is 1.4410. Furthermore, when subjected to electromagnetic radiation, including visible light, Ca_3PCl_3 perovskite exhibits a certain quantity of light that it reflects. Depending on a variety of parameters, including surface shape, crystal orientation and composition, perovskite materials can display significant changes in their overall reflectance [64]. However, the reflectivity of the Ca_3PCl_3 perovskite can be affected by both the wavelength of light and the angle of contact with the substance. The reflectivity of Ca_3PCl_3 is 0.0326, as depicted in Fig 7(d).

Ca_3PCl_3 complex coefficient reflects the compound's geometric image's imaginary unit coefficient. The chemical composition Ca_3PCl_3 contains calcium, phosphorus, and chlorine. Under certain conditions, a molecule with an imaginary coefficient may undergo complex bonding or phase transition.

Table 4. Real and optical properties of Ca_3PCl_3 perovskite

Material	Properties		Units	Values
Ca_3PCl_3	Real	Absorption coefficient	cm^{-1}	404615 (3.2 eV)
		Extinction coefficient	-	3.6963×10^{-5}
		Refractive Index	-	1.4410
		Reflectivity	-	0.0326
	Complex	Optical Conductivity	$AV^{-1}cm^{-1}$	1760.05 (3.12 eV)
		Dielectric constant	-	2.0766
		Polarizability	cm^2v^{-1}	2.0602×10^{-39}
		Susceptibility	-	1.0766

Optical conductivity is a property of a material that quantifies the correlation between the magnitude of the electric current generated in the material and its current density, leading to the generation of an electric field at a particular frequency [65]. As shown in Fig. 8(a) the value of real optical conductivity is 1760.05 $AV^{-1}cm^{-1}$ at 3.12 eV. Whereas the real part of the dielectric constants predicts the value of 2.0766, as shown in Fig 8(b), indicating reduced internal power dissipation.

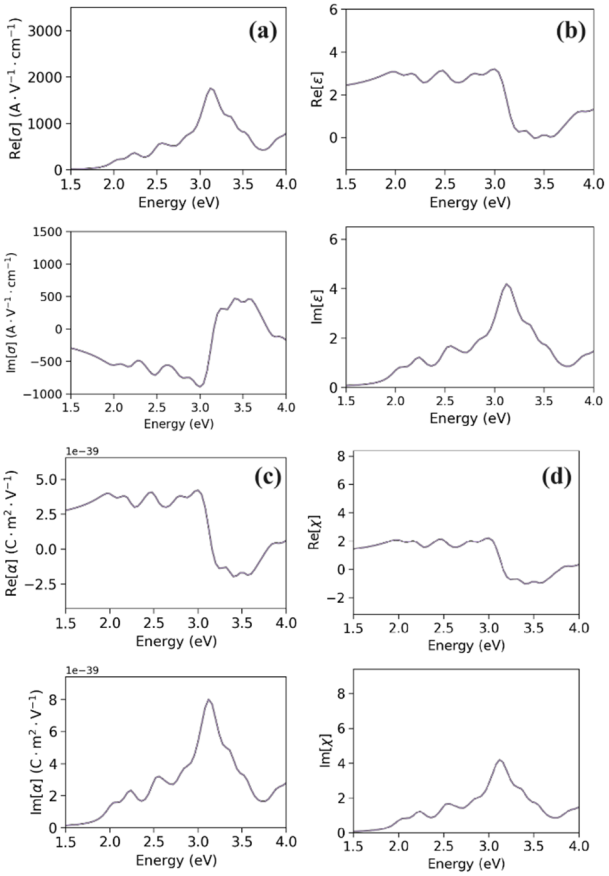

Figure 8. The optical constants Ca_3PCl_3 are determined by the complex coefficients of optical conductivity (σ), dielectric constant (ε), polarizability (α), and susceptibility (χ)

This is beneficial for enhancing solar cell efficiency. Furthermore, the actual Re[α] component of dielectric constant represents influence of polarization and dispersion on material. Figure 8 (c) depicts the polarizability of recently discovered halide perovskite. This graphic includes both the real Re[α] polarizability and an imaginary Im[α] polarizability. The real polarizability value of Ca_3PCl_3 is $2.0602\times10^{-39}cm^2\ V^{-1}$. We have also calculated the value of susceptibility of Ca_3PCl_3 as shown in Fig 8(d), the calculated real value Re[χ] is 1.0766 reported in our work. According to the findings, Ca_3PCl_3 possesses excellent features for converting solar energy, especially in terms of its optical conductivity, which makes it best use in solar cells.

CONCLUSIONS

In a nutshell, our investigation consisted of utilizing DFT calculation in order to investigate the material Ca_3PCl_3, with a particular emphasis on the structures, optical properties, electrical properties, and mechanical properties of the material. The value of 2.035 eV was discovered to represent the direct bandgap of Ca_3PCl_3.The material Ca_3PCl_3 exhibits exceptional potential for application in the fields of solar cells and optoelectronics. Additionally, the computed elastic constants for this structure were as follows: C_{11} = 744.78, C_{12} = 11.25 and C_{44} = 15.82. Whereas the calculated value of refractive index is 1.4410. This is because it offers crucial information regarding the propagation of light through a substance. As it explains the phenomenon of light propagation through a material. However, the value of dielectric constant is 2.0766 also the calculated value of extinction coefficient is 3.69638×10^5, which can be used to calculate the ability of a molecule to absorb light at a particular frequency. The findings of this work are expected to provide guidance for the development of flexible electronic devices, such as solar cells, optoelectronic devices, and other devices that could potentially make use of this material due to its potential applications.

ORCID

Krishna Kumar Mishra, https://orcid.org/0000-0001-6888-7654; **Rajnish Sharma,** https://orcid.org/0000-0001-8644-016X

REFERENCES

[1] M. Victoria, N. Haegel, I.M. Peters, R. Sinton, A. Jäger-Waldau, C. del Canizo, C. Breyer, et al. "Solar photovoltaics is ready to power a sustainable future," Joule, **5**(5), 1041-1056 (2021). https://doi.org/10.1016/j.joule.2021.03.005

[2] T. Jackson, and M. Oliver, "The viability of solar photovoltaics," Energy policy, **28**(14), 983-988 (2000). https://doi.org/10.1016/s0301-4215(00)00085-9

[3] Md.F. Rahman, J. Hossain, A. Kuddus, S. Tabassum, M.H.K. Rubel, Md.M. Rahman, Y. Moriya, *et al*. "A novel CdTe ink-assisted direct synthesis of CdTe thin films for the solution-processed CdTe solar cells," Journal of materials science, **55**, 7715-7730 (2020). https://doi.org/10.1007/s10853-020-04578-7

[4] M.K. Hossain, G.F.I. Toki, D.P. Samajdar, M. Mushtaq, M.H.K. Rubel, R. Pandey, J. Madan, *et al*. "Deep insights into the coupled optoelectronic and photovoltaic analysis of lead-free CsSnI3 perovskite-based solar cell using DFT calculations and SCAPS-1D simulations," ACS omega, **8**(25), 22466-22485 (2023). https://doi.org/10.1021/acsomega.3c00306

[5] Q. Ma, S. Huang, S. Chen, M. Zhang, C.F.J. Lau, M.N. Lockrey, H.K.Mulmudi, *et al*. "The effect of stoichiometry on the stability of inorganic cesium lead mixed-halide perovskites solar cells," The Journal of Physical Chemistry C, **121**(36), 19642-19649 (2017). https://doi.org/10.1021/acs.jpcc.7b06268

[6] Md.E. Islam, Md.R. Islam, S. Ahmmed, M.K. Hossain, and Md.F. Rahman, "Highly efficient SnS-based inverted planar heterojunction solar cell with ZnO ETL," Physica Scripta, **98**(6), 065501 (2023). https://doi.org/10.1088/1402-4896/accb13

[7] Y. Zhou, L. You, S. Wang, Z. Ku, H. Fan, D. Schmidt, A. Rusydi, *et al*. "Giant photostriction in organic–inorganic lead halide perovskites," Nature communications, **7**(1), 11193 (2016). https://doi.org/10.1038/ncomms11193

[8] M.M. Abdelhamied, Y. Song, W. Liu, X. Li, H. Long, K. Wang, B. Wang, and P. Lu, "Improved photoemission and stability of 2D organic-inorganic lead iodide perovskite films by polymer passivation," Nanotechnology, **31**(42), 42LT01 (2020). https://doi.org/10.1088/1361-6528/aba140

[9] J. Di, J. Chang, and S. Liu, "Recent progress of two-dimensional lead halide perovskite single crystals: crystal growth, physical properties, and device applications," EcoMat, **2**(3), e12036 (2020). https://doi.org/10.1002/eom2.12036

[10] S. Wu, Z. Li, M.-Q. Li, Y. Diao, F. Lin, T. Liu, J. Zhang, *et al*. "2D metal–organic framework for stable perovskite solar cells with minimized lead leakage,' Nature Nanotechnology, **15**(11), 934-940 (2020). https://doi.org/10.1038/s41565-020-0765-7

[11] W. Shen, Y. Zhao, and F. Liu, "Highlights of mainstream solar cell efficiencies in 2021," Front. Energy, **16**, 1–8 (2022). https://doi.org/10.1007/s11708-022-0816-x

[12] H. Liu, L. Xiang, P. Gao, D. Wang, J. Yang, X. Chen, S. Li, Y. Shi, F. Gao, and Y. Zhang, "Improvement strategies for stability and efficiency of perovskite solar cells," Nanomaterials, **12**(19), 3295 (2022). https://doi.org/10.3390/nano12193295

[13] P. Roy, N.K. Sinha, S. Tiwari, and A. Khare, "A review on perovskite solar cells: Evolution of architecture, fabrication techniques, commercialization issues and status," Solar Energy, **198**, 665-688 (2020). https://doi.org/10.1016/j.solener.2020.01.080

[14] Y. Yuan, J. Chae, Y. Shao, Q. Wang, Z. Xiao, A. Centrone, and J. Huang, "Photovoltaic switching mechanism in lateral structure hybrid perovskite solar cells," Advanced Energy Materials, **5**(15), (2015). https://doi.org/10.1002/aenm.201500615

[15] K. Zheng, and T. Pullerits, "Two dimensions are better for perovskites," The Journal of Physical Chemistry Letters, **10**(19), 5881-5885 (2019). https://doi.org/10.1021/acs.jpclett.9b01568

[16] G.E. Eperon, S.D. Stranks, C. Menelaou, M.B. Johnston, L.M. Herz, and H.J. Snaith, "Formamidinium lead trihalide: a broadly tunable perovskite for efficient planar heterojunction solar cells," Energy & Environmental Science, **7**(3), 982-988 (2014). https://doi.org/10.1039/C3EE43822H

[17] Mishra, Krishna Kumar, "Exploring the physical, electrical and optical properties of $Cs_2LiInBr_6$ Perovskite: an extensive study utilizing DFT based GGA-PBE and HSE06 functionals." Brazilian Journal of Physics, 55(1), 31 (2025). https://doi.org/10.1007/s13538-024-01653-1

[18] B. Wang, J. Iocozzia, M. Zhang, M. Ye, S. Yan, H. Jin, S. Wang, Z. Zou, and Z. Lin, "The charge carrier dynamics, efficiency and stability of two-dimensional material-based perovskite solar cells," Chemical Society Reviews, **48**(18), 4854-4891 (2019). https://doi.org/10.1039/c9cs00254e

[19] G.M. Wilson, M. Al-Jassim, W.K. Metzger, S.W. Glunz, P. Verlinden, G. Xiong, L.M. Mansfield, *et al*. "The 2020 photovoltaic technologies roadmap," Journal of Physics D: Applied Physics, **53**(49), 493001 (2020). https://doi.org/10.1088/1361-6463/ab9c6a
[20] M. Aaogi, Y. Shirako, H. Kojitani, T. Nagakari, H. Yusa, and K. Yamaura, "High-pressure transitions in $NaZnF_3$ and $NaMnF_3$ perovskites, and crystal-chemical characteristics of perovskite–postperovskite transitions in ABX3 fluorides and oxides," Physics of the Earth and Planetary Interiors, **228**, 160-169 (2014). https://doi.org/10.1016/j.pepi.2013.09.001
[21] A. Alhashmi, M.B. Kanoun, and S. Goumri-Said, "Machine learning for halide perovskite materials ABX_3 (B= Pb, X= I, Br, Cl) assessment of structural properties and band gap engineering for solar energy," Materials, **16**(7), 2657 (2023). https://doi.org/10.3390/ma16072657
[22] R.S. Roth, "Classification of perovskite and other ABO_3-type compounds," Journal of Research of the National Bureau of Standards, **58**(2), 75-88 (1957). https://doi.org/10.6028/jres.058.010
[23] C. Moure, and O. Peña, "Recent advances in perovskites: Processing and properties," Progress in Solid State Chemistry, **43**(4), 123-148 (2015). https://doi.org/10.1016/j.progsolidstchem.2015.09.001
[24] X. Liu, J. Fu, and G. Chen, "First-principles calculations of electronic structure and optical and elastic properties of the novel ABX 3-type LaWN 3 perovskite structure," RSC advances, **10**(29), 17317-17326 (2020). https://doi.org/10.1039/c9ra10735e
[25] H.-J. Feng, and Q. Zhang, "Predicting efficiencies> 25% A3MX3 photovoltaic materials and Cu ion implantation modification," Applied Physics Letters, **118**(11), (2021). https://doi.org/10.1063/5.0039936
[26] Md.F. Rahman, Md. Al Ijajul Islam, Md.R. Islam, Md.H. Ali, P. Barman, Md.A. Rahman, Md. Harun-Or-Rashid, *et al*. "Investigation of a novel inorganic cubic perovskite Ca3PI3 with unique strain-driven optical, electronic, and mechanical properties," Nano Select, (2023). https://doi.org/10.1002/nano.202300066
[27] Y. Li, and K. Yang, "High-throughput computational design of halide perovskites and beyond for optoelectronics," Wiley Interdisciplinary Reviews: Computational Molecular Science, **11**(3), e1500 (2021). https://doi.org/10.1002/wcms.1500
[28] S. Binetti, M. Acciarri, A. Le Donne, M. Morgano, and Y. Jestin, "Key success factors and future perspective of silicon-based solar cells," International Journal of Photoenergy, **2013**(1), 249502 (2013). https://doi.org/10.1155/2013/249502
[29] J. Singh, and A. Agrahari, "The progression of silicon technology acting as substratum for the betterment of future photovoltaics," International Journal of Energy Research, **43**(9), 3959-3980 (2019). https://doi.org/10.1002/er.4402
[30] J. Shim, E.-K. Lee, Y.J. Lee, and R.M. Nieminen, "Density-functional calculations of defect formation energies using the supercell method: Brillouin-zone sampling," Physical Review B—Condensed Matter and Materials Physics, **71**(24), 245204 (2005). https://doi.org/10.1103/physrevb.71.245204
[31] S. Luo, T. Li, X. Wang, M. Faizan, and L. Zhang, "High-throughput computational materials screening and discovery of optoelectronic semiconductors," Wiley Interdisciplinary Reviews: Computational Molecular Science, **11**(1), e1489 (2021). https://doi.org/10.1002/wcms.1489
[32] Z. Liu, G. Na, F. Tian, L. Yu, J. Li, and L. Zhang, "Computational functionality-driven design of semiconductors for optoelectronic applications," InfoMat, **2**(5), 879-904 (2020). https://doi.org/10.1002/inf2.12099
[33] S. Kang, D. Lee, J. Kim, A. Capasso, H.S. Kang, J.-W. Park, C.-H. Lee, and G.-H. Lee, "2D semiconducting materials for electronic and optoelectronic applications: potential and challenge," 2D Materials, **7**(2), 022003 (2020). https://doi.org/10.1088/2053-1583/ab6267
[34] Y. Xue, T. Yang, Y. Zheng, K. Wang, E. Wang, H. Wang, L. Zhu, *et al*. "Heterojunction engineering enhanced self-polarization of PVDF/$CsPbBr_3$/$Ti_3C_2T_x$ composite fiber for ultra-high voltage piezoelectric nanogenerator," Advanced Science, **10**(18), 2300650 (2023). https://doi.org/10.1002/advs.202300650
[35] M. Pagliaro, R.a Ciriminna, and G. Palmisano, "Flexible solar cells," ChemSusChem: Chemistry & Sustainability Energy & Materials, **1**(11), 880-891 (2008). https://doi.org/10.1002/cssc.200800127
[36] K. Rana, J. Singh, and J.-H. Ahn, "A graphene-based transparent electrode for use in flexible optoelectronic devices," Journal of Materials Chemistry C, **2**(15), 2646-2656 (2014). https://doi.org/10.1039/c3tc32264e
[37] Y.-F. Liu, J. Feng, Y.-G. Bi, D. Yin, and H.-B. Sun, "Recent developments in flexible organic light-emitting devices," Advanced Materials Technologies, **4**(1), 1800371 (2019). https://doi.org/10.1002/admt.201800371
[38] J. Lewis, "Material challenge for flexible organic devices," Materials today, **9**(4), 38-45 (2006). https://doi.org/10.1016/S1369-7021(06)71446-8
[39] S. Chahar, P. Sharma, K.K. Mishra, and R. Sharma, "A Review Article on the usage of Different Materials and Different Device architectures in the Design of Tunnel Field Effect Transistor," in: *2022 IEEE International Conference of Electron Devices Society Kolkata Chapter (EDKCON)*, (IEEE, 2022), pp. 592-597.
[40] Y. Wang, S. Bai, L. Cheng, N. Wang, J. Wang, F. Gao, and W. Huang, "High-efficiency flexible solar cells based on organometal halide perovskites," Advanced Materials **28**(22), 4532-4540 (2016). https://doi.org/10.1002/adma.201504260
[41] Q. Chen, N. De Marco, Y.M. Yang, T.-B. Song, C.-C. Chen, H. Zhao, Z. Hong, *et al*. "Under the spotlight: The organic–inorganic hybrid halide perovskite for optoelectronic applications," Nano Today, **10**(3), 355-396 (2015). https://doi.org/10.1016/j.nantod.2015.04.009
[42] S. Huang, Y. Liu, Y. Zhao, Z. Ren, and C.F. Guo, "Flexible electronics: stretchable electrodes and their future," Advanced Functional Materials, **29**(6), 1805924 (2019). https://doi.org/10.1002/adfm.201805924
[43] J.P. Perdew, J.A. Chevary, S.H. Vosko, K.A. Jackson, M.R. Pederson, D.J. Singh, and C. Fiolhais, "Atoms, molecules, solids, and surfaces: Applications of the generalized gradient approximation for exchange and correlation," Physical review B, **46**(11), 6671 (1992). https://doi.org/10.1103/physrevb.46.6671
[44] J.P. Perdew, K. Burke, and M. Ernzerhof, "Generalized gradient approximation made simple," Physical review letters, **77**(18), 3865 (1996). https://doi.org/10.1103/physrevlett.77.3865
[45] QuantumATK version U-2023.09, Synopsys QuantumATK, https://www.synopsys.com/silicon/quantumatk.html (accessed: October 2023).
[46] I.K.G.G. Apurba, Md.R. Islam, Md.S. Rahman, Md.F. Rahman, and J. Park, "Tuning the physical properties of inorganic novel perovskite materials Ca_3PX_3 (X= I, Br and Cl): Density function theory," Heliyon, **10**(7), (2024). https://doi.org/10.1016/j.heliyon.2024.e29144
[47] Md.R. Islam, A. Zahid, M.A. Rahman, Md.F. Rahman, M.A. Islam, M.K. Hossain, M.A. Ali, M.A. Iqbal, F.I. Bakhsh, and S. Ahmad, "Tuning the optical, electronic, and mechanical properties of inorganic Ca_3PCl_3 perovskite via biaxial strain," Journal of Physics and Chemistry of Solids, **184**, 111722 (2024). https://doi.org/10.1016/j.jpcs.2023.111722

[48] S.-J. Zou, Y. Shen, F.-M. Xie, J.-D. Chen, Y.-Q. Li, and J.-X. Tang, "Recent advances in organic light-emitting diodes: toward smart lighting and displays," Materials Chemistry Frontiers, **4**(3), 788-820 (2020). https://doi.org/10.1039/C9QM00716D
[49] Q. Dai, Q.-Q. Liang, T.-Y. Tang, H.-X. Gao, S.-Q. Wu, and Y.-L. Tang, "The structural, stability, electronic, optical and thermodynamic properties of Ba_2AsXO_6 (X= V, Nb, Ta) double perovskite oxides: A First-Principles study," Inorganic Chemistry Communications, **166**, 112591 (2024). https://doi.org/10.1016/j.inoche.2024.112591
[50] T. Tang, and Y. Tang, "First principle comparative study of transitional elements Co, Rh, Ir (III)-based double halide perovskites," Materials Today Communications, **34**, 105431 (2023). https://doi.org/10.1016/j.mtcomm.2023.105431
[51] T. Yao, Y. Wang, H. Li, J. Lian, J. Zhang, and H. Gou, "A universal trend of structural, mechanical and electronic properties in transition metal (M= V, Nb, and Ta) borides: First-principle calculations," Computational materials science, **65**, 302-308 (2012). https://doi.org/10.1016/j.commatsci.2012.07.021
[52] Md.A. Rahman, I. Ria, A. Ghosh, A.A.A. Bahajjaj, and R.J. Ramalingam, "A Novel Investigation into Strain-Induced Changes in the Physical Properties of Lead-Free Ca_3ncl_3 Perovskite," Preprint, https://dx.doi.org/10.2139/ssrn.4782983
[53] F. Mouhat, and F.-X. Coudert, "Necessary and sufficient elastic stability conditions in various crystal systems," Physical review B, **90**(22), 224104 (2014). https://doi.org/10.1103/PhysRevB.90.224104
[54] M. Maghrabi, A.Y. Al-Reyahi, N. Al Aqtash, S.M. Al Azar, A. Shaheen, A. Mufleh, and B. Shaban, "Investigating the physical properties of lead-free halide double perovskites Cs_2AgXBr_6 (X= P, As, Sb) for photovoltaic and thermoelectric devices using the density functional theory," Materials Today Communications **37**, 107541 (2023). https://doi.org/10.1016/j.mtcomm.2023.107541
[55] K.K. Mishra, "Study on Structural, Mechanical, Electronic, Vibrational, Optical and Thermo-Dynamical Behaviour of ZB Structured BeZ (Z=S, Se and Te) Using ATK-DFT," Metallurgical and Materials Engineering, **26**(3), 253-278 (2020). https://doi.org/10.30544/475
[56] M. Ahmad, G. Rehman, L. Ali, M. Shafiq, R. Iqbal, R. Ahmad, T. Khan, S. Jalali-Asadabadi, *et al*. "Structural, electronic and optical properties of $CsPbX_3$ (X= Cl, Br, I) for energy storage and hybrid solar cell applications," Journal of Alloys and Compounds, **705**, 828-839 (2017). https://doi.org/10.1016/j.jallcom.2017.02.147
[57] A.V. Kuklin, and H. Ågren, "Quasiparticle electronic structure and optical spectra of single-layer and bilayer $PdSe_2$: Proximity and defect-induced band gap renormalization," Physical Review B, **99**(24), 245114 (2019). https://doi.org/10.1103/physrevb.99.245114
[58] S. Chahar, K.K. Mishra, and R. Sharma, "Investigation of Structural, Electronic, and Optical Characteristics of a Novel Perovskite Halide, Mg_3AsCl_3, for Electronic Applications," Physica status solidi (b), 2400171. https://doi.org/10.1002/pssb.202400171
[59] P. Barman, Md.F. Rahman, Md.R. Islam, M. Hasan, M. Chowdhury, M.K. Hossain, J.K. Modak, *et al*. "Lead-free novel perovskite Ba_3AsI_3: First-principles insights into its electrical, optical, and mechanical properties," Heliyon, 9(11), (2023). https://doi.org/10.1016/j.heliyon.2023.e21675
[60] Md.S. Alam, Md. Saiduzzaman, A. Biswas, T. Ahmed, A. Sultana, and K.M. Hossain, "Tuning band gap and enhancing optical functions of $AGeF_3$ (A= K, Rb) under pressure for improved optoelectronic applications," Scientific Reports, **12**(1), 8663 (2022). https://doi.org/10.1038/s41598-022-12713-4
[61] M.H.K. Rubel, M.A. Hossain, M.K. Hossain, K.M. Hossain, A.A. Khatun, M.M. Rahaman, Md.F. Rahman, *et al*. "First-principles calculations to investigate structural, elastic, electronic, thermodynamic, and thermoelectric properties of $CaPd_3B_4O_{12}$ (B=Ti,V) perovskites," Results in Physics, **42**, 105977 (2022). https://doi.org/10.1016/j.rinp.2022.105977
[62] A. Ghosh, Md.F. Rahman, Md.R. Islam, Md.S. Islam, M.K. Hossain, S. Bhattarai, R. Pandey, *et al*. "Structural, electronic and optical characteristics of inorganic cubic perovskite Sr_3AsI_3," Optics Continuum, **2**(10), 2144-2153 (2023). https://doi.org/10.1364/optcon.495816
[63] Md.Z. Rahman, S.S. Hasan, Md.Z. Hasan, Md. Rasheduzzaman, Md.A. Rahman, Md.M. Ali, A. Hossain, *et al*. "Insight into the Physical Properties of the Chalcogenide $XZrS_3$ (X= Ca, Ba) Perovskites: A First-Principles Computation," Journal of Electronic Materials, 1-17 (2024). https://doi.org/10.1007/s11664-024-11120-x
[64] A. Ghosh, Md.F. Rahman, Md.R. Islam, Md.S. Islam, M. Amami, M.K. Hossain, and A.B.Md. Ismail, "Inorganic novel cubic halide perovskite Sr_3AsI_3: Strain-activated electronic and optical properties," Heliyon, **9**(8), no. 8 (2023). https://doi.org/10.1016/j.heliyon.2023.e19271
[65] D.O. Obada, S.B. Akinpelu, S.A. Abolade, E. Okafor, A.M. Ukpong, Syam Kumar R, and A. Akande, "Lead-free double perovskites: a review of the structural, optoelectronic, mechanical, and thermoelectric properties derived from first-principles calculations, and materials design applicable for pedagogical purposes," Crystals, **14**(1), 86 (2024). https://doi.org/10.3390/cryst14010086

АНАЛІЗ СТРУКТУРНИХ, ЕЛЕКТРОННИХ ТА ОПТИЧНИХ ВЛАСТИВОСТЕЙ ПЕРОВСКИТУ Ca_3PCl_3 ДЛЯ ЗАСТОСУВАННЯ В ЗЕЛЕНІЙ ЕНЕРГЕТИЦІ ТА ОПТОЕЛЕКТРОНІЦІ

Чакшу Малан[1], Крішна Кумар Мішра[1], Раджніш Шарма[2]
[1]Інститут інженерії та технологій Університету Чіткара, Університет Чіткара, Раджпура, Пенджаб-140401, Індія
[2]Школа інженерії та технологій Університету Чіткара, Солан, Хімачал-Прадеш-174103, Індія

Метою цього дослідження є детальне вивчення способів покращення ефективності перовскіту Ca_3PCl_3 в оптоелектронній галузі та галузі сонячних елементів. Речовина, відома як Ca_3PCl_3, класифікується в тій самій категорії, що й перовскіти, що складаються з неорганічних галогенідів металів. У рамках цього дослідження для вивчення оптичних, електричних та структурних характеристик було використано теорію функціоналу густини (DFT), яка є базовими принципами. Узагальнене градієнтне наближення (GGA), функціонали Пердью Берка-Ернцергофа та калькулятор лінійної комбінації атомних орбіталей – це інструменти, які використовуються для розуміння характеристик перовскіту Ca_3PCl_3. Ключовим моментом є ширина забороненої зони матеріалу, яка, за вимірюваннями, становить 20,35 еВ у точці Г. Також було виявлено, що діелектрична функція та спектри поглинання змінюються залежно від енергії фотона. Повідомлялося, що значення коефіцієнта екстинкції становить $3{,}6963\times10^4$, а значення показника відбиття – 1,4410. Тому вивчення оптичних властивостей Ca_3PCl_3 має вирішальне значення для розгляду цього матеріалу для майбутнього використання у фотоелектричних та оптоелектронних пристроях.

Ключові слова: *структурні властивості; оптичні властивості; електричні властивості; розділення шарів*

EAST EUROPEAN JOURNAL OF PHYSICS. 4. 506-511 (2025)
DOI:10.26565/2312-4334-2025-4-51 ISSN 2312-4334

LOCAL VARIATION OF SCATTERING LIGHT INTENSITY IN MANGANESE ION IMPLANTED SILICON SINGLE CRYSTALS

E.U. Arzikulov[1,2,3]*, F.A. Salaxitdinov[1], Wang Yujin[2], Shaowei Lu[3], Teng Liu[3], Zhisheng Nong[3], M.D. Toshboyev[1]

[1]*Samarkand State University named after Sharof Rashidov, 140104, 15, University Blvd., Samarkand, Republic of Uzbekistan*
[2]*State Key Laboratory of Precision Welding & Joining of Materials and Structures, School of Material Science and Engineering, Harbin Institute of Technology Yikuang Street, Nangang District, Harbin 150001, China*
[3]*School of Material Science and Engineering, Shenyang Aerospace University, 37 Daoyi South Avenue, Shenyang, China*
**Corresponding Author e-mail: eshkuvata@gmail.com*
Received September 2, 2025; revised October 22, 2025; accepted November 4, 2025

This article presents the results of experimental studies of local changes in the scattered light intensity and surface morphology in Mn implanted single-crystal silicon samples with electron conductivity and [100] crystalline orientation. The manganese ion energy, implantation dose, and phosphorus concentration in substrate were 40 keV, $5\cdot10^{15}\div1\cdot10^{17}$ ion/cm^2, and ~ $9.3\cdot10^{14}$ cm^{-3}, respectively. Atomic force microscopy (AFM) and Raman spectroscopy, using the backscattering geometry of surface-scattered light, were applied to analyze the surface morphology before and after implantation. AFM micrographs of the surface show characteristic nanometer-sized roughnesses, the shape and size of which strongly depend on the implantation dose. These nanoscale objects are not present on the non-implanted substrate surface. In the Raman spectra of the samples not subjected to implantation, the main Lorentz-type peak is always observed, which is characteristic of single-crystal silicon and centered at 520.0±1.0 cm^{-1}, corresponding to the phonon wave vector. Several peaks are observed in the Raman spectra of manganese ion-implanted silicon samples (184, 291, 373, 468, 659, 798, and 804 cm^{-1}), presumably associated with the formation of radiation defects and nanoscale objects on the surface of single-crystal silicon during ion implantation with the participation of silicon, manganese, phosphorus, and other impurity atoms. These structural defects in the silicon crystal lattice at the surface and near-surface caused by manganese ion bombardment lead to the excitation of new vibrational modes not observed in the initial silicon. These modes are manifested in Raman scattering spectra.
Key words: *Local intensity; Ion implantation; Raman scattering; Silicon; Nanoscale objects; Wave vector*
PACS: 33.20. Fb; 42.68. Mj; 61.72. Tt

INTRODUCTION

Recently, there has been significant interest in the development and study of silicon nanocrystals and their nanostructures, particularly their optical, electronic, and other properties. This is due to their possible implementation in different devices, such as high-performance solar cells, non-volatile memory devices, biomedical devices and sensors, anode materials for lithium-ion batteries, active materials for thermoelectric devices, and efficient photon sources. Ion implantation (II) is an advanced technique for forming nanoscale structures in the surface and near-surface regions of semiconductors, enabling the design of nanoelectronic devices. The properties of nanoelectronic devices depend largely on the size, shape, and concentration of nanoscale structures in the surface and near-surface layers of the semiconductor substrate.

The study of nanoscale structure formation involving impurities in solids, especially semiconductors such as silicon, is of significant scientific and practical interest. This interest stems from two factors: (1) these structures significantly alter the physicochemical properties of the material, often imparting unique characteristics, and (2) these materials enable the development of highly sensitive sensors for various external stimuli [1]. Impurities are introduced into semiconductors primarily through diffusion, ion implantation, or doping during growth [2]. Impurities from transition metals create deep energy levels in the silicon band gap, significantly altering its generation-recombination properties. These deep levels modify the properties of silicon typically doped with shallow-level impurities, enabling new phenomena with potential applications in modern electronics. Transition metal impurities are typically introduced into the silicon volume via high-temperature diffusion. However, diffusion doping has a significant drawback: the limited solubility of transition metal impurities in silicon restricts the practical use of diffusion-doped materials. Ion implantation overcomes this limitation [3]. It allows the introduction of impurities into the semiconductor at concentrations far exceeding their maximum solubility [4]. By introducing sufficient impurities via ion implantation, self-organized nanoscale structures can form, involving impurities and structural defects. This significantly modifies the properties of the original material, imparting tailored characteristics that underscore the relevance of this work. This article presents an experimental study of local variations in scattered light intensity on the surface of Mn implanted monocrystalline silicon samples containing nanoscale structures. It also examines their surface morphology, geometric dimensions, and shapes.

Cite as: E.U. Arzikulov, F.A. Salaxitdinov, W. Yujin, S. Lu, T. Liu, Z. Nong, M.D. Toshboyev, East Eur. J. Phys. 4, 506 (2025), https://doi.org/10.26565/2312-4334-2025-4-51

MATERIALS AND METHODS

Bilaterally polished single-crystal silicon plates with electron conductivity and crystallographic orientation [100] were chosen as the substrate material for the ion-implantation process. The electron concentration in the substrate was approximately ~ $9.3 \cdot 10^{14}$ cm^{-3}. Implantation of manganese ions with an energy of 40 keV was performed on the ILU-3 linear ion accelerator at room temperature. The implantation dose varied in the $5{,}0 \cdot 10^{15} \div 1{,}0 \cdot 10^{17}$ ion/cm^2 range.

In modern conditions, highly sensitive microscopic, X-ray, spectroscopic, and other methods are mainly used to detect nanocrystals and nanostructures in solids or low-dimensional systems. In particular, the Raman (Micro Raman or μ-Raman) and AFM methods have recently become one of the generally accepted tools for studying bulk and low-dimensional materials, especially single-crystal silicon and nanostructures based on it [5-9].

In this studies was used AFM and Raman spectroscopy to characterize the surface morphology and dimensions of nanoscale structures. It is known that both of these methods are highly accurate and informative tools for studying the formation of nanoscale structures in various materials. In addition, Raman spectroscopy provides valuable information on local atomic ordering and phonon modes [10, 11]. For the effective practical application of ion-implanted materials, it is necessary to know their physical properties in damaged surface layers: phase state, concentration of free charges, etc. Recent studies by the authors of [10] have shown that Raman scattering is a powerful tool for determining the physical characteristics of ion-implanted silicon layers. Our experiments recorded Raman spectra using a Renishaw InVia micro-Raman spectrometer at room temperature in the wavenumber range of 50 to 1000 cm^{-1}. The spectra were recorded in the backscattering geometry with a spectral resolution better than 2.0 cm^{-1}. The incident radiation was not polarized, and the optical recording scheme also did not include polarizing filters. A Cobalt CW DPSS solid-state laser with a wavelength of 532 nm and a nominal power of 50 mW was used as an excitation source. The exciting laser beam was focused on the sample surface using a 100× objective. A similar procedure was used to collect scattered light. The obtained spectra were processed using the Origin Pro 18 software package.

To study the surface morphology of monocrystalline silicon samples, a multifunctional AFM Core 300 was used in the static force mode. AFM Core 300 is a device with a unique set of capabilities for studying various properties of surfaces (and chips) of materials with high (up to atomic) resolution. The operating principle of this device is based on scanning the surface with solid-state sharp probes (needles) in the process of their mutual movement according to specified algorithms. A distinctive feature of the AFM, along with high resolution, is the ability to obtain a pseudo-three-dimensional image of the surface with visualization of quantitative data on its electrical, magnetic, topographic and other characteristics.

RESULTS AND DISCUSSION

The results of the experiments on Raman spectroscopy are shown in Figure 1. The measurements were carried out at three different points on surface of initial and manganese ion-implanted monocrystalline silicon samples.

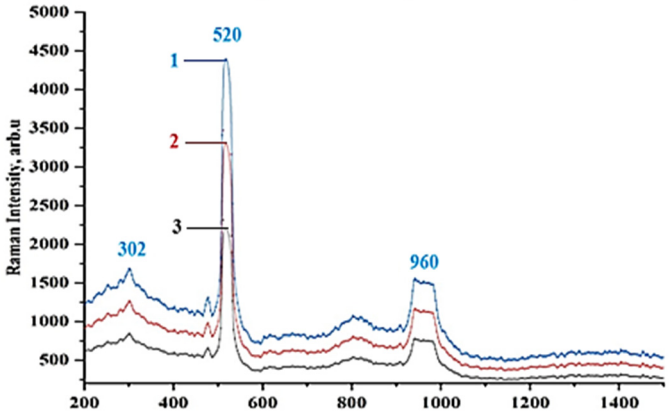

Figure 1. Raman spectra for the original bulk sample (1) with thickness of 3 mm, (2) and (3) with thicknesses of 500 and 200 μm, as well as for a plate of single-crystal silicon doped with phosphorus

As shown in Figure 1, the Raman spectrum of the original (non-implanted) silicon samples contains the main peak with a wave number of 520 cm^{-1} and accompanying peaks (satellites) at frequencies of 301 cm^{-1} and in the range of 900-971 cm^{-1}. It is known that Raman spectroscopy is especially sensitive to the surface condition and thickness of the samples. To clarify the effect of thickness on the appearance of the Raman spectra and the intensity of the peaks in them, we measured the dependence of the Raman spectra on the thickness of the semiconductor substrate. Our experimental results showed that increasing the thickness of non-implanted samples from 200 μm to 3 mm leads to an approximately 50% decrease in the intensity of the main Raman peak at 520 cm^{-1}, while its spectral position remains unchanged. The measured full width at half maximum (FWHM) of this peak for the 3-mm-thick sample was 3.9 cm^{-1}, and for the 200-μm-thick sample, it was 4.2 cm^{-1}. Analysis of these results suggests that sample thickness significantly influences the Raman spectra. This is due to the penetration depth of the exciting light, the energy of which E_0=1.95 eV is greater than the band gap of single-crystal silicon equal to E_g=1.12 eV, and energy scattering in the volume. Secondary radiation

occurs only in a thin near-surface layer with a thickness of several microns. Thus, thicker samples result in greater attenuation of secondary order scattered light, reducing its intensity, as observed in our experiments. This means that the analysis of the Raman spectra provides information only on the near-surface layer. Thus, it can be argued that the observed features of the Raman spectra, such as local intensity, position, and shape of the phonon band, etc., provide valuable information about nanoscale objects, their composition and structure of both original and ion-implanted single-crystal samples and thin silicon wafers.

The Raman spectra shown in Figure 1 (a), (b) clearly show the main Lorentzian peak characteristic of crystalline silicon (c-Si). This peak is centered at approximately 520.0±1.0 cm^{-1} and corresponds to the phonon wave vector. The recorded Raman spectral parameters, such as peak position and intensity, are consistent with data reported in the [12, 13]. The long-range translational symmetry of crystalline silicon potentially allows the appearance of additional peaks in the range of 100÷1100 cm^{-1}. Although their intensity is considerably weaker than that of the main first-order longitudinal-transverse optical (LTO) phonon peak [14]. Additionally, these spectra (Figure 1a, b) contain a broad band in the range of 925÷985 cm^{-1}. A similar broad band in the range of 900÷1100 cm^{-1} was previously reported in the spectra of nanocrystalline silicon [11, 15], attributed to the scattering of multiple transverse optical (2TO) phonons and their overtone states.

Figure 2 shows the Raman spectra of Mn implanted silicon samples. These spectra, acquired at three distinct surface locations, reveal several additional bands of varying intensities. The number and intensity of these bands vary significantly with implantation dose.

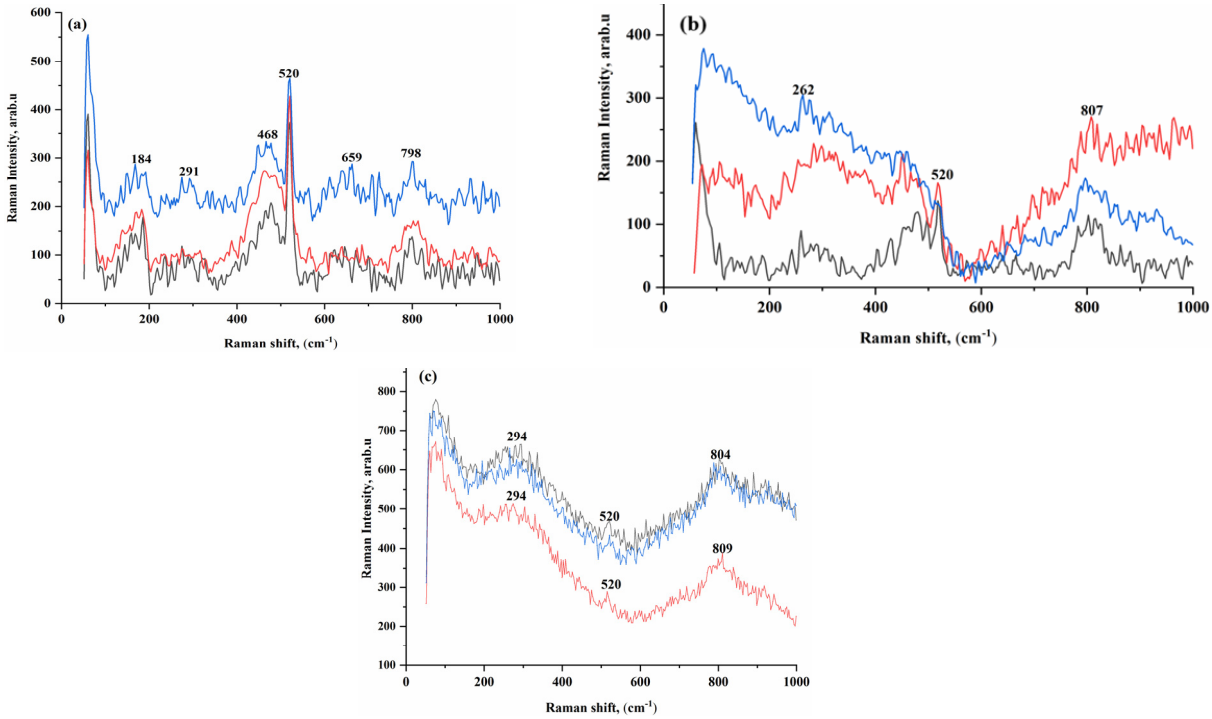

Figure 2. Change in the local intensity of the Raman spectra of ion-implanted silicon samples measured at three different points on the surface depending on the implantation dose, ion/cm^2: (a) – $5{,}0\cdot10^{15}$, (b) – $5{,}0\cdot10^{16}$, (c) – $1{,}0\cdot10^{17}$; ion energy 40 keV; T = 300 K

Thus, for example, at relatively low (Figure 2, (a)) doses equal to $5{,}0\cdot10^{15}$ ion/cm^2 in the Raman spectra, a sufficiently intense main peak of the quasi-Lorentz shape, characteristic of crystalline silicon (c-Si), is still clearly expressed and it retains its position relative to the center located at approximately a frequency of 520.0±1.0 cm^{-1} and still corresponds to the phonon wave vector. It should be noted that at low implantation doses, only a decrease in the intensity of the Raman peaks is observed, associated with both fundamental and higher scattering orders, which probably contributed to the formation of point defects. In addition, in the Raman spectra, a number of satellites are observed located relative to the central peak corresponding to 520.0 cm^{-1} both toward low (184, 291, 468 cm^{-1}) and toward high frequencies (659, 798 cm^{-1}), which can probably be associated with the formation of nanosized defect structures of the silicon crystal lattice that arose under the influence of the II process. As shown in Figure 2(b), increasing the implantation dose significantly alters the Raman spectral profile and the intensities of its peaks.

Starting with a dose of $5{,}0\cdot10^{16}$ ion/cm^2, although the position of the central peak remains unchanged, its intensity decreases approximately 2,6 times and new satellites appear located at frequencies of 262 and 807 cm^{-1} with very low intensity, indicating a violation of the crystal lattice, and correlating with the one-phonon density of states. Further increase of the implantation dose to $1{,}0\cdot10^{17}$ ion/cm^2 (Figure 2, (c)) leads to the virtual disappearance of the central peak (its intensity is at the noise level), the low-frequency satellite shifts toward high frequencies (294 cm^{-1}), and the high-frequency satellite is in the frequency range of 804÷807 cm^{-1}.

Our previous studies [16] investigated the generation mechanisms of nanoscale structures in Mn implanted single-crystal silicon. Using Raman spectroscopy and AFM, we obtained detailed information on both initial and ion-implanted samples. According to [16], increasing implantation dose results in the formation of various phase states in the near-surface layers of silicon. Their characteristics, such as the position in the spectrum and intensity, depend on the implantation dose and the position of the laser radiation incidence point on the sample, which is confirmed by our results. The experimental results on the dose dependence of Raman scattering in silicon samples implanted with manganese ions can be explained as follows. At relatively low implantation doses, the damage to the silicon crystal lattice is insignificant, which causes the existence of a peak with a frequency of 520.0 cm^{-1} corresponding to single-crystal silicon, and a decrease in its intensity can be associated with partial destruction of the crystal lattice. It can be stated that the intensity of the peak with a frequency of 520.0 cm^{-1} corresponding to single-crystal silicon can be considered as an indicator of the substrate crystallinity. The lower its intensity, the stronger the destruction of its crystallinity. The appearance of low- and high-frequency satellites in the Raman spectra can be associated with nanoscale structural defects, as well as defects involving manganese atoms (ions) and other impurity atoms. This assumption is also supported by the change in the position and intensity of such satellites depending on the implantation dose. With an increase in the implantation dose, the substrate surface begins to transform into an amorphous state, which in turn is characterized by a random arrangement of matrix atoms (silicon), manganese ions and other foreign atoms. As was said above, the Raman spectroscopy method is sensitive to the environment of the matrix (substrate) atoms. The presence and arrangement of impurities around silicon atoms notably alter the Raman spectral profile, including the position of the high-frequency satellite peak (Figure 2(c)). We have suggested that the detected peaks arise from radiation-induced defects in the crystal structure and nanoscale structures formed primarily from silicon, manganese, phosphorus, and other impurities on the surface of single-crystal silicon during ion irradiation. To test this hypothesis, we conducted additional studies of the surface morphology of the samples before and after implantation using the AFM method. To analyze the surface morphology of single-crystal silicon samples before and after implantation, an AFM from Nano Surf, Core AFM 300, was used. The obtained images of the surface topology of the manganese-implanted single-crystal silicon samples we studied showed that they contain roughness with dimensions of the order of nanometers (Figure 3).

In addition, the obtained AFM images revealed the presence of various types of nanosized objects on the sample surface, presumably bound by silicon and phosphorus atoms, with embedded manganese ions and a number of other impurity atoms, or the formation of nanosized structural radiation defects during II. To analyze changes in the surface morphology of the samples before and after ion beam treatment, its surface was measured using AFM in the electrostatic force mode. Figure 3 shows AFM images demonstrating the surface relief features of nanostructured silicon samples.

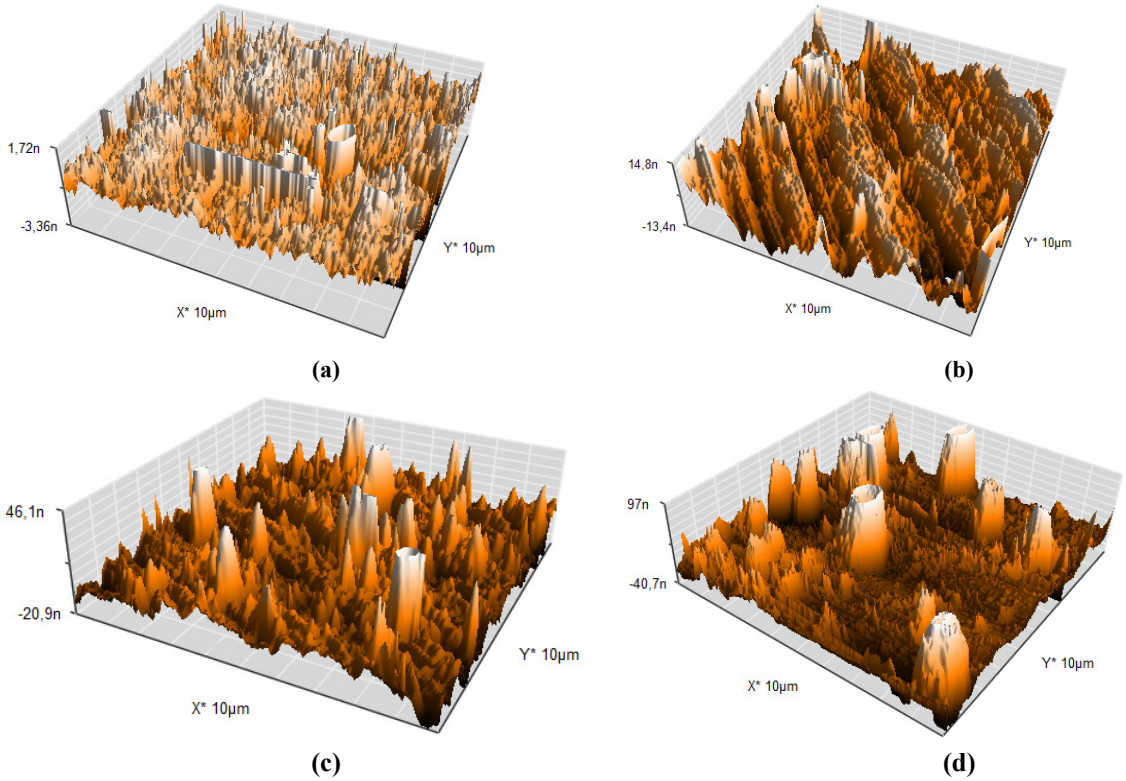

Figure 3. AFM images of the surface of single-crystal silicon before (a) and after manganese ion implantation (40 keV, 300 K) at doses of: (b) $5{,}0\cdot10^{15}$ ion/cm^2, (c) $5{,}0\cdot10^{16}$ ion/cm^2, (d) $1{,}0\cdot10^{17}$ ion/cm^2.

Analysis of Figure 3 demonstrates that an increase in the implantation dose dramatically transforms the surface topography, making it noticeably rougher. The surface roughness of the original, non-implanted samples is relatively

smoother (Figure 3(a)) than that of those implanted with doses: $5{,}0\cdot10^{15}$ ion/cm^2 (Figure 3(b)); $5{,}0\cdot10^{16}$ ion/cm^2 (Figure 3(d)) and $1{,}0\cdot10^{17}$ ion/cm^2 (Figure 3(c)). In parallel with this, the dimensions of the nanostructures formed on the surface increase as the dose of implanted ions increases. In addition, the results of AFM studies confirm the presence of silicon nanowires or nanocrystals on the substrate surface. The transverse dimensions of these formations increase significantly depending on the concentration of implanted ions: from approximately 9 nm at a dose of $5{,}0\cdot10^{15}$ ion/cm^2 (Figure. 3(b)) to ~ 200 nm at a dose of $1{,}0\cdot10^{17}$ ion/cm^2 (Figure. 3(d)). It is known that II causes the formation of various radiation defects on the surface and near it, which significantly changes the properties of the material. The nature, type, structure and composition of these defects change significantly with increasing energy and implantation dose. Examples of such defects in silicon include vacancies associated with oxygen or phosphorus [17-20]. According to [21], ion implantation leads to the appearance of structural defects. The appearance of new peaks in the Raman spectra of ion-implanted samples is probably due to these radiation-induced structural defects. External defects may also be present, such as impurity elements (non-silicon atoms) that may occupy interstitial or nodal positions (substitutional impurities). As a result of the activation of these impurities under various external influences, they may lead to the formation of more complexes, such as impurity-vacancy pairs, etc. [22].

CONCLUSIONS

In the Raman spectra of the studied samples of manganese ion implanted single-crystal silicon with an energy of 40 keV and with different implantation doses, new peaks were recorded at frequencies of 184, 291, 373, 468, 659, 798 and 804 cm^{-1}, which are located relative to the central peak corresponding to the frequency of 520.0 cm^{-1} both toward low (184, 291, 373, 468 cm^{-1}) and toward high frequencies (659, 798, 804 cm^{-1}), which can probably be associated with the formation of nanoscale defect structures of the silicon crystal lattice that arose under the influence of the ion irradiation process.

Local variations in scattered light intensity and the Raman phonon band's position and shape provide important information insights into the structure and composition of nanoscale features in ion-implanted single-crystal silicon samples.

Analysis of the first-order Raman spectral shift indicates that thickness-dependent differences are likely due to variations in light penetration depth in the near-surface region and energy dissipation within the sample.

The occurrence of secondary peaks in the Raman spectra is associated with the formation of nanoscale objects consisting mainly of matrix atoms (silicon), phosphorus, manganese ions and other impurity atoms, as well as radiation-induced structural defects arising under the influence of the ion implantation process.

Analysis of AFM images of Mn implanted single-crystal silicon surfaces revealed silicon nanowires or nanocrystals, with their sizes increasing with implantation dose. The transverse dimensions of these structures increase significantly with ion dose, from approximately 9 nm at 5.0×10^{15} ions/cm^2 to ~200 nm at 1.0×10^{17} ions/cm^2. Thus, ion implantation induces significant structural changes in silicon, forming defects and nanoscale structures that can be characterized using Raman spectroscopy and AFM.

ORCID

Eshkuvat U. Arzikulov, https://orcid.org/0000-0001-9179-3402; **Wang Yujin**, https://orcid.org/0000-0002-8710-1108

REFERENCES

[1] P. Jagadeesh, S.M. Rangappa, and S. Siengchin, Adv. Ind. and Eng. Poly. Res. **7**, 122 (2024). https://doi.org/10.1016/j.aiepr.2023.03.002
[2] S.K. Jha, and M. Kumar, International Open-Access, Double-Blind, Peer-Reviewed, Refereed, Multidisciplinary Online Journal (IJARSCT), **4**, 685 (2024). https://doi.org/10.48175/IJARSCT-19475
[3] Y.G. Abov, F.S. Dzheparov, N.O. Elyutin, D.V. Lvov, and A.N. Tyulyusov, Physics of Atomic Nuclei, **79**, 617 (2016). https://doi.org/10.1134/S1063778816040037
[4] S. Cho, and B.-G. Park, in: *Doping: Properties, Mechanisms and Applications,* edited by Lixin Yu (Nanchang University, PR China, 2013), https://novapublishers.com/wp-content/uploads/2019/08/978-1-62618-097-0_ch4
[5] C. Meiera, S. Lu, V.G. Kravets, H. Nienhaus, A. Lorke, and H. Wiggers, Physica E, **32**, 155 (2006). http://dx.doi.org/10.1016/j.physe.2005.12.030
[6] Z. Guoliang, L. Pan, Z. Chengxi, G. Xinran, D. Ronglu, and Y. Liangbao, Anal. Chem. **97**, 5612 (2025). https://doi.org/10.1021/acs.analchem. 4c0629
[7] M.I. Suib, A.F.A. Rahim, L.N. Ismail, K.Y. Lee, and A.R.M. Radzol, in: *2024 IEEE-EMBS Conference on Biomedical Engineering and Sciences (IECBES) Proceedings*, (Penang, Malaysia, 2024), pp. 483-488. https://doi.org/10.1109/IECBES61011.2024. 10990872
[8] Y. Duan, J.F. Kong, and W.Z. Shen, J. Raman Spec. **43**, 756 (2012). https://doi.org/10.1002/jrs.3094.
[9] M. Khorasaninejad, J. Walia, and S. Saini, Nanotechnology **23**, 275706 (2012). https://doi.org/10.1088/0957-4484/23/27/275706
[10] E. Smith, and G. Dent, *Modern Raman spectroscopy: a practical approach,* 2nd ed, (Wiley, Hoboken, NJ, 2019), pp. 23-67. https://doi.org/10.1002/0470011831.ch5
[11] M. Cardona, *Light Scattering in Solids*. (Springer, Berlin, Heidelberg, 1982), pp.147–248.
[12] H. Richter, Z.P. Wang, and L. Ley, Solid State Communications, **39**, 625 (1981). https://doi.org/10.1016/0038-1098(81)90337-9
[13] F. Minoru, K. Yoshihiko, H. Shinji, and Y. Keiichi, Phys. Rev. B, **54**, R8373(R) (1996). https://doi.org/10.1103/PhysRevB.54.R8373
[14] I. Iatsunskyi, G. Nowaczyk, S. Jurga, V. Fedorenko, M. Pavlenko, and V. Smyntyna, Int. J. for Light and Elec. Opt. **126**, 1650 (2016).

[15] Á. Fernández-Galiana, O. Bibikova, S.V. Pedersen, and M.M. Stevens, Adv. Mater. **36**, 2210807 (2024). https://doi.org/10.1002/adma. 202210807
[16] E.U. Arzikulov, F.A. Salakhitdinov, F. Kholmurodov, and M.D. Tashboev, J. of Phys.: Conference Series, **2573**, (2023). https://doi.org/10.1088/1742-6596/2573/1/012015
[17] V. Pelenitsyn, and P. Korotaev, Comput. Mat. Sci. **207**, 111273 (2022). https://doi.org/10.1016/j.commatsci.2022.111273
[18] M.D. McCluskey, and A. Janotti, Appl. Phys. **127**, 190401 (2020). https://doi.org/10.1063/5.0012677
[19] M.D. McCluskey, and E.E. Haller, *Dopants and Defects in Semiconductors*, 2nd ed. (CRC Press, 2018).
[20] F. Tuomisto, *Characterization and Control of Defects in Semiconductors*, (IET, 2019).
[21] L.P. Avakyants, V.S. Gorelik, and E.D. Obraztsova, J. of Molecular Structure, **219**, 141 (1990).
[22] F. Cristiano, PhD. Dissertation, Université Paul Sabatier - Toulouse III, 2013.

ЛОКАЛЬНА ВАРІАЦІЯ ІНТЕНСИВНОСТІ РОЗСІЯНОГО СВІТЛА В МОНОКРИСТАЛАХ КРЕМНІЮ З ІМПЛАНТАЦІЄЮ ІОНІВ МАРГАНЦЮ

Е.У. Арзікулов[1,2,3], Ф.А. Салаксітдінов[1], Ван Юйцзінь[2], Шаовей Лу[3], Тен Лю[3], Чжишен Нун[3], М.Д. Тошбоєв[1]
[1]Самаркандський державний університет імені Шарофа Рашидова,
140104, бульвар Університету, 15, Самарканд, Республіка Узбекистан
[2]Державна ключова лабораторія прецизійного зварювання та з'єднання матеріалів і конструкцій, Школа матеріалознавства та інженерії, Харбінський технологічний інститут, вул. Ікуан, район Нанган, Харбін 150001, Китай
[3]Школа матеріалознавства та інженерії, Шеньянський аерокосмічний університет, проспект Даої Саут, 37, Шеньян, Китай

У цій статті представлені результати експериментальних досліджень локальних змін інтенсивності розсіяного світла та морфології поверхні у зразках монокристалічного кремнію з електронною провідністю та кристалічною орієнтацією [100], імплантованих Mn. Енергія іонів марганцю, доза імплантації та концентрація фосфору в підкладці становили 40 кеВ, $5\cdot10^{15}\div1\cdot10^{17}$ іонів/см^2 та ~$9{,}3\cdot10^{14}$ см$^{-3}$ відповідно. Для аналізу морфології поверхні до та після імплантації було застосовано атомно-силову мікроскопію (АСМ) та раманівську спектроскопію з використанням геометрії зворотного розсіювання поверхнево розсіяного світла. АСМ-мікрофотографії поверхні показують характерні нанометрові шорсткості, форма та розмір яких сильно залежать від дози імплантації. Ці нанорозмірні об'єкти відсутні на поверхні неімплантованої підкладки. У раманівських спектрах зразків, що не піддавалися імплантації, завжди спостерігається основний пік лоренцовського типу, характерний для монокристалічного кремнію та зосереджений на 520.0±1.0 см$^{-1}$, що відповідає фононному хвильовому вектору. У раманівських спектрах зразків кремнію, імплантованого іонами марганцю, спостерігається кілька піків (184, 291, 373, 468, 659, 798 та 804 см$^{-1}$), ймовірно пов'язаних з утворенням радіаційних дефектів та нанорозмірних об'єктів на поверхні монокристалічного кремнію під час іонної імплантації за участю атомів кремнію, марганцю, фосфору та інших домішок. Ці структурні дефекти кристалічної решітки кремнію на поверхні та поблизу поверхні, спричинені бомбардуванням іонами марганцю, призводять до збудження нових коливальних мод, які не спостерігаються у вихідному кремнії. Ці моди проявляються у спектрах комбінаційного розсіювання.

Ключові слова: *локальна інтенсивність; іонна імплантація; комбінаційне розсіювання; кремній; нанорозмірні об'єкти; хвильовий вектор*

East European Journal of Physics. 4. 512-516 (2025)
DOI:10.26565/2312-4334-2025-4-52 ISSN 2312-4334

LIE ALGEBRAIC MODELING OF VIBRATIONAL FREQUENCIES IN HEXACHLOROBENZENE: A SYMMETRY-ADAPTED APPROACH FOR THE D_{6h} POINT GROUP

D. Rajani[1], T. Sreenivas[2,3], J. Vijayasekhar[4]*
[1]*Department of Mathematics, Siddhartha Academy of Higher Education, Deeemed to be University, Vijayawada 520007, Andhra Pradesh, India*
[2]*Department of Mathematics, Jawaharlal Nehru Technological University, Kakinada, India*
[3]*Department of Mathematics, Anil Neerukonda Institute of Technology & Sciences (ANITS), Visakhapatnam, India*
[4]*Department of Mathematics and Statistics, School of Science, GITAM (Deemed to be University), Hyderabad, India*
**Corresponding Author e-mail: vijayjaliparthi@gmail.com*
Received August 31, 2025; accepted October 16, 2025

This work uses a symmetry-adapted Lie algebraic framework to study the vibrational frequencies of hexachlorobenzene (C_6Cl_6). A U(2)-based vibrational Hamiltonian captures the fundamental modes and the first and second overtones by exploiting the molecule's D_{6h} point group symmetry. The algebraic approach considers anharmonicity and symmetry constraints to provide a compact and manageable analytical portrayal of the vibrational spectrum. The computed fundamental frequencies agree strongly with the observed values, validating the approach. Moreover, the extension to overtones underlines the algebraic model's capability to evaluate higher-order vibrational excitations in polyatomic molecules systematically. These results confirm the effectiveness of Lie algebraic methods in modelling vibrational features of highly symmetric molecules and serve as a solid basis for further work in molecular spectroscopy.
Keywords: *Hexachlorobenzene; Vibrational spectra; Lie algebraic modelling; Symmetry-adapted Hamiltonian; D_{6h} point group*
PACS: 33.20.Tp, 33.15.Mt, 03.65.Fd, 02.20.Sv, and 61.50.Ah

1. INTRODUCTION

Hexachlorobenzene (HCB) has been noted as an aromatic hydrocarbon that has been fully chlorinated, attracting much attention from scholars because of its remarkable stability, environmental longevity, and toxicity. Its diverse industrial applications and use as a fungicide were prominent in the past. However, it has become glaringly apparent that its biological consequences, alongside its long half-life in the environment, result in its classification as a persistent organic pollutant, which goes against international agreements. Reports indicate bioaccumulation of the compound in humans and animals, in which the toxin is contained within the adipose tissues. This results in neurotoxicity, hepatotoxicity, immunotoxicity, and endocrine disruption. Such results are noted as disturbing, especially in children and pregnant women, who are the most vulnerable [1].

The theory of symmetry states that a point group is associated with molecules that have planar structures, are of extreme symmetry, have angle and side counts, and cross elements of 12, like a hexagon. Thus, HCB can be derived from benzene and its six hydrogens replaced with chlorines. The high symmetry planar molecules can thus be characterised and have set vibrational modes that can be useful for modelling vibrational systems. Saeki (1962) states that there are 30 normal vibrational modes of HCB, and they can be divided into three parts: Raman modes, Infrared modes, and inactive (B_{2g}, B_{1u}, E_{2u}, A_{1u}) modes. The inactive modes can be characterised to determine structure, space location, and environmental impacts [2,3,4,].

HCB is a model used to study the vibrational states, and HCB and its depletion have many satellites and data files associated with them. Many techniques have been used to study the vibrational spectra of HCB. HCB has an abundance of data made from approaches for predicting the molecular rotational structures of HCB, like using DFT for electronic charge and spectrum analysis of HCB, and DFT and SQMFF and the DFT approaches with Raman and Infrared spectra techniques [5]. These approaches have proven helpful in many scenarios. However, the approach must be altered regarding computational symmetry, molecules, and the border set. It involves a high cost for experimental observations, resulting in a loss of molecular symmetry and anharmonicity in many systems.

The Lie algebraic approach provides an alternative method for vibrational analysis that is compact, and symmetry driven. It involves the construction of vibrational Hamiltonians in terms of U(2) Lie algebra generators and number, Casimir, and Majorana operator terms. Due to the symmetry and anharmonic effects incorporated within the approach, a more intuitive and physically more precise representation of vibrational states is obtained. In contrast to standard ab initio methods, the algebraic approach does not depend on potential energy surfaces and offers an algebraic formulation for vibrational levels [6-14].

The exceptionally well-defined vibrational characteristics of HCB and high D_{6h} symmetry make it a perfect subject for algebraic modelling. An adapted symmetry Hamiltonian readily provides analysis of overtone and combination bands with a reduced set of adjustable parameters. In this paper, we use the U(2) Lie algebraic approach to compute the fundamental vibrational frequencies of HCB and to compare these with experimental results to illustrate the usefulness of the approach [2].

Cite as: D. Rajani, T. Sreenivas, J. Vijayasekhar, East Eur. J. Phys. 4, 512 (2025), https://doi.org/10.26565/2312-4334-2025-4-52

2. MOLECULAR STRUCTURE AND SYMMETRY-BASED VIBRATIONAL MODE CLASSIFICATION

HCB comprises a benzene ring in which all its six hydrogen atoms are replaced with chlorine atoms. The molecule is fully substituted in this form, retains its planar form, and maintains D_{6h} symmetry. X-ray crystallographic and other structural studies have demonstrated that the molecule is also planar in the solid and gas phases [3]. The D_{6h} point group is one of the highest symmetries possible for a molecule, characterised by having a C_6 principal rotation axis, six C_2 perpendicular axes, horizontal and vertical mirror planes (σ_h and σ_v), dihedral planes, and an inversion centre (i) [2].

The symmetry of HCB is so high that it profoundly constrains the vibrational activity of the molecule in the Raman and infrared spectra. The molecule in question, containing 12 atoms, has 3N- 6 = 30 normal vibrational modes, all governed by the D_{6h} symmetry group. The Raman-active modes are the A_{1g}, E_{2g}, and E_{1g}, while the infrared-active modes are E_{1u} and A_{2u}. The representations B_{2g}, B_{1u}, E_{2u}, and A_{1u} are all silent in the spectrum.

Experimental investigations have assigned detailed vibrations of modes. Saeki (1962) recorded a strong A_{1g} symmetric C–Cl stretching mode at ~1225 cm^{-1} and a breathing mode close to 377 cm^{-1}. E_{2g} modes at ~692 cm^{-1} are considered in-plane deformations of C–C–C. Kopelman and Schnepp (1959) reported strong IR-active E_{1u} modes at 696 cm^{-1} and 1340 cm^{-1}, associated with asymmetric C–Cl stretching vibrations. The empirical work of Zhang et al. (2011) regarding comparative Raman studies of benzene and HCB documented how substituting chlorine with benzene alters the vibrational frequencies and symmetry assignments. The authors reported low-frequency bands in the 219-377 cm^{-1} range attributed to Cl-bending and A_{2u} and E_{1u} Cl shear vibrations [2,3,4].

Computational studies have further improved the clarity of the spectral interpretations. Castillo et al. (2015) applied DFT with SQMFF correction, using B3LYP/6-31G* and 6-311++G** with geometry optimisation and frequency calculation in DFT, and validated the results with D_{6h} symmetry possession and experimental Raman and IR spectra. Their work reinforces the remaining theoretical and experimental analyses of vibrational spectral data by supporting the' detailed assignments of their findings [5].

The classification of HCB vibrational modes under D_{6h} symmetry has been precisely defined, which makes it useful for algebraic modelling. The ease of construction of symmetry-adapted Lie algebraic Hamiltonians, because of the regularity and degeneracy of the vibrational levels, makes the anterior framework simple to calculate and valuable for an analytical approach to vibrational frequencies. These aspects make it the core of the study at hand.

3. U(2) LIE ALGEBRAIC VIBRATIONAL HAMILTONIAN OF HEXACHLOROBENZENE

The U(2) Lie algebraic approach identifies bosonic realisations of U(2) algebras with each of the vibrational modes of a molecule. For a molecule of vibrational type, the Hamiltonian is expressed through the number operators, Majorana interaction terms, and Casimir invariants [15, 16]. For polyatomic molecules, Iachello, Levine, and Oss formulated the general algebraic Hamiltonian as

$$H = E_0 + \sum_{i=1}^{n} A_i\, C_i + \sum_{i<j}^{n} A_{ij}\, C_{ij} + \sum_{i<j}^{n} \lambda_{ij}\, M_{ij} \tag{1}$$

where:

- $\langle C_i \rangle = -4(N_i v_i - v_i^2)$ is the Casimir invariant of U(2) for the *i* th mode,
- $\langle N_i, v_i; N_j, v_j | C_{ij} | N_i, v_i; N_j, v_j \rangle = 4(v_i + v_j)(v_i + v_j - N_i - N_j)$ is the two-mode Casimir interaction term between modes *i* and *j*,
- $\left.\begin{aligned} &\langle N_i, v_i; N_j, v_j | M_{ij} | N_i, v_i; N_j, v_j \rangle = v_i N_j + v_j N_i - 2 v_i v_j \\ &\langle N_i, v_i + 1; N_j, v_j - 1 | M_{ij} | N_i, v_i; N_j, v_j \rangle = -[v_j (v_i + 1)(N_i - v_i)(N_j - v_j + 1]^{1/2} \\ &\langle N_i, v_i - 1; N_j, v_j + 1 | M_{ij} | N_i, v_i; N_j, v_j \rangle = -[v_i (v_j + 1)(N_j - v_j)(N_i - v_i + 1]^{1/2} \end{aligned}\right\}$ denotes the Majorana interaction operator representing dynamic coupling,
- $A_i, A_{ij}, \lambda_{ij}$ are empirical parameters,
- $N_i (= N), i = 1,2,3,4,5,6$ is the boson number associated with mode *i*,
- v_i is the vibrational quantum number for mode *i*.

The boson number *N* determines the basis set size for describing molecular vibrations and is defined as:

$$N = \frac{\omega_e}{\omega_e \chi_e} - 1,$$

where ω_e and $\omega_e \chi_e$ denote the harmonic and anharmonic spectroscopic constants of the C-Cl and C-C bonds, respectively, as reported by Karl K. Irikura [17].

There are three classes of non-diagonal interactions within the benzene framework of the HCB molecule. They are represented as couplings associated with various positions of the structure's hexagonal bent carbon vibrational modes [15].

First-neighbour couplings (nearest-neighbour interactions): Couplings of adjacent carbon atoms in the ring.
Examples: (1-2), (2-3), (3-4), (4-5), (5-6), (6-1).

Second-neighbour couplings (next-nearest-neighbour interactions): Couplings of carbon atoms with a spacing of one bond.
Examples: (1-3), (2-4), (3-5), (4-6), (5-1), (6-2).

Third-neighbour couplings (opposite interactions): Couplings of carbon atoms located diametrically opposite the ring.
Examples: (1-4), (2-5), (3-6)

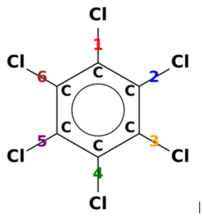

Figure 1. HCB structure with labelled C–Cl bonds

Consider S^I (C-H type first neighbour interactions), S^{II} (C-H type second neighbor interactions), S^{III} (C-H type third neighbor interactions) are symmetry-adapted operators. In the context of the HCB D_{6h} symmetry, the symmetry-adapted operators pertain to precisely these couplings, which are

$$S^I = \sum_{i<j}^{6} k'_{ij}\, M_{ij}, \quad S^{II} = \sum_{i<j}^{6} k''_{ij}\, M_{ij}, \quad S^{III} = \sum_{i<j}^{6} k'''_{ij}\, M_{ij}$$

With

$$k'_{12} = k'_{23} = k'_{34} = k'_{45} = k'_{56} = k'_{16} = 1,$$
$$k'_{13} = k'_{24} = k'_{35} = k'_{46} = k'_{15} = k'_{26} = 0,$$
$$k'_{14} = k'_{25} = k'_{36} = 0,$$
$$k''_{12} = k''_{23} = k''_{34} = k''_{45} = k''_{56} = k''_{16} = 0,$$
$$k''_{13} = k''_{24} = k''_{35} = k''_{46} = k''_{15} = k''_{26} = 1,$$
$$k''_{14} = k''_{25} = k''_{36} = 0,$$
$$k'''_{12} = k'''_{23} = k'''_{34} = k'''_{45} = k'''_{56} = k'''_{16} = 0$$
$$k'''_{13} = k'''_{24} = k'''_{35} = k'''_{46} = k'''_{15} = k'''_{26} = 0$$
$$k'''_{14} = k'''_{25} = k'''_{36} = 1$$

For the case of the HCB molecule, in which all the molecule's bonds are equivalent, the most general and most basic, as well as the lowest-order, Hamiltonian describing the C-H stretching vibrations can be formulated as follows:

$$H = E_o + A\sum_{i}^{6} C_i + A'\sum_{i<j}^{6} C_{ij} + \lambda' S^I + \lambda'' S^{II} + \lambda''' S^{III}$$

Given the equivalent bonds, the vibron numbers N_i must hold the same value, i.e., $N_i = N$. Consequently, the molecule's symmetry establishes specific requirements on the coefficients within equation (1), as follows:

$$N_i = N,\ A_i = A,\ \ A_{ij} = A'$$
$$\lambda_{12} = \lambda_{23} = \lambda_{34} = \lambda_{45} = \lambda_{56} = \lambda_{61} = \lambda'$$
$$\lambda_{13} = \lambda_{24} = \lambda_{35} = \lambda_{46} = \lambda_{15} = \lambda_{26} = \lambda''$$
$$\lambda_{14} = \lambda_{25} = \lambda_{36} = \lambda'''$$

The distinctive attributes of $C-H$ stretching vibrations in benzene encompass five quantities: $A, A', \lambda', \lambda'', \lambda'''$. The initial guess for the fundamental mode parameters A is obtained from the single-oscillator energy expressions:

$$A = -\frac{E}{4(N-1)}.$$

The initial values of interaction parameters $\lambda', \lambda'', \lambda'''(=0)$ are given by:

$$\lambda' = \frac{|E'_1 - E'_2|}{2N}, \lambda'' = \frac{|E'_1 - E'_2|}{6N},$$

where E_1 and E_2 represent the symmetric and antisymmetric energy combinations of the two local modes. The parameters are optimised using least-square regression fitting, while A' is initially set to zero to ensure a systematic optimization procedure using the available observed data reported by Saeki (1962). The optimised parameter values are: $N^{C-Cl} = 160$, $N^{C-C} = 134, A = -3.52$, $A' = 0.73$, $\lambda' = 1.81, \lambda'' = 0.26$.

4. RESULTS AND DISCUSSION

The vibrational spectrum of HCB was successfully predicted using the symmetry-adapted U(2) Lie algebraic Hamiltonian. Table 1 presents the predicted fundamental frequencies, which align remarkably well with the corresponding experimental data. The small Deviations, encapsulated by an root mean square (RMS) error of 5.21 cm^{-1}, underscore the exceptional fit achieved by the algebraic approach across the entire vibrational region. A comprehensive study of the overtones was conducted, and the results, including both the first and second overtones, are detailed in Table 2. The remarkably low RMS value underscores the reliability of the Lie algebraic framework. Its succinct nature, in terms of the number of fitting parameters and algebraic complexity, makes it a trustworthy choice. When compared to conventional approaches at the same accuracy level, the algebraic treatment eliminates much of the nucleation and convergence uncertainty, providing a pragmatic and trustworthy route for precise vibrational modelling without the need for multiple layers of fitted functional input.

Table 1. Fundamental Vibrational frequencies (in cm^{-1}) for HCB

Vibrational Mode	Mode	Activity	Symmetry Species	Fundamental	
				Observed [2]	Calculated
ν_1	C-Cl stretching	Raman	A_{1g}	1225	1221.03
ν_{13}	C-Cl stretching	IR	E_{1u}	696	697.27
ν_{12}	Ring Stretching	IR	E_{1u}	1350	1346.51
ν_{15}	Ring Stretching	Raman	E_{1u}	1522	1519.55
ν_{18}	C-Cl in -plane bending	Raman	E_{2g}	322	329.90
ν_{11}	C-Cl in -plane bending	Raman	E1g	213	221.04

Table 2. First and second overtone Vibrational frequencies (in cm^{-1}) for HCB

Vibrational Mode	Mode	Symmetry Species	Vibrational Frequencies	
			I Overtone	II Overtone
ν_1	C-Cl stretching	A1g	2426.6	3616.72
ν_{13}	C-Cl stretching	E1u	1375.71	2055.33
ν_{12}	Ring Stretching	E1u	2665.98	3988.4
ν_{15}	Ring Stretching	E1u	3016.87	4507.95
ν_{18}	C-Cl in -plane bending	E2g	641.62	957.17
ν_{11}	C-Cl in -plane bending	E1g	430.28	644.73

5. CONCLUSIONS

The present study shows that using symmetry-adapted U(2) Lie algebra techniques leads to an accurate yet computationally efficient description of the vibrational spectrum of hexachlorobenzene. Computed fundamental frequencies align extremely well with observed values, yielding a root mean square deviation of only 5.21 cm^{-1}, which attests to the method's robustness. Extending the algebraic model to predict overtone bands underscores its ability to treat anharmonicity and symmetry constraints simultaneously and elegantly. In summary, the symmetry-adapted U(2)-algebraic engine delivers a compact formulation that rivals the precision of extensive quantum chemistry calculations while remaining straightforward. These attributes provide a solid foundation for applying the approach to other polyatomic species possessing high symmetry in forthcoming work.

ORCID

J. Vijayasekhar, https://orcid.org/0000-0002-2745-7401

REFERENCES

[1] L. Casadó, J.P. Arrebola, A. Fontalba, and A. Muñoz, "Adverse effects of hexachlorobenzene exposure in children and adolescents," Environ. Res. **176**, 108421 (2019). https://doi.org/10.1016/j.envres.2019.03.059

[2] S. Saeki, "The assignment of the molecular vibrations of hexachlorobenzene," Bull. Chem. Soc. Jpn. **35**, 322–328 (1962). https://doi.org/10.1246/bcsj.35.322

[3] R. Kopelman, and O. Schnepp, "Infrared spectrum of hexachlorobenzene," J. Chem. Phys. **30**, 597–598 (1959). https://doi.org/10.1063/1.1730006

[4] X. Zhang, Q. Zhou, Y. Huang, Z. Li, and Z. Zhang, "Contrastive analysis of the Raman spectra of polychlorinated benzene: hexachlorobenzene and benzene," Sensors, **11**, 11510–11515 (2011). https://doi.org/10.3390/s111211510

[5] M.V. Castillo, M.E. Manzur, L. Di Marco, V. Runco, and S.A. Brandán, "Structural and vibrational study of a powerful environmental pollutant agent, the hexachlorobenzene compound," in: *Vibrational Spectroscopy and Structural Characterization*, Chap. 7, (2015).

[6] F. Iachello, and S. Oss, "Stretching vibrations of benzene in the algebraic model," Chem. Phys. Lett. **187**, 500–505 (1991). https://doi.org/10.1016/0009-2614(91)80290-E

[7] S. K. Singha, A. Kalyan, R. Sen, and R. Bhattacharjee, "Successful applications of Lie algebraic model to analyze the vibrational spectra of fluorobenzene," Polycycl. Aromat. Compd. **34**, 135–142 (2014). https://doi.org/10.1080/10406638.2013.861497

[8] J. Vijayasekhar, P. Suneetha, and K. Lavanya, "Vibrational spectra of cyclobutane-d8 using symmetry-adapted one-dimensional Lie algebraic framework," Ukr. J. Phys. Opt. **24**, 193–199 (2023). https://doi.org/10.3116/16091833/24/3/193/2023

[9] S. K. Singha, A. Kalyan, R. Sen, and R. Bhattacharjee, "The vibrational spectra of monomer and dimer of benzene: An algebraic approach," Polycycl. Aromat. Compd. **34**, 388–396 (2014). https://doi.org/10.1080/10406638.2014.892891
[10] S. Teppala, and V. Jaliparthi, "Exploring cyclohexane vibrational dynamics through a Lie algebraic Hamiltonian framework," Ukr. J. Phys. Opt. **25**, 03093–03100 (2024). https://doi.org/10.3116/16091833/Ukr.J.Phys.Opt.2024.03093
[11] V. Jaliparthi, and M. R. Balla, "Vibrational Hamiltonian of tetrachloro-, tetrafluoro-, and mono-silanes using U(2) Lie algebras," Spectrochim. Acta A Mol. Biomol. Spectrosc. **264**, 120289 (2022). https://doi.org/10.1016/j.saa.2021.120289
[12] F. Iachello, and S. Oss, "Algebraic methods in quantum mechanics: from molecules to polymers," Eur. Phys. J. D **19**, 307–314 (2002). https://doi.org/10.1140/epjd/e20020089
[13] N.K. Sarkar, J. Choudhury, S.R. Karumuri, and R. Bhattacharjee, "An algebraic approach to the comparative study of the vibrational spectra of monofluoroacetylene (HCCF) and deuterated acetylene (HCCD)," Mol. Phys. **106**, 693–702 (2008). https://doi.org/10.1080/00268970801939019
[14] S. Nallagonda, and V. Jaliparthi, "Higher overtone vibrational frequencies in naphthalene using the Lie algebraic technique," Ukr. J. Phys. Opt. **25**, 02080–02085 (2024). https://doi.org/10.3116/16091833/Ukr.J.Phys.Opt.2024.02080
[15] F. Iachello, and R.D. Levine, *Algebraic Theory of Molecules*, (Oxford University Press, Oxford, 1995).
[16] S. Oss, "Algebraic models in molecular spectroscopy," Adv. Chem. Phys. **145**, 455–469 (2009). https://doi.org/10.1002/9780470141526.ch8
[17] K.K. Irikura, "Erratum: Experimental vibrational zero-point energies: Diatomic molecules, J. Phys. Chem. Ref. Data, **36**, 389-397 (2007)," J. Phys. Chem. Ref. Data **38**, 749 (2009). https://doi.org/10.1063/1.3167794

АЛГЕБРАЇЧНЕ МОДЕЛЮВАННЯ ЛІ КОЛИВАЛЬНИХ ЧАСТОТ У ГЕКСАХЛОРБЕНЗЕНІ: ПІДХІД, АДАПТОВАНИЙ ДО СИМЕТРІЇ ДЛЯ ТОЧКОВОЇ ГРУПИ D_{6h}

Д. Раджані[1], Т. Сріновас[2,3], Дж. Віджаясекар[4]
[1]Кафедра математики, академія вищої освіти Сіддхартхи, (вважається університетом), Віджаявада 520007, Андхра-Прадеш, Індія
[2]Кафедра математики, технологічний університет імені Джавахарлала Неру, Какінада, Індія
[3]Кафедра математики, технологічний та науковий інститут Аніла Неруконди (ANITS), Вішакхапатнам, Індія
[4]Кафедра математики та статистики, школа наук, GITAM (вважається університетом), Хайдарабад, Індія

У цій роботі використовується адаптована до симетрії алгебраїчна структура Лі для вивчення коливальних частот гексахлорбензолу (C_6Cl_6). Вібраційний гамільтоніан на основі U(2) фіксує фундаментальні моди та перший і другий обертони, використовуючи симетрію точкової групи D_{6h} молекули. Алгебраїчний підхід враховує обмеження ангармонізму та симетрії, щоб забезпечити компактне та кероване аналітичне зображення коливального спектру. Обчислені фундаментальні частоти добре узгоджуються зі спостережуваними значеннями, що підтверджує правильність підходу. Більше того, розширення на обертони підкреслює здатність алгебраїчної моделі систематично оцінювати коливальні збудження вищого порядку в багатоатомних молекулах. Ці результати підтверджують ефективність алгебраїчних методів Лі в моделюванні коливальних характеристик високосиметричних молекул і служать міцною основою для подальшої роботи в молекулярній спектроскопії.

Ключові слова: *гексахлорбензол; вібраційні спектри; алгебраїчне моделювання Лі; симетрійно-адаптований гамільтоніан; точкова група D_{6h}*

East European Journal of Physics. 4. 517-526 (2025)
DOI:10.26565/2312-4334-2025-4-53 ISSN 2312-4334

DIELECTRIC CONSTANTS AND TRANSVERSE EFFECTIVE CHARGES IN THE QUINARY ALLOY $Ga_xIn_{1-x}N_ySb_zAs_{1-y-z}$ LATTICE MATCHED TO InAs, GaSb AND GaAs

H. Zerroukhi[1#], H. Abid[1], H. Baaziz[2,3], T. Ghellab[2,3], Z. Charifi[2,3]*
[1]*Applied Materials Laboratory, Research Center, sidi Bel Abbes University, 22000 Algeria*
[2]*Department of Physics, Faculty of Science, University of M'sila, 28000 M'sila, Algeria*
[3]*Laboratory of physics and chemistry of materials, University of M'sila, Algeria*
** Corresponding author e-mail: hakim.baaziz@univ-msila.dz; houari.zerroukhi@univ-sba.dz*
Received July 9, 2025; revised October 21, 2025; accepted October 23, 2025

This study provides a comprehensive theoretical analysis of the dielectric properties and transverse effective charges of the pentanary alloy $Ga_xIn_{1-x}N_ySb_zAs_{1-y-z}$, focusing on compositions that are lattice-matched to InAs, GaSb, and GaAs substrates. The investigation employs the local empirical pseudopotential method (EPM) in conjunction with the virtual crystal approximation (VCA) and the Harrison bond-orbital model to evaluate key parameters, including the static and high-frequency dielectric constants, ionicity, polarity, and transverse effective charge. These computational approaches were chosen due to their ability to accurately describe electronic interactions in complex alloy systems while maintaining computational efficiency. The results demonstrate strong consistency with available experimental data for the constituent binary compounds, reinforcing the reliability of the theoretical framework. Additionally, the study reveals systematic trends in the dielectric behavior as a function of composition, providing insights into the role of atomic substitution in tuning these properties. To the best of our knowledge, this work represents the first detailed theoretical assessment of $Ga_xIn_{1-x}N_ySb_zAs_{1-y-z}$ alloys in this context. While experimental validation remains necessary, our findings establish a valuable theoretical benchmark for future studies and potential applications in optoelectronic and semiconductor device engineering, particularly in the design of advanced infrared detectors and high-frequency electronic components.
Keywords: *EPM; Polarity; Dielectric constants; Transverse effective charge; Lattice matched alloys; Pentanary*
PACS: 77.22.Ch; 78.55.Cr; 71.22.+I; 71.15.Dx; 71.23.-k

1. INTRODUCTION

The integration of III-N-V semiconductors into modern optoelectronic and high-frequency microelectronic devices has gained significant attention due to their unique electronic and optical properties [1]. These materials exhibit direct band gaps [2], high carrier mobilities, and tunable electronic characteristics, making them essential for applications such as infrared photodetectors, laser diodes, and high-speed transistors [3,4]. In particular, they are widely used in fiber-optic communication systems, where the 1.3 μm and 1.5 μm wavelength regimes are critical for minimizing signal attenuation [5]. The incorporation of nitrogen into III-V semiconductors plays a crucial role in band gap engineering, as even small amounts of nitrogen induce a substantial reduction in the band gap [6], thereby allowing for precise control of optical and electronic properties.

Among the various III-N-V compounds, the pentanary alloy $Ga_xIn_{1-x}N_ySb_zAs_{1-y-z}$ presents a promising material system with highly tunable properties while maintaining lattice-matching conditions with widely used substrates such as InAs, GaSb, and GaAs. Ensuring lattice matching is essential for epitaxial growth, as strain-induced defects can significantly degrade the material's electronic transport properties, optical efficiency, and thermal stability. The ability to engineer the band gap and dielectric properties of pentanary alloys while preserving structural compatibility with established semiconductor platforms opens new avenues for the development of advanced optoelectronic devices. Despite their technological potential, pentanary III-N-V alloys remain largely unexplored in terms of their dielectric response and transverse effective charge behavior. While binary and ternary III-V semiconductors have been extensively studied, the complexity introduced by five constituent elements makes direct experimental characterization particularly challenging. This necessitates a rigorous theoretical investigation to systematically analyze the dielectric properties of $Ga_xIn_{1-x}N_ySb_zAs_{1-y-z}$, providing critical insights that can serve as a theoretical foundation for experimental studies and device optimization.

To achieve an accurate and predictive description of the dielectric properties of these alloys, we employ a combination of well-established theoretical approaches. The local empirical pseudopotential method (EPM) is utilized to model electron-ion interactions, providing an effective means of describing the electronic band structure of complex multi-component alloys [7,8]. This method has been extensively validated against experimental data for binary III-V semiconductors, demonstrating its reliability in capturing essential electronic properties. The virtual crystal approximation (VCA) [9] is employed to treat the pentanary alloy as an effective medium, where the electronic properties are approximated as a weighted average of the constituent binaries. This approximation offers a computationally efficient means of estimating key dielectric parameters, ionicities, and transverse effective charges, enabling a predictive framework for understanding composition-dependent variations in material properties. Additionally, Harrison's bond-orbital model [10,11] is incorporated to refine the description of chemical bonding, interatomic interactions, and charge transfer effects. This analytical approach allows the

Cite as: H. Zerroukhi, H. Abid, H. Baaziz, T. Ghellab, Z. Charifi, East Eur. J. Phys. 4, 517 (2025), https://doi.org/10.26565/2312-4334-2025-4-53

calculation of dielectric constants, ionicity, and the transverse effective charge by explicitly accounting for orbital hybridization effects, thereby providing deeper insight into the polarization dynamics and dielectric response of the alloy.

The primary objective of this work is to conduct a comprehensive theoretical analysis of the static and high-frequency dielectric constants, ionicity, polarity, and transverse effective charge of the pentanary alloy $Ga_xIn_{1-x}N_ySb_zAs_{1-y-z}$ while maintaining lattice-matching conditions with InAs, GaSb, and GaAs substrates. The study aims to determine how the dielectric response evolves as a function of alloy composition, how substrate selection influences the transverse effective charge and ionicity, and how these properties can be optimized for optoelectronic applications, particularly in the mid-infrared spectral range. A key aspect of this investigation is to establish quantitative relationships between alloying effects and dielectric behavior, providing fundamental insights into the design of III-N-V materials for advanced photonic and electronic applications. Given the absence of experimental data for pentanary III-N-V alloys, the findings presented in this work serve as a benchmark for future experimental validation and materials engineering efforts.

2. THEORETICAL FORMALISM

To better understand the structural and electronic properties of semiconductor materials, we rely on the interpretation of various experiments, whose coherence depends on an accurate representation of their electronic structures based on band theory. Given the impossibility of solving the Schrödinger equation exactly for an n-body system, approximation methods have been employed to achieve the best possible agreement between calculated and measured values of key quantities such as energy levels and bond lengths. Over the past decades, numerous electronic structure calculation techniques have been developed, particularly empirical methods, which have now become fundamental tools for computing complex structural and electronic properties. These methods also serve as valuable tools for predicting the properties of new materials.

In the empirical pseudopotential approach, the potential of a semiconductor is typically described as the sum of local and nonlocal pseudo-atomic contributions, given by $V = V_L + V_{NL}$. However, in the present study, the nonlocal term (V_{NL}) is neglected. The corresponding pseudopotential Hamiltonian is formulated as $H = (-h/2m)\nabla^2 + V_L(r)$, where the effective potential $V_L(r)$ is expressed as a Fourier expansion in the reciprocal lattice space [7-14]. The lattice parameter of the pentanary alloy $Ga_xIn_{1-x}N_ySb_zAs_{1-y-z}$ obeys the following relationship:

$$a\left(Ga_xIn_{1-x}N_ySb_zAs_{1-y-z}\right) = xya(GaN) + xza(GaSb) + x(1-y-z)a(GaAs) \\ +(1-x)ya(InN) + (1-x)za(InSb) + (1-x)(1-y-z)a(InAs) \quad (1)$$

Where (a(GaN)), (a(GaAs)), (a(GaSb)), (a(InN)), (a(InAs)), and (a(InSb)) represent the lattice parameters of the binary constituents forming the GaInNAsSb alloy, their values are determined based on Vegard's law [12,13].

Utilizing the virtual crystal approximation (VCA) [14], the pseudopotential form factors for the alloy can be formulated as a sum of nonlinear contributions:

$$V^{s,a}_{Ga_xIn_{1-x}N_ySb_zAs_{1-y-z}} = xyV^{s,a}_{GaN} + xzV^{s,a}_{GaSb} + x(1-y-z)V^{s,a}_{GaAs} \\ +(1-x)yV^{s,a}_{InN} + (1-x)zV^{s,a}_{InSb} + (1-x)(1-y-z)V^{s,a}_{InAs} \quad (2)$$

Where $V^{s,a}$ are the symmetric and antisymmetric pseudopotential form factors at the reciprocal lattice vector G(111), (see Table 1) optimized using the nonlinear least-squares method [15].

Table 1. Presents the optimized local pseudopotential form factors at the Γ, X, and L high-symmetry points of the Brillouin zone (in q^{Ry}) for the relevant binary compounds. Additionally, the corresponding lattice constants (in nd) utilized in the calculations are provided

Compound	Form factors						Lattice constant Å
	Vs(3)	Vs(8)	Vs(11)	Va(3)	Va(4)	Va(11)	
GaAs	-0.239833	0.012600	0.059625	0.060536	0.050000	0.010000	5.653 [a]
InAs	-0.182147	0	0.047107	0.094714	0.05	0.03	6.058 [a]
GaSb	-0.191206	0.005	0.043533	0.04534	0.03	0	6.118 [a]
InSb	-0.201822	0.01	0.028443	0.064645	0.03	0.015	6.4794 [b]
GaN	-0.346925	0.161439	-0.016000	0.200000	0.211824	0.135	4.4878 [c]
InN	-0.328532	0.091201	0.003930	0.320000	- 0.033147	-0.006892	4.9868 [c]

[a] ref. [16]; [b] ref. [17]; [c] ref. [18].

Table 2. The calculated direct and indirect band-gaps energy (in ^{eV}) of our binaries in comparison with the experimental and others works ones

Compound	Band-gap energy (eV)					
	E_g^{Γ}		E_g^{x}		E_g^{L}	
	Exp. Others	Our cal.	Exp. Others	Our cal.	Exp. Others	Our cal.
GaAs	1.424[a]	1.421	1.81[a]	1.814	1.72[a]	1.722
InAs	0.36[b]	0.324	1.37[b]	1.374	1.07[b]	1.072
GaSb	0.725[c]	0.727	1.03[d]	1.015	0.761[d]	0.778
InSb	0.18[b]	0.174	1.63[b]	1.63	0.93[b]	0.93
GaN	3.2[e]	3.20	4.7[e]	4.602	6.2[e]	6.045
InN	0.7[f]	0.778	2.51[g]	2.518	5.82[h]	5.825

[a] ref. [19]; [b] ref. [20]; [c] ref. [21]; [d] ref. [22]; [e] ref. [7]; [f] ref. [23]; [g,h] ref. [8].

The eigenvalue problem in this study is characterized by a 136×136 matrix. The pseudopotential form factors are determined by the magnitudes of the reciprocal lattice vectors (G). To ensure computational accuracy, a cutoff value of $|G|^2 = 11(2\pi/a)^2$ is applied.

The lattice-matching condition for the pentanary alloy $Ga_xIn_{1-x}N_ySb_zAs_{1-y-z}$ on InAs, GaSb and GaAs substrates is obtained from Equation (1) and can be expressed as follows:

$$y = \frac{a\,sub + 0.405\,x - 0.4214\,z - 0.0436\,xz - 6.058}{-(0.094x + 1.0712)} \tag{3}$$

Where $a_{sub} = a_{InAs} = 6.058$ Å for InAs substrate, $a_{sub} = a_{GaSb} = 6.118$ Å for GaSb substrate and $a_{sub} = a_{GaAs} = 5.653$ Å for GaAs substrate.

By employing the Herve and Vandamme expression [22], the refractive index *n* was determined, which is essential for designing quantum well lasers and solar cell applications. This expression is valid in the low-frequency limit $\omega \ll \omega_0$, where ω_0 represents the ultraviolet resonance frequency.

$$n = \sqrt{1 + \left(\frac{A}{E_g + B}\right)^2} \tag{4}$$

where E_g is the fundamental band-gap energy and A=13.6 eV and B =3.4 eV.

The optical high-frequency dielectric constant (ε_∞) is given by the square of the refractive index, n^2 [23].

$$\varepsilon_\infty = n^2 \tag{5}$$

Using the Harrison model [24], the static dielectric constant ε_0 can be expressed in terms of the optical high-frequency dielectric constant (ε_∞) through the following relation:

$$\frac{\varepsilon_0 - 1}{\varepsilon_\infty - 1} = 1 + v \tag{6}$$

Where v is given by [25],

$$v = \frac{\alpha_p^2\,(1 + 2\alpha_c^2)}{2\alpha_c^4} \tag{7}$$

The covalency α_c of the material under study is associated with its polarity α_p through the following relationship:

$$\alpha_c = (1 - {\alpha_p}^2)^{1/2} \tag{8}$$

The polarity α_p is defined by Vogl [25] as

$$\alpha_p = \frac{-V^a(3)}{V^s(3)} \tag{9}$$

$V^s(3)$ and $V^a(3)$ represent the symmetric and antisymmetric pseudopotential form factors at the reciprocal lattice vector G(111). The transverse effective charge (e_T^*) is computed using the following expression [26]:

$$2e_T^* = -\Delta_Z^* + \frac{8\alpha_p}{1 + {\alpha_p}^2} \tag{10}$$

Where

$$\Delta_z^* = xz_{Ga}^* + (1 - x)z_{In}^* - yz_N^* - zz_{Sb}^* - (1 - y - z)z_{As}^* \tag{11}$$

In last, we have the iconicity f_i given by,

$$f_i = 1 - {\alpha_c}^3 \tag{12}$$

3. NUMERICAL RESULTS

Allowed lattice-matching relations between x, y, and z for the $Ga_xIn_{1-x}N_ySb_zAs_{1-y-z}$ alloy with the substrates GaAs, InAs, and GaSb are shown in Figures 1a, 1b, and 1c. These figures provide critical insights into the compositional constraints required to achieve lattice-matching with different substrates, an essential factor in optimizing semiconductor heterostructures for device applications.

The study of static and high-frequency dielectric constants, transverse effective charge, and ionicity in multi-component alloys such as GaInNAsSb is crucial in modern material research. A deep understanding of these parameters enables the design and optimization of materials for semiconductor applications, leading to technological advancements in optoelectronic devices, high-speed electronics, and infrared photodetectors. This motivates our investigation into these fundamental properties.

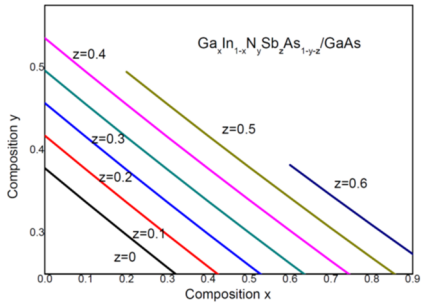

Figure 1a. Allowed lattice-matching relations between x, y, and z for the $Ga_xIn_{1-x}N_ySb_zAs_{1-y-z}$ with the substrate GaAs

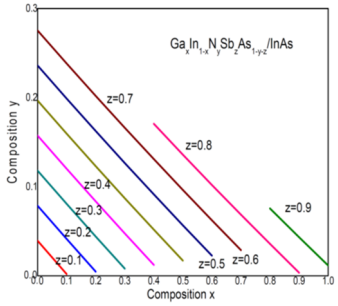

Figure 1b. Allowed lattice-matching relations between x, y, and z for the $Ga_xIn_{1-x}N_ySb_zAs_{1-y-z}$ with the substrate InAs

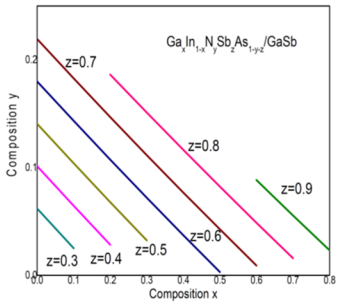

Figure 1c. Allowed lattice-matching relations between x, y, and z for the $Ga_xIn_{1-x}N_ySb_zAs_{1-y-z}$ with the substrate GaSb

Table 3. Optical static dielectric constant (ε_0), optical high-frequency dielectric constant (ε_∞), and transverse effective charge (e_T^*) of binaries of interest

Compound	ε_0		ε_∞		e_T^*	
	Exp.	Our cal.	Exp.	Our cal.	Exp.	Our cal.
GaAs	12.9[a]	9.78	10.9[a]	8.95	2.07[b]	1.95
InAs	15.15[a]	22.66	12.3[c]	14.33	2.53[c]	2.63
GaSb	15.7[a]	12.85	14.4[c]	11.86	2.15[c]	1.90
InSb	16.8[a]	18.05	15.7[c]	15.48	2.42[c]	2.16
GaN	9.7[d]	7.16	5.30[d]	5.25	2.51[e]	2.53
InN	8.40[f]	8.43	8.4[f]	7.58	3.04[e]	2.03

[a] ref. [27]; [b] ref. [28]; [c] ref. [29]; [d] ref. [26]; [e] ref. [30]; [f] ref. [31]

Table 3 presents the calculated values of the optical static dielectric constant (ε_0), optical high-frequency dielectric constant (ε_∞), and transverse effective charge (e_T^*) for the relevant binary compounds, compared with available experimental data. The computed values generally follow the expected trend, where compounds with higher dielectric constants exhibit stronger polarization and lower band gaps. GaAs, InAs, and GaSb exhibit relatively high (ε_0), indicating strong electronic polarizability, while GaN and InN have significantly lower values due to their wider band gaps. The agreement between computed and experimental values validates the accuracy of our theoretical model.

The transverse effective charge reflects the bond ionicity and charge transfer characteristics of the materials. The results indicate that InAs and InSb exhibit higher (e_T^*) values than GaAs and GaSb, suggesting a greater degree of ionicity and charge asymmetry in their bonding. GaN and InN show relatively high transverse effective charges, consistent with their polar nature and strong ionicity. The theoretical values are in good agreement with experimental references, confirming the reliability of our computational framework. Minor discrepancies, such as a slight underestimation of (ε_0) for GaAs and overestimation for InSb, can be attributed to computational approximations, particularly in electron-phonon interactions.

The binary dielectric properties in Table 3 provide a foundation for understanding the behavior of GaInNAsSb. By tuning the composition (x, y, z), the dielectric response can be engineered for specific applications, such as optimizing (ε_∞) for better light absorption and carrier confinement in quantum wells, adjusting (e_T^*) to enhance electronic polarization and charge transport in infrared and terahertz applications, and controlling dielectric screening for high-speed transistors and photodetectors. The results obtained in this study demonstrate strong agreement with experimental data, confirming the suitability of the theoretical approach in predicting dielectric and charge transport properties in complex semiconductor alloys.

Figures 2 and 3 illustrate the calculated optical static dielectric constant (ε_0) and the high-frequency dielectric constant (ε_∞) for the pentanary alloy $Ga_xIn_{1-x}N_ySb_zAs_{1-y-z}$, considering two different lattice-matching conditions: InAs and GaSb. These figures provide valuable insight into the role of nitrogen incorporation on the dielectric properties of the material.

The static dielectric constant (ε_0) shown in Figure 2 exhibits a monotonic increase with increasing nitrogen content (y) in the range ($0 \leq y \leq 0.218$). This trend can be attributed to the larger polarizability of the alloy as more nitrogen is incorporated, which alters the local bonding environment and enhances the dielectric response. The increase in (ε_0) is evident for both lattice-matching conditions, but the GaSb-matched alloy exhibits a slightly higher dielectric constant than the InAs-matched one. This difference suggests that GaSb exerts a stronger influence on dielectric screening, likely due to its effect on strain and electronic band structure.

In contrast, Figure 3 shows that the high-frequency dielectric constant (ε_∞) decreases as the nitrogen content increases. This decline suggests that the electronic band structure is modified in a way that reduces the material's ability to respond to high-frequency optical fields. Interestingly, at low nitrogen concentrations ($y<0.138$), the GaSb-matched alloy has a slightly higher (ε_∞) than the InAs-matched one. However, beyond ($y= 0.138$), an opposite trend emerges where

the InAs-matched alloy exhibits a larger (ε_∞) than the GaSb-matched alloy. This crossover behavior indicates a transition in the dominant dielectric response mechanism, highlighting the impact of substrate selection on optical properties.

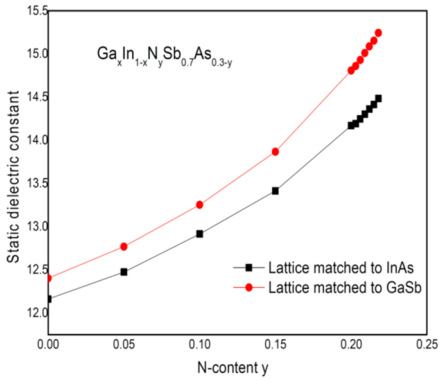

Figure 2. Static dielectric constant ε_0 in $Ga_xIn1_{-x}N_ySb_{0.7}As_{0.3-y}$ lattice matched to InAs and GaSb as a function of various N-content

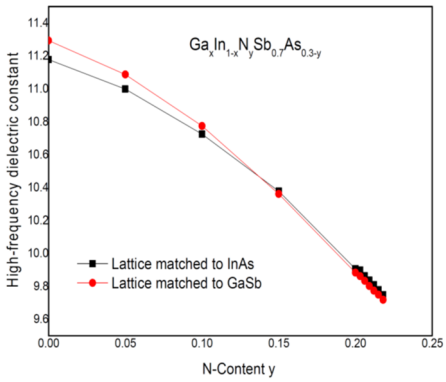

Figure 3. High-frequency dielectric constant ε_∞ in $Ga_xIn_{1-x}N_ySb_{0.7}As_{0.3-y}$ lattice matched to InAs and GaSb as a function of various N-content

The observed trends in (ε_0) and (ε_∞) can be understood through the interplay of nitrogen incorporation, strain effects from the substrate, and modifications in the electronic band structure. The increase in (ε_0) with nitrogen content is a direct consequence of increased lattice distortion and bond polarity. The decline in (ε_∞) suggests a reduction in free carrier screening at optical frequencies, which may be linked to increased localization effects introduced by nitrogen. Additionally, the switching behavior of (ε_∞) at (y = 0.138) emphasizes the substrate's role in influencing the dielectric response, affecting both static and optical properties.

These findings demonstrate the significant impact of nitrogen incorporation and substrate selection on the dielectric properties of $Ga_xIn_{1-x}N_ySb_zAs_{1-y-z}$. The variations in ($\varepsilon_0$) and ($\varepsilon_\infty$) highlight the potential for tailoring these properties for optoelectronic applications. The observed trends could be particularly relevant in designing materials with optimized dielectric screening and optical performance for infrared and telecommunication applications.

From the fit of the static and high-frequency dielectric constants data by a least-squares procedure, the expressions of the computed parameters are:

$$\varepsilon_0 = 12.175 + 4.24y + 28.51y^2 \text{ for } Ga_xIn_{1-x}N_ySb_{0,7}As_{0,3-y}/InAs \quad (13.a)$$

$$\varepsilon_0 = 12.432 + 3.84y + 40.63y^2 \text{ for } Ga_xIn_{1-x}N_ySb_{0,7}As_{0,3-y}/GaSb \quad (13.b)$$

$$\varepsilon_\infty = 11.178 - 2.74y - 17.58y^2 \text{ for } Ga_xIn_{1-x}N_ySb_{0,7}As_{0,3-y}/InAs \quad (14.a)$$

$$\varepsilon_\infty = 11.301 - 3.68y - 16.66y^2 \text{ for } Ga_xIn_{1-x}N_ySb_{0,7}As_{0,3-y}/GaSb \quad (14.b)$$

From the least-squares fitting of the calculated dielectric constant data, the obtained quadratic expressions reveal distinct behaviors for the static dielectric constant (ε_0) and high-frequency dielectric constant (ε_∞) as functions of nitrogen content (y) in $Ga_xIn_{1-x}N_ySb_{0.7}As_{0.3-y}$ alloys lattice-matched to GaSb and InAs. The fitted expressions for (ε_0) indicate a strong non-linear dependence on nitrogen content, as evidenced by the significant upward bowing parameters. The bowing parameter for (ε_0) is larger for the GaSb-matched alloy (+40.63) compared to the InAs-matched alloy (+28.51), suggesting that nitrogen incorporation strongly enhances the static dielectric response, likely due to increased bond ionicity and polarization effects. The more pronounced bowing in the GaSb-matched alloy indicates a stronger influence of nitrogen on dielectric screening, which may be attributed to the different strain conditions induced by the lattice-matching requirement. The static dielectric constant varies between 12.40 and 15.24 for the GaSb-matched alloy, whereas for the InAs-matched alloy, it ranges from 12.16 to 14.48. The slightly higher values in the GaSb case suggest stronger dielectric screening, which could impact carrier mobility and optical absorption properties in optoelectronic applications.

Unlike (ε_0), the high-frequency dielectric constant (ε_∞) exhibits a downward bowing with nitrogen incorporation, with nearly identical bowing parameters of -16.66 for the GaSb-matched alloy and -17.58 for the InAs-matched alloy. This downward bowing indicates that increasing nitrogen content reduces the material's ability to respond to optical frequencies, likely due to modifications in the electronic band structure, particularly a reduction in the bandgap and an increase in carrier localization effects. The similar bowing parameters for both substrate conditions suggest that the primary factor influencing (ε_∞) is the electronic structure modification induced by nitrogen, rather than substrate-related strain effects. The high-frequency dielectric constant decreases from 11.29 to 9.71 for the GaSb-matched alloy, while for the InAs-matched alloy, it ranges from 11.17 to 9.74. The reduction in (ε_∞) with increasing nitrogen content is consistent with the expected bandgap widening and reduced free carrier screening, which has direct implications for optical applications.

The observed differences in (ε_0) and (ε_∞) between the GaSb-matched and InAs-matched alloys highlight the role of ionicity in dielectric behavior. Higher ionicity leads to stronger dipole interactions, affecting dielectric screening and optical response. This is particularly relevant for laser devices and infrared detectors, where dielectric properties directly

influence carrier recombination rates and absorption spectra. Additionally, the transverse effective charge plays a crucial role in the electromechanical coupling of the material. Since (ε_∞) is related to the dynamic response of the lattice to external perturbations, its behavior provides valuable insights into how the alloy interacts with electromagnetic fields, making it critical for designing high-performance optoelectronic and electro-optic devices.

The quadratic fitting expressions provide a comprehensive understanding of the evolution of dielectric properties in $Ga_xIn_{1-x}N_\gamma Sb_{0.7}As_{0.3-y}$ alloys. The strong upward bowing in (ε_0) emphasizes enhanced dielectric screening due to nitrogen incorporation, whereas the downward bowing in (ε_∞) suggests reduced optical response at higher nitrogen concentrations. The differences between GaSb-matched and InAs-matched alloys highlight the substrate effect on dielectric behavior, which must be carefully considered for device engineering in optoelectronic applications, such as lasers, infrared photodetectors, and modulators.

The computed ionicity and transverse effective charge for $Ga_xIn_{1-x}N_ySb_{0.7}As_{0.3-y}$ alloys lattice-matched to InAs and GaSb exhibit an increasing trend with nitrogen content (y) up to 0.218, as shown in Figures 4 and 5. The steady increase in ionicity with increasing (y) suggests that the incorporation of nitrogen enhances the degree of ionicity in the alloy. This behavior can be attributed to the introduction of highly electronegative nitrogen atoms, which alter the charge distribution and strengthen the ionic character of chemical bonds. The ionicity values for the GaSb-matched alloy are systematically higher than those of the InAs-matched alloy, indicating that GaSb provides a more pronounced ionic environment compared to InAs. This difference can be linked to the larger electronegativity contrast in the GaSb system, leading to stronger dipolar interactions and modifications in the electronic band structure.

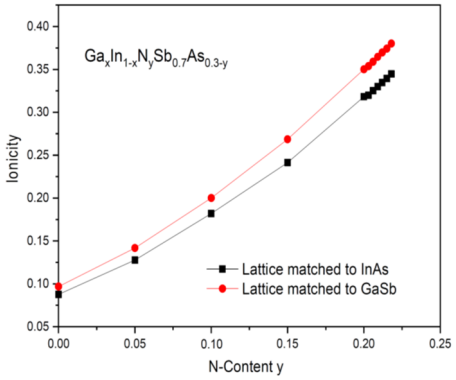

Figure 4. Ionicity in $Ga_xIn_{1-x}N_ySb_{0.7}As_{0.3-y}$ lattice matched to InAs and GaSb as a function of various N-content

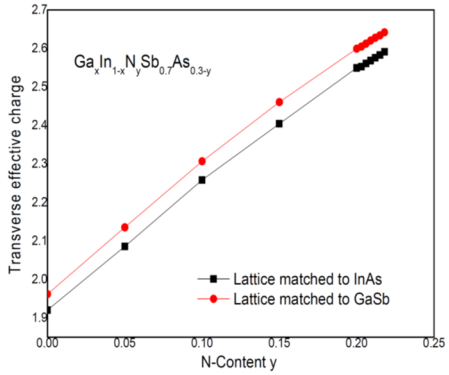

Figure 5. Transverse effective charge in $Ga_xIn_{1-x}N_ySb_{0.7}As_{0.3-y}$ lattice matched to InAs and GaSb as a function of various N-content

Similarly, the transverse effective charge also increases with nitrogen incorporation, emphasizing the role of nitrogen in modulating the electromechanical response of the material. The observed trend suggests that nitrogen atoms introduce additional polarizability in the alloy, thereby enhancing its response to external electric fields. The GaSb-matched alloy consistently exhibits a higher transverse effective charge than the InAs-matched counterpart, reinforcing the idea that the host lattice plays a crucial role in determining the material's electromechanical coupling. This increasing behavior of transverse effective charge is essential for understanding the dielectric screening and phonon interactions within the alloy system, which have direct implications for optoelectronic and high-frequency applications.

The fitted analytical expressions obtained through the least-squares method provide quantitative descriptions of these trends, allowing for predictive modeling of ionicity and transverse effective charge as functions of nitrogen content. The observed variations highlight the fundamental impact of nitrogen incorporation on the dielectric and electromechanical properties of $Ga_xIn_{1-x}N_ySb_{0.7}As_{0.3-y}$ alloys. These findings are particularly relevant for applications where precise control over ionicity and electromechanical coupling is required, such as infrared photodetectors, high-performance laser devices, and electro-optic modulators.

$$fi = 0.087 + 0.71y + 2.12y^2 \text{ for } Ga_xIn_{1-x}N_ySb_{0,7}As_{0,3-y}/InAs \quad (15.a)$$

$$fi = 0.096 + 0.8y + 2.27y^2 \text{ for } Ga_xIn_{1-x}N_ySb_{0,7}As_{0,3-y}/GaSb \quad (15.b)$$

$$e_T^* = 1.917 + 3.59y - 2.28y^2 \text{ for } Ga_xIn_{1-x}N_ySb_{0,7}As_{0,3-y}/InAs \quad (16.a)$$

$$e_T^* = 1.96 + 3.74y - 2.8y^2 \text{ for } Ga_xIn_{1-x}N_ySb_{0,7}As_{0,3-y}/GaSb \quad (16.b)$$

The computed expressions for ionicity (f_i) and transverse effective charge (e_T^*) provide valuable insights into the dielectric and electromechanical properties of $Ga_xIn_{1-x}N_ySb_{0,7}As_{0,3-y}$ alloys. As observed from equations (15.a) to (16.b), the alloy lattice-matched to GaSb exhibits slightly higher ionicity than its InAs-matched counterpart. This can be attributed to the stronger electronegativity contrast between Ga and Sb atoms, which enhances the ionic nature of chemical bonds in the GaSb lattice. The presence of nitrogen further amplifies this effect, as its high electronegativity increases the polarity of the bonding environment. The quadratic dependence of ionicity on nitrogen content (y) indicates a nonlinear enhancement of ionic character, suggesting that nitrogen plays a crucial role in modifying the alloy's electronic charge

distribution. The larger bowing parameter in the GaSb-matched alloy (+2.27) compared to the InAs-matched alloy (+2.12) reinforces the idea that the host lattice composition significantly influences the ionicity of the material.

Similarly, the transverse effective charge (e_T^*) exhibits a systematic increase with nitrogen incorporation in both alloys, further supporting the role of nitrogen in modulating the electromechanical response of the system. The presence of a negative quadratic term in equations (16.a) and (16.b) suggests that at higher nitrogen concentrations, the rate of increase in transverse effective charge slows down, likely due to saturation effects in charge redistribution. Notably, the GaSb-matched alloy consistently displays a higher transverse effective charge than the InAs-matched alloy, which can be linked to the differences in dielectric screening and bonding strength between the two lattice-matched structures. The stronger dipolar interactions in the GaSb lattice contribute to a greater electromechanical response, making it a more favorable candidate for applications requiring high dielectric tunability and efficient phonon coupling.

Expanding the analysis to the pentanary alloy $Ga_xIn_{1-x}N_ySb_{0.7}As_{0.3-y}$ lattice-matched to GaAs, the study examines the variations in ionicity and transverse effective charge over the nitrogen composition range (y = 0.16) to (0.416) for different arsenic proportions (z = 0.1, 0.2, 0.3, 0.4). These findings provide a deeper understanding of how nitrogen and arsenic jointly influence the electronic properties of the alloy, offering crucial information for optimizing its optoelectronic performance. The interplay between these elements determines the material's dielectric behavior and electromechanical coupling, which are essential parameters for applications in infrared photodetectors, high-frequency transistors, and laser devices.

The calculated optical static dielectric constant (ε_0) and high-frequency dielectric constant (ε_∞) for various nitrogen (N) contents in the pentanary alloy $Ga_xIn_{1-x}N_ySb_zAs_{1-y-z}$, lattice-matched to GaAs, are presented in Figures 6 and 7. Their analytical expressions are given by:

$$\varepsilon_0 = 13.92 - 31.38y + 95.64y^2 \text{ for } Ga_xIn_{1-x}N_ySb_{0.1}As_{0.9-y}/GaAs \quad (17.a)$$

$$\varepsilon_0 = 12.32 - 16.54y + 60.97y^2 \text{ for } Ga_xIn_{1-x}N_ySb_{0.2}As_{0.8-y}/GaAs \quad (17.b)$$

$$\varepsilon_0 = 11.33 - 6.72y + 38.05y^2 \text{ for } Ga_xIn_{1-x}N_ySb_{0.3}As_{0.7-y}/GaAs \quad (17.c)$$

$$\varepsilon_0 = 12.90 - 12.11y + 35.84y^2 \text{ for } Ga_xIn_{1-x}N_ySb_{0.4}As_{0.6-y}/GaAs \quad (17.d)$$

$$\varepsilon_\infty = 9.52 + 3.64y - 20.37y^2 \text{ for } Ga_xIn_{1-x}N_ySb_{0.1}As_{0.9-y}/GaAs \quad (18.a)$$

$$\varepsilon_\infty = 9.31 + 5.68y - 23.49y^2 \text{ for } Ga_xIn_{1-x}N_ySb_{0.2}As_{0.8-y}/GaAs \quad (18.b)$$

$$\varepsilon_\infty = 9.16 + 7.65y - 26.47y^2 \text{ for } Ga_xIn_{1-x}N_ySb_{0.3}As_{0.7-y}/GaAs \quad (18.c)$$

$$\varepsilon_\infty = 11.13 - 2.73y - 13.20y^2 \text{ for } Ga_xIn_{1-x}N_ySb_{0.4}As_{0.6-y}/GaAs \quad (18.d)$$

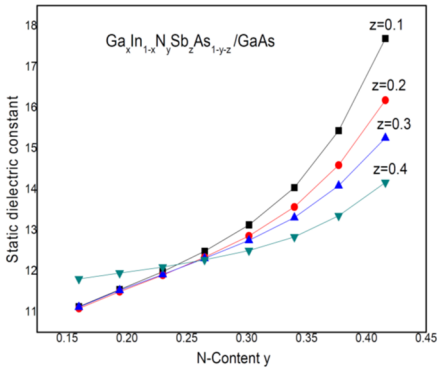

Figure 6. Static dielectric constant ε_0 in $Ga_xIn_{1-x}N_ySb_zAs_{1-y-z}$/GaAs as a function of various N-content with different As-proportion

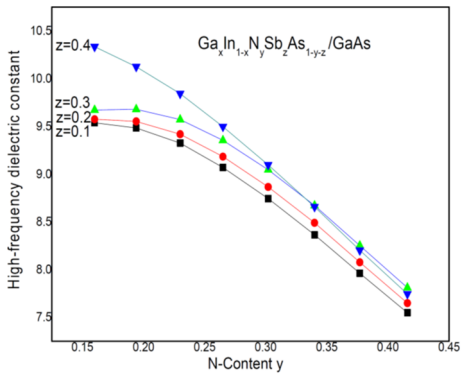

Figure 7. High-frequency dielectric constant ε_∞ in $Ga_xIn_{1-x}N_ySb_zAs_{1-y-z}$/GaAs as a function of various N-content with different As-proportion

The expressions for (ε_0) indicate a strong bowing effect, suggesting significant deviations from a linear interpolation between the parent binaries. Among the compositions studied, $Ga_xIn_{1-x}N_ySb_{0.4}As_{0.6-y}$/GaAs (Eq. 17.d) exhibits a similar behavior to $Ga_xIn_{1-x}N_ySb_{0.7}As_{0.3-y}$/InAs, with a comparable bowing parameter (+35.84) vs. (+28.51). This suggests that, in terms of dielectric response, this composition behaves similarly to an InAs-matched alloy. Conversely, $Ga_xIn_{1-x}N_ySb_{0.3}As_{0.7-y}$/GaAs (Eq. 17.c) exhibits a dielectric behavior comparable to $Ga_xIn_{1-x}N_ySb_{0.7}As_{0.3-y}$/GaSb, as reflected in their nearly identical bowing parameters (+38.05) vs. (+40.63). This suggests that increasing the Sb content in GaAs-matched alloys leads to behavior more characteristic of GaSb-matched alloys.

Unlike (ε_0), the high-frequency dielectric constant decreases with increasing nitrogen content, reflecting reduced electronic polarizability due to shorter bond lengths and increased ionicity. The bowing parameter for (ε_∞) in $Ga_xIn_{1-x}N_ySb_{0.1}As_{0.9-y}$ /GaAs (Eq. 18.a) is comparable to that in $Ga_xIn_{1-x}N_ySb_{0.7}As_{0.3-y}$/InAs) (-20.37) vs. (-17.58), indicating similar electronic screening effects. Conversely, the bowing parameter for (ε_∞) in $Ga_xIn_{1-x}N_ySb_{0.4}As_{0.6-y}$/GaAs (Eq. 18.d)

is close to that of $Ga_xIn_{1-x}N_ySb_{0.7}As_{0.3-y}$/GaSb (-13.20) vs. (-16.66), reinforcing the similarity between these two alloy types.

These results suggest that careful tuning of the composition parameters (x), (y), and (z) allows for the engineering of dielectric properties to match specific applications. For instance, if a material with a higher static dielectric constant is needed (e.g., for high-capacitance device applications), a composition with higher nitrogen and lower arsenic content may be favorable. Conversely, for applications where a lower (ε_∞) is preferred (e.g., to reduce optical losses in high-frequency optoelectronic devices), compositions with lower nitrogen content may be advantageous. Importantly, the close agreement between specific GaAs-matched and InAs- or GaSb-matched alloys implies that a suitable choice of substrate could help mitigate strain effects while maintaining desirable dielectric properties.

The dielectric properties of the pentanary alloy $Ga_xIn_{1-x}N_ySb_zAs_{1-y-z}$, lattice-matched to GaAs, exhibit significant nonlinearity due to strong bowing effects. The similarity in dielectric response between certain compositions and InAs- or GaSb-matched alloys highlights the potential for substrate engineering in device applications. By adjusting the composition parameters, this material system offers a wide range of possibilities for optimizing dielectric constants and transverse effective charges for high-performance optoelectronic and electronic applications.

On the other hand, structural defects and local clustering can greatly influence the dielectric properties of complex pentanary alloys. Defects such as vacancies and lattice dislocations disrupt the periodicity of the crystal structure, leading to the formation of localized electronic states and modifications in the electronic and ionic components of the dielectric constant. At the same time, the local clustering of atoms such as nitrogen or antimony causes compositional inhomogeneity and local strains, resulting in spatial variations in polarization. These effects produce nonuniformities in dielectric properties and deviations from the ideal values predicted by the Virtual Crystal Approximation (VCA), emphasizing the importance of considering real structural defects when comparing theoretical results with experimental data.

Figures 8 and 9 illustrate the computed ionicity f_i and transverse effective charge e_T^* in $Ga_xIn_{1-x}N_ySb_zAs_{1-y-z}$ lattice matched to GaAs as a function of nitrogen content (y) over the range 0.16–0.416 for different arsenic proportions. The fitted data obtained using the least-squares method yield the following analytical expressions:

$$fi = 0.063 + 0.28y + 2.36y^2 \quad (19.a)$$

$$fi = 0.064 + 0.25y + 2.17y^2 \quad (19.b)$$

$$fi = 0.064 + 0.23y + 2y^2 \quad (19.c)$$

$$fi = 0.062 + 0.22y + 1.84y^2 \quad (19.d)$$

$$e_T^* = 1.535 + 4.52y - 3.27y^2 \quad (20.a)$$

$$e_T^* = 1.551 + 4.21y - 2.79y^2 \quad (20.b)$$

$$e_T^* = 1.561 + 3.94y - 2.40y^2 \quad (20.c)$$

$$e_T^* = 1.564 + 3.73y - 2.09y^2 \quad (20.d)$$

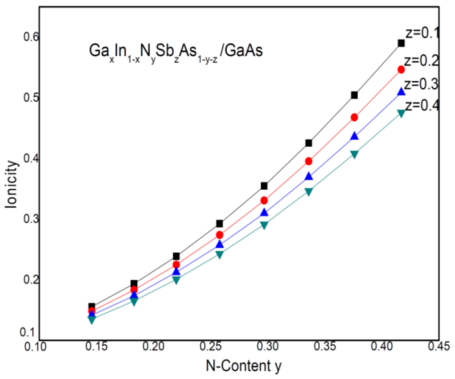

Figure 8. Ionicity in $Ga_xIn_{1-x}N_ySb_zAs_{1-y-z}$ lattice matched to GaAs as a function of various N-content with different As-proportion

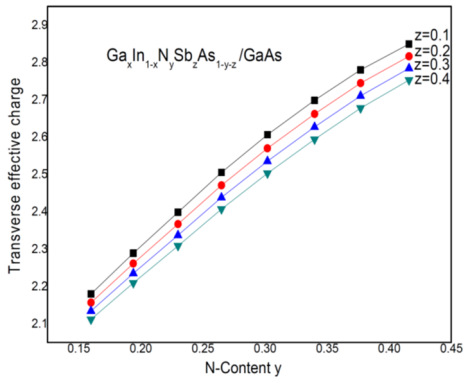

Figure 9. Transverse effective charge in $Ga_xIn_{1-x}N_ySb_zAs_{1-y-z}$ lattice matched to GaAs as a function of various N-content with different As-proportion

The results show a nonlinear increase in ionicity as nitrogen content increases. This is expected because nitrogen, being more electronegative than arsenic and antimony, enhances the ionic character of the bonds in the alloy. The higher the nitrogen incorporation, the greater the charge separation between cations and anions, leading to a more pronounced ionicity.

The transverse effective charge also increases with nitrogen content but exhibits a downward curvature at higher *y* values. This suggests that while nitrogen initially enhances charge transfer effects due to bond polarity, at higher concentrations, structural distortions or charge redistribution effects may counteract this trend. Such behavior is crucial for understanding the dielectric response of these alloys, which impacts their optical and electronic applications.

By comparing these fitted expressions with those obtained for $Ga_xIn_{1-x}N_ySb_zAs_{1-y-z}$ lattice matched to other substrates (InAs and GaSb), notable similarities emerge. The ionicity behavior of $Ga_xIn_{1-x}N_ySb_{0.2}As_{0.8-y}$ lattice matched to GaAs (Eq. 19.b) closely resembles that of $Ga_xIn_{1-x}N_ySb_{0.7}As_{0.3-y}$ lattice matched to InAs (Eq. 15.a). Similarly, the ionicity of $Ga_xIn_{1-x}N_ySb_{0.1}As_{0.9-y}$ lattice matched to GaAs (Eq. 19.a) is comparable to that of $Ga_xIn_{1-xNySb0.7}As_{0.3-y}$ lattice matched to GaSb (Eq. 15.b). These trends indicate that the ionicity in certain GaAs-lattice-matched alloys follows a pattern similar to that of InAs- and GaSb-matched counterparts, suggesting that the As/Sb ratio plays a crucial role in determining bond character.

The transverse effective charge in $Ga_xIn_{1-x}N_ySb_{0.3}As_{0.7-y}$ lattice matched to GaAs (Eq. 20.c) behaves similarly to that of $Ga_xIn_{1-x}N_ySb_{0.7}As_{0.3-y}$ lattice matched to InAs (Eq. 16.a). Likewise, e^*_T in $Ga_xIn_{1-x}N_ySb_{0.2}As_{0.8-y}$ lattice matched to GaAs (Eq. 20.b) exhibits a trend comparable to that of $Ga_xIn_{1-x}N_ySb_{0.7}As_{0.3-y}$ lattice matched to GaSb (Eq. 16.b). These similarities suggest that the charge transfer properties in GaAs-matched alloys can be approximated using those of InAs- and GaSb-matched systems, which is valuable for predicting dielectric behavior in different lattice-matching conditions.

The computed ionicity and transverse effective charge in $Ga_xIn_{1-x}N_ySb_zAs_{1-y-z}$ alloys exhibit well-defined trends as a function of nitrogen content. The increasing ionicity with y highlights the role of nitrogen in modifying bond polarity, while the nonlinear behavior of e^*_T suggests complex charge redistribution effects at higher nitrogen concentrations. Furthermore, the observed similarities between the GaAs-lattice-matched alloys and those matched to InAs and GaSb provide valuable insights into the impact of composition on electronic properties, aiding in the design of materials for optoelectronic applications.

4. CONCLUSIONS

The dielectric constants and transverse effective charges of the pentanary alloy $Ga_xIn_{1-x}N_ySb_zAs_{1-y-z}$, lattice-matched to InAs, GaSb, and GaAs, have been systematically investigated using the pseudopotential approach within the virtual crystal approximation, combined with the Harrison bond-orbital model. The computed results exhibit reasonable agreement with available experimental data, validating the reliability of the adopted theoretical framework. However, just like other calculation models, our EPM-VCA-Harrison model has its limitations, especially in the detailed description of microscopic-scale effects such as the position of electronic states, local lattice distortions, as well as the disorder phenomena specific to multi-anionic alloys like GaInNAsSb.

Our analysis reveals that the dielectric constants and transverse effective charges exhibit distinct trends as a function of nitrogen composition (y), highlighting the significant influence of nitrogen incorporation on bond polarity and charge transfer mechanisms. Specifically, the ionicity increases nonlinearly with increasing nitrogen content due to its higher electronegativity, while the transverse effective charge follows a complex behavior, initially increasing before showing a downward curvature at higher (y) values. These trends underscore the interplay between electronic structure modifications and lattice distortions induced by compositional variations.

Moreover, the observed similarities between the dielectric properties of $Ga_xIn_{1-x}N_ySb_zAs_{1-y-z}$ alloys lattice-matched to different substrates (InAs, GaSb, and GaAs) suggest that the As/Sb ratio plays a crucial role in determining the bond character and charge redistribution. Such insights provide a predictive framework for optimizing these alloys for specific optoelectronic and electronic applications, where precise control over dielectric response and charge transport is required. Overall, our findings indicate that $Ga_xIn_{1-x}N_ySb_zAs_{1-y-z}$ is a promising material system for tailoring dielectric constants and transverse effective charges. These results open pathways for the design and discovery of new semiconductor materials with engineered dielectric and electronic properties, making them suitable for advanced applications in infrared optoelectronics, high-speed electronics, and photonic devices. Further experimental validation and computational studies incorporating many-body effects and strain considerations could refine these predictions and expand the applicability of these alloys.

Acknowledgments

The authors (T. Ghellab, Z. Charifi and H. Baaziz) would like to thank the general directorate for scientific research and technological development for their financial support during the realization of this work.

ORCID

Abid Hamza, https://orcid.org/0000-0001-9647-7425; **Baaziz Hakim,** https://orcid.org/0000-0003-4860-2740
Torkia Ghellab, https://orcid.org/0009-0001-6823-4335; **Zoulikha Charifi,** https://orcid.org/0000-0003-3875-4716

REFERENCES

[1] G. Li, *et al*. J. Mater. Chem. C, **12**, 12150 (2024). https://doi.org/10.1039/D4TC02615B
[2] S. Nakamura, J. Vac. Sci. Technol. A, **13**, 705 (1995). https://doi.org/10.1116/1.579811
[3] I. Vurgaftman, J.R.M. Meyer, and J.R. Ram-Mohan, J. Appl. Phys. **89**, 5815 (2001). http://dx.doi.org/10.1063/1.1368156
[4] K. Iga, and S. Kinoshita, *Process Technology for Semiconductor Lasers*, (Springer, Berlin, 1996).
[5] A.R. Kovsh, *et al*. Proc. of SPIE, **5349**, (2004). https://doi.org/10.1117/12.531245
[6] B. Merabet, A. Lachebi, and H. Abid, Turk. J. Phys, **35**(1), 13 (2011). https://doi.org/10.3906/fiz-0907-21
[7] H. Aourag, B. Bouhafs, and M. Certier, Phys. Stat. Sol (b), **201**, 117(1997). https://doi.org/10.1002/1521-3951(199705)201:1%3C117::AID-PSSB117%3E3.0.CO;2-8
[8] K. Kassali, and N. Bouarissa, Microelectron. Eng, **54**, 277 (2000). https://doi.org/10.1016/S0167-9317(00)00409-3

[9] H. Abid, N. Badi, M. Driz, N. Bouarissa, K. H. Benkabou, B. Khelifa, and H. Aourag, Microelectron. Eng B**, 33** 133 (1995).
[10] C. Skierbiszewski, P. Perlin, P. Wisniewski, W. Knap, T. Suski, W. Walukiewicz, W. Shan, *et al*. J. Appl. Phys, **76**, 2409 (2000). https://doi.org/10.1063/1.126360
[11] H.P. Xin, K.L. Kavanagh, M. Kondow, and C.W. Tu, J. Cryst. Growth, **201/202**, 419 (1999). https://doi.org/10.1016/S0022-0248(98)01366-9
[12] N. Bouarissa, H. Baaziz, Z. Charifi, Phys. Status Solidi, B: Basic Res, **231** 403 (2002). https://doi.org/10.1002/1521-3951(200206)231:2%3C403::AID-PSSB403%3E3.0.CO;2-6
[13] L. Vegard, Z. Phys. **5**, 17 (1921).
[14] T. Kobayasi, H. Nara, Bull. Coll. Med. Sci. Tohoku Univ, **2**, 7 (1993).
[15] H. Baaziz, Z. Charifi, and N. Bouarissa, Mater. Lett. **60**, 39 (2006). https://doi.org/10.1016/j.matlet.2005.07.067
[16] H. Mathieu, *Physique des semiconducteurs et des composants électroniques*, 5e éd., (Dunod, 2004).
[17] D.E. Aspnes, C.G. Olson, and D.W. Lynch, Phys. Rev. Lett, **37**, 766 (1976). https://doi.org/10.1103/PhysRevLett.37.766
[18] S. Adachi, J. Appl. Phys. **61**, 4869 (1987). https://doi.org/10.1063/1.338352
[19] S. Zollner, M. Garriga, J. Humlicek, S. Gopalan, and M. Cardona, Phys. Rev B, **43** 4349 (1991). https://doi.org/10.1103/PhysRevB.43.4349
[20] C. Alibert, A. Joullie, A.M. Joullie, and C. Ance, Phys. Rev. B, **27** 4946 (1983). https://doi.org/10.1103/PhysRevB.27.4946
[21] W.W. Walukiewicz, Physica E, **20** 300 (2004). https://doi.org/10.1016/j.physe.2003.08.023
[22] P.J.L. Herve, and L.K.J. Vandamme, Infrared Phys. Technol. **35**, 609 (1994). https://doi.org/10.1016/1350-4495(94)90026-4
[23] G.A. Samara, Phys. Rev. B, **27**, 3494 (1983). https://doi.org/10.1103/PhysRevB.27.3494
[24] S.Yu. Davydov, and S.K. Tikhonov, Semiconductors, **32**, 947 (1998). https://doi.org/10.1134/1.1187520
[25] P. Vogl, J. Phys. C: Solid State Phys, **11**, 251 (1978). https://doi.org/10.1088/0022-3719/11/2/011
[26] H. Baaziz, Z. Charifi, and N. Bouarissa, Mater. Chem. Phys. **68**, 197 (2001). https://doi.org/10.1016/S0254-0584(00)00352-7
[27] M. Levinshtein, S. Rumyantsev, and M. Shur, editors, *Handbook Series on Semiconductor Parameters*, vol. 2, (World Scientific, Singapore, 1999).
[28] P. Giannozzi, S. de Gironcoli, P. Pavone, and S. Baroni, Phys. Rev. B, 43, 7231 (1991). https://doi.org/10.1103/PhysRevB.43.7231
[29] V. Bougrov, M.E. Levinshtein, S.L. Rumyantsev, and A. Zubrilov, *Properties of Advanced Semiconductor Materials GaN, AlN, InN, BN, SiC, SiGe*, edited by M.E. Levinshtein, S.L. Rumyantsev, and M.S. Shur, (Wiley, New York, 2001), pp. 1–30.
[30] A. Zoroddu, F. Bernardini, P. Ruggerone, and V. Fiorentini, Phys. Rev. B, **64**, 045208 (2001). https://doi.org/10.1103/PhysRevB.64.045208
[31] T.L. Tansley, in: *Properties of Group III Nitrides*, edited by J.H. Edgar, (INSPEC, London, 1994).

ДІЕЛЕКТРИЧНІ КОНСТАНТИ ТА ПОПЕРЕЧНІ ЕФЕКТИВНІ ЗАРЯДИ У П'ЯТИКОМПОНЕНТНОМУ СПЛАВІ $Ga_xIn_{1-x}N_ySb_zAs_{1-y-z}$ З ҐРАТКОЮ, УЗГОДЖЕНОЮ З InAs, GaSb ТА GaAs

Х. Зеррухі[1], Х. Абід[1], Х. Баазіз[2,3], Т. Геллаб[2,3], З. Шаріфі[2,3]
[1]Лабораторія прикладних матеріалів, Дослідницький центр, Університет Сіді Бель Аббес, 22000 Алжир
[2]Кафедра фізики, Факультет природничих наук, Університет Мсила, 28000 Мсила, Алжир
[3]Лабораторія фізики та хімії матеріалів, Університет Мсила, Алжир

Це дослідження пропонує комплексний теоретичний аналіз діелектричних властивостей та поперечних ефективних зарядів п'ятикомпонентному сплаві $Ga_xIn_{1-x}N_ySb_zAs_{1-y-z}$, зосереджуючись на композиціях, ґратки яких узгоджені з підкладками InAs, GaSb та GaAs. У дослідженні використовується метод локального емпіричного псевдопотенціалу (EPM) у поєднанні з наближенням віртуального кристала (VCA) та моделлю зв'язків-орбіталей Гаррісона для оцінки ключових параметрів, включаючи статичну та високочастотну діелектричну константу, іонність, полярність та поперечний ефективний заряд. Ці обчислювальні підходи були обрані завдяки їхній здатності точно описувати електронні взаємодії в складних системах сплавів, зберігаючи при цьому обчислювальну ефективність. Отримані результати демонструють значну узгодженість з експериментальними даними, доступними для складових бінарних сполук, що підтверджує надійність теоретичної бази. Крім того, дослідження виявляє систематичні тенденції в діелектричній поведінці як функції складу, надаючи розуміння ролі атомного заміщення в налаштуванні цих властивостей. Наскільки нам відомо, ця робота являє собою першу детальну теоретичну оцінку сплавів $Ga_xIn_{1-x}N_ySb_zAs_{1-y-z}$ у цьому контексті. Хоча експериментальна перевірка залишається необхідною, наші результати встановлюють цінний теоретичний орієнтир для майбутніх досліджень та потенційних застосувань в оптоелектронній та напівпровідниковій приладобудуванні, зокрема в розробці передових інфрачервоних детекторів та високочастотних електронних компонентів.

Ключові слова: *EPM; полярність; діелектричні константи; поперечний ефективний заряд; сплави з узгодженою ґраткою; пентанарій*

EAST EUROPEAN JOURNAL OF PHYSICS. 4. 527-536 (2025)
DOI:10.26565/2312-4334-2025-4-54 ISSN 2312-4334

EFFECT OF BORIC AND OXALIC ACID ON NUCLEATION MECHANISM, COMPOSITION, MORPHOLOGY AND STRUCTURE OF ELECTRODEPOSITED Ni FILMS

F.Z.K. Hamdi[1]*, A. Rahmani[1,2], A. Hamdi[1]
[1]*Laboratory of Physical Chemistry of Materials (LPCM), Faculty of Sciences, University of Amar Telidji, 03000, Laghouat, Algeria*
[2]*Laboratory MONARIS, UMR 8233, Sorbonne Université, 4 place Jussieu, 75005 Paris, France*
**Corresponding Author e-mail: f.hamdi@lagh-univ.dz*
Received August 23, 2025; revised October 16, 2025; accepted October 23, 2025

Nickel thin films were electrodeposited onto copper substrates at room temperature using an aqueous electrolyte containing nickel sulfate, nickel chloride, and sodium sulfate. The effects of two additives (boric acid and oxalic acid) on the nucleation mechanism, crystallographic structure, surface morphology, and chemical composition of the resulting Ni films were systematically investigated using cyclic voltammetry (CV), chronoamperometry (CA), X-ray diffraction (XRD), scanning electron microscopy (SEM), and energy-dispersive X-ray spectroscopy (EDS). CV analysis revealed that the presence of additives shifted the cathodic peak potentials toward more negative values, suggesting an inhibition effect on nickel reduction. Chronoamperometric studies confirmed that Ni deposition followed a three-dimensional instantaneous nucleation mode, unaffected by the additives. XRD patterns showed that all Ni films had a face-centered cubic (FCC) structure with strong (111) orientation, while SEM images indicated denser and more homogeneous surface morphology in the presence of additives. EDS analysis confirmed the presence of Ni in all samples.
Keywords: *Nickel; Electrodeposited; Additives; Boric acid; Oxalic acid; Nucleation*
PACS: 81.15.Pq; 81.10.Aj; 68.55.-a; 68.35.B-

1. INTRODUCTION

Nickel (Ni) coatings are widely used in various industrial applications, including catalysis [1], electronic components [2], decorative purposes [3], and corrosion protection, due to their excellent properties such as oxidation resistance [4], high corrosion and wear resistance [5−8], and good optical, magnetic, and mechanical characteristics [9]. Several physical and chemical methods have been employed to synthesize Ni thin films, including chemical vapor deposition (CVD) [10], the sol–gel method [11], spray pyrolysis [12], sputtering [13], thermal evaporation [14], and electrodeposition [15]. Among these, electrodeposition is widely used due to its simplicity, low cost, high efficiency [16,17], and low processing temperature [18]. In electrodeposition, the properties of the resulting films are influenced by several parameters, including deposition time, current density, applied potential, electrolyte temperature, pH, bath composition, stirring speed, and the use of additives [19–21]. Small amounts of additives in the electrolyte have been shown to significantly influence the microstructure, morphology, and overall quality of the deposit. These characteristics are closely linked to the nucleation and growth mechanisms occurring during the initial stages [2].

In this study, we aim to investigate the effect of two additives (boric acid and oxalic acid) on the nucleation and growth mechanisms of nickel electrodeposited on a copper substrate at room temperature. Cyclic voltammetry (CV) and chronoamperometry (CA) were employed to analyze the electrochemical behavior. The surface morphology, chemical composition, and crystal structure of the resulting films were also characterized using scanning electron microscopy (SEM), energy-dispersive X-ray spectroscopy (EDS), and X-ray diffraction (XRD), respectively.

2. MATERIALS AND METHODS

Nickel films were deposited at room temperature using a basic three-electrode electrochemical setup, linked to a PGZ402 potentiostat/galvanostat (Radiometer Analytical). The system included a saturated calomel electrode (SCE) as the reference, a platinum foil as the counter, and a copper disc (1.50 cm × 1.00 cm) acting as the working electrode. Before any deposition, the copper samples were polished by hand using silicon carbide papers ranging from 1200 to 2000 grit. After polishing, the surface was cleaned in acetone, rinsed with distilled water, and left to dry in air. No extra surface treatment was done. All electrolytes were freshly prepared using deionized water and analytical-grade chemicals. The pH of each bath was adjusted to around 2.8 using either NaOH or H_2SO_4. Table 1 lists the full composition of the bath and the main deposition parameters.

To investigate the electrodeposition process, we used both cyclic voltammetry (CV) and chronoamperometry (CA). CV scans were run between 0 and –1.4 V vs SCE, with a scan rate fixed at 20 mV/s.

For surface and structural analysis, ESEM (Thermo Scientific™ Quattro S) was used in combination with EDS to examine the morphology and composition of the films. Structural information was obtained using X-ray diffraction (XRD), performed on a PANalytical Empyrean diffractometer operating at 40 kV and 30 mA. Measurements used Cu Kα radiation (λ = 1.54060 Å) with a Ni filter. The 2θ range was set from 30° to 100°, with a scan step of 0.02°/s.

Cite as: F.Z.K. Hamdi, A. Rahmani, A. Hamdi, East Eur. J. Phys. 4, 527 (2025), https://doi.org/10.26565/2312-4334-2025-4-54

Table 1. The electrolyte compositions and plating parameters

Bath composition		Plating parameters	
Chemicals	**Concentrations [g L^{-1}]**		
$NiSO_4 \cdot 6H_2O$	60		
$NiCl_2.6H_2O$	8.2	pH	≈ 2.8
Na_2SO_4	0.5	Room temperature	25°C
		Room temperature	5 min
Additives		Deposition potential	-1000 mV
$C_2H_2O_4.2H_2O$	0.84		
H_3BO_3	24.7		

3. RESULTS AND DISCUSSIONS

3.1. Cyclic voltametric studies

The cyclic voltammetry technique is widely employed in electrochemistry, revealing electrode/electrolytic solution behavior and enabling the prediction of ideal conditions for the metal ions electrodeposition mechanism [16]. Figure 1 shows the CV curves of nickel thin films electrodeposited onto a copper substrate at room temperature, both in the absence and presence of additives. The potential was swept from 0 V vs. SCE toward the cathodic side, down to -1.4 V vs. SCE, and then reversed back to the starting point, with a scan rate set at 20 mV/s.

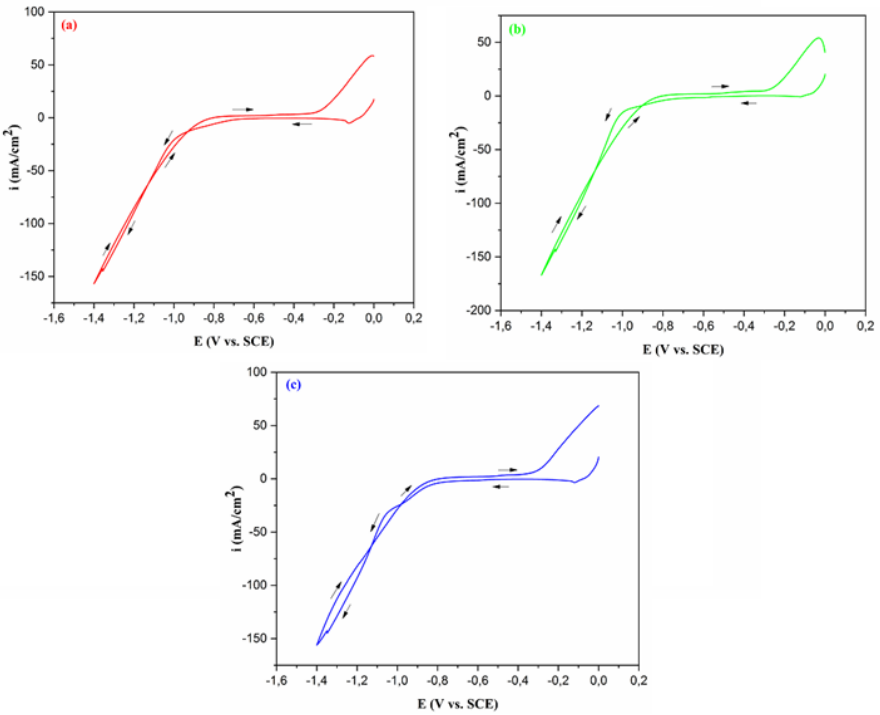

Figure 1. Cyclic voltammograms for copper substrate in solution containing: (a) 60 g L^{-1} $NiSO_4 \cdot 6H_2O$, 8.2 g L^{-1} $NiCl_2.6H_2O$ and 0.5 g L^{-1} Na_2SO_4 (b) 60 g L^{-1} $NiSO_4 \cdot 6H_2O$, 8.2 g L^{-1} $NiCl_2.6H_2O$, 0.5 g L^{-1} Na_2SO_4 and 24.7 g L^{-1} H_3BO_3 and (c) 60 g L^{-1} $NiSO_4 \cdot 6H_2O$, 8.2 g L^{-1} $NiCl_2.6H_2O$, 0.5 g L^{-1} Na_2SO_4 and 0.84 g L^{-1} $C_2H_2O_4.2H_2O$. (T = 25°C, v = 20 mVs^{-1})

In the additive-free bath (Figure 1(a)), the reduction of Ni^{2+} ions begins at around -0.70 V, following the reaction shown in Equation (1). As the potential becomes more negative, a noticeable rise in current density is observed, mainly due to the concurrent hydrogen evolution reaction, described by Equation (2):

$$Ni^{2+} + 2e^- \rightarrow Ni \quad (1)$$

$$2H^+ + 2e^- \rightleftharpoons H_2 \quad (2)$$

During the return scan, the dissolution of metallic Ni to Ni^{2+} appears an potential of -0.260 V.

With the addition of boric acid in the electrolyte (Figure 1(b)), the reduction of nickel begins at E = -0.980 V. In anodic part, an anodic peak observed at E= -0.030 V is due to the oxidation of the nickel deposited during the cathodic part according to Eq. (3).

$$Ni \rightarrow Ni^{2+} + 2e \quad (3)$$

When oxalic acid is added (Figure 1(c)), the reduction of nickel starts at a potential of approximately -0.820 V, and the dissolution of Ni occurs at about -0.304 V.

The introduction of additives (boric and oxalic acid) in the bath solution shifted the cathodic peak potential negatively. This indicates that these additives inhibited nickel electrodeposition, and the force of the inhibition effect followed this order: H_3BO_3 > $C_2H_2O_4$. The hydrogen reaction occurs at a more negative potential in the presence of additives, indicating that boric and oxalic acid had a significant inhibition effect on hydrogen reduction.

The presence of the crossover in the cyclic voltammograms (CVs) indicates the existence of a nucleation and growth process [22].

3.2. Chronoamperometry

3.2.1. Current density-time curves

To study the effect of additives on a Ni electrodeposition nucleation/growth mechanism, chronoamperometry was employed. Figure 2 illustrates the current density transient curves of nickel thin films electrodeposited on copper substrate at different potentials in the absence and presence of additives. For all films, the transients have the same form. These curves show three parts. In the first part, the current density decreases abruptly due to the charge of the double layer and the formation of the first germs of Ni on the electrode surface. Then, in the second part, the current density increases, reaching a maximum value, imax, at a maximum time, tmax, due to the growth of Ni nuclei. Finally, in the last part, the current density decreases and stabilizes as the deposition potentials increase, indicating that the growth process of nickel is controlled by the diffusion regime [23,24]. We can conclude that these current–time transients are a typical characteristic of a three-dimensional nucleation with diffusion-controlled growth [1].

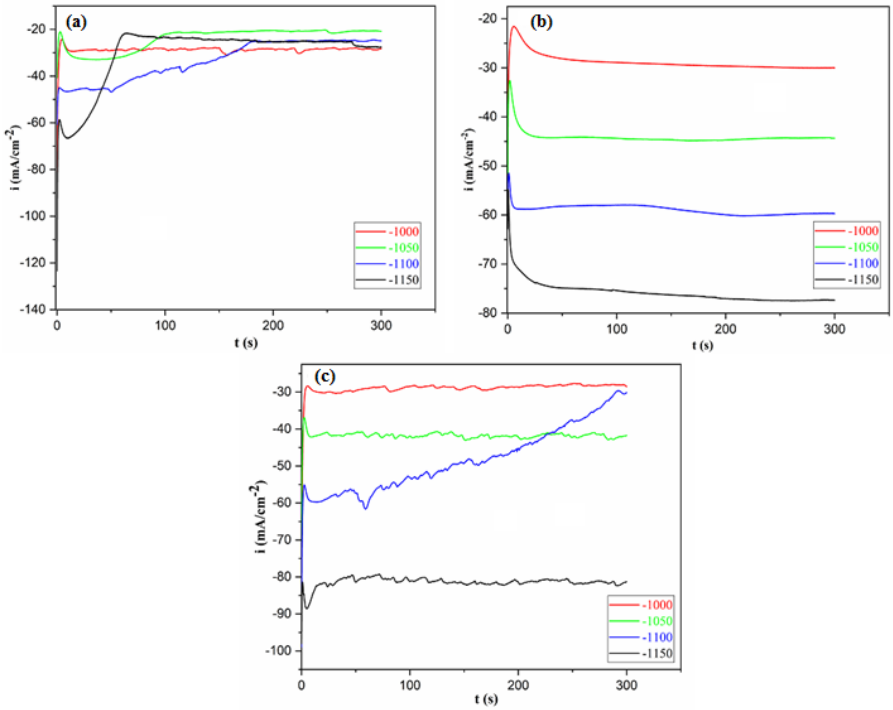

Figure 2. Typical current transient curves of Ni films electrodeposited on Cu substrate at different potentials in solution containing: (a) 60 g L^{-1} $NiSO_4{\cdot}6H_2O$, 8.2 g L^{-1} $NiCl_2.6H_2O$ and 0.5 g L^{-1} Na_2SO_4 (b) 60 g L^{-1} $NiSO_4{\cdot}6H_2O$, 8.2 g L^{-1} $NiCl_2.6H_2O$, 0.5 g L^{-1} Na_2SO_4 and 24.7 g L^{-1} H_3BO_3 and (c) 60 g L^{-1} $NiSO_4{\cdot}6H_2O$, 8.2 g L^{-1} $NiCl_2.6H_2O$, 0.5 g L^{-1} Na_2SO_4 and 0.84 g L^{-1} $C_2H_2O_4.2H_2O$.(t= 5 min, T= 25°C)

3.2.2. Nucleation mechanisms

To further understand the nucleation mechanism of nickel deposition, the mathematical model developed by Scharifker and Hills (SH) [25] was used. According to this model, the nucleation mechanism includes instantaneous and progressive 3D nucleation [20]. The mechanism is described by the following Eq. (4) and (5) [26]:

Instantaneous nucleation:

$$i^2/i_{max}^2 = 1.9542(t/t_{max})^{-1}[1 - \exp(-1.2564(t/t_{max}))]^2 \quad (4)$$

Progressive nucleation:

$$i^2/i_{max}^2 = 1.2254(t/t_{max})^{-1}[1 - \exp(-2.3367(t^2/t_{max}^2))]^2 \quad (5)$$

where i_{max} and t_{max} are the maximum current density and the corresponding time, respectively.

Figures 3, 4, and 5 represent the dimensionless theoretical $(i/i_{max})^2$ vs (t/t_{max}) plots resulting from Eq. (4) and (5), and experimental current density transients during the electrodeposition of nickel on a copper substrate at different

potentials in the absence and presence of additives in the electrolyte. It can be seen that at $(t/t_{max}) \leq 1$, the experimental plots at different applied potentials (with and without additives) tend to the instantaneous nucleation model. Hence, the electrodeposition of nickel on copper substrate nucleation follows the 3D instantaneous nucleation mode at short time [23,27], which indicates that the addition of additives did not change the nucleation mechanism of the nickel. For (t/tm > 1, the experimental curves show a negligible difference from the Scharifker model. This difference is related to the proton reduction on the copper surface [28].

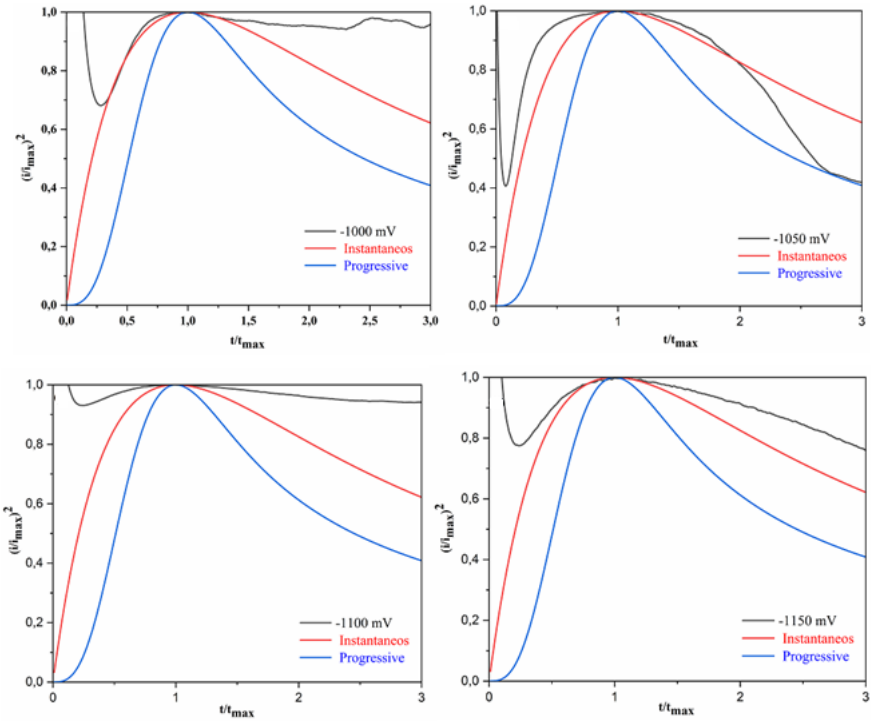

Figure 3. Comparison of theoretical non-dimensional $(i/i_{max})^2$ vs (t/t_{max}) plots for instantaneous nucleation from Eq. (4) and progressive nucleation from Eq. (5) to experimental current density transients for the electrodeposition of nickel on a copper substrate at different potentials in the absence of additives

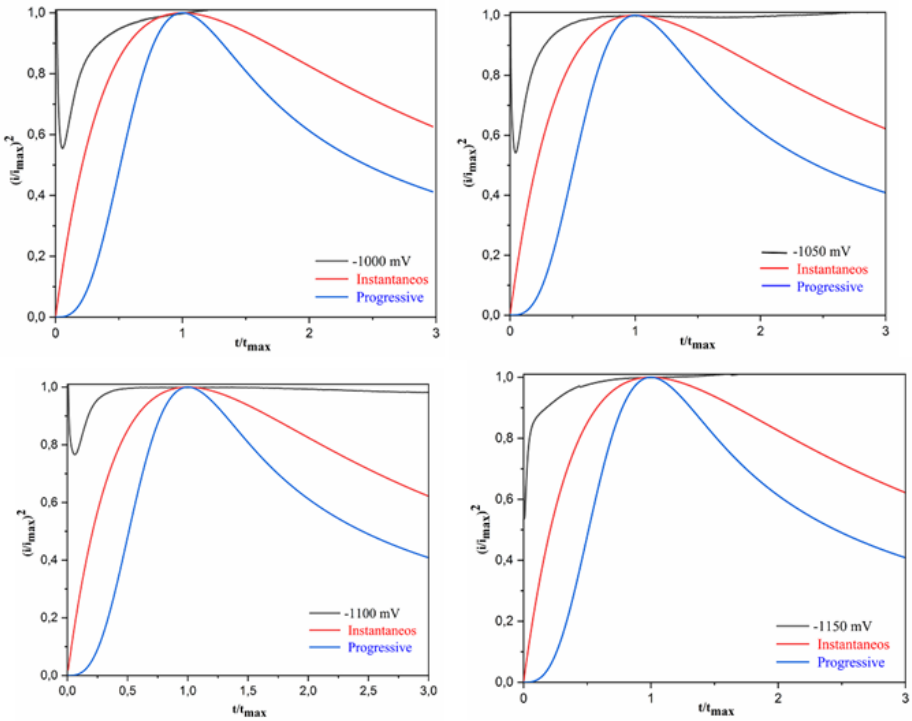

Figure 4. Comparison of theoretical non-dimensional $(i/i_{max})^2$ vs (t/t_{max}) plots for instantaneous nucleation from Eq. (4) and progressive nucleation from Eq. (5) to experimental current density transients for the electrodeposition of nickel on a copper substrate at different potentials in the presence of 24.7 g L^{-1} H_3BO_3 in the bath

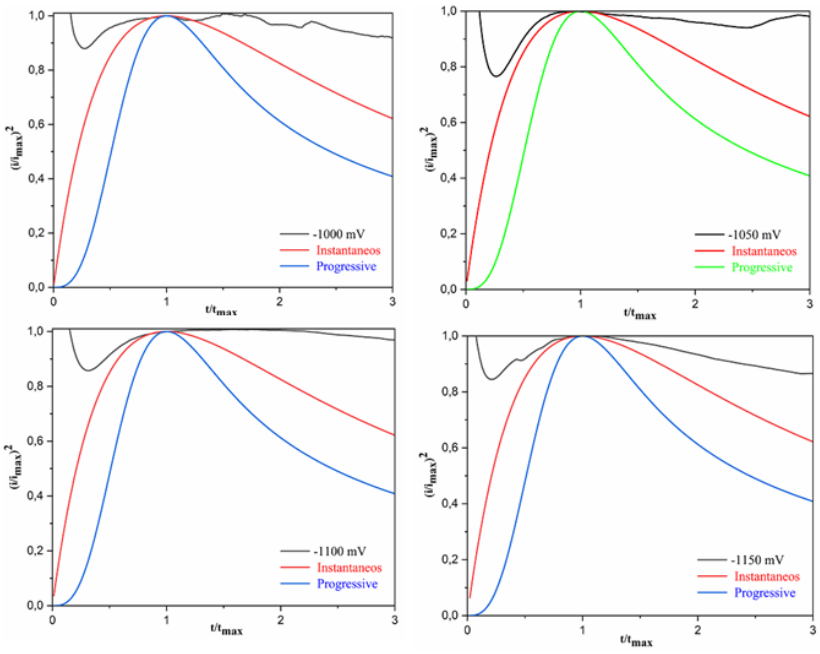

Figure 5. Comparison of theoretical non-dimensional $(i/i_{max})^2$ vs (t/t_{max}) plots for instantaneous nucleation from Eq. (4) and progressive nucleation from Eq. (5) to experimental current density transients for the electrodeposition of nickel on a copper substrate at different potentials in the presence of 0.84 g L^{-1} $C_2H_2O_4$ in the bath

3.2.3. Kinetic parameters of the nickel electrodeposition

According to Scharifker and Hills model, the diffusion coefficient (D_{inst}), the number of active nucleation sites (N_0), and the nucleation rate (A) can be determined from the current density transients using the following equations [29,30]:

$$D = \frac{i_{max}^2 t_{max}^2}{0.1629(nFC)^2} \quad (6)$$

$$N_0 = 0.065\left(\frac{8\pi CM}{\rho}\right)^{-1/2}\left(\frac{nFC}{i_{max}t_{max}}\right)^2 \quad (7)$$

$$A = N_0\pi\left(\frac{8\pi CM}{\rho}\right)^{1/2} D \quad (8)$$

where n is the number of transferred electrons, M is the atomic weight, t is time, F is the Faraday constant (96500 C/mol), C is the concentration of the electroactive species (mol/l), and ρ is the density of the Ni deposit.

Values of t_{max}, i_{max}, D, A and N_0 at different potentials are shown in Table 2. It is clear that as the applied potential increase, the maximum current density increases, and the maximum time (tmax) decreases. This feature is typical of three-dimensional electrochemical nucleation and growth of a new phase governed by diffusion control. The number of active nucleation sites (N_0) increases in the presence and absence of additives in the bath, but the nucleation rate (A) decreases. These results are characteristic for 3D instantaneous nucleation process.

Table 2. The values of t_{max}, i_{max}, D, A, and N_0 for electrodeposition of Ni in the absence and presence of additives at deposition potentials obtained from current density transient curves using Eq. (6), (7) and (8)

Additive Composition	E (mV)	t_{max} (s)	$-i_{max}$ (mA cm^{-2})	D (cm^2 s^{-1})	A (s^{-1})	N_0 (cm^{-2})
Without additive	-1000	15.50	29.45	$4.99.10^{-4}$	1.26	$1.23.10^2$
	-1050	36.30	32.97	$0.34.10^{-4}$	0.01	$0.17.10^2$
	-1100	9.30	46.63	$4.50.10^{-4}$	1.23	$1.33.10^2$
	-1150	9.40	66.65	$9.41.10^{-4}$	1.24	$0.64.10^2$
With boric acid	-1000	100.90	28.94	0.02	0.82	$0.02.10^2$
	-1050	40.30	44.28	$0.76.10^{-4}$	0.01	$0.07.10^2$
	-1100	15.18	58.83	$0.19.10^{-4}$	0.01	$0.31.10^2$
	-1150	58.80	74.99	0.04	0.83	$0.01.10^2$
With oxalic acid	-1000	20.70	30.24	$9.39.10^{-4}$	1.20	$0.62.10^2$
	-1050	9.60	42.17	$3.93.10^{-4}$	1.24	$1.53.10^2$
	-1100	8.40	59.52	$5.99.10^{-4}$	1.23	$1.00.10^2$
	-1150	4.70	88.57	$4.15.10^{-4}$	1.24	$1.45.10^2$

3.3. Structure analysis

The structural properties of the nickel deposit were determined by (XRD) measurements. Figure 6 exhibited the X-ray diffraction (XRD) patterns (40° ≤ 2θ ≤ 100°) of Ni electrodeposited on copper substrate in the absence and presence of different additives at 25.0 ºC at the deposition potential of -1000 mV. The results revealed that the obtained films are polycrystalline structure. All films show diffraction peaks located at 2θ = 43.91°, 50.97°, 74.43° and 90.43°, corresponding to (111), (200), (220) and (311) crystalline planes of Cu substrate according to ICDD card no. 00-003-1018, respectively. However, the peaks observed at around 44.03°, 51.10° and 79.76°, corresponding to (111), (200) and (220) reflections planes of Ni (ICSD n° 01-089-7128 and ICSD n° 01-088-2326), as indicated by the face-centered cubic (FCC) structure of nickel. The addition of additives shifted slightly these peaks toward lower 2θ values. The (111) plane is the stronger, indicating that it is the preferential orientation. In the presence of boric acid in the bath, the intensity of this peak increases. The XRD pattern revealed two distinct diffraction peaks at 2θ = 66.53° and 71.07°, which correspond to the (411) and (332) planes of tetragonal Cu_4O_3 (ICSD n° 01-083-1665). This mixed-valence copper oxide phase most likely developed as a result of partial oxidation of exposed copper substrate regions where nickel electrodeposition was not complete. Local oxidation may have resulted from the presence of microbubbles created by hydrogen evolution during the deposition process, which prevented uniform Ni coverage. Interestingly, samples with continuous nickel films did not exhibit these Cu_4O_3 related peaks, demonstrating that complete surface coverage successfully shields the underlying copper from oxidation.

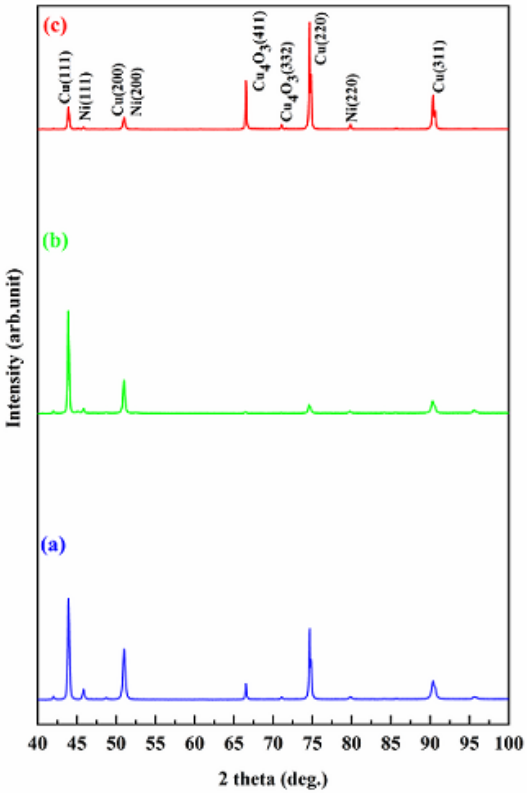

Figure 6. X-ray diffractograms of Ni films electrodeposited at -1000 mV and t= 5 min in solution containing: (a) 60 g L^{-1} $NiSO_4 \cdot 6H_2O$, 8.2 g L^{-1} $NiCl_2.6H_2O$ and 0.5 g L^{-1} Na_2SO_4 (b) 60 g L^{-1} $NiSO_4 \cdot 6H_2O$, 8.2 g L^{-1} $NiCl_2.6H_2O$, 0.5 g L^{-1} Na_2SO_4 and 24.7 g L^{-1} H_3BO_3 and (c) 60 g L^{-1} $NiSO_4 \cdot 6H_2O$, 8.2 g L^{-1} $NiCl_2.6H_2O$, 0.5 g L^{-1} Na_2SO_4 and 0.84 g L^{-1} $C_2H_2O_4.2H_2O$

The lattice parameters were calculated using XRD data as follows [30]:

$$a = d_{hkl}\sqrt{h^2 + k^2 + l^2} \tag{9}$$

and

$$\frac{1}{d_{hkl}^2} = \frac{4}{3}\left(\frac{h^2+hk+k^2}{a^2}\right) + \frac{l^2}{c^2} \tag{10}$$

where d_{hkl} is interplanar spacing, (h k l) are Miller indices, a and c are the lattice parameters, respectively [18]. The average crystallite size (D) was evaluated by Debye Sheerer's equation [32]:

$$D = \frac{K\,\lambda}{\beta\cos\theta} \tag{11}$$

where K is the Scherrer constant (= 0.94), λ is the X-ray wavelength (λ = 1.54060 Å), β is the full width at half maximum (FWHM) value, and θ is the Bragg diffraction angle.

The dislocation density (δ) was estimated by following relation [33]:

$$\delta = \frac{1}{D^2} \tag{12}$$

The microstrain (ε) was also calculated using the following formula [34]:

$$\varepsilon = \frac{\beta \cos\theta}{4} \tag{13}$$

The FWHM values, the crystalline sizes, diffraction angle 2θ, the microstrain and dislocation densities of the Ni thin films were mesured using the (111) diffraction peak are presented in Table 3. It is clear that the introduction of boric and oxalic acid in the electrolyte decreases the FWHM. In addition, the lattice parameters (a) and the crystallite size of the films increased in the presence of additives. Thus, it can be said that the crystallinity of coating is extremely affected by the addition of additives on the bath. The obtained results show that the microstrain and dislocation densities values of the Ni films were reduced with the addition of additives.

Table 3. Structural parameters of the nickel thin films

Ni Films	FWHM	2θ (°)	a (Å)	(hkl)	d_{hkl} (Å)	D (nm)	δ×10^{-3} (Lines/m^2)	ε ×10^{-2}
without additives	0,19	44.03	3.567	(111)	2,0599	10.598	8.91	3.41
with H_3BO_3	0,13	44.01	3.569	(111)	2,0609	15.488	4.17	2.34
with $C_2H_2O_4$	0,16	44.02	3.568	(111)	2,0604	12.583	6.32	2.88

3.4. SEM analysis

The surface morphology of the e nickel films was examined using high-resolution SEM imaging at 50,000× magnification, and the results are presented in Figure 7. The three micrographs correspond to Ni films deposited at room temperature and –1000 mV, obtained without any additive (Figure 7(a)), with boric acid (Figure 7(b)), and with oxalic acid (Figure 7(c)).

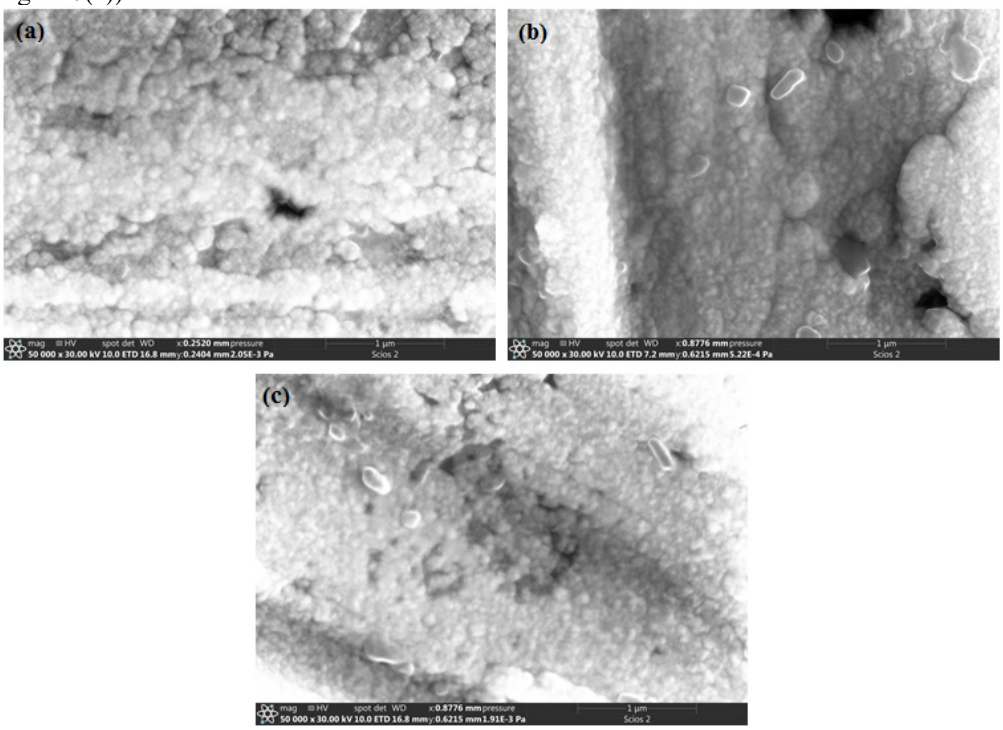

Figure 7. SEM micrographs of nickel thin films electrodeposited at -1000 mV and t= 5 min in solution containing: (a) 60 g L^{-1} $NiSO_4{\cdot}6H_2O$, 8.2 g L^{-1} $NiCl_2.6H_2O$ and 0.5 g L^{-1} Na_2SO_4 (c) 60 g L^{-1} $NiSO_4{\cdot}6H_2O$, 8.2 g L^{-1} $NiCl_2.6H_2O$, 0.5 g L^{-1} Na_2SO_4 and 24.7 g L^{-1} H_3BO_3 and (e) 60 g L^{-1} $NiSO_4{\cdot}6H_2O$, 8.2 g L^{-1} $NiCl_2.6H_2O$, 0.5 g L^{-1} Na_2SO_4 and 0.84 g L^{-1} $C_2H_2O_4.2H_2O$

Without additives (Figure 7(a)), the film shows a porous, kind of rough surface, with spherical grains that aren't packed tightly and have different sizes. Many voids and pits are visible, probably due to hydrogen bubbles that got stuck during deposition. This interuption in the growth causes poor coverage and uneven distribution over the copper surface, which also means nucleation wasn't very efficient.

With the addition of boric acid (Figure 7(b)), the surface looks clearly better. The film is more compact and much smoother, grains are finer too. No major cracks or flaws were observed, and the substrate seems fully covered. Most likely, boric acid helps keeping the local pH steady and also minimizes hydrogen evolution, which makes the whole process of deposition more controlled.

As for the film with oxalic acid (Figure 7(c)), it also seems denser, although the grains here are a bit larger and less packed compared to the boric acid one. Still, the surface stays relatively smooth, and there's no serious defect you can spot. This might be because oxalic acid interacts with Ni^{2+} ions differently, maybe slowing down the reaction by forming weak complexes, which changes how the film grows.

Overall, adding these acids to the bath significantly improves the coating. Both boric and oxalic acid enhanced the surface coverage and adhesion, but boric acid led to a film that's clearly more uniform and compact.

3.5. EDS analysis

EDS (Energy dispersive Xray spectroscopy) was used to assess the elemental composition of the Ni films deposited on copper substrate under different bath conditions, and the results are summarized in Figure 8(a–c).

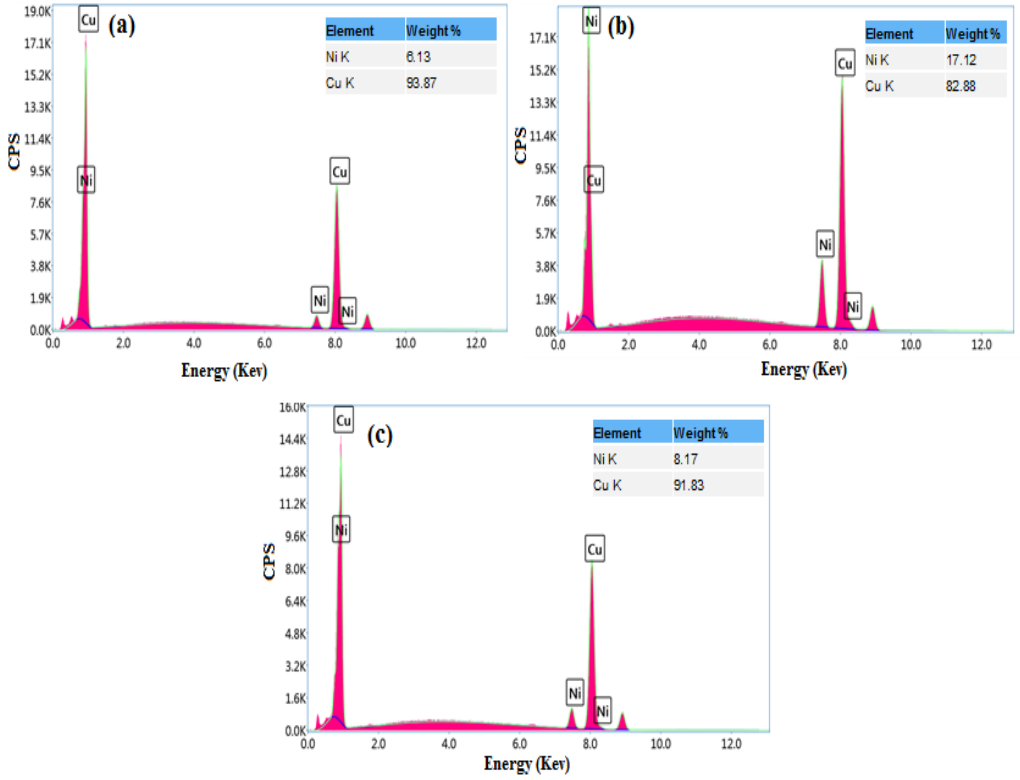

Figure 8. EDS spectrum of nickel coatings electrodeposited at -1000 mV and t= 5 min in solution containing: (a) 60 g L^{-1} $NiSO_4{\cdot}6H_2O$, 8.2 g L^{-1} $NiCl_2.6H_2O$ and 0.5 g L^{-1} Na_2SO_4 (c) 60 g L^{-1} $NiSO_4{\cdot}6H_2O$, 8.2 g L^{-1} $NiCl_2.6H_2O$, 0.5 g L^{-1} Na_2SO_4 and 24.7 g L^{-1} H_3BO_3 and (e) 60 g L^{-1} $NiSO_4{\cdot}6H_2O$, 8.2 g L^{-1} $NiCl_2.6H_2O$, 0.5 g L^{-1} Na_2SO_4 and 0.84 g L^{-1} $C_2H_2O_4.2H_2O$

Each spectrum displays characteristic peaks for Ni and Cu, indicating the coexistence of both elements in the analyzed area. The relative weight percentages give further insight into how effectively the nickel coating formed in each case.

In the sample without any additives (Figure 8(a)), the nickel content is notably low, with Ni accounting for only about 6.13 wt%. This weak signal is consistent with the SEM observations, which show poor surface coverage. The dominant Cu signal (93.87 wt%) suggests that the underlying copper substrate is largely exposed, indicating either a very thin Ni layer or incomplete film formation. This aligns well with the porous and uneven morphology previously observed.

When boric acid is used in the electrolyte (Figure 8(b)), the nickel content significantly increases to 17.12 wt%, while the copper signal drops to 82.88 wt%. This suggests a much thicker and more complete nickel deposit on the substrate. The improved Ni/Cu ratio is in line with the denser, more uniform coating observed in the SEM image (Fig. 5b), confirming that boric acid promotes more efficient metal deposition and better surface coverage.

The film deposited from the bath containing oxalic acid (Figure 8(c)) shows an intermediate composition. The nickel weight percentage rises slightly to 8.17 wt%, higher than the additive-free condition but still significantly lower than with boric acid. This implies partial improvement in Ni deposition and coverage, though not as effective as with boric acid. The Cu peak remains relatively strong (91.83 wt%), reflecting limited shielding of the substrate. This result also matches the SEM image in Fig. 5c, where the surface appeared smoother but with larger grains and less compact packing.

Overall, the EDX results confirm that both boric and oxalic acid additives enhance nickel deposition efficiency. However, boric acid appears more effective in promoting thick, uniform coatings with higher Ni content, likely due to its buffering capacity and suppression of parasitic hydrogen evolution.

4. CONCLUSIONS

In this paper, nickel films have been successfully prepared on copper substrates using the electrodeposition method. The effect of the additives (boric acid and oxalic acid) on the nickel nucleation process, surface morphologies, chemical composition, and crystal structure was investigated. The (CV) analysis showed that the electrodeposition of Ni has been started at potential of approximately -0.70 V vs SCE and the presence of additives in the solution shifted negatively the cathodic peak potential. The (CA) analysis revealed that the electrochemical deposition of Ni followed the 3D instantaneous nucleation process and the presence of additives in the electrolyte did not affect the nucleation mechanism of Ni. XRD measurements showed that all nickel electrodeposited films had the face-centered cubic (FCC) structure with a (111) preferential orientation. In the presence of boric acid in the bath, the intensity of this peak increases. SEM analysis indicated that the thin films obtained from the solution containing additives exhibit good adhesion to copper substrates with a denser crystal size. EDS analysis confirmed the presence of Ni in all coatings.

ORCID

F.Z.K. Hamdi, https://orcid.org/0000-0001-9370-7715

REFERENCES

[1] A. Sahlaoui, Y. Lghazi, B. Youbi, M. Ait Himi, J. Bahar, C. El Haimer, A. Aynaou, *et al*., Moroccan Journal of Chemistry, **11**, 541 (2023). https://doi.org/10.48317/IMIST. PRSM/morjchem-v11i2.36809
[2] F. Zhang, S. Liu, and F. Wang, RSC advances, **12**, 11052 (2022). https://doi.org/10.1039/D1RA08926A
[3] S. Elsharkawy, D. Kutyła, and P. Żabiński, Coatings, **14**, 1459 (2024). https://doi.org/10.3390/coatings14111459
[4] X. Wang, G. Wang, W. Wang, X. Liu, Y. Liu, Y. Jin, and Y. Zhang, Journal of Alloys and Compounds, **1032**, 181014 (2025). https://doi.org/10.1016/j.jallcom.2025.181014
[5] H.F. Alesary, S. Cihangir, A.D. Ballantyne, R.C. Harris, D.P. Weston, A.P. Abbott, and K.S. Ryder, Electrochimica Acta, **304**, 118 (2019). https://doi.org/10.1016/j.electacta.2019.02.090
[6] S. Umrao, J. Jeon, S.M. Jeon, Y.J. Choi, and S. Lee, Nanoscale, **9**, 594 (2017). https://doi.org/10.1039/C6NR07240B
[7] B. Abedini, N.P. Ahmadi, S. Yazdani, and L. Magagnin, Transactions of Nonferrous Metals Society of China, **30**, 548 (2020). https://doi.org/10.1016/S1003-6326(20)65234-7
[8] Y. Xu, H. Jiao, M. Wang, and S. Jiao, Journal of Alloys and Compounds, **779**, 22 (2019). https://doi.org/10.1016/j.jallcom.2018.11.232
[9] K.D.M. Abro, A. Sanou, and E.K.I. Kwa-Koff, American Journal of Physical Chemistry, **13**, 1 (2024). https://doi.org/10.11648/j.ajpc.20241301.11
[10] E. Bouabdalli, M. El Jouad, T. Garmim, A. Louardi, B. Hartiti, M. Monkade, S. Touhtouh, and A. Hajjaji, Materials Science and Engineering: B. 286, 116044 (2022), https://doi.org/10.1016/j.mseb.2022.116044
[11] A. Shamim, Z. Ahmad, S. Mahmood, U. Ali, T. Mahmood and Z. Nizami, Open Journal of Chemistry, **2**, 16 (2019). https://www.doi.org/10.30538/psrp-ojc2019.0009
[12] A. Rahmani, L. Remache, M. Guendouz, N. Lorrain, A. Djermane, and L. Hadjeris, Surface Review and Letters, **29**, 2250039 (2021). https://doi.org/10.1142/S0218625X22500391
[13] F. Lekmine, I. Zidani, A. Chala, and A. Gana, Journal of nano- and electronic physics, **14**, 06022-1 (2022), https://doi.org/10.21272/jnep.14(6).06022
[14] N. Guermat, W. Daranfed, I. Bouchama, and N. Bouarissa, Journal of Molecular Structure, **1225**, 129134 (2021). https://doi.org/10.1016/j.molstruc.2020.129134
[15] G. Qadr, M.I. Awad, K. Haji, J.A. Jumaa, and H.H. Abdallah, Journal of Molecular Liquids, **378**, 121584 (2023). https://doi.org/10.1016/j.molliq.2023.121584
[16] C. El Haimer, Y. Lghazi, J. Bahar, B. Youbi, M. Ait Himi, A. Ouedrhiri, A. Aynaou, and I. Bimaghra, Materials Today: Proceedings, **66**, 37 (2022), https://doi.org/10.1016/j.matpr.2022.03.107
[17] X. Fu, C. Zhan, R. Zhang, B. Wang, H. Sun, and J. Sun, Journal of Solid State Electrochemistry, **26**, 2713 (2022). https://doi.org/10.1007/s10008-022-05282-z
[18] S. Saha, M. Johnson, F. Altayaran, Y. Wang, D. Wang, and Q. Zhang, Electrochem. **1**, 286 (2020). https://doi.org/10.3390/electrochem1030019
[19] I.M. Beker, F.B. Dejene, L.F. Koao, J.J. Terblans, S.Z. Werta, and A.U. Yimamu, Journal of Electronic Materials, **54**, 6575 (2025). https://doi.org/10.1007/s11664-025-12082-4
[20] L. Yuan, J. Chen, J. Zhang, and L. Sun, Crystals, **12**, 43 (2021), https://doi.org/10.3390/cryst12010043
[21] X. Wu, X. Zhao, P. Lin, C. Tan, C. Wang and W. Chen, Journal of Materials Research and Technology. **36**, 1789-1801 (2025), https://doi.org/10.1016/j.jmrt.2025.03.212
[22] F.Z. Hamdi, A. Hamdi, S. Khenchoul, A. Rahmani, A. Cheriet, L. Aissani and A. Alhussein, Journal of the Indian Chemical Society. **99**, 100498-100503 (2022), https://doi.org/10.1016/j.jics.2022.100498
[23] H. Rao, W. Li, Z. Luo, H. Liu, L. Zhu, and H. Chen, Journal of Materials Research and Technology, **30**, 3079 (2024). https://doi.org/10.1016/j.jmrt.2024.04.008
[24] R. Li, Q. Chu, and J. Liang, Rsc Advances, **5**, 44933 (2015). https://doi.org/10.1039/C5RA05918F
[25] B. Scharifker, and G. Hills, Electrochimica Acta, **28**, 879 (1983). https://doi.org/10.1016/0013-4686(83)85163-9
[26] M.R. Khelladi, L. Mentar, A. Azizi, F. Kadirgan, G. Schmerber, and A. Dinia, Applied surface science. **258**, 3907-3912 (2012). https://doi.org/10.1016/j.apsusc.2011.12.060
[27] A. Mashreghi, and H. Zare, Current Applied Physics, **16**, 599 (2016). https://doi.org/10.1016/j.cap.2016.03.008
[28] X. Cao, H. Wang, T. Liu, Y. Shi, and X. Xue, Materials, **16**, 415 (2023). https://doi.org/10.3390/ma16010415
[29] L. Mentar, Ionics, **18**, 223 (2012). https://doi.org/10.1007/s11581-011-0602-y
[30] J. Bahar, Y. Lghazi, B. Youbi, M. Ait Himi, C. El Haimer, A. Ouedrhiri, A. Aynaou, and I. Bimaghra, Materials Today: Proceedings, **66**, 187 (2022). https://doi.org/10.1016/j.matpr.2022.04.445

[31] A. El-Shaer, S. Ezzat, M.A. Habib, O.K. Alduaij, T.M. Meaz, and S.A. El-Attar, Crystals, **13**, 788 (2023). https://doi.org/10.3390/cryst13050788
[32] D. Abou-Ras, G. Kostorz, A. Romeo, D. Rudmann, and A.N. Tiwari, Thin Solid Films, **480**, 118 (2005). https://doi.org/10.1016/j.tsf.2004.11.033
[33] A.A. Ojo, and I.M. Dharmadasa, Coatings. **9**, 370 (2019). https://doi.org/10.3390/coatings9060370
[34] S.W. Pawar, V.A. Tabhane, P.E. Lokh, F. Khan, J. Kaur, A. Al-Ahmed, and H.M. Pathan, ES Energy & Environment, **17**, 106 (2022). https://doi.org/10.30919/esee8c652

ВПЛИВ БОРНОЇ ТА ЩАВЛЕВОЇ КИСЛОТИ НА МЕХАНІЗМ ЗАРОДЖЕННЯ, СКЛАД, МОРФОЛОГІЮ ТА СТРУКТУРУ ЕЛЕКТРООСАДЖЕНИХ НІКЕЛЕВИХ ПЛІВОК

Ф.З.К. Хамді[1], А. Рахмані[1,2], А. Хамді[1]

[1]*Лабораторія фізичної хімії матеріалів (LPCM), Факультет наук, Університет Амар Теліджі, 03000, Лагуат, Алжир*
[2]*Лабораторія MONARIS, UMR 8233, Університет Сорбонни, 4-та площа Жюссьє, 75005 Париж, Франція*

Тонкі нікелеві плівки були електроосаджені на мідні підкладки за кімнатної температури з використанням водного електроліту, що містить сульфат нікелю, хлорид нікелю та сульфат натрію. Вплив двох добавок (борної кислоти та щавлевої кислоти) на механізм зародження, кристалографічну структуру, морфологію поверхні та хімічний склад отриманих плівок Ni було систематично досліджено за допомогою циклічної вольтамперометрії (CV), хроноамперометрії (CA), рентгенівської дифракції (XRD), скануючої електронної мікроскопії (SEM) та енергодисперсійної рентгенівської спектроскопії (EDS). CV-аналіз показав, що присутність добавок зміщує потенціали катодних піків у бік більш негативних значень, що свідчить про гальмівний ефект відновлення нікелю. Хроноамперометричні дослідження підтвердили, що осадження Ni відбувалося в тривимірному режимі миттєвого зародження, на яке не впливали добавки. Рентгенограми показали, що всі плівки Ni мали гранецентровану кубічну (FCC) структуру з сильною орієнтацією (111), тоді як SEM-зображення вказували на щільнішу та однорідніщу морфологію поверхні за наявності добавок. EDS-аналіз підтвердив присутність Ni у всіх зразках.

Ключові слова: *нікель; електроосадження; добавки; борна кислота; щавлева кислота; зародження*

East European Journal of Physics. 4. 537-541 (2025)
DOI:10.26565/2312-4334-2025-4-55 ISSN 2312-4334

EMITTANCE OF A LOW-POWER RF ION SOURCE WITH A MICROMETER-SCALE EXTRACTION APERTURE

Vitalii I. Voznyi*, Aleksandr G. Ponomarev, Dmytro V. Mahilin, Dmytro P. Shulha, Volodymyr A. Rebrov

Institute of Applied Physics NAS of Ukraine, 58, Petropavlivska Str., 40000 Sumy, Ukraine
**Corresponding Author: vozny56@gmail.com*
Received August 18, 2025; October 13, 2025; accepted October 26, 2025

The concept of a compact nuclear microprobe is based on specialized ion sources with beam currents not exceeding a few nanoamperes and a small energy spread. At the Institute of Applied Physics, NAS of Ukraine, a low-power RF ion source has been developed for application in a compact nuclear microprobe. The source operates at low RF power (< 10 W) and is designed to generate a $^1H^+$ ion beam required for standard techniques such as PIXE, RBS, and proton beam writing. To reduce the beam emittance and improve the spatial resolution of the microprobe, the source extraction aperture diameter was reduced to 50 μm. This paper reports measurements of the total beam current and emittance extracted from the low-power RF ion source with a micrometer-scale extraction aperture. Data on the beam profile, its diameter, and divergence angle are also presented. The main parameters of the RF source are as follows: quartz chamber diameter – 34 mm, length – 70 mm, working gas – hydrogen, extraction aperture diameter – 50 μm, RF power ≤ 10 W, frequency – 45 MHz, ion current up to 100 nA. The extraction voltage varies from 10 to 300 V, while the beam energy ranges from 1 to 6.5 keV. Beam emittance was measured using an electrostatic Allison-type scanner. The minimum emittance containing 90% of the total beam current was found to be ε_{90} = 1.36 π·mm·mrad, while the rms-emittance is ε_{rms} = 0.32 mm·mrad. The normalized emittance is ε_N = 0.003 π·mm·mrad, and the energy-normalized emittance equals 0.1 π·mm·mrad·(MeV)$^{1/2}$. It is shown that reducing the diameter of the extraction aperture of the ion source to 50 μm results in a significant improvement in the ion-optical characteristics of the extracted beam.
Keywords: *Ion beam; Radiofrequency Ion source; Beam current density; Extractor; Emittance*
PACS: 29.25.Ni; 41.75.Ak; 41.85.Qg; 41.85.Ne

Nuclear microprobe facilities are intended for local, non-destructive microanalysis of materials of diverse origin as well as for the fabrication of high-quality micro- and nanostructures. Modern microprobe systems represent one of the analytical channels within multi-purpose complexes based on electrostatic accelerators. These accelerators typically deliver ion beam energies of several MeV and currents up to 100 μA [1–3]. To achieve significant demagnification factors in the ion-optical system, the overall length of the microprobe beamline may extend to about 10 m.

At the Institute of Applied Physics, NAS of Ukraine, a concept for a compact nuclear microprobe has been proposed [4], based on ion sources with beam currents up to 10 nA and an energy spread of about 10 eV.

To achieve high spatial resolution in low-energy (~30 keV) microprobe systems, liquid-metal ion sources, field ion sources [5], or electron-impact ion sources with emission aperture sizes of 0.1–1 μm [6, 7] are commonly employed. However, due to their technical limitations, such sources are not suitable in compact microprobe designs.

In view of this, an inductive RF ion source has been developed at the IAP NAS of Ukraine for application in the injector of a compact nuclear microprobe [8]. The source operates at low RF power (<10 W) and is intended for generating $^1H^+$ ion beams required for standard techniques such as PIXE, RBS, and proton beam writing.

The source operates with hydrogen as the working gas, at an RF power level below 10 W. It is equipped with a 0.6 mm extraction aperture and delivers beam currents up to 3.5 μA with a proton fraction of about 10%. The relatively low RF power enables a reduction of the ion energy spread to 7.5–9 eV. The geometric emittance containing 90% of the total beam current was measured to be ε_{90} = 9.8 π·mm·mrad, while the energy-normalized emittance of the source equals 0.8 π·mm·mrad·(MeV)$^{1/2}$.

To further enhance the spatial resolution and overall performance of the microprobe, it is essential to extract an ion beam with the lowest possible emittance from the ion source. For this purpose, measurements of the emittance of the ion beam extracted from the low-power RF source with an extraction aperture diameter of 50 μm have been carried out.

This paper presents measurements of the total current and emittance of an ion beam extracted from an RF ion source with a micrometer-scale extraction aperture. Data on the beam profile and divergence angle are also reported.

RF ION SOURCE AND BEAM CURRENT

The schematic of the inductive RF ion source and its operating principle are described in detail in [8]. The source comprises a cylindrical quartz discharge chamber (Ø 34 mm, length 70 mm) surrounded by a six-turn copper coil. An RF voltage of up to 10 W at 45 MHz is applied to the coil. Hydrogen at ~1 Pa is contained within the chamber. The coil's alternating magnetic field induces an azimuthal RF electric field, which is absorbed by electrons in the gas,

Cite as: V.I. Voznyi, A.G. Ponomarev, D.V. Mahilin, D.P. Shulha, V.A. Rebrov, East Eur. J. Phys. 4, 537 (2025), https://doi.org/10.26565/2312-4334-2025-4-55

leading to excitation and ionization and forming an RF plasma discharge. Positive ions are extracted by an extraction electrode, while an accelerating electrode focuses the resulting ion beam.

The consumed power of the RF generator is approximately 8 W. Considering the generator efficiency, the RF power absorbed by the plasma does not exceed 5 W.

Fig. 1a shows the dimensions of the extractor with a 50 μm aperture. The aperture is fabricated from platinum.

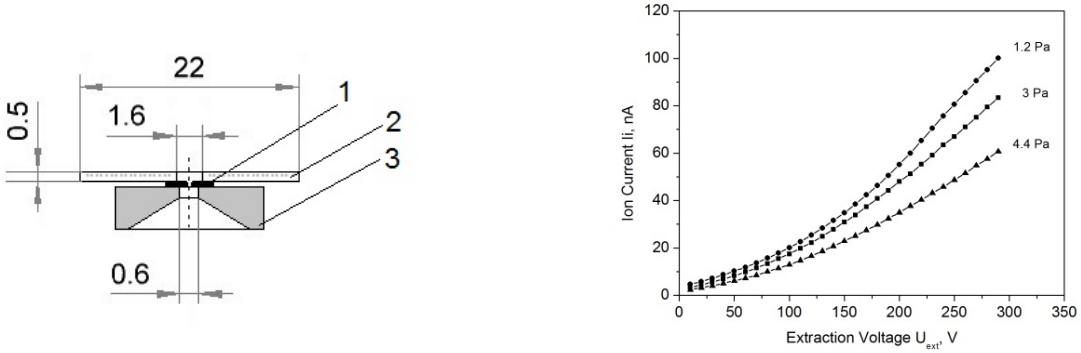

a b

Figure 1. a – extractor with a 50 μm aperture: 1 – aperture, 2 – quartz diaphragm, 3 – extractor. b – ion beam current as a function of extraction voltage for different hydrogen pressures

Measurements of the ion-optical characteristics of the RF source were performed on the experimental setup, the schematic of which is shown in [8]. The ion source was connected to a vacuum chamber with a volume of approximately 6 L, evacuated by a Leybold-360 turbomolecular pump with a pumping speed of 360 L/s. The vacuum chamber was evacuated to a pressure of 1×10^{-4} Pa, measured with a VMB-14 magnetic vacuum gauge.

Hydrogen was introduced into the source via a SNA-2 gas supply system. Within the operational range of gas flow, the hydrogen pressure in the source was varied between 0.5 and 5 Pa. Correspondingly, the pressure in the vacuum chamber of the setup ranged from $(3–9)\times10^{-4}$ Pa.

The current–voltage characteristic of the source, representing the dependence of the ion beam current I_i on the extraction voltage U_{ext}, was measured using a Faraday cup located 100 mm from the source. The Faraday cup, with a diameter of 22 mm, was equipped with a suppressor biased at -290 V to eliminate the influence of secondary electrons on the current measurement.

Fig. 1b shows the dependence of the ion beam current I_i on the extraction voltage U_{ext} at different hydrogen pressures in the source chamber in the range of 1.2–4.4 Pa. The extraction voltage U_{ext} was varied from 10 V to 290 V at a constant accelerating voltage of U_{acc} = 4 kV.

As seen in Fig. 1b, the ion beam current increases monotonically with extraction voltage and decreases with increasing gas pressure. The maximum current of I_i=100 nA is obtained at an extraction voltage of U_{ext}=290 V and a low gas pressure of p=1.2 Pa.

At a gas pressure of p=1.2 Pa, the ion current curve is well approximated by a power-law function $I_i = 5.26 + 4.5\cdot10^{-3}\cdot U_{ext}^{1.76}$, where the ion current I_i is expressed in nA and the extraction voltage U_{ext} in Volts. At a pressure of p=4.4 Pa, the ion current curve is approximated by the function $I_i = 2.32 + 7.4\cdot10^{-3}\cdot U_{ext}^{1.58}$.

This form of the ion current dependence on the extraction voltage is characteristic of plasma ion sources, in which the plasma emission boundary forms a meniscus. The emission boundary changes shape with plasma density n_e, electron temperature T_e, and extraction voltage U_{ext}. The shape of the current–voltage curves is determined by the Child–Langmuir law: $j_i = (4\varepsilon_0/9)\sqrt{2e/m}\cdot(U_{ext}^{3/2}/d^2)$, where ε_0 is the vacuum permittivity, e is the electron charge, m is the electron mass, and d is the distance from the plasma boundary to the extraction electrode.

Since in a plasma source the value of distance d depends on both n_e and U_{ext}, the exponent of the power function deviates from the value of 3/2.

The beam current density can be estimated as $j_i = I_i/S_a$, where S_a is the area of the extraction aperture. For I_i=100 nA, the current density is j_i=5 mA/cm^2.

BEAM EMITTANCE

The RF source's emittance was measured using an electrostatic scanner, whose design and operation are described in detail in [9]. The device is based on the Allison–type scheme [10, 11].

The scanner consists of two parallel deflection plates supplied with a sawtooth voltage, an entrance and exit slit, and a Faraday cup for measuring the ion current transmitted through both slits. The scanner is moved transversely to the beam in the vertical x-direction by a stepper motor. The plates along the beam axis are 120 mm long, with a plate separation of 10 mm. The widths of the entrance and exit slits are 200 μm. The scanner's spatial resolution is 4.8 μm, with a scanning range of 0–20 mm.

The scanner was mounted at a distance approximately 55 mm from the ion source. Scanning along the x-axis was carried out over a range of 0-7 mm with a step size of 93.75 μm. The voltage applied to the deflection plates was varied from -50 V to +50 V in steps of 1 V.

The angular resolution of the scanner depends on the beam energy E. For the energy of E = 6 keV and a voltage-scanning step of 1 V, the angular resolution is 0.42 mrad.

The determination of the emittance is based on measuring the ion beam intensity distribution $Z(x, x')$ as a function of the coordinate x and angle x'. The measured two-dimensional array of ion beam intensity $Z(x, x')$ represents the beam current density distribution in the x-x' phase space. The array $Z(x, x')$ enables the determination of key beam parameters: geometric emittance ε_{90}, the rms-emittance ε_{rms} and the ion beam current profile $Z(x)$.

A cross-section of the distribution $Z(x, x')$ at a given threshold value defines the emittance diagram, the area of which, devided by π, corresponds to the beam emittance. For a threshold value corresponding to 90% of the total beam current, the resulting emittance diagram represents the contour of the geometric emittance ε_{90}, which encloses 90% of the total beam current.

During beam acceleration, its emittance decreases. The quantity that remains constant under beam acceleration is the normalized emittance, defined as $\varepsilon_N=\varepsilon\cdot\beta\cdot\gamma$, where β and γ are the relativistic beta and gamma factors. For non-relativistic beams, the expression for the normalized emittance is given by $\varepsilon_N = \varepsilon_{90}\cdot 4{,}6\cdot 10^{-5}\sqrt{E/A}$, where E is the beam energy, eV, and A is the ion mass number.

In addition to the geometric interpretation of the emittance as the area of the contour enclosing 90% of all beam particles, there exists a statistical approach in which the beam is considered as a statistical ensemble of points in the two-dimentional phase space x-x' [12, 13]. Particles within the space x-x' can be treated as a statistical distribution with mean values ⟨x⟩ and ⟨x′⟩.

In this case, the rms-emittance ε_{rms} is determined by the standard deviations from these mean values, σ_x, $\sigma_{x'}$, and $\sigma_{xx'}$, where $\sigma_x^2=\langle x^2\rangle$, $\sigma_x^2=\langle x^2\rangle$ and $\sigma_{xx'}^2=\langle xx'\rangle^2$ are the second-order moments of the phase-space distribution function. The expression for calculating the rms-emittance is given by: $\varepsilon_{rms}=\sqrt{\langle x^2\rangle\langle x'^2\rangle-\langle xx'\rangle^2}=\sqrt{\sigma_x^2\sigma_{x'}^2-\sigma_{xx'}^2}$.

Emittance measurements of the ion beam were performed for various extraction voltages in the range of U_{ext}=150-300 V and acceleration voltages in the range of U_{acc}=1.5-6.5 kV. The hydrogen pressure in the source chamber was maintained constant at p=1.2 Pa.

Fig. 2a shows the 3D-intensity distribution surface $Z(x, x')$ of the ion beam current, measured at an extraction voltage of U_{ext}=280 V and an acceleration voltage of U_{acc}=6.0 kV. The corresponding emittance diagram, illustrating the contour of the emittance ε_{90} enclosing 90% of the total beam current, is shown in Fig. 2b.

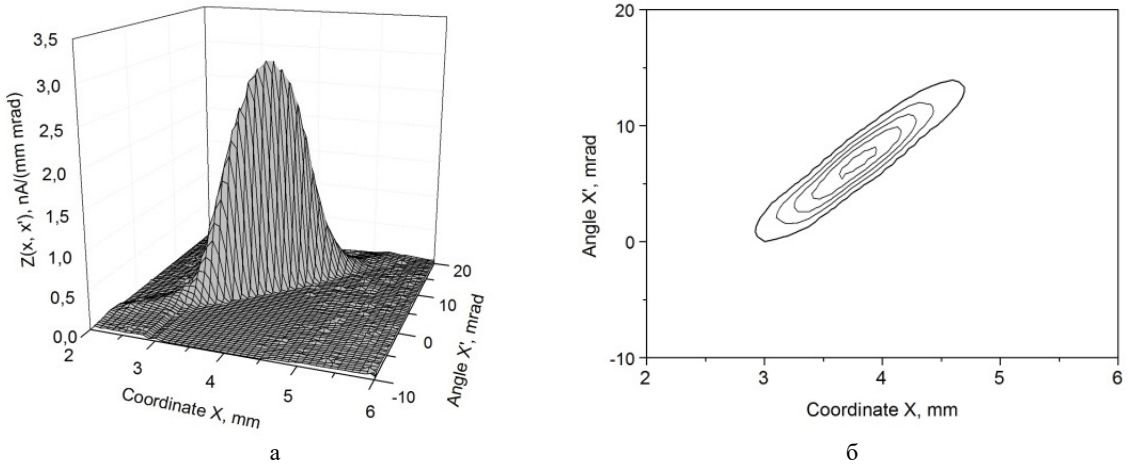

а б

Figure 2. a – 3D surface of the current intensity distribution $Z(x, x')$, b – contour of ε_{90} beam emittance

At a beam energy of E=6 keV, the geometric emittance was found to be ε_{90}=1.9 π·mm·mrad. The rms-emittance was ε_{rms}=0.44 mm·mrad. The ratio $\varepsilon_{90}/\varepsilon_{rms}$ is close to the theoretical value of 4.6 for beams with a Gaussian intensity distribution [14, 15]. The normalized emittance was determined to be ε_N=0.0047 π·mm·mrad for A=2.

For comparing the emittances of ion sources with different beam energies, the quantity of the energy-normalized emittance, defined as $\varepsilon\cdot E^{1/2}$, is often used. The energy-normalized emittance of the beam was determined to be 0.15 π·mm·mrad·(MeV)$^{1/2}$.

The minimum emittance was obtained at an extraction voltage of U_{ext}=220 V and an acceleration voltage of U_{acc}=5.5 kV. Under these conditions, the geometric emittance was ε_{90}=1,36 π·mm·mrad, and rms-emittance was ε_{rms}=0.32 mm·mrad, giving ratio $\varepsilon_{90}/\varepsilon_{rms}$=4,2. The normalized emittance was ε_N=0.003 π·mm·mrad (A=2). The energy-normalized emittance was 0.1 π·mm·mrad·(MeV)$^{1/2}$.

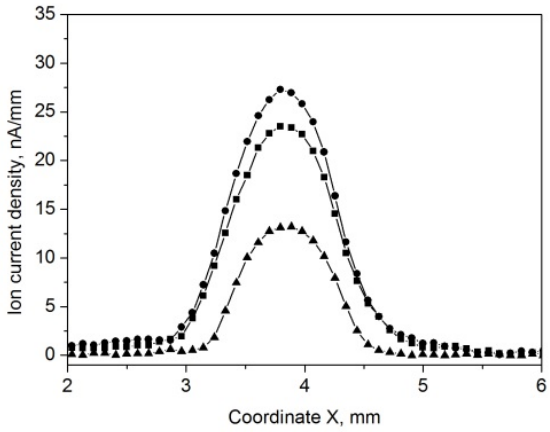

Figure 3 – The current density distribution (beam profile) along the coordinate x

The ion beam current profile, or the current density distribution along the coordinate x, is obtained by summing the elements of the array $Z(x)=\sum_{x'} Z(x,x')$ over all values of the angle x' for each coordinate x, resulting in a profile expressed in nA/mm. Figure 3 shows the ion beam profiles measured for three different extraction voltages. The profiles were measured at a distance of approximately 55 mm from the ion source (~120 mm from the extractor).

In the first case, at U_{ext}=220 V and U_{acc}=5.5 kV, the beam profile is indicated by triangles. The ion beam diameter is $d=3.2\sigma_x$=1 mm, and the full divergence angle is $\theta=3.2\sigma_{x'}$=8.3 mrad. The beam emittance is ε_{90}=1.36 π·mm·mrad.

The beam profile, indicated by squares, corresponds to the case, where the extraction voltage is U_{ext}=280 V and acceleration voltage is U_{acc}=6.0 kV. In this case the beam diameter is $d=3.2\sigma_x$=1.3 mm, and the divergence angle is $\theta=3.2\sigma_{x'}$=10.2 mrad. The beam emittance equals ε_{90}=1.9 π·mm·mrad.

In the third case, at U_{ext}=300 V and U_{acc}=6.5 kV, the beam profile is indicated by dots. The beam diameter is $d=3.2\sigma_x$=1.4 mm, and the divergence angle is $\theta=3.2\sigma_{x'}$=11.2 mrad. The beam emittance is ε_{90}=2.0 π·mm·mrad.

CONCLUSIONS

At the Institute of Applied Physics of NAS of Ukraine, an inductive RF ion source was developed for use in the injector of a compact nuclear microprobe. The source operates at a low RF power of less than 10 W and is designed to generate a $^1H^+$ ion beam required for standard techniques such as PIXE, RBS, and proton-beam writing.

To reduce the ion beam emittance and thereby improve the spatial resolution of the microprobe, the source extraction aperture diameter was reduced from 0.6 mm to 50 μm.

The measurements of the ion-optical beam characteristics showed that:

- the total beam current decreased from 3.5 μA to 100 nA, while the ion current density increased from 1.2 mA/cm^2 to 5 mA/cm^2;
- the geometric emittance was reduced from ε_{90}=9.8 π·mm·mrad to ε_{90}=1.4-2.0 π·mm·mrad;
- the rms-emittance decreased from ε_{rms}=2.2 mm·mrad to ε_{rms}=0.33-0.44 mm·mrad;
- the energy-normalized emittance was 0.1-0.15 π·mm·mrad·(MeV)$^{1/2}$ instead of 0.8 π·mm·mrad·(MeV)$^{1/2}$;
- the ion beam diameter decreased from 3.6 mm to 1-1.4 mm;
- the full beam divergence angle decreased from 30.8 mrad to 8.3-11.2 mrad.

Thus, reducing the ion source extraction aperture diameter to 50 μm greatly enhanced the ion-optical properties of the extracted beam.

This work was carried out within the framework of the project “Investigation of physical processes of ion beam formation in a compact nuclear microprobe based on an immersion probe-forming system”, State registration number 0120U101035, under the Priority thematic area of scientific research and scientific-technical developments in Ukraine “Fundamental problems of physics, astrophysics, materials science, nuclear energy, and radiation safety”.

ORCID

Vitalii I. Voznyi, https://orcid.org/0000-0002-9979-639X; **Aleksandr G. Ponomarev**, https://orcid.org/0000-0002-4517-5635
Dmytro V. Mahilin, https://orcid.org/0009-0005-7024-7142; **Dmytro P. Shulha**, https://orcid.org/0000-0002-4359-3446
Volodymyr A. Rebrov, https://orcid.org/0000-0002-4710-4670

REFERENCES

[1] S. Matsuyama, M. Miwa, S. Toyama, T. Kamiya, Y. Ishii, and T. Satoh, Nucl. Instr. and Meth. B. **539**, 79 (2023). http://doi.org/10.1016/j.nimb.2023.03.023

[2] M. Jaksic, G. Provatas, I. Bozicevic Mihalic, A. Crnjac, D. Cosic, T. Dunatov, O. Romanenko, and Z. Siketic, Nucl. Instr. and Meth. B, **539**, 120 (2023). http://doi.org/10.1016/j.nimb.2023.03.031
[3] G. Nagy, H.J. Whitlow, and D. Primetzhofer, Nucl. Instr. and Meth. B, **533**, 66 (2022). http://doi.org/10.1016/j.nimb.2022.10.017
[4] A.G. Ponomarev, and A.A. Ponomarov, Nucl. Instr. and Meth. B, **497**, 15 (2021). http://doi.org/10.1016/j.nimb.2021.03.024
[5] S. Kalbitzer, Nucl. Instr. and Meth. B, **158**, 53 (1999). https://doi.org/10.1016/s0168-583x(99)00324-9
[6] J.A. van Kan, R. Pang, T. Basu, Y. Dou, Gokul, N. Tarino, J. Tregidga, *et al*. Rev. Sci. Instrum. **91**, 013310 (2020). https://doi.org/10.1063/1.5128657
[7] Y. Dou, T. Osipovicz, and J.A. van Kan, Ultramicroscopy, **253** 113812 (2023). https://doi.org/10.1016/j.ultramic.2023.113812
[8] V.I. Voznyi, A.G. Ponomarev, D.V. Mahilin, D.P. Shulha, and V.A. Rebrov, PAST, (3), 94 (2025). https://doi.org/10.46813/2025-157-094
[9] V.I. Voznyi, M.O. Sayko, A.G. Ponomarev, S.O. Sadovyi, O.V. Alexenko, and R.O. Shulipa, East Eur. J. Phys. (3), 46 (2020). https://doi.org/10.26565/2312-4334-2020-3-06
[10] P.W. Allison, J.D. Sherman, and D.B. Holtkamp, IEEE Trans. Nucl. Sci. **30**(4), 2204 (1983), https://doi.org/10.1109/TNS.1983.4332762
[11] C. Poggi, E. Sartori, M. Tollin, M. Brombin, M. Zaupa, E. Fagotti, and G. Serianni, Rev. Sci. Instrum. **91**, 013328 (2020). https://doi.org/10.1063/1.5129650
[12] J.D. Lawson, *The Physics of Charged Particle Beams*, 2nd ed. (Clarendon Press, Oxford, 1988), pp. 200.
[13] P.M. Lapostolle, IEEE Trans. Nucl. Sci. **18**(3), 1101 (1971). https://doi.org/10.1109/TNS.1971.4326292
[14] D.P. Moehs, J. Peters, and J. Sherman, IEEE Trans. Plasma Sci. **33**(6), 1786 (2005). https://doi.org/10.1109/TPS.2005.860067
[15] M. Reiser, *Theory and Design of Charged Particle Beams*, 2nd ed. (Wiley-VCH, Weinheim, 2008), pp. 53. http://dx.doi.org/10.1002/9783527622047

ЕМІТТАНС ІОННОГО ВЧ ДЖЕРЕЛА МАЛОЇ ПОТУЖНОСТІ З МІКРОМЕТРОВИМ ЕКСТРАКЦІЙНИМ ОТВОРОМ

Віталій І. Возний, Олександр Г. Пономарьов, Дмитро В. Магілін, Дмитро П. Шульга, Володимир А. Ребров
Інститут прикладної фізики НАН України, 58, вул. Петропавлівська, 40000 Суми, Україна

Концепція компактного ядерного мікрозонда ґрунтується на використанні спеціалізованих джерел іонів зі струмом, що не перевищує декількох наноампер і малим розкидом по енергії. В ІПФ НАН України розроблено іонне ВЧ джерело для використання у компактному ядерному мікрозонді. Джерело працює при низькій ВЧ потужності < 10 Вт і призначене для генерації пучка іонів $^1H^+$, необхідного для стандартних методик, таких як PIXE, RBS та протонно-променева літографія. З метою зменшення еміттансу пучка та підвищення просторової роздільної здатності мікрозонда, діаметр екстракційного отвору джерела зменшено до 50 мкм. У роботі приводяться результати вимірювання загального струму та еміттансу пучка, який екстрагується з іонного ВЧ джерела малої потужності з мікрометричним екстракційним отвором. Наведено дані щодо вимірювання профілю пучка, його діаметра та кута розходження. ВЧ джерело має параметри: діаметр кварцової колби - 34 мм, довжина - 70 мм, робочий газ-водень, діаметр отвору екстракції – 50 мкм, ВЧ-потужність ≤10 Вт, частота - 45 МГц, іонний струм до 100 нА. Напруга екстракції змінюється від 10 до 300 В, енергія пучка 1-6,5 кеВ. Вимірювання еміттансу пучка проводилося за допомогою електростатичного сканера, виконаного за схемою Аллісона. Найменше значення еміттансу, що містить 90% повного струму пучка, дорівнює ε_{90}=1,36 π·мм·мрад, а rms-еміттанс- ε_{rms}=0,32 мм·мрад. Нормалізований еміттанс становить ε_N=0,003 π·мм·мрад, а енергетично нормалізований емітанс дорівнює 0,1 π·мм·мрад·(МеВ)$^{1/2}$. Таким чином, зменшення діаметра екстракційного отвору іонного джерела до 50 мкм призвело до помітного підвищення іонно-оптичних характеристик екстрагованого пучка.

Ключові слова: *іонний пучок; високочастотне джерело іонів; щільність струму пучка; екстрактор; еміттанс*

EAST EUROPEAN JOURNAL OF PHYSICS. 4. 542-549 (2025)
DOI:10.26565/2312-4334-2025-4-56 ISSN 2312-4334

SECOND HARMONIC GENERATION OF HIGH-POWER ELLIPTICAL BEAM IN THERMAL QUANTUM PLASMA

Keshav Walia[1]*, Kulkaran Singh[1], Anuj Vijay[2], Deepak Tripathi[3]
[1]*Department of Physics, DAV University Jalandhar, India*
[2]*Department of Physics, GLA University Mathura (U.P.), India-281406*
[3]*Physics Department, USAR, Guru Gobind Singh Indraprastha University, East Delhi Campus, Delhi, India-110032*
**Corresponding Author e-mail: keshavwalia86@gmail.com*
Received September 2, 2025; revised November 9, 2025; accepted November 17, 2025

The current study investigates second harmonic generation of elliptical beam in thermal quantum plasma (TQP) by taking relativistic-ponderomotive (RP) forces together. There is change in mass of electrons due to RP force thereby producing change in background density profile in a direction transverse to main beam. The main beam gets self-focused. The established density gradients excites electron plasma wave (EPW) at pump wave frequency. The excited EPW further interacts with pump wave to produce second harmonic generation (SHG). The widely accepted WKB and paraxial approximations are employed for deriving the 2nd order ODEs for semi major and semi-minor axes of elliptical beam with normalized propagation distance and efficiency of second harmonics. Furthermore, the influence of varying suitable laser-plasma parameters on beam waist dynamics and efficiency of 2nd harmonics are also explored.
Keywords: *Elliptical Cross-section; Quantum Plasma; RP force; Electron Plasma Wave; Paraxial Theory; WKB approximation*
PACS: 52.38.Hb, 52.35.Mw, 52.38.Dx

1. INTRODUCTION

The laser-plasma interaction is vibrant research field as a result of its direct relevance to many applications including X-ray lasers, laser induced, and acceleration of plasma species [1-8]. Recent advancement in laser technology has made possible the production of lasers with intensities exceeding $10^{18}\ W/cm^2$. At such intensity, intense lasers interaction with plasmas has led to interesting nonlinear physics. Because, in this region the behavior of plasma electrons is highly nonlinear. The laser-plasma interaction has led to production of nonlinear phenomena including harmonics production, scattering instabilities, self-focusing and filamentation [9-17]. The complete knowledge of laser-plasma interaction physics requires investigation of these instabilities. These instabilities cause great reduction in efficiency of laser-plasma coupling. So, these instabilities could be minimized if we are having their in-depth knowledge. In 1962, Askaryan initially identified phenomenon of self-focusing [18]. The other nonlinear processes are directly affected due to self-focusing phenomena. Self-focusing process causes in change in dielectric and optical properties of plasma medium. Further, there is displacement of plasma electrons towards less intense portion as a result of ponderomotive mechanism in collisionless plasma. This in fact results in carrier redistribution in plasma. In laser-plasma interaction, generation of harmonics play a major role. The generation of harmonics is greatly influences propagation of lasers through plasma medium. The power of beam gets penetrated in the overdense portion as a result of production of harmonics. The harmonics production is valuable tool for retrieving information about pivotal parameters like expansion velocity, electron density, and opacity [19-20]. SHG helps in tracking transition of laser beam through plasma targets. The pulse duration of radiations of 2nd harmonics is very small. This really makes them suitable for plenty applications in UV spectroscopy [21-24]. The harmonics can be produced in laser produced plasmas through many techniques such as excitation of EPW, acceleration of photons, induced density gradients etc. [25-29]. The most frequently way of producing 2nd harmonics is with the help of excitation process of EPW. The production of density gradients in plasmas causes EPW excitation at pump wave frequency. The interaction of excited EPW with pump beam generates 2nd harmonics. Researchers have investigated SHG both theoretically and experimentally in the past [30-36]. It is quite clear from literature review that majority research on SHG has been explored in classical plasmas, which have less density and high temperature. Recently, a new plasma regime known as quantum plasmas has been explored. This regime has less temperature and high density. Researchers are highly motivated in exploring lasers interaction with quantum regime as a result of its applicability to plenty applications such as fusion science, nanotechnology, astrophysics etc. [37-42]. Further, nonlinear effects get amplified due to quantum effects. If the plasma temperature, Fermi temperature are denoted by T and T_F respectively. Then, quantum contribution can be expressed through parameter $\chi = \frac{T_F}{T}$. For $\chi \geq 1$, quantum effects become more pronounced. One can get overall details of quantum plasmas through FD-statistics. The De-Broglie wavelength λ_B differentiates quantum regime from classical regime. For the case of classical plasmas, λ_B has a very low value. Whereas, for quantum plasmas $\lambda_B \geq$ interatomic distance. Most of the research on SHG is either done through classical plasmas or through cylindrical Gaussian beams. In current study, we are exploring for the first time SHG of elliptical laser beam through TQP under

Cite as: K. Walia, K. Singh, A. Vijay, D. Tripathi, East Eur. J. Phys. 4, 542 (2025), https://doi.org/10.26565/2312-4334-2025-4-56

combined influence of RP force. The elliptical beam introduces anisotropy in self-focusing, an unequal waists along two transverse axes produce non-uniform intensity and asymmetric plasma density redistribution. This modifies local refractive index and phase matching for SHG. In Section 2, The well-established WKB and Paraxial theory are used for deriving 2nd order ODE for semi-major axis and semi-minor axis of laser beam having elliptical cross-section. In Section 3, we derived expression for the amplitude of EPW which act as 2nd harmonic source equation. The efficiency of second harmonics is derived in Section 4. In Section 5, detailed discussion of the results obtained is discussed and finally conclusion of results obtained is discussed in Section 6.

2. EVOLUTION OF SPOT SIZE OF LASER BEAM

Consider a laser beam having elliptical cross-section be transiting along z-axis. We have taken the transition of elliptical laser beam in TQP along z-axis. The present study incorporates both relativistic & ponderomotive nonlinear effects. Field amplitude for elliptical beams is taken as

$$E = E_0 exp\left(-\frac{x^2}{2a^2} - \frac{y^2}{2b^2}\right) \tag{1}$$

In Eq. (1), a & b denote initial beam radii of the semi-major axis and semi-minor axis respectively. E_0 is the maximum field amplitude. For, isotropic plasmas i.e, $J = 0, \rho = 0, \mu = 0$ the expressions for Faraday's law and Ampere's law becomes

$$\nabla \times B = \frac{1}{c}\frac{\partial D}{\partial t} \tag{2}$$

$$\nabla \times E = -\frac{1}{c}\frac{\partial B}{\partial t} \tag{3}$$

In Eqs. (2) & (3), E, B & $D = \varepsilon E$ correspond to electric vector, magnetic vector and electric displacement vector respectively. One can combine Eqs. (2) & (3) to obtain wave equation for electric vector as

$$\nabla^2 E - \nabla(\nabla \cdot E) + \frac{\omega^2}{c^2}\varepsilon E = 0 \tag{4}$$

In Eq. (4), we can ignore the term $\nabla(\nabla \cdot E)$ assuming that $\frac{1}{k^2}|\nabla^2 ln \in| \ll 1$ with k being propagation vector. Here, ω & ε correspond to angular frequency and dielectric function respectively. One can re-write Eq. (4) as

$$\nabla^2 E + \frac{\omega^2}{c^2}\varepsilon E = 0 \tag{5}$$

Under the joint contribution of quantum effects, Fermi pressure, and Bohm potential, the overall dielectric function for TQP takes the form [42-43]

$$\epsilon = 1 - \frac{\omega_p^2}{\gamma\omega^2}\left(1 - \frac{k^2 v_f^2}{\omega^2} - \frac{\delta q}{\gamma}\right)^{-1} \tag{6}$$

In Eq.(6), $v_f = \sqrt{\frac{2K_B T_f}{m}}$ denotes Fermi speed, γ is relativistic factor expressed as $\gamma = (1 + \alpha EE^*)^{1/2}$, and $\delta q = \frac{4\pi^4 h^2}{m^2\omega^2\lambda^4}$ respectively. If we substitute $T_f -> 0$ in Eq. (6), then we get ϵ for cold quantum plasma (CQP). Further, setting $T_f -> 0, \frac{h}{2\pi} -> 0$ in Eq. (6), we get ϵ for classical relativistic plasma (CRP). Further, $\omega_p = \sqrt{\frac{4\pi ne^2}{m}}$ denotes plasma frequency. The electron number density gets modified due to ponderomotive force. One can express this changed number density as [42-43]

$$n = n_0 exp\left(-\frac{mc^2}{T}(\gamma - 1)\right) \tag{7}$$

The general form for ε for TQP can be expressed as

$$\varepsilon = \varepsilon_0 + \varphi(EE_0^*) \tag{8}$$

In Eq. (8), the linear and nonlinear parts of ε can be expressed as $\varepsilon_0 = 1 - \frac{\omega_p^2}{\omega_0^2}$ & $\Phi(EE^*)$ respectively. Under combined action of RP force, the nonlinear part $\Phi(EE^*)$ of the dielectric function in TQP becomes

$$\Phi(EE^*) = \frac{\omega_{p0}^2}{\omega^2}\left[1 - \frac{1}{\gamma}\left(1 - \frac{k^2 v_f^2}{\omega^2} - \frac{\delta q}{\gamma}\right)^{-1} \exp\left(-\frac{mc^2}{T}(\gamma - 1)\right)\right] \tag{9}$$

Where $\omega_{p0} = \sqrt{\frac{4\pi n_0 e^2}{m}}$.

Following [44-45], the solution of Eq. (5) can be represented as

$$E = E_0 \exp\left[i\left(\omega t - k(S+z)\right)\right] \tag{10}$$

$$E_0^2 = \frac{E_{00}^2}{f_1 f_2} exp\left[-\frac{x^2}{a^2 f_1^2} - \frac{y^2}{b^2 f_2^2}\right] \tag{11}$$

$$S = \frac{x^2}{2}\beta_1(z) + \frac{y^2}{2}\beta_2(z) + \Phi_0(z) \tag{12}$$

$$k = \frac{\omega}{c}\sqrt{\varepsilon_0} \tag{13}$$

'S' represents eikonal for the beam with elliptical cross-section, $\beta_1(z) = \frac{1}{f_1}\frac{df_1}{dz}$ and $\beta_2(z) = \frac{1}{f_2}\frac{df_2}{dz}$ denote wavefront's curvature along X & Y axes respectively, $\Phi_0(z)$ is phase shift connected with beam, f_1 & f_2 denote beam widths of beam having elliptical cross-section and satisfy following 2nd order differential equations

$$\frac{d^2 f_1}{d\eta^2} = \frac{1}{f_1^3} - \left(\frac{\omega_p a}{c}\right)^2 \frac{\alpha E_{00}^2}{2 f_1^2 f_2} \frac{exp\left(-\frac{mc^2}{T_e}\left[\sqrt{1+\frac{\alpha E_{00}^2}{f_1 f_2}}-1\right]\right)}{\left(1+\frac{\alpha E_{00}^2}{f_1 f_2}\right)^{3/2}\left(1-\frac{k^2 v_f^2}{\omega^2}-\frac{\delta q}{\sqrt{1+\frac{\alpha E_{00}^2}{f_1 f_2}}}\right)^2}\left[\left(1-\frac{k^2 v_f^2}{\omega^2}\right)+\frac{mc^2}{T_e}\sqrt{1+\frac{\alpha E_{00}^2}{f_1 f_2}}\left(1-\frac{k^2 v_f^2}{\omega^2}-\frac{\delta q}{\sqrt{1+\frac{\alpha E_{00}^2}{f_1 f_2}}}\right)\right] \tag{14}$$

$$\frac{d^2 f_2}{d\eta^2} = \frac{a^4}{b^4 f_2^3} - \left(\frac{\omega_p a}{c}\right)^2 \frac{\alpha E_{00}^2}{2 f_2^2 f_1}\left(\frac{a}{b}\right)^2 \frac{exp\left(-\frac{mc^2}{T_e}\left[\sqrt{1+\frac{\alpha E_{00}^2}{f_1 f_2}}-1\right]\right)}{\left(1+\frac{\alpha E_{00}^2}{f_1 f_2}\right)^{3/2}\left(1-\frac{k^2 v_f^2}{\omega^2}-\frac{\delta q}{\sqrt{1+\frac{\alpha E_{00}^2}{f_1 f_2}}}\right)^2}\left[\left(1-\frac{k^2 v_f^2}{\omega^2}\right)+\frac{mc^2}{T_e}\sqrt{1+\frac{\alpha E_{00}^2}{f_1 f_2}}\left(1-\frac{k^2 v_f^2}{\omega^2}-\frac{\delta q}{\sqrt{1+\frac{\alpha E_{00}^2}{f_1 f_2}}}\right)\right] \tag{15}$$

In Eqs. (14) & (15), $\eta = z/ka^2$ is dimensionless propagation distance. Here, ka^2 denotes the Rayleigh length of beam. The boundary conditions selected for numerical calculation of these equations are $f_1 = f_2 = 1$ and $\frac{df_1}{d\eta} = \frac{df_2}{d\eta} = 0$ at $\boldsymbol{\eta} = 0$.

3. EXCITATION PROCESS OF EPW

We are incorporating motion of plasma electrons only for investigating excitation mechanism of EPW. Ions are excluded from excitation dynamics due to their heavy and immobile nature. The relativistic-ponderomotive force causes density fluctuations leading to excitation process of EPW. An analysis of the EPW excitation mechanism can be carried out through the following well-known standard equations;

(a) Continuity Equation

$$\frac{\partial N_e}{\partial t} + \nabla \cdot (N_e V) = 0 \tag{16}$$

(b) Poisson's Equation

$$\nabla \cdot E = 4\pi(ZN_{oi} - N_e)e \tag{17}$$

(c) Equation of State

$$\frac{P}{N_e^{\gamma}} = Constant \tag{18}$$

(d) Equation of Motion

$$m\left[\frac{\partial V}{\partial t} + (V\cdot\nabla)\mathrm{V}\right] = -e\left[E + \frac{1}{c}V \times B\right] - 2\Gamma m V - \frac{\gamma}{N_e}\nabla P_e \tag{19}$$

Through the application of standard procedures, one arrives at the following equation for EPW:

$$-\omega_0^2 n_1 - v_{th}^2 \nabla^2 n_1 + 2\iota\Gamma\omega_0 n_1 + \omega_p^2\left[\frac{1}{\gamma}\left(1-\frac{k^2 v_f^2}{\omega^2}-\frac{h^2 k^4}{16\gamma\pi^2\omega^2 m^2}\right)^{-1}\exp\left(-\frac{mc^2}{T}(\gamma-1)\right)\right]^2 \quad n_1 \cong \frac{e}{m}(n_0\vec{\nabla}.\vec{E}) \tag{20}$$

Incorporating Eq. (11) into Eq. (20) leads to the SHG source equation

$$n_1 = \frac{en_0}{m}\frac{E_{00}}{\sqrt{f_1 f_2}} exp\left(-\frac{x^2}{2a^2 f_1^2}\right) exp\left(-\frac{y^2}{2b^2 f_2^2}\right)\left(\frac{x}{a^2 f_1^2}+\frac{y}{b^2 f_2^2}\right)\frac{1}{\left\{\omega_0^2 - k^2 v_{th}^2 - \omega_p^2\left(\frac{1}{\gamma}\left(1-\frac{k^2 v_f^2}{\omega^2}-\frac{h^2 k^4}{16\gamma\pi^2\omega^2 m^2}\right)^{-1}\exp\left(-\frac{mc^2}{T}(\gamma-1)\right)\right)^2\right\}} \tag{21}$$

4. YIELD OF SECOND HARMONICS

Excited EPW interacts with main beam leading to SHG production. With Maxwell's equations as the foundation, one can obtain SHG field equation E_2 as

$$\nabla^2 E_2 + \frac{\omega_2^2}{c^2}\varepsilon_2(\omega_2)E_2 = \frac{\omega_p^2}{c^2}\frac{n_1}{n_0}E_0 \tag{22}$$

2nd harmonic radiations have frequency represented by $\omega_2 = 2\omega_0$ and dielectric function expressed as ε_2. The expression for E_2 can be written as

$$E_2 = \frac{\omega_p^2}{c^2}\frac{n_1}{n_0}\frac{E_{00}}{\sqrt{f_1 f_2}} exp\left(-\frac{x^2}{2a^2 f_1^2}\right) exp\left(-\frac{y^2}{2b^2 f_2^2}\right)\frac{1}{(k_2^2-4k^2)} \tag{23}$$

Now, SHG yield can be obtained as

$$Y_2 = \frac{\omega_p^4 e^2 E_{00}^2}{m_0^2 c^4 f_1 f_2} exp\left(-\frac{x^2}{a^2 f_1^2}\right) exp\left(-\frac{y^2}{b^2 f_2^2}\right)\left(\frac{x}{a^2 f_1^2}+\frac{y}{b^2 f_2^2}\right)^2 \frac{1}{(k_2^2-4k^2)^2} \frac{1}{\left\{\omega_0^2-k^2 v_{th}^2-\omega_p^2\left(\frac{1}{\gamma}\left(1-\frac{k^2 v_f^2}{\omega^2}-\frac{h^2 k^4}{16\gamma\pi^2\omega^2 m^2}\right)^{-1}\exp\left(-\frac{mc^2}{T}(\gamma-1)\right)\right)^2\right\}^2} \tag{24}$$

5. DISCUSSION

Since, it is not feasible to have analytical solution of Eqs. (14), (15) and (24). So, we have employed a numerical method. In fact, we have obtained accurate as well as stable solutions through fourth-order Runge–Kutta (RK4) method. In fact, RK4 is found to be best method for solving ordinary differential equations. We have employed established parameters for exploring the behavior of solutions as follows; $\alpha E_{00}^2 = 3.0, 4.0, 5.0$, $\frac{\omega_p^2}{\omega_0^2} = 0.4, 0.5, 0.6$, $T_f = 10^7 K, 10^8 K, 10^9 K$

The right side of Eqs. (14) and (15) contains two terms with distinct physical interpretations. In both equations, 1st terms belong to divergence effect thereby causing beam spreading, while 2nd terms belong to convergence effect thereby prompting beam focusing. During laser beam propagation inside plasma, these two terms govern overall evolution of beam width. When there is domination of 1st term, then beam spreading takes place leading to increase in its beam width. When there is domination of 2nd term, then beam focusing takes place leading to decrease in its beam width. When these opposing factors are exactly equal in magnitude, then we achieve self-trapping condition, where natural diffraction phenomenon is balanced by nonlinear focusing, maintaining a constant beam width.

Figures 1(a) & 1(b) illustrate variation of f_1 & f_2 as function of the normalized distance η for different laser intensity values $\alpha E_{00}^2 = 3.0, 4.0, 5.0$ respectively. Blue, green, and red color codes are used to denote $\alpha E_{00}^2 = 3.0, 4.0,$ and 5.0 respectively. The shifting of minimum values of f_1 & f_2 towards higher η is found with increasing αE_{00}^2 parameter. This indicates that beam focusing is delayed by higher laser intensity. In other words, beam's focusing efficiency is reduced with increasing αE_{00}^2 parameter. The observed trend is found due to diminished strength of the nonlinear focusing term in relation to the diffraction term as αE_{00}^2 parameter increases.

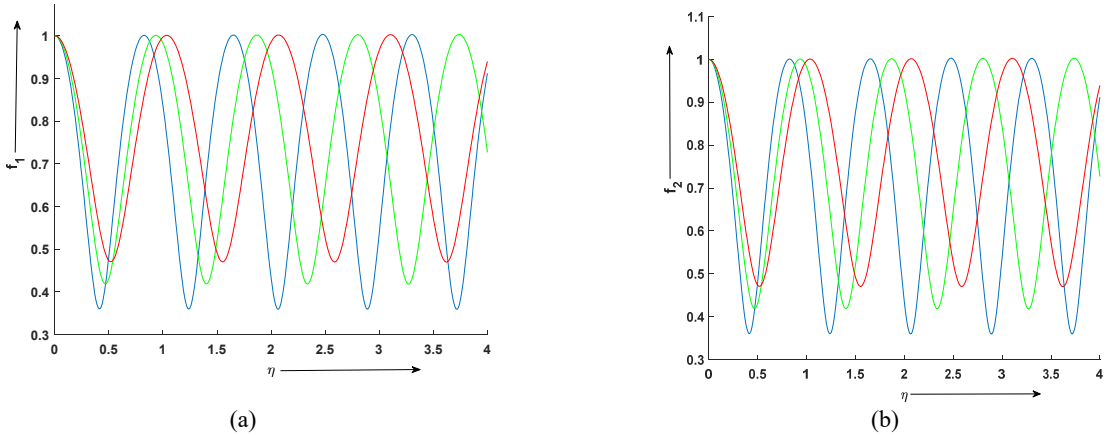

(a) (b)

Figure 1. Variation of f_1 & f_2 as function of the normalized distance η for different laser intensity values $\alpha E_{00}^2 = 3.0, 4.0, 5.0$ respectively. Blue, green, and red color codes are used to denote $\alpha E_{00}^2 = 3.0, 4.0,$ and 5.0 respectively

Figures 2(a) & 2(b) illustrate variation of f_1 & f_2 as function of the normalized distance η for different plasma density $\frac{\omega_p^2}{\omega_0^2} = 0.4, 0.5, 0.6$ respectively. Blue, green, and red color codes are used to denote $\frac{\omega_p^2}{\omega_0^2} = 0.4, 0.5,$ and 0.6 respectively. The shifting of minimum values of f_1 & f_2 towards smaller η is found with increasing $\frac{\omega_p^2}{\omega_0^2}$ parameter. This indicates that beam focusing is enhanced by higher plasma density. In other words, beam's focusing efficiency is

enhanced with increasing $\frac{\omega_p^2}{\omega_0^2}$ parameter. The observed trend is found due to diminished strength of the diffraction term in relation to the nonlinear focusing term as $\frac{\omega_p^2}{\omega_0^2}$ parameter increases.

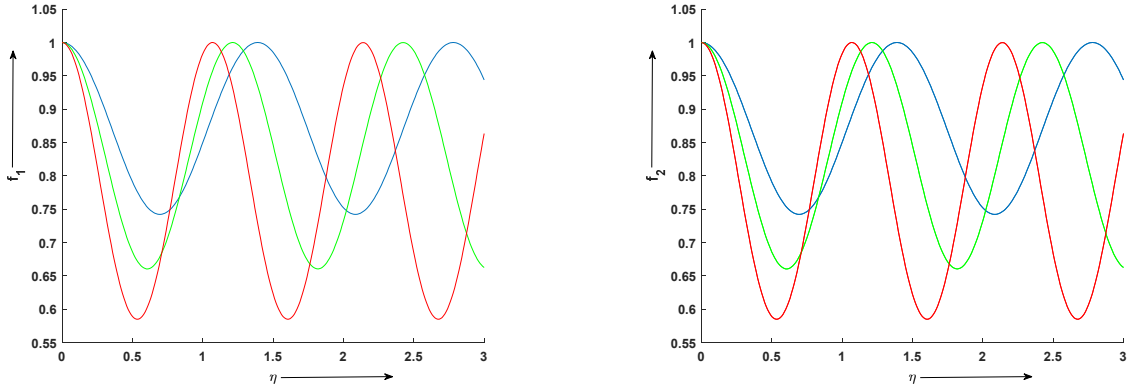

(a) (b)

Figure 2. Variation of f_1 & f_2 as function of the normalized distance η for different plasma density $\frac{\omega_p^2}{\omega_0^2} = 0.4, 0.5, 0.6$ respectively. Blue, green, and red color codes are used to denote $\frac{\omega_p^2}{\omega_0^2} = 0.4, 0.5,$ and 0.6 respectively

Figures 3(a) & 3(b) illustrate variation of f_1 & f_2 as function of the normalized distance η for different Fermi temperature $T_f\left(T_f = 10^7K, 10^8K, 10^9K\right)$ respectively. Blue, green, and red color codes are used to denote $T_f = 10^7K, 10^8K, 10^9K$ respectively. The shifting of minimum values of f_1 & f_2 towards smaller η is found with increasing T_f parameter. This indicates that beam focusing is enhanced by higher Fermi temperature. The higher Fermi temperature increases the Fermi pressure and electron degeneracy, leading to stronger plasma density redistribution. This enhances refractive index gradient and weakens diffraction spreading. As a result, nonlinear focusing effect dominates, causing the beam to self-focus more efficiently with increasing T_f.

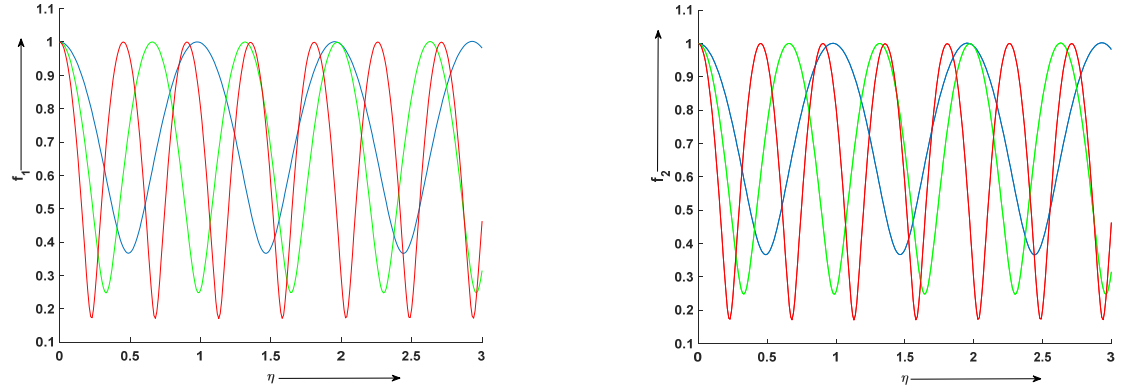

(a) (b)

Figure 3. Variation of f_1 & f_2 as function of the normalized distance η for different Fermi temperature $T_f\left(T_f = 10^7K, 10^8K, 10^9K\right)$ respectively. Blue, green, and red color codes are used to denote $T_f = 10^7K, 10^8K, 10^9K$ respectively

Figures 4(a) & 4(b) illustrate variation of f_1 & f_2 as function of the normalized distance η for different plasma regimes. Blue and red color codes are used for TQP and CRP cases. The more shifting of minimum values of f_1 & f_2 towards smaller η is found in TQP case as compared to CRP case. This indicates that beam focusing is enhanced by quantum effects. In other words, beam's focusing efficiency is enhanced with quantum contributions. Actually, quantum effects make the plasma respond more efficiently to intensity variations of laser beam, thereby enhancing nonlinear refractive index and promoting stronger self-focusing.

Figure 5 illustrates variation of SHG yield Y_2 as function of the normalized distance η for different laser intensity values $\alpha E_{00}^2 = 3.0, 5.0$ respectively. Blue and red color codes are used to denote $\alpha E_{00}^2 = 3.0$ and 5.0 respectively. It is found that the yield Y_2 gets reduced with decrease in αE_{00}^2. This reduction is attributed to the weaker self-focusing of the pump beam at higher αE_{00}^2 values. Since, magnitude of yield Y_2closely linked with effect of self-focusing, an increase in αE_{00}^2 leads to weaker self-focusing, thereby resulting in a reduced Y_2 value.

Figure 6 illustrates variation of SHG yield Y_2 as function of the normalized distance η for different plasma density $\frac{\omega_p^2}{\omega_0^2} = 0.4, 0.6$ respectively. Blue and red color codes are used to denote $\frac{\omega_p^2}{\omega_0^2} = 0.4$ and 0.6 respectively. It is found that

the yield Y_2 gets enhanced with increase in $\frac{\omega_p^2}{\omega_0^2}$. This reduction is attributed to the stronger self-focusing of the pump beam at higher $\frac{\omega_p^2}{\omega_0^2}$ values. Since, magnitude of yield Y_2closely linked with effect of self-focusing, an increase in $\frac{\omega_p^2}{\omega_0^2}$ leads to stronger self-focusing, thereby resulting in higher Y_2 value.

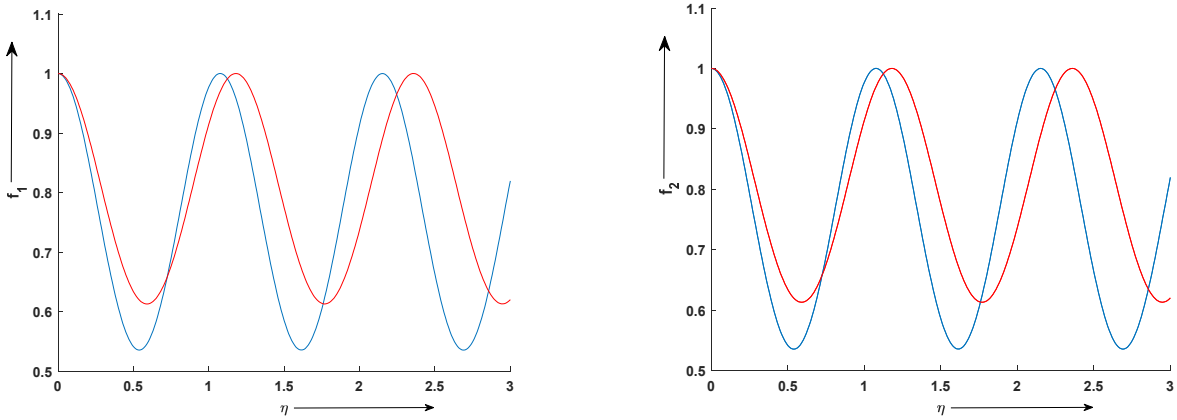

(a) (b)

Figure 4. Variation of f_1 & f_2 as function of the normalized distance η for different plasma regimes. Blue and red color codes are used for TQP and CRP cases

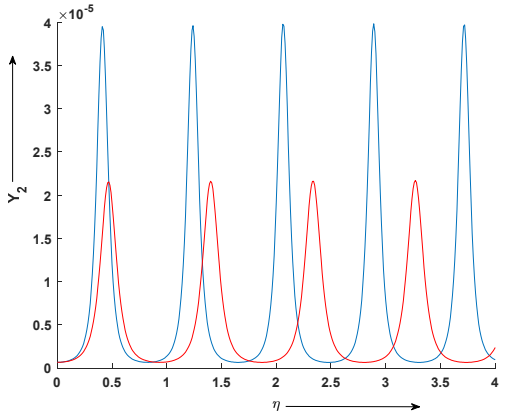

Figure 5. Variation of SHG yield Y_2 as function of the normalized distance η for different laser intensity values $\alpha E_{00}^2 = 3.0, 5.0$ respectively. Blue and red color codes are used to denote $\alpha E_{00}^2 = 3.0$ and 5.0 respectively

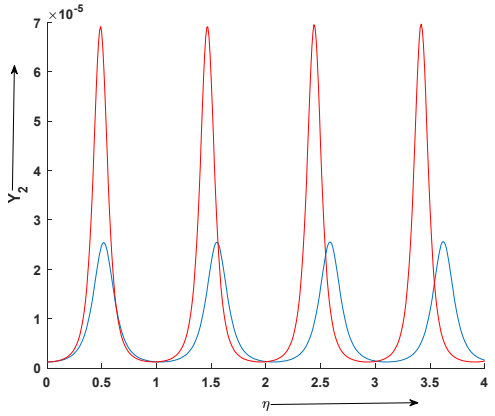

Figure 6. Variation of SHG yield Y_2 as function of the normalized distance η for different plasma density $\frac{\omega_p^2}{\omega_0^2} = 0.4, 0.6$ respectively. Blue and red color codes are used to denote $\frac{\omega_p^2}{\omega_0^2} = 0.4$ and 0.6 respectively

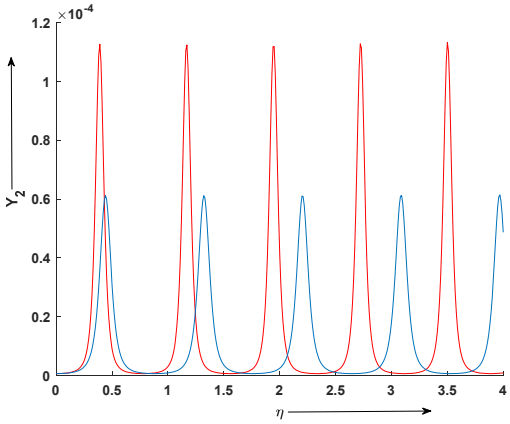

Figure 7. Variation of SHG yield Y_2 as function of the normalized distance η for different Fermi temperature $T_f(T_f = 10^7K, 10^9K)$ respectively. Blue and red color codes are used to denote $T_f = 10^7K$ and 10^9K respectively

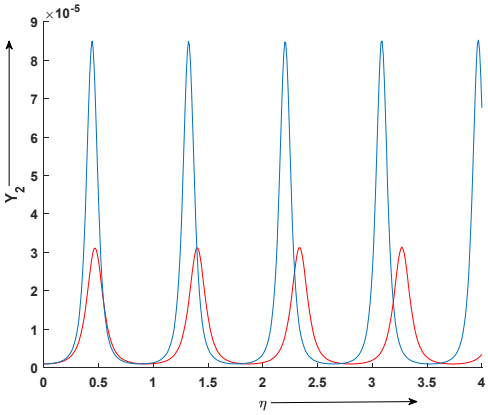

Figure 8. Variation of SHG yield Y_2 as function of the normalized distance η for different plasma regimes. Blue and red color codes are used to denote TQP and CRP respectively

Figure 7 illustrates variation of SHG yield Y_2 as function of the normalized distance η for different Fermi temperature $T_f(T_f = 10^7K, 10^9K)$ respectively. Blue and red color codes are used to denote $T_f = 10^7K$ and 10^9K respectively. It is found that the yield Y_2 gets enhanced with increase in T_f. This reduction is attributed to the stronger self-focusing of the pump beam at higher T_f values. Since, magnitude of yield Y_2closely linked with effect of self-focusing, an increase in T_f leads to stronger self-focusing, thereby resulting in higher Y_2 value.

Figure 8 illustrates variation of SHG yield Y_2 as function of the normalized distance η for different plasma regimes. Blue and red color codes are used to denote TQP and CRP respectively. In TQP, the value of Y_2 is significantly enhanced in comparison to CRP case. This enhancement is directly linked with process of self-focusing, as magnitude of Y_2 is strongly affected by self-focusing phenomenon. In Figures 7 & 8, beam focusing is found to be more dominant in TQP case followed by CRP case. Similar behavior is found for present study as well.

6. CONCLUSIONS

The current study explores SHG of elliptical laser beam in TQP. We have taken together relativistic and ponderomotive (RP) forces in current study. The results drawn from this study are mentioned below;

(1) There is increment in tendency of beam to focus with increase in $\frac{\omega_p^2}{\omega_0^2}$ and T_f parameters.
(2) The increase in αE_{00}^2 tends to reduction in beam focusing tendency.
(3) With inclusion of quantum effects, the beam exhibits better focusing characteristics.
(4) There is an enhancement in SHG yield Y_2 with enhancement in plasma density, Fermi temperature and with lowering in beam intensity values.
(5) The magnitude of Y_2 gets enhanced with inclusion of quantum effects.

These results are extremely useful for researchers exploring laser-plasma interaction physics.

ORCID

Keshav Walia, https://orcid.org/0000-0001-9547-3027; **Kulkaran Singh,** https://orcid.org/0000-0002-5982-8983
Deepak Tripathi, https://orcid.org/0000-0001-9945-4069; **Anuj Vijay,** https://orcid.org/0000-0001-6610-3844

REFERENCES

[1] S.C. Wilks, J.M. Dawson, W.B. Mori, T. Katsouleas, and M.E. Jones, "Photon accelerator," Phys. Rev. Lett. **62**, 2600 (1989). https://doi.org/10.1103/physrevlett.62.2600
[2] K.A. Brueckner, and S. Jorna, "Laser-driven fusion," Rev. Mod. Phys. **46**, 325(1974). https://doi.org/10.1103/RevModPhys.46.325
[3] J. Faure, Y. Glinec, A. Pukhov, S. Kiselev, S. Gordienko, E. Lefebvre, J.P. Rousseau, *et al*., "A laser-plasma accelerator producing monoenergetic electron beams," Nature, **431**, 541(2004). https://doi.org/10.1038/nature02963
[4] P.E. Young, H.A. Baldis, R.P. Drake, E.M. Campbell, and K.G. Estabrook, "Direct Evidence of Ponderomotive Filamentation in a Laser-Produced Plasma," Phys. Rev. Lett. **61**, 2336 (1988). https://doi.org/10.1103/physrevlett.61.2336
[5] K. Walia, "Self-focusing of q-Gaussian beam in unmagnetized plasma and its impact on second harmonic generation," Optik, **277**, 170681 (2023). https://doi.org/10.1016/j.ijleo.2023.170681
[6] A. Singh, and K. Walia, "Relativistic self-focusing and self-channeling of Gaussian laser beam in plasma," Appl. Phys. B Lasers Opt. **101**, 617 (2010). https://doi.org/10.1007/s00340-010-4230-4
[7] P.B. Corkum, C. Rolland, and T. Rao, "Supercontinuum Generation in Gases," Phys. Rev. Lett. **57**, 2268 (1986). https://doi.org/10.1103/physrevlett.57.2268
[8] P. Sprangle, E. Esarey, and J. Krall, "Laser driven electron acceleration in vacuum, gases, and plasmas," Phys. Plasmas, **3**, 2183 (1996). https://doi.org/10.1063/1.871673
[9] W.F. Utlaut, and R. Cohen, "Modifying the ionosphere with intense radio waves," Science, **174**, 245(1971). https://doi.org/10.1126/science.174.4006.245
[10] K. Walia, "Nonlinear Interaction of High Power Elliptical Laser Beam with Cold Collisionless Plasma," J. Fusion Energ. **35**, 446 (2016). https://doi.org/10.1007/s10894-016-0059-0
[11] P. Kaw, G. Schmidt, and T. Wilcox, "Filamentation and trapping of electromagnetic radiation in plasmas," Phys. Fluids, **16**, 1522 (1973). https://doi.org/10.1063/1.1694552
[12] A. Bers, I.P. Shkarofsky, and M. Shoucri, "Relativistic Landau damping of electron plasma waves in stimulated Raman scattering," Physics of Plasmas. **16**, 022104 (2009). https://doi.org/10.1063/1.3073678
[13] D. Tripathi, T. Singh, A. Vijay, and K. Walia, "Second Harmonic Generation of q-Gaussian Laser Beam in Thermal Quantum Plasma," J. Contemp. Phys. **60**, 171(2025). https://doi.org/10.1134/s1068337225700574
[14] K. Walia, "Propagation characteristics of a high-power beam in weakly relativistic-ponderomotive thermal quantum plasma," Commun. Theor. Phys. **75**, 95501 (2023). https://doi.org/10.1088/1572-9494/accf82
[15] K. Walia, "Nonlinear interaction of high power beam in weakly relativistic and ponderomotive cold quantum plasma," Optik, **219**, 165040 (2020). https://doi.org/10.1016/j.ijleo.2020.165040
[16] C. Deutsch, A. Bret, M.C. Firpo, L. Gremillet, E. Lefebvre, and A. Lifschitz, "Onset of coherent electromagnetic structures in the relativistic electron beam deuterium-tritium fuel interaction of fast ignition concern," Laser Part. Beams, **26**, 157 (2008). https://doi.org/10.1017/s0263034608000189
[17] D. Tripathi, S. Kaur, A. Vijay, and K. Walia, "Nonlinear Dynamics of q-Gaussian Laser Beam in Collisional Plasma: Effect of Linear Absorption," J. Contemp. Phys. **60**, 16 (2025). https://doi.org/10.1134/s1068337225700409
[18] G.A. Askaryan, "Effects of the Gradient of a Strong Electromagnetic Beam on Electrons and Atoms," JETP, **15**, 1088 (1962).
[19] U. Teubner, and P. Gibbon, "High-order harmonics from laser-irradiated plasma surfaces," Rev. Mod. Phys. **8**, 445 (2009). https://doi.org/10.1103/revmodphys.81.445

[20] J.A. Stamper, R.H. Lehmberg, A. Schmitt, M.J. Herbst, F.C. Young, J.H. Gardner, and S.P. Obenschain, "Evidence in the second-harmonic emission for self-focusing of a laser pulse in a plasma," Phys. Fluids, **28**, 2563–2569 (1985). https://doi.org/10.1063/1.865264
[21] C. Winterfeldt, C. Spielmann, and G. Gerber, "Optimal control of high-harmonic generation," Rev. Mod. Phys. **80**, 117 (2008). https://doi.org/10.1103/revmodphys.80.117
[22] L. Nugent-Glandorf, M. Scheer, D.A. Samuels, A.M. Mulhisen, E.R. Grant, X. Yang, V.M. Bierbaum, and S.R. Leone, "Ultrafast Time-Resolved Soft X-Ray Photoelectron Spectroscopy of Dissociating Br," Phys. Rev. Lett. **87**, 193002 (2001). https://doi.org/10.1103/physrevlett.87.193002
[23] R.I. Tobey, M.E. Siemens, O. Cohen, M.M. Murnane, H.C. Kapteyn, and K.A. Nelson, "Ultrafast extreme ultraviolet holography: dynamic monitoring of surface deformation," Opt. Lett. **32**, 286-288 (2007). https://doi.org/10.1364/OL.32.000286
[24] M. Bauer, C. Lei, K. Read, R. Tobey, J. Gland, M.M. Murnane, and H.C. Kapteyn, "Direct observation of Surface Chemistry Using Ultrafast Soft-X-Ray Pulses," Phys. Rev. Lett. **87**, 025501 (2001). https://doi.org/10.1103/physrevlett.87.025501
[25] M.S. Sodha, J.K. Sharma, D.P. Tewari, R.P. Sharma, and S.C. Kaushik, "Plasma wave and second harmonic generation," Plasma Phys. **20**, 825 (1978). https://doi.org/10.1088/0032-1028/20/8/007
[26] J. Parashar, and H.D. Pandey, "Second-harmonic generation of laser radiation in a plasma with a density ripple," IEEE Trans. Plasma Sci. **20**, 996 (1992). https://doi.org/10.1109/27.199564
[27] F. Brunel, "Harmonic generation due to plasma effects in a gas undergoing multiphoton ionization in the high-intensity limit," J. Opt. Soc. Am. B, **7**, 521 (1990). https://doi.org/10.1364/josab.7.000521
[28] K. Singh, and K. Walia, "Second Harmonic Generation of High Power Cosh-Gaussian Beam in Thermal Quantum Plasma: Effect of Relativistic and Ponderomotive Nonlinearity," J. Contemp. Phys. **59**, 244 (2024). https://doi.org/10.1134/s1068337224700488
[29] K. Singh, and K. Walia, "Influence of Self-Focused Elliptical Laser Beam on Second Harmonic Generation in Cold Quantum Plasma," J. Contemp. Phys. **59**, 154 (2024). https://doi.org/10.1134/s1068337224700300
[30] K. Walia, N. Mehra, and S. Pandit, "Propagation Characteristics of q-Gaussian Laser Beam in Cold Collisionless Plasma," J. Contemp. Phys. **59**, 378 (2024). https://doi.org/10.1134/s1068337225700203
[31] K. Walia, "Effect of self-focusing of elliptical laser beam on second harmonic generation in collisionless plasma," Optik, **127**, 6618 (2016). https://doi.org/10.1016/j.ijleo.2016.04.043
[32] S. Kaur, A.K. Sharma, and H.A. Salih, "Resonant second harmonic generation of a Gaussian electromagnetic beam in a collisional Magnetoplasma," Phys. Plasmas, **16**, 042509 (2009). https://doi.org/10.1063/1.3135230
[33] N.H. Burnett, H.A. Baldis, M.C. Richardson, and G.D. Enright, "Harmonic generation in CO_2 laser target interaction," Appl. Phys. Lett. **31**, 172 (1977). https://doi.org/10.1063/1.89628
[34] R.L. Carman, D.W. Forslund, and J.M. Kindel, "Visible Harmonic Emission as a Way of Measuring Profile Steepening," Phys. Rev. Lett. **46**, 29 (1981). https://doi.org/10.1103/physrevlett.46.29
[35] T. Singh, and K. Walia, "Impact of High-Power Cosh-Gaussian Beam on Second Harmonic Generation in Collisionless Magnetoplasma," J. Contemp. Phys. **59**, 254 (2024). https://doi.org/10.1134/s106833722470049x
[36] N. Kant, and A.K. Sharma, "Effect of pulse slippage on resonant second harmonic generation of a short pulse laser in a plasma," J. Phys. D: Appl. Phys. **37**, 998 (2004).
[37] E. Ozbay, "Plasmonics: merging photonics and electronics at nanoscale dimensions," Science, **311**, 189 (2006). https://doi.org/10.1126/science.1114849
[38] L. Wei, and Y. Wang, "Quantum ion-acoustic waves in single-walled carbon nanotubes studied with a quantum hydrodynamic model," Phys. Rev. B, **75**, 193407 (2007). https://doi.org/10.1103/physrevb.75.193407
[39] G. Shpatakovskaya, "Semiclassical model of a one-dimensional quantum dot," J. Exp, Theor. Phys. **102**, 466 (2006). https://doi.org/10.1134/s1063776106030095
[40] Z. Chunyang, L. Zhanjun, Z. Shao-ping, and H. Xiantu, "Self-Focusing of High-Power Laser Beam through Plasma," J. Plasma Fusion Res. **6**, 333 (2004).
[41] A.V. Andreev, "Self-consistent equations for the interaction of an atom with an electromagnetic field of arbitrary intensity," J. Exp, Theor. Phys. Lett. **72**, 238 (2000). https://doi.org/10.1134/1.1324018
[42] D. Lai, "Matter in strong magnetic fields," Rev. Mod. Phys. **73**, 629 (2001). https://doi.org/10.1103/revmodphys.73.629
[43] Y. Jung, and I. Murakami, "Quantum effects on magnetization due to ponderomotive force in cold quantum plasmas," Phys. Lett. A, **373**, 969 (2009). https://doi.org/10.1016/j.physleta.2009.01.024
[44] M.S. Sodha, A.K. Ghatak, and V.K. Tripathi, *Progress in Optics*, (North Holland, Amsterdam, 1976).
[45] S.A. Akhmanov, A. Sukhorukov, and R. Khokhlov, "Self-focusing and diffraction of light in a nonlinear medium," Sov. Phys. Uspekhi, **10**, 609 (1968).

ГЕНЕРАЦІЯ ДРУГОЇ ГАРМОНІКИ ПОТУЖНОГО ЕЛІПТИЧНОГО ПРОМЕНЯ В ТЕПЛОВІЙ КВАНТОВІЙ ПЛАЗМІ

Кешав Валья[1], Кулкаран Сінгх[1], Анудж Віджай[2], Діпак Тріпаті[3]
[1]Кафедра фізики, Університет DAV, Джаландхар, Індія
[2]Кафедра фізики, Університет GLA, Матхура (У.П.), Індія-281406
[3]Кафедра фізики, USAR, Університет Гуру Гобінд Сінгх Індрапрастха, кампус Східного Делі, Делі, Індія-110032

У цьому дослідженні досліджується генерація другої гармоніки еліптичного променя в тепловій квантовій плазмі (TQP) шляхом об'єднання релятивістсько-пондеромоторних (RP) сил. Спостерігається зміна маси електронів через силу РП, що призводить до зміни профілю фонової густини в напрямку, поперечному до основного променя. Основний промінь самофокусується. Встановлені градієнти густини збуджують електронну плазмову хвилю (ЕПХ) на частоті хвилі накачування. Збуджена ЕПХ додатково взаємодіє з хвилею накачування, створюючи генерацію другої гармоніки (ГДГ). Для отримання звичайних диференціальних рівнянь 2-го порядку для великої та малої напівосей еліптичного променя з нормалізованою дальністю поширення та ефективністю других гармонік використовуються широко прийняті наближення ВКБ та параксіальна теорія. Крім того, також досліджується вплив зміни відповідних параметрів лазерної плазми на динаміку перетяжки променя та ефективність других гармонік.

Ключові слова: *еліптичний поперечний переріз; квантова плазма; сила рп; електронна плазмова хвиля; параксіальна теорія; наближення ВКБ*

East European Journal of Physics. 4. 550-554 (2025)
DOI:10.26565/2312-4334-2025-4-57 ISSN 2312-4334

ESTIMATING THE TOTAL DOSE OF X-RAY BREMSSTRAHLUNG FROM A POWERFUL PULSED SOURCE DRIVEN BY A HIGH-CURRENT ELECTRON BEAM

A.B. Batrakov*, S.I. Fedotov, I.N. Onishchenko, E.G. Glushko, A.M. Gorban, O.L. Rak, O.V. Nevara, Yu.N. Volkov
National Science Center «Kharkiv Institute of Physics and Technology», Kharkiv, Ukraine
**Corresponding Author E-mail: a.batrakov67@gmail.com*
Received August 3, 2025; revised October 27, 2025; accepted November 18, 2025

The paper reports the results of measuring the total dose of X-ray bremsstrahlung from a powerful X-ray source based on the high-current pulsed direct-action electron accelerator "Temp-B". The parameters of the high-current, tubular relativistic electron beam from the accelerator were as follows**:** energy 600 keV, current 13.5 kA, and pulse duration 1.0 μs. Using the pulsed magnetic field of a solenoid, the electron beam generated in a magnetically isolated diode was transported over a 55 cm distance toward the molybdenum converter. An auxiliary coil, connected in series with the solenoid, was placed adjacent to it to provide the desired magnetic field in the converter region and avoid beam losses. The methodology for determining the total dose of the produced X-ray bremsstrahlung is described. Polycrystalline detectors were used for measuring the X-ray bremsstrahlung dose. They were located 80 mm behind the converter in the polar plane, with a 20° separation. Measurements of the dose distribution over the polar angle showed symmetrical distributions of the radiation at both polar and azimuthal angles relative to the axis. Taking into account such symmetry and the fact that the electron beam radiates solely into the forward hemisphere, the integration over the entire sphere can be reduced to integration over just a fraction of 1/8 of the spherical surface, thereby reducing the required number of sensors. The experimentally obtained value of the total dose of the X-ray bremsstrahlung is 388.5 Gy per single pulse of the accelerator current, which is concentrated in a 120° cone in the direction of the beam movement.
Keywords: *High-current pulsed direct-action electron accelerator*; *Relativistic electron beam*; *Converter*; *X-ray bremsstrahlung, Thermo-luminescent detector*; *Intensity, Dose.*
PACS: 41.50.+ h; 41.60.Gr

INTRODUCTION

Charged-particle accelerators and gamma-emitting isotopes are widely used to produce powerful fluxes of hard X-ray radiation. Isotopic sources are structurally simpler, while accelerator-based sources deliver higher radiation powers, which is essential for their integration into high-performance production lines. To generate bremsstrahlung X-rays with relativistic electron beams (REBs), two types of converters are used in the form of transmitting and reflecting targets, which expands the possibilities of controlling the radiation flux. The hard X-ray radiation generated by REBs is widely used in industrial processes, security systems, and non-destructive testing technologies due to its great penetration depth and high spatial resolution. In addition, there has been recent interest in the use of powerful pulsed X-ray sources in medicine [3]. Currently, extensive work is underway on both the creation of new X-ray sources based on direct-action electron accelerators [4 - 7] and the improvement of methods for transporting and controlling the X-ray flux [8]. A feature of most such installations is the placement of the converter directly at the output of the accelerating diode, or its manufacture as a diode element. However, sometimes it is desirable to place the converter remotely from the accelerator, which requires transporting the electron beam over a considerable distance. At NSC "KIPT", for quite some time, work has been carried out on the creation and operation of appropriate radiation-beam complexes [1, 9 - 11]. This work presents the design of a radiation-beam complex for the development of a powerful bremsstrahlung X-ray source based on the high-current pulsed electron accelerator "Temp-B," with the converter located remotely from the magnetically isolated accelerator diode, and the results of measuring the total radiation dose per pulse.

EXPERIMENTAL SETUP

The accelerator "Temp-B" consists of the following main elements: a pulsed voltage generator (PVG), a magnetically isolated vacuum diode, a chamber for REB transport, a converter, a magnetic system, and devices for recording accelerator parameters and X-ray bremsstrahlung radiation. The PVG provides a 600 kV pulse with a duration of 1.0 μs. To reduce the inductance of the PVG and the current load on the discharge electrodes, a design consisting of 4 parallel Marx generators is implemented, placed in a metal tank filled with transformer oil. In this case, the current load on the spark gap is reduced by 4 times, and the total inductance of the PVG is 1.5 times smaller. To reduce the total number of spark gaps by 2, a bipolar charging system is used (±100 kV instead of a unipolar 100 kV system) with two capacitors in series per stage. This successfully solves the problem of simultaneously switching the generators onto a standard load.

The source of the high-current REB in the accelerator is a magnetically isolated vacuum diode with an explosive-emission cathode. The design of the vacuum diode with magnetic isolation is shown in Fig. 1.

Cite as: A.B. Batrakov, S.I. Fedotov, I.N. Onishchenko, E.G. Glushko, A.M. Gorban, O.L. Rak, O.V. Nevara, Yu.N. Volkov, East Eur. J. Phys. 4, 550 (2025), https://doi.org/10.26565/2312-4334-2025-4-57

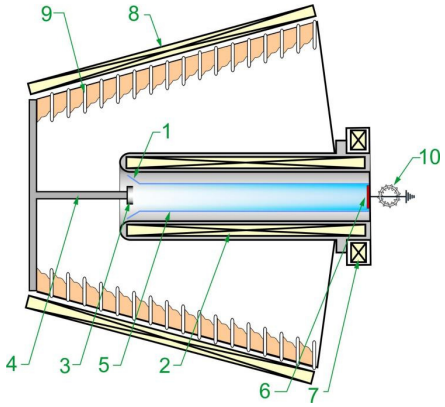

Figure 1. Scheme of the diode and the chamber for beam transport

It is assembled according to a scheme in which the anode (1) is a conical insert connected to the beam transport chamber (5). The use of an anode insert allows for electron flow parallel to the uniform external magnetic field in the drift chamber. The magnetic isolation of such a diode is carried out by the magnetic field of the left edge of the solenoid (2). The sharp front edge of the tubular cylindrical cathode (3), of a 60 mm diameter, mounted on the cathode holder (4), is located in the region of the increasing magnetic field of the solenoid (2),

The beam-transport chamber (5) is a thin-walled stainless steel cylinder with an inner diameter of 70 mm and a length of 550 mm. It connects the diode to the converter region (6). The chamber is placed inside the solenoid of the guiding magnetic field (2), which has 188 turns arranged in two layers, with a 150 mm diameter. For the current pulse of 2 kA and duration of 10 ms feeding the solenoid, the magnetic field strength in the beam transport chamber is 640 kA/m. Furthermore, an auxiliary coil (7), which has 34 turns in two layers at a diameter of 250 mm and is connected in series with solenoid, is located in the interaction chamber region. It is designed to provide the necessary magnetic field strength in the converter region. The calculated and experimentally implemented magnetic field parameters ensured magnetic insulation and the transport of the electron beam with a current of 13.5 kA and an energy of 600 keV to the converter without losses. Outside the vacuum diode chamber, a conical, two-layer insulating magnetic field coil (8) with 208 turns is located. It is powered by a separate source and is intended to increase the electrical strength of the accelerating column insulator (9). A Rogowski coil (10) was used to measure the beam current.

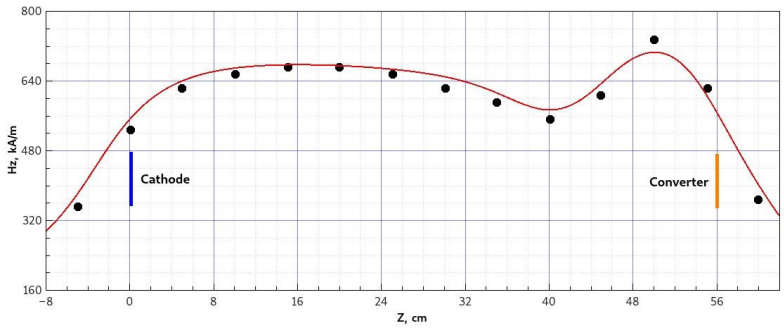

Figure 2. Profile of the longitudinal magnetic field in the chamber for beam transporting

Fig. 2 shows a graph of the calculated longitudinal magnetic field profile (solid curve) in the beam transport chamber. It shows the results of summing the fields from the solenoid, the auxiliary coil, and the conical insulating field coil. On the graph, the origin of coordinates is aligned with the cathode's end face, and the converter is located 56 cm from the cathode. Experimentally measured magnetic field strengths are marked with dots. To calculate the magnetic field strength of the solenoid and a combination of several coils, they are considered as a set of ring currents, and the magnetic field at a given point is determined by the total contribution of the magnetic fields of all ring currents, according to [12]. In this case, all currents are assumed to be stationary, and the possible influence of other structural elements is not considered. The calculations are consistent with the measurements within the apparatus's 5% error.

EXPERIMENTAL RESULTS

In Fig. 3, the voltage applied to the magneto-isolated diode is shown. A 60 mm-diameter, one mm-thick tubular cathode was used to produce a relativistic electron beam. The beam, with a diameter of 53 mm, energy of 600 keV, current of 13.5 kA, and duration of 1 μs, was delivered from the diode by the magnetic field to a molybdenum converter of a 0.5 mm wall thickness. Figure 4 shows a photograph of the beam imprint on the surface of the molybdenum converter after two electron beam pulses. The good repeatability of the imprints should be noted. At a converter plate thickness of 0.5 mm, signs of the onset of its destruction process are clearly visible.

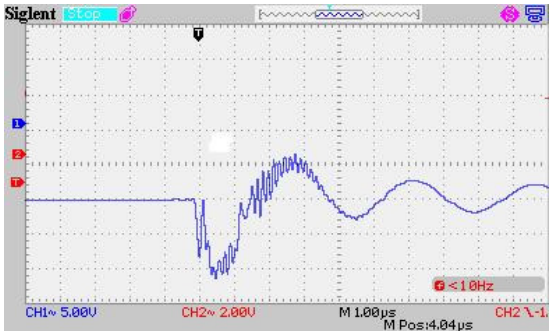

Figure 3. Oscillogram of the voltage across the diode

Figure 4. Electron beam imprint on the surface of a molybdenum converter

Thermo-luminescent detectors (TLDs) of types MTS-6 and MTS-7 [14] were used to determine the angular distribution of the X-ray bremsstrahlung radiation resulting from the interaction of the relativistic electron beam with the converter. These detectors are polycrystalline LiF "tablets", doped with Mg and Ti atoms with a dose measurement range from 10^{-4} Gy to 1 Gy in the X-ray and gamma radiation energy range, specifically from 20 keV to 6 MeV. Their diameter is 3.5 mm, area equals 9.62 mm^2, and thickness is 2 mm. Such detectors allow the measurement, with appropriate calibration, of absorbed doses over a wide energy interval. The measured results were processed using the automatic device RADOS TLD RE-2000 [13], which automatically reads the values stored in the dosimeters. The X-ray detectors were placed 8 cm from the converter and positioned at 20-degree intervals relative to the electron beam axis. A total of 5 detectors were used (Fig. 5).

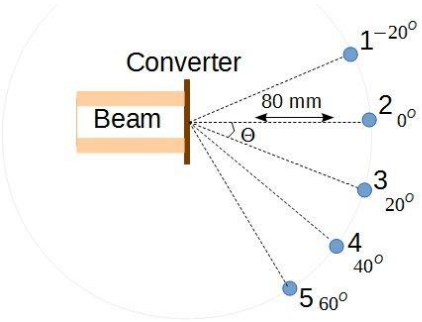

Figure 5. Disposition of the X-ray radiation detectors

Table 1 presents the results of measuring the generated dose absorbed by the detector in a series of two electron beam pulses. The detector numbers correspond to those indicated in Fig. 5.

Table 1. Results of measuring the generated dose, absorbed by the detector

Detector Number	1	2	3	4	5
Angle relative to the beam axis, degrees (°)	-20^0	0^0	20^0	40^0	60^0
Absorbed Dose (from RE-2000 reader), mGy	403.643	417.884	410.272	211.88	181.332

The measurement results for detectors 1 and 3 are approximately the same, indicating a symmetrical distribution of X-ray radiation relative to the polar angle Θ in the azimuthal plane where the detectors are located. For angles greater than 60^0, it was impossible to place the detectors due to structural reasons of the source. Nevertheless, a decrease in dose with increasing angle is observed, such that the radiation in the 120^{0}cone is close to the radiation dose in the forward hemisphere, and therefore to the total dose of the source, as the beam only radiates into the forward hemisphere.

To measure the total radiation dose in the forward hemisphere, it is sufficient to measure its distribution over a spherical surface of a given radius. The total X-ray dose was calculated as follows. Considering that the element of area *dS* of a sphere with radius *r* is:

$$dS = r^2 sin\Theta d\Theta d\varphi,$$

where Θ and ϕ are the polar and azimuthal angles, respectively, the dose value *D*, distributed over the hemisphere, is:

$$D = \int_0^{2\pi} d\varphi \int_0^{\pi/2} d(\Theta) r^2 sin\Theta d\Theta. \quad (1)$$

Here, $d(\Theta)$ is the surface dose density on the sphere of radius *r*. All detectors are placed in the polar plane. Since $d(\Theta)$ depends only on Θ, and the integration over φ simply gives a factor of 2π, due to the azimuthal symmetry of the radiation distribution, Eq. (1) can be written as:

$$D = 2\pi r^2 \int_0^{\pi/2} d(\Theta) sin\Theta d\Theta. \quad (2)$$

The dose d_i, measured by a detector of an area $S = 9.62mm^2$ is a discrete estimate $d(\Theta) = d_i/S$.

To calculate the total dose, we use the trapezoidal rule. In our case, the last detector in the row is placed at an angle of 60°. Therefore, we estimate the dose within the limits (in degrees) $-60 \leqslant \Theta \leqslant 60$, such that

$$D \simeq \frac{2\pi r^2}{S} \cdot \frac{\pi/2}{3}\left[\frac{f_2+f_5}{2} + f_3 + f_4\right] = 2188.685 \cdot \left[\frac{f_2+f_5}{2} + f_3 + f_4\right] \simeq 777.058Gy$$

The magnitudes assumed by members of the integrand in (2) are given in Table 2.

Table 2. Initial data for calculating the radiation dose.

Detector Number	Angle, °	Dose in detector d_I,, mGy	$f_i=d_I\ sin\ \Theta$
2	0^0	417.884	0
3	20^0	410.272	140.321
4	40^0	211.88	136.194
5	60^0	181.332	157.038

Thus, the dose of X-ray radiation limited by the source measurement angle of 120°, which is close to the full dose of radiation from the source, per one electron beam pulse with an energy of 600 kV, a current of 13.5 kA and a duration of 1 μs, is D=777/2=388.5 Gray/pulse.

CONCLUSIONS

The doses of X-ray bremsstrahlung radiation, realizable per one current pulse from the high-current "Temp-B" accelerator, have been estimated for a variety of angles relative to the direction of the relativistic electron beam's motion.

The magnitude of the total radiation dose has been estimated. For the beam of a 600 keV energy, a 13.5 kA current magnitude, and a 1 μs duration, the total radiation dose from the source was 388,5 Gy/pulse.

As found, most of the X-ray radiation is confined within a 120° cone about the beam propagation direction.

ORCID

A.B. Batrakov, https://orcid.org/0000-0001-6158-2129; **S.I. Fedotov**, https://orcid.org/0000-0002-7216-0615
I.N. Onishchenko, https://orcid.org/0000-0002-8025-5825; **E.G. Glushko,** https://orcid.org/0000-0001-8398-9915
A.M. Gorban, https://orcid.org/0000-0001-8303-0739; **O.L. Rak**, https://orcid.org/0009-0000-6683-1235
O.V. Nevara, https://orcid.org/0009-0009-3929-082X; **Yu.N. Volkov**, https://orcid.org/0009-0002-0557-8090

REFERENCES

[1] Yu.V. Tkach, V.T. Uvarov, N.P. Gadetskiy, *et. al*. "Investigation of a high-current diode with magnetic isolation of microsecond duration," in: *VIII All-Union Seminar on Linear Accelerators*, Abstracts of reports. (NSC KIPT, Kharkiv, 1983). p.107, (in Russian)

[2] T.C. Genoni, and R.B. Miller, "Limiting currents in shielded source configurations," Physics of Fluids, **24**(7) 1397–1398 (1981).

[3] H.S.Li, R. Tang, H.S. Shi, *et al*. "Ultra-high dose rate radiotherapy overcomes radioresistance in head and neck squamous cell carcinoma," Sig. Transduct. Target Ther. **10**(82), (2025). https://doi.org/10.1038/s41392-025-02184-0

[4] H. Shi, C. Zhang, P. Zhang, Y. Wang, W. Yuan, L. Chen, X. Li, J. Wu, and A. Qiu, "Sub-millimeter hard x-ray source based on wire-shorted low-impedance rod pinch diode," IEEE Trans. Plasma Sci. **51**(4), 1142–1149 (2023). https://doi.org/10.1109/tps.2023.3254654

[5] P. Zhang, H. Shi, Y. Wang, C. Zhang, M. Xu, D. Wang, X. Li, *et al*. "X-ray spectrum estimation of a low-impedance rod pinch diode via transmission-absorption measurement and Monte-Carlo simulation," J. Appl. Phys. **133**, 243301 (2023). https://doi.org/10.1063/5.0151604

[6] Lai Dingguo, Qiu Mengtong, Yang Shi, *et al*. "An intense pulsed hard X-ray source based on series diode technology," High Power Laser and Particle Beams, **33,** 035001 (2021) https://doi.org/10.11884/HPLPB202133.200269

[7] M. Seltzer, J.P. Farrell, and J. Silverman, "Bremsstrahlung Beams from High-Power Electron Accelerators for Use in Radiation Processing,". IEEE Transactions on Nuclear Science, **30**(2), 1629-1633 (1983) https://doi.org/10.1109/TNS.1983.4332602

[8] M. Vassholz, and T. Salditt, "Observation of electron-induced characteristic x-ray and bremsstrahlung radiation from a waveguide cavity," Science Advances, **7**(4), (2021) https://doi.org/10.1126/sciadv.abd5677

[9] A.B. Batrakov, E.G. Glushko, A.M. Yegorov, *et al*. "Study of hard braking X-ray radiation on the radiation-beam complex «Temp-B»", Problems of Atomic Science and Technology. (6(100)), 100-104 (2015).

[10] A.A. Zinchenko, Yu.F. Lonin, A.G. Ponomarev, and S.I. Fedotov, "Pulsed magnetic system of the relativistic electron beam accelerator "Temp-B"". Problems of Atomic Science and Technology. Series: Plasma electronics and new acceleration methods., (4(86)), 7–9 (2013).

[11] A.B. Batrakov, I.N. Onishchenko, S.I. Fedotov, *et al*. "Power enhancement of the source of bremsstrahlung X-ray radiation based on a high current pulsed electron accelerator "Temp-B"," Problems of Atomic Science and Technology. (1(155)), 61-64 (2025). https://doi.org/10.46813/2025-155-061

[12] R.J. Thome, and J.M. Tarrh, *MHD and Fusion Magnets*, (JW&S, NY, 1982). pp. 247-248.
[13] https://www.radpro-int.com/tld-1/rados-tld-reader/
[14] E. Villegas, and F. Somarriba, "Characterization of MTS-6 and MTS-7 TLD Crystals for Personal Dosimetry in 241AMBE and 137CS for Nuclear Gauge Operators," in: *International Conference on Radiation Safety: Improving Radiation Protection in Practice. Extended Abstracts*, IAEA-CN-279 305–306 (2021).

ВИЗНАЧЕННЯ ПОВНОЇ ДОЗИ ПОТУЖНОГО ІМПУЛЬСНОГО ДЖЕРЕЛА ГАЛЬМІВНОГО РЕНТГЕНІВСЬКОГО ВИПРОМІНЮВАННЯ ЗБУДЖУВАНОГО СИЛЬНОСТРУМОВИМ ЕЛЕКТРОННИМ ПУЧКОМ

А.Б. Батраков, С.І. Федотов, І.М. Оніщенко, Є.Г. Глушко, А.М. Горбань, О.Л. Рак, О.В. Невара, Ю.М. Волков
Національний науковий центр «Харківський фізико-технічний інститут», Харків, Україна

Представлено експериментальне вимірювання повної дози потужного джерела гальмівного рентгенівського випромінювання, базованого на імпульсному прискорювачі електронів прямої дії з параметрами сильнострумового релятивістського трубчастого електронного пучка: енергія 600 кеВ, струм 13,5 кА і тривалість імпульсу 1,0 мкс. Транспортування електронного пучка, отримуваного в магнітоізольованому діоді, до молібденового конвертера на відстань 55 см здійснювалось імпульсним магнітним полем соленоїда. До нього примикає додаткова котушка, з'єднана послідовно з ним, для забезпечення магнітного поля в області конвертера та уникнення втрат пучка. Описана методика визначення повної дози гальмівного рентгенівського випромінювання. Для вимірювання дози гальмівного рентгенівського випромінювання використовувалися полікристалічні детектори, які розташовувалися на відстані 80 мм за конвертором. Детектори розміщувалися в полярній площині з кроком 20°. Виміри розподілу доз за полярним кутом показали симетрію випромінювання за полярним та азимутальним кутами відносно оси. Беручи до уваги, що пучок випромінює тільки передню напівсферу, то разом з виміряною симетрією можливо інтегрування по всій сфері звести до інтегрування лише по 1/8 площині сфери, зменшивши кількість датчиків. Експериментально отримана величина повної дози гальмівного рентгенівського випромінювання 388,5 Гр за один імпульс струму прискорювача, яка зосереджена в куті 120° в напрямку руху пучка.

Ключові слова: *сильнострумовий імпульсний електронний прискорювач прямої дії; релятивістський електронний пучок; конвертор; гальмівне рентгенівське випромінювання; термолюмінесцентний детектор; інтенсивність; доза*

East European Journal of Physics. 4. 555–559 (2025)
DOI: 10.26565/2312-4334-2025-4-58 ISSN 2312-4334

FAST NEUTRON DISCRIMINATION USING THE STILBENE SCINTILLATOR

I. Yakymenko[1*], **G. Onyshchenko**[1], **O. Sidletskiy**[1,3], **V. Trusova**[2], **O. Tarasenko**[1,5], **P. Kuznietsov**[1], **S. Lytovchenko**[4], **O. Kuzin**[1], **O. Shchus**[1]

[1]*O.I. Akhiezer Department for Nuclear Physics and High Energy Physics, V.N. Karazin Kharkiv National University, Kharkiv, Ukraine*
[2]*Department of Medical Physics and Biomedical Nanotechnologies, V.N. Karazin Kharkiv National University, Kharkiv, Ukraine*
[3]*Crystal Growth Technology Department, Institute for Scintillation Materials NAS of Ukraine: Kharkiv, Ukraine*
[4]*Department of Reactor Engineering Materials and Physical Technologies, V.N. Karazin Kharkiv National University, Kharkiv, Ukraine*
[5]*Heterostructured Materials Department, Institute for Scintillation Materials NAS of Ukraine, Kharkiv, Ukraine*
[*]*Corresponding Author e-mail: ivan.yakymenko@karazin.ua*

Received August 25, 2025; revised October 15, 2025; accepted November 10, 2025

In this research, we have studied a speed system for neutron flux estimation used in experimental works with radiation protection design and for applications where materials identification based on neutron backscattering is crucial. The most effective approach is neutron-gamma discrimination using the stilbene scintillator. We performed a discrimination with the charge integration technique. The data acquisition was implemented using a high sampling rate oscilloscope. Crystalline stilbene is an organic scintillator that is well-suited for fast neutron identification in environments with high gamma-ray-associated irradiation.

Keywords: *Charge integration; scintillators; neutron gamma discrimination; landmine detection; neutron backscattering*

PACS: 29; 29.40.Mc; 29.40.-n

1. INTRODUCTION

In this research, we have studied neutron gamma discrimination using the stilbene scintillator for applications where neutron flux estimations are crucial. One of the approaches is to use charge integration. Organic scintillating materials are frequently used for measurements that require sensitivity to gamma and fast neutron radiation due to their pulse shape discrimination (PSD) nature. The primary reaction for neutron detection is elastic neutron scattering [1, 2]. Experimental particle type identification is commonly taken using both charge integration and pulse shape discrimination methods. Recent research works in PSD methods demonstrate the effectiveness of charge-integration along with the new techniques [3]. The pattern-recognition method offers a short data processing time. A classical neutron gamma discrimination [4] can operate in a wide dynamic range up to 4MeV and demonstrates a lowest energy threshold down to 30 KeV but has a specific requirements for setup tuning. A few works demonstrate a great pulse shape discrimination capability for simultaneous detection of gamma-rays, slow and fast neutrons using only the one detector [5]. Recent algorithms of neutron/gamma discrimination, such as the use of neural networks [6]. For portable applications, for example, in evaluative tasks, data could be taken with digital oscilloscopes [7]. The minimum requirements for an oscilloscope are a sampling rate of 1 GS/s, 8-bit vertical resolution, and a bandwidth of 200 MHz. The described method's precision is comparable to the classic technique of zero crossing of two signals from the last dynode and photocathode, with further signal analysis on the time to digital converter (TAC) and spectrometer. In particular, the charge-integration method allows for highly accurate discrimination between photons and neutrons at high-energy depositions. This paper describes the algorithm and experimental details of the algorithm implementation for neutron gamma discrimination using the oscilloscope.

2. MATERIALS AND METHODS

The raw scintillation pulses were recorded with the oscilloscope GW Instek GDS-3504 [10] Digital Oscilloscope 500 MHz 4 GSa/s. It accumulated more than 100k pulses from the stilbene scintillator size of 40 mm x 40 mm, wrapped in PTFE tape. The leading-edge trigger threshold was set as the lowest possible 50 mV according to baseline noise and in terms of energy < 1 MeV. The data was obtained using a Pu-Be neutron source 10^5, which produces neutrons and instant gamma-rays. A used photomultiplier tube, PMT Hamamatsu R1307 [9], operating at 972 V, was installed in a dark box. To avoid signal distortion, it was used one-stage buffer amplifier with a 2 us integration time directly connected to the oscilloscope. An internal oscilloscope termination of 50 Ohms is used to avoid signal reflection. Fig. 1 presents the block scheme of the experimental setup used for data accumulation. The Pu-Be source is installed 15 cm from the detector. The stilbene crystal was coupled with optical glue Cargile [8] to the PMT window, a single-stage amplifier connected directly to the oscilloscope. Selected trigger holdoff (timing gate) was in the range of 300 ns.

Cite as: I. Yakymenko, G. Onyshchenko, O. Sidletskiy, V. Trusova, O. Tarasenko, P. Kuznietsov, S. Lytovchenko, S. Lytovchenko, O. Kuzin, O. Shchus, East Eur. J. Phys. 4, 555 (2025), https://doi.org/10.26565/2312-4334-2025-4-58

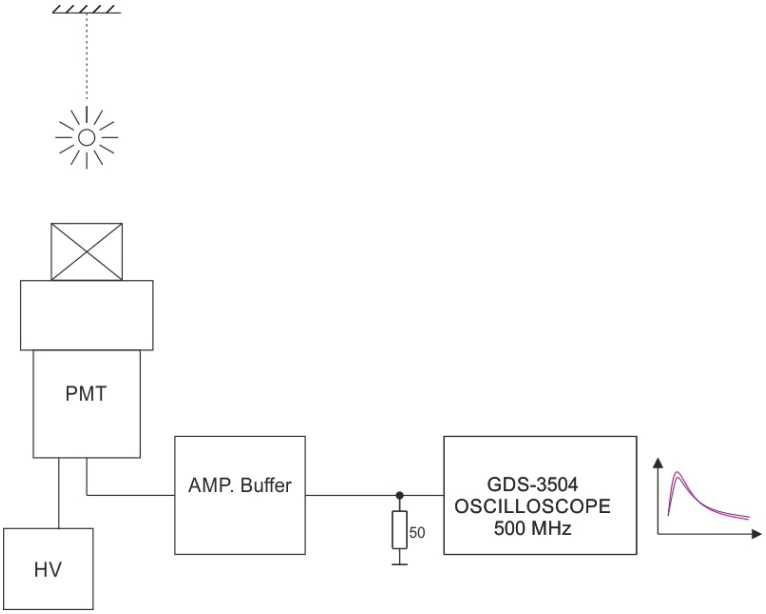

Figure 1. Experimental setup. Equipment used to measure the n-y discrimination by the charge integration method.

3. ALGORITHM AND DATA PROCESSING

The charge comparison method provides the most common pulse shape discrimination (PSD). The ratio between neutron 1 and gamma rays could be measured based on charge comparison of the entire signal Q total and the charge of the slow part of the signal tail Q slow.

$$R = Q_s/Q_t \tag{1}$$

Typical neutron and gamma-ray pulse signals are shown in Fig. 2 The ratio Qs/Qt is the main criterion of the method to classify pulses as neutron or gamma interactions with the scintillator. Neutron pulses – red line, gamma – blue line. The ranges of integration Qs (from 50 to 200 ns) have been fitted to have the best discrimination in terms of figure of merit (FOM).

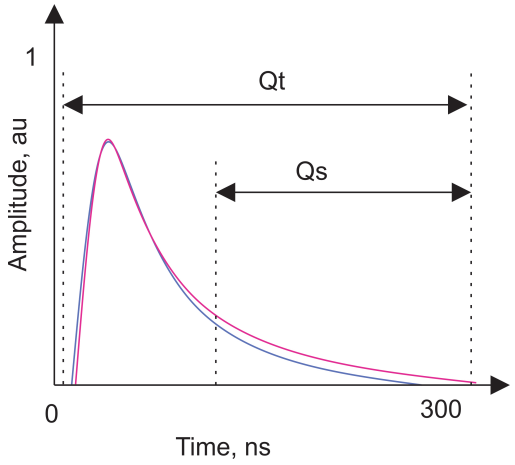

Figure 2. Charge integration principle, long gate Qt and the slow gate Qs selected for the charge comparison method.

Finally, to calculate the quality of neutron/gamma discrimination of the stilbene scintillator used the figure of merit (FOM), which is:

$$FOM = D/(FWHM_n + FWHM_\gamma) \tag{2}$$

Both neutron and gamma are semi-Gaussian functions; D is a metric of peak separation. To account for a variation of rise time for the pulses with the different amplitudes (rise time correction), the constant fraction discrimination function (CFD) was applied to the accumulated dataset. By varying the slow gate position to the long gate, it was solved the best position for the FOM was solved during the fitting process. An algorithm has been developed that is capable of automatically calculating the area integrals for predefined gates (Q_t and Q_s). Using the Python code, the raw amplitude

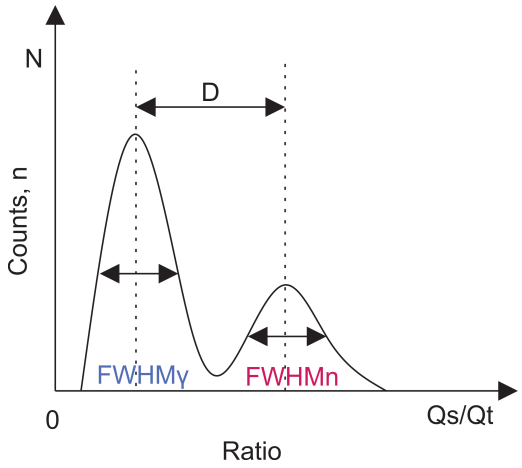

Figure 3. FOM calculation: distance D between neutron and gamma peaks, full widths at half maximum for gamma and neutron peaks.

pulses were recorded from the oscilloscope during the exposition time to the host PC. After gate selection, for each recoded pulse, the Ratio Qs/Qt was calculated. At the end of the ratio calculation, the resulting FOM is used to adjust the gate and recalculate the FOM.

4. EXPERIMENTAL RESULTS

Similar results but with different equipment were examined by many researcher groups [11, 12] and our implementation following the main principle of charge integration. As a result, the measured FOM for stilbene scintillator was 0.715.

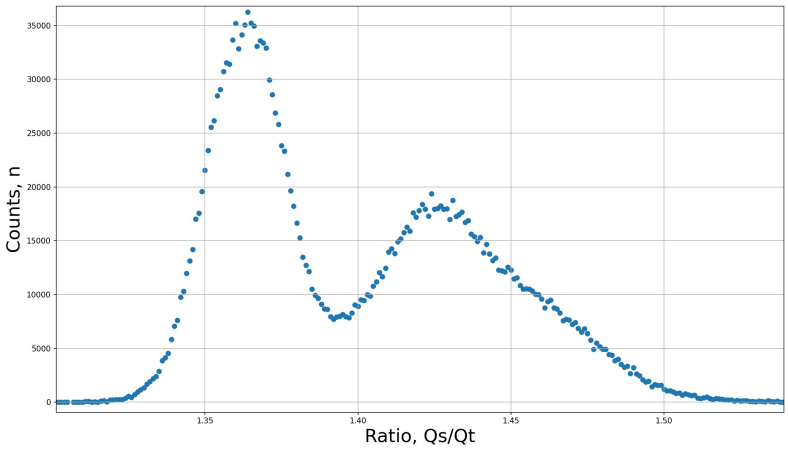

Figure 4. The n-y discrimination spectra for stilbene scintillator 40 mm x 40 mm, PMT Hamamatsu R1307, Pu-Be source.

The shaping time of the amplifier was 2.0 μs for all expositions, which is longer than the scintillation decay time. The conventional organic scintillator stilbene corresponds to standard parameters in experiments, and it's possible to use a simplified acquisition path to evaluate the discrimination ratio.

5. DISCUSSION AND CONCLUSION

Our research shows a comprehensive approach to measuring FOM with modern oscilloscope equipment. The quality of the stilbene scintillator may affect the resulting FOM. High-grade discrimination could be achieved with the simplified electronic path, compared to classic zero-crossing (ZC) techniques, which utilize a more complex timing circuit [link]. An obtained experimental dataset could be used for further analysis, for example, to train AI-based recognition models [link]. The energy threshold of the detecting system could be estimated with calibration at different energy sources [13]. The charge integration method is effective for 100 keV electron energy with a range up to 4 MeV. The drawback of the charge comparison method is mainly the higher lowest threshold energy. The method needs an oscilloscope with a bandwidth of at least 500MHz, vertical resolution might be 8-bit, but a 12-bit ADC will provide a better particle identification (in a noisy environment). PMT dynamic gain is important to achieving better discrimination at energy applications below 50 keV. A

fitting procedure and data processing have been written using Python. Our approach demonstrates potential applications for this setup in portable systems, especially in cost-efficient systems.

6. DECLARATION OF COMPETING INTEREST

The authors declare that they have no known competing financial interests or personal relationships that could have appeared to influence the work reported in this paper.

7. ACKNOWLEDGMENTS

This work was supported by the Ministry of Education and Science of Ukraine (the projects: № 0124U000837, № ДЗ/174-2025 and 0125U001050). Partly supported by the U.S. National Academy of Sciences (NAS) and the Office of Naval Research (ONRG) through the Science and Technology Center in Ukraine (STCU) under STCU contract number [7120] in the framework of the International Multilateral Partnerships for Resilient Education and Science System in Ukraine (IMPRESS-U).

ORCID

I. Yakymenko, https://orcid.org/0000-0002-0194-8376; **G. Onyshchenko**, https://orcid.org/0000-0001-6945-8413; **O. Sidletskiy**, https://orcid.org/0000-0003-0865-6517; **V. Trusova**, https://orcid.org/0000-0002-7087-071X; **O. Tarasenko**, https://orcid.org/0000-0002-8152-2198; **P. Kuznietsov**, https://orcid.org/0000-0001-8477-1395; **S. Lytovchenko**, https://orcid.org/0000-0002-3292-5468; **O. Kuzin**, https://orcid.org/0009-0004-3159-1680; **O. Shchus**, https://orcid.org/0000-0001-6063-197X

REFERENCES

[1] M. Cieślak, K. Gamage, and R. Glover, "Critical review of scintillating crystals for neutron detection," Crystals, **9(9)**, 480 (2019). https://doi.org/10.3390/cryst9090480

[2] G. Onyshchenko, V. Ryzhikov, I. Yakymenko, V. Khodusov, S. Naydenov, A. Opolonin, and S. Makhota, "The Investigation of Mechanisms of Fast Neutron Registration in Oxide Scintillators," East Eur. J. Phys. (3), 54-62 (2019). https://doi.org/10.26565/2312-4334-2019-3-07

[3] D. Takaku, T. Oishi, and M. Baba, "Development of a neutron-gamma discrimination technique using a pattern-recognition method with digital signal processing," Progress in Nuclear Science and Technology, **1**, 210–213 (2011). https://doi.org/10.15669/pnst.1.210

[4] D. Wolski, M. Moszynski, T. Ludziejewski, A. Johnson, W. Klamra, and Ö. Skeppstedt, "Comparison of n-γ discrimination by zero-crossing and digital charge comparison methods," Nuclear Instruments & Methods in Physics Research Section A-accelerators Spectrometers Detectors and Associated Equipment, **360**, 584-592 (1995). https://doi.org/10.1016/0168-9002(95)00037-2

[5] M.G. Kobylka, T. Szczesniak, L. Swiderski, K. Brylew, M. Moszyński, J. Valiente-Dobón, P.Schotanus, *et al*. "Comparison of detectors with pulse shape discrimination capability for simultaneous detection of gamma-rays, slow and fast neutrons," Nuclear Instruments and Methods in Physics Research Section a Accelerators Spectrometers Detectors and Associated Equipment, **1019**, 165858 (2021). https://doi.org/10.1016/j.nima.2021.165858

[6] J. Lu, X. Tuo, H. Yang, Y. Luo, H. Liu, C. Deng, and Q. Wang, "Pulse-Shape discrimination of SIPM Array-Coupled CLYC detector using convolutional neural network," Applied Sciences, **12**(5), 2400 (2022). https://doi.org/10.3390/app12052400

[7] S. Baselga, and E. Montbarbon, "Neutron and gamma pulse shape discrimination by robust determination of the decay shape," Applied Sciences, **14**(13), 5532 (2024b). https://doi.org/10.3390/app14135532

[8] Cargille Laboratories 55 Commerce Rd. Cedar Grove, NJ 07009, https://www.cargille.com/optical-gels/

[9] Hamamatsu Photonics K.K. and its affiliates, https://www.hamamatsu.com/us/en/product/optical-sensors/pmt/pmt_tube-alone/head-on-type/R1307.html

[10] Good Will Instrument Co., Ltd. https://www.gwinstek.com/en-global/products/detail/GDS-3000

[11] T. Yanagida, K. Watanabe, and Y. Fujimoto, "Comparative study of neutron and gamma-ray pulse shape discrimination of anthracene, stilbene, and p-terphenyl," Nuclear Instruments and Methods in Physics Research Section a Accelerators Spectrometers Detectors and Associated Equipment, **784**, 111–114 (2014). https://doi.org/10.1016/j.nima.2014.12.031

[12] J. Polack, M. Flaska, A. Enqvist, C. Sosa, C. Lawrence, and S. Pozzi, "An algorithm for charge-integration, pulse-shape discrimination and estimation of neutron/photon misclassification in organic scintillators," Nuclear Instruments and Methods in Physics Research Section a Accelerators Spectrometers Detectors and Associated Equipment, **795**, 253–267 (2015). https://doi.org/10.1016/j.nima.2015.05.048

[13] G.M. Onyshchenko, V.D. Ryzhikov, I.I. Yakymenko, and O.P. Shchus', "The Threshold of Detection of Fission Materials by ZnWO4 and Bi4Ge3O12 Scintillation Detectors," East Eur. J. Phys. (4), 91-94 (2019). https://doi.org/10.26565/2312-4334-2019-4-10

[14] N.D. Quang, H. Kim, P.Q. Vuong, N.D. Ton, U. Nam, W. Park, J. Sohn, *et al*. "Measuring and unfolding fast neutron spectra using solution-grown trans-stilbene scintillation detector," Nuclear Engineering and Technology, **55**(3), 1021–1030 (2022). https://doi.org/10.1016/j.net.2022.10.041

ДИСКРИМІНАЦІЯ ШВИДКИХ НЕЙТРОНІВ З ВИКОРИСТАННЯМ СЦИНТИЛЯТОРУ СТИЛЬБЕНУ

І. Якименко[1], **Г. Онищенко**[1], **О. Сідлецький**[1,3], **В. Трусова**[2], **О. Тарасенко**[1,5], **П. Кузнєцов**[1], **С. Литовченко**[4], **О. Кузін**[1], **О. Щусь**[1]

[1]*Кафедра фізики ядра та високих енергій імені О.І. Ахієзера, Харківський національний університет імені В.Н. Каразіна, Харків, Україна*

[2]*Кафедра медичної фізики та біомедичних нанотехнологій, Харківський національний університет імені В.Н. Каразіна, Харків, Україна*

[3]*Відділ технології вирощування кристалів, Інститут сцинтиляційних матеріалів, НАН України, Харків, Україна*

[4]*кафедра матеріалів реакторобудування та фізичних технологій, Харківський національний університет імені В.Н. Каразіна, Харків, Україна*

[5]*Відділ гетероструктурованих матеріалів, Інститут сцинтиляційних матеріалів, НАН України, Харків, Україна*

У цьому дослідженні ми досліджували систему швидкісної оцінки потоку нейтронів, яка використовується в експериментальних роботах з проектування радіаційного захисту та для застосувань, де ідентифікація матеріалів на основі зворотного розсіювання нейтронів є критично важливою. Найефективнішим підходом є нейтронно-гамма дискримінація з використанням сцинтилятора стильбену. Ми реалізували дискримінацію за допомогою методу інтегрування заряду. Збір даних було здійснено за допомогою осцилографа з високою частотою дискретизації. Кристалічний стильбен – це органічний сцинтилятор, який добре підходить для швидкої ідентифікації нейтронів у середовищах з високим опроміненням, супутнім гамма-випромінюванням.

Ключові слова: *інтегрування заряду; сцинтилятори; нейтронно-гамма-дискримінація; виявлення наземних мін; зворотне розсіювання нейтронів*

East European Journal of Physics. 4. 560-574 (2025)
DOI:10.26565/2312-4334-2025-4-59 ISSN 2312-4334

OPTIMIZING HEAD AND NECK CANCER RADIOTHERAPY: A DOSIMETRIC COMPARISON OF FF AND FFF BEAMS IN VMAT

Reham S. Sherif[1]*, Limam A. Neya[2#], Ahmed M. Abdelaal[2], Ehab M. Attalla[3], Reem H. El-Gebaly[1]
[1]*Department of Biophysics, Faculty of Science, Cairo University, Giza, Egypt*
[2]*Nasser Institute, Cairo, Egypt*
[3]*Radiotherapy & Nuclear Medicine Department, National Cancer Institute, Cairo University, Cairo, Egypt*
**Corresponding Author E-mail: rsalah@sci.cu.edu.eg; #limammdi11@gmail.com*
Received July 19, 2025; revised August 20, 2025; in final form September 2, 2025; accepted September 21, 2025

Aim: Head and neck cancer (HNC) is a significant global health concern, with rising incidence rates and a high prevalence in South Asia, particularly in India. Radiation therapy, including advanced techniques like Volumetric-Modulated Arc Therapy (VMAT) and Intensity-Modulated Radiotherapy (IMRT), plays a crucial role in treating HNC. This study aims to compare the dosimetric and biological and second cancer risk estimation differences between flattened (FF) and flattening filter-free (FFF) beams in VMAT treatment plans for HNC, focusing on the impact of 6 MV and 10 MV energies.
Methods: Twenty HNC patients underwent replanning using VMAT on an ELEKTA VERSA HD linear accelerator with 6 MV FF, 6 MV FFF, 10 MV FF, and 10 MV FFF beams. Dosimetric parameters evaluated included dose distribution to planning target volumes (PTVs) and dose delivered to 98% of the target (D98), 50% (D50), and 2% (D2), as well as doses to organs at risk (OARs)., monitor units per segment (MU/Segment), number of MU/cGy, treatment delivery time, conformity index, and homogeneity index, also biological parameters (NTCP and EUD) and second cancer risk estimation were evaluated.
Results: The results showed that 6 MV FFF beams provided slightly better dose-sparing for OARs compared to 6 MV FF, with no significant differences in target volume coverage. Both FF and FFF beams demonstrated comparable conformity indices, but FF beams had better homogeneity indices. FFF beams required more monitor units (MUs) and segments but offered reduced treatment delivery times. For 10 MV beams, FFF showed marginal advantages in dose homogeneity and sparing of normal tissues at lower doses, though it required more MUs and segments, this study found that NTCP and EUD were largely comparable between FF and FFF types, with minor but statistically significant differences for the brainstem (favoring FFF) and heart. Second cancer risks varied slightly by energy and technique 6MV FFF reduced parotid risks (though increased larynx risk).
Conclusion: 6 MV beams, particularly FFF, showed slight advantages in sparing OARs and target volume coverage compared to 10 MV beams. This study highlights the dosimetric comparability of FF and FFF beams in HNC treatment, with FFF offering potential benefits in treatment efficiency and reduced delivery times. This study also shows that FF and FFF types yield comparable radiobiological outcomes, though 6MV FFF beams slightly reduce doses to critical organs without sacrificing efficacy. Both types perform similarly, with minor risk variations by energy.
Keywords: *Head and neck cancer; Volumetric Modulated Arc Therapy (VMAT); Flattening filter (FF); Flattening filter-free (FFF); 6MV; 10 MV*
PACS: 29.38.Db

1. INTRODUCTION

Head and neck cancer (HNC) ranks as the seventh most prevalent cancer worldwide, with approximately 660,000 new cases diagnosed each year, contributing to nearly half of all cancer-related deaths. The incidence of HNC has been increasing annually. About 55% to 60% of HNC cases occur in South Asia. In India specifically, HNC represents roughly one-third of all cancer diagnoses, following cervical and breast cancer. The majority of HNC patients are male, with around 70% to 75% presenting at advanced stages of the disease [1].

Radiation therapy for head and neck cancers continues to present significant challenges due to the severe side effects experienced by patients. For individuals with cancers located outside the oral cavity who are undergoing definitive treatment aimed at organ preservation, the established standard of care involves concurrent chemoradiation. In the postoperative context, radiation therapy is often employed based on specific risk factors, accompanied by concurrent chemotherapy in cases where there are positive surgical margins or extravasation of cancer cells (ECE) [2].

Radiotherapy is a crucial element in the treatment of head and neck cancers. Volumetric-Modulated Arc Therapy (VMAT) and Intensity-Modulated Radiotherapy (IMRT) are prevalent treatment techniques for head and neck cancers due to their dosimetric advantages, along with the preservation of nearby critical organs, which improves survival and quality of life.

VMAT and IMRT are advanced techniques in radiation therapy used to target cancerous tumors with precision while minimizing damage to surrounding healthy tissues. VMAT delivers radiation by rotating the machine around the patient in one or more continuous arcs. This technique modulates the dose dynamically as the machine moves, allowing for a more complex and conformal dose distribution. As a result, VMAT can be faster, reducing treatment time and patient movement. In contrast, IMRT employs multiple static or non-rotational beams from different angles to deliver radiation.

Cite as: R.S. Sherif, L.A. Neya, A.M. Abdelaal, E.M. Attalla, R.H. El-Gebaly, East Eur. J. Phys. 4, 560 (2025), https://doi.org/10.26565/2312-4334-2025-4-59

The intensity of each beam is adjusted using multi-leaf collimators (MLCs) to shape the dose distribution, which can make IMRT slower compared to VMAT due to the need for precise beam angle adjustments and patient repositioning.

Regarding treatment planning and dosimetry, VMAT planning can be more complex due to the need to optimize dose distribution over a continuous arc. However, it often provides highly conformal dose distributions with fewer beams, potentially offering better sparing of healthy tissues. IMRT, on the other hand, requires the creation of intricate beam arrangements and intensity maps, which can be time-consuming but achieve precise dose distributions. VMAT typically results in shorter treatment times and improved patient comfort due to its continuous arc delivery, whereas IMRT may have longer treatment times. [3], because of the multiple beam angles and adjustments required [4], [5].

Flattening Filter (FF) and Flattening Filter-Free (FFF) are terms related to different configurations of linear accelerators used in external beam radiotherapy. Flattening filter to create a uniform dose distribution across the treatment field, ensuring that the radiation dose is evenly spread over the target area. However, the flattening filter can introduce some variation in the dose distribution, resulting in a dose fall-off at the edges (penumbra) and FF beams have longer delivery time which can lead to decreased patient comfort during treatment [6].

In contrast, FFF (Flattening Filter-Free) does not use a flattening filter, leading to a non-uniform dose distribution with a higher dose rate at the central axis and a dose decreasing towards the edges of the field [7].

Treatment plans need to use more MUs to ensure that the entire target volume receives the appropriate dose, while also effectively sparing surrounding healthy tissues [1].

Additionally, FFF can provide higher dose rates, which can shorten treatment times and improve efficiency. This makes it particularly advantageous for techniques that require high precision and rapid delivery.

This study seeks to quantify and contrast treatment plan differences in terms of dosimetric parameters, radio-biological response, and second primary cancer risk when using conventional flattened versus flattening-filter-free (FFF) photon beams for head and neck malignancies. It further examines how beam energy levels (6 MV and 10 MV) influence these parameters across both irradiation techniques.

2. MATERIALS AND METHODS

Twenty patients with head and neck cancer were included in this study, and underwent replanning with VMAT under ELEKTA VERSA HD using 6MV FF and 6MV FFF also 10MV FF, and 10MV FFF. All 20 patients were treated at the National Cancer Institute (NCI), Cairo, Egypt, the patients all males between the age of 40 and 60 with low grade tumors are selected for this study.

Each patient underwent CT simulation using the Siemens SOMATOM Ratproof Computed Tomography (Siemens Healthineers) with a dedicated protocol, with a 3 mm slice thickness. The simulation was performed head-first in a supine position using a mask for immobilization.

All patients' CT images were transmitted to the Monaco Sim system (ELEKTA MONACO 5.51.10). The physician delineated the target volumes and organs at risk (OARs).

After the delineation of the target and OARs was completed, the CT structure was transferred to the Monaco workstation to design the VMAT planning (FF and FFF) facility for each case using energies 6MV and 10MV in the planning, the prescribed dose 36Gy per 18 fractions of all cases for radical intent. Then it was transferred by the mosaic system to begin radiation delivery.

Using two-photon beams of VERSA HD LINAC, 80 VMAT plans were created by directly changing the original plan radiation energy 6MV (FF beam) to 6MV with FFF beam.

The same thing happened with 10 MV (FF beam) preplanned to 10 MV with FFF beam while maintaining the original plan optimization parameters unchanged. Then the optimization was performed inversely using the original plan parameters and doses were calculated using the Monte Carlo (MC) algorithm.

VERSA HD LINAC is equipped with an agility head with MLC of 5mm (160 leaves) with 6MV FF and 10MV FF. The beam quality for High dose (HD) values for the FFF energies is the same as that of flattened energies. The effective leaf speed is 6.5cm/s which is important for FFF, and dynamic treatment.

All plans were produced with the Monaco treatment planning system (TPS) (ELEKTA MONACO 5.51.10,) this allowed plan evaluation for the PTVs, the relevant organs at risk (OARs) as well as mean dose (D mean), maximum dose (D max.), 95% dose (D95), 98%(D98), 50%(D50), 2% (D2), monitor units per segment (MU/Segment), and the number of MU/cGy in addition to treatment delivery time and conformity index.

Each pair of plans (FF and FFF for the same patient) and FF in both energies (6MV, 10MV), and FFF in both energies (6MV, 10MV) were compared and then the statistical analysis was made Radiobiological models are commonly employed to calculate the outcomes of treatment plans, particularly by utilizing dose-volume histograms (DVH). One such model is Niemierko's EUD-based NTCP mathematical model. To implement these models and generate corresponding program code, MATLAB was selected as the platform. MATLAB is a high-level technical computing language and an interactive environment that facilitates the development and execution of such models.

The risk of radiation-induced secondary cancer is estimated using guidelines from ICRP (International Commission on Radiological Protection) Publication 103.[8]

The calculation is performed in two steps. First, the equivalent dose is calculated by multiplying the absorbed dose (in Gy) by the radiation weighting factor (wR). For photon radiation, wR=1, meaning the equivalent dose (in Sv) is numerically equal to the absorbed dose. Second, the equivalent dose is multiplied by the nominal risk coefficient

(NRC) for the specific organ or tissue, as defined in ICRP 103. This approach provides a standardized method for estimating the long-term risk of secondary cancers following radiation exposure.

For example, if the absorbed dose to the salivary glands is 9.78 Gy, the equivalent dose is 9.78 Sv. Using an NRC of 0.0005 per Sv, the risk of secondary cancer is calculated as 9.78×0.0005=0.004899.78(or 0.489%). This method ensures a standardized approach to estimating long-term risks associated with radiation exposure in radiotherapy.

Statistical analysis

Statistical analysis was done using Excel Microsoft Office 2019 to compare means using a *t*-test and to estimate the significant difference between the two techniques. If the P value < 0.05, then the result was considered statistically significant.

3. RESULTS

The following figures and tables show the mean values of 20 patients replanned 80 VMAT plans with two energies 6 and 10 MV both with the FF and FFF beam type.

Comparison between FF and FFF beam configuration for the energy 6 MV

3.1.1. Comparison between the mean doses of the OARs for both types at 6 MV

Figure 1 compares the mean doses received by organs at risk (OARs) for 20 head and neck (H&N) cancer patients treated with volumetric modulated arc therapy (VMAT) using 6MV flattened filter (FF) and flattening filter-free (FFF) beams.

The brainstem (maximum dose) received the highest dose, with values of 34.53 Gy for the FF beam type and 35.03 Gy for the FFF mode. However, the difference was not statistically significant (p = 0.23). Conversely, the heart (mean dose) received the lowest dose, with 2.6 Gy for the FF mode and 2.2 Gy for the FFF mode, also showing no significant difference (p = 0.20).

It can be noticed that some of the OARs received slightly higher doses in FF mode like the right parotid (mean dose) (9.78Gy for FF mode, 9.5Gy for FFF mode). There is no significant difference where the p-value equals 0.19. The left parotid was (mean dose) (12.36Gy for FF mode, and 12.28Gy for FFF mode) where the p-value is 0.39 which indicates that there is no significant difference between them.

No significant differences were observed in most organs at risk (OARs) between FF and FFF beam types. The right eye (maximum dose) (10.52 Gy FF, 10.04 Gy FFF; p=0.25), right lens (maximum dose) (5.96 Gy FF, 5.9 Gy FFF; p=0.40), right cochlea (mean dose) (19.1 Gy FF, 18.28 Gy FFF; p=0.14), right optic nerve (maximum dose) (14.66 Gy FF, 13.34 Gy FFF; p=0.10), right lung (mean dose) (8.6 Gy FF, 7.75 Gy FFF; p=0.25), left lung (mean dose) (9.75 Gy FF, 8.6 Gy FFF; p=0.25), and oral cavity (mean dose) (7.36 Gy FF, 6.96 Gy FFF; p=0.07) all showed no notable differences.

Similarly, some OARs received slightly higher doses in FFF beam configuration, but without significant differences: left eye (maximum dose) (19.32 Gy FF, 20.72 Gy FFF; p=0.23), left lens (maximum dose) (8.78 Gy FF, 8.82 Gy FFF; p=0.47), left cochlea (mean dose) (20.7 Gy FF, 20.81 Gy FFF; p=0.45), left optic nerve (maximum dose) (17.32 Gy FF, 18.92 Gy FFF; p=0.09), spinal cord (maximum dose) (26.38 Gy FF, 27.33 Gy FFF; p=0.21), larynx (mean dose) (14.52 Gy FF, 14.97 Gy FFF; p=0.19), optic chiasm (maximum dose) (27.66 Gy FF, 28.82 Gy FFF; p=0.29), and esophagus (mean dose) (11.87 Gy FF, 11.91 Gy FFF; p=0.45).

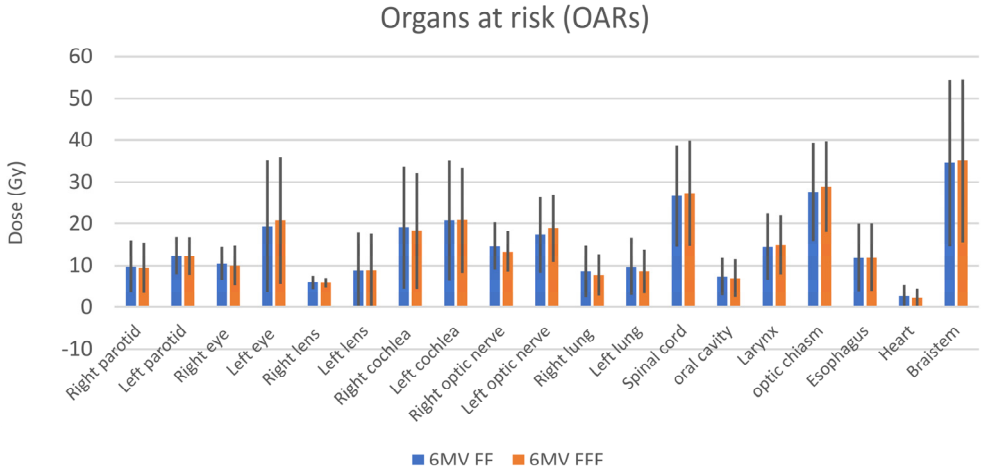

Figure 1. A comparison between the mean doses for the OARs of the H&N patients treated with VMAT technique with the energy 6MV in both FF and FFF types

3.1.2. Comparison between the planning target volumes for both types at 6 MV

Table 1. compares the average PTV volumes for the patients treated using FF and FFF types for 6 MV. The dose delivered to 95% of the target volume was 33.63 Gy for FF and 33.57 Gy for FFF. There is no statistically significant difference between them (p-value was 0.23).

The dose delivered to 98% of the target volume was 33.04 Gy for FF and 32.84 Gy for FFF. There is no significant difference (p-value is 0.08). FFF delivers a slightly lower dose to 98% of the target compared to FF.

The dose received by 50% of the target volume (D50%), which typically represents the central and most intense region of the target, was 35.3 Gy for FF and 35.33 Gy for FFF. The difference was minimal and not statistically significant ($p = 0.34$).

The dose delivered to the 2% of the target volume receiving the highest dose (D2%), representing the maximum dose applied to a small portion of the target, was 36.43 Gy for FF and 36.48 Gy for FFF. This difference was also not significant ($p = 0.21$).

Table 1. A comparison between the mean value of the PTV of the H&N patients treated using the VMAT technique with the energy 6 MV in both FF and FFF types, where SD means standard deviation.

	6MV			
Planning target volumes	**FF**	**SD**	**FFF**	**SD**
D95%	33.63	±12.92	33.57	±12.97
D98%	33.04	±12.67	32.84	±12.83
D50%	35.3	±13.46	35.33	±13.54
D2%	36.43	±13.83	36.48	±13.84

3.1.3. Comparison between the dosimetric parameters for both types at 6 MV

Table 2 compares the dosimetric parameters for FF and FFF types. Both types have a perfect conformity index (CI) of 1, indicating that both techniques deliver an equally precise radiation dose to the target, with minimal exposure to surrounding healthy tissues.

The homogeneity index (HI) in the case of FF (0.086) is significantly lower compared to FFF (0.104) with a p-value of 0.023. The number of segments used in FF (259.42) was slightly lower than in FFF (290.69), but the difference was not statistically significant ($p = 0.15$).

However, the monitor units (MU) for FF (1028.6) were significantly lower compared to FFF (1390.6), with a significant difference ($p = 0.0001$).

Table 2. A comparison between the dosimetric parameters using the VMAT technique for the energy 6 MV in both FF and FFF types.

	6MV			
Dosimetric parameters	**FF**	**SD**	**FFF**	**SD**
Conformity index (CI)	1	Identical	1	Identical
Homogeneity index (HI)	0.086	±0.01	0.104	±0.02
Number of segments	259.42	±179.03	290.69	±215.97
Monitor unit (MU)	1028.6	±341.04	1390.6	±475.58

3.2. Comparison between FF and FFF beam type for the energy 10 MV

3.2.1. Comparison between the mean doses of the OARs for both types at 10 MV

Figure 2 shows a comparison of the mean doses received by the OARs in the twenty H&N patients treated using VMAT of energy 10 MV for FF and FFF beams.

The results indicate that the brainstem (maximum dose) received the highest dose, with 35.26 Gy in FF beam type and 36.33 Gy in FFF beam configuration, showing no significant difference between the two beam types ($p = 0.20$). In contrast, the heart (mean dose) received the lowest dose, with 2.45 Gy in both FF and FFF types, also demonstrating no notable difference ($p = 0.50$).

Some of the OARs received slightly higher doses in the case of using FF beam type, although the differences were not statistically significant: right eye (maximum dose) (10.7 Gy FF, 10.3 Gy FFF; $p = 0.14$), left eye (maximum dose) (20.52 Gy FF, 19.92 Gy FFF; $p = 0.15$), right lens (maximum dose) (6.38 Gy FF, 5.68 Gy FFF; $p = 0.10$), left lens (maximum dose) (9.16 Gy FF, 8.8 Gy FFF; $p = 0.30$), right cochlea (mean dose) (18.78 Gy FF, 18.26 Gy FFF; $p = 0.16$), spinal cord (maximum dose) (27.43 Gy FF, 27.18 Gy FFF; $p = 0.34$), and larynx (mean dose) (15.6 Gy FF, 15.07 Gy FFF; $p = 0.34$).

Conversely, some OARs exhibited slightly higher doses in the case of using FFF beam configuration, also without statistically significant differences: right parotid (mean dose) (10.2 Gy FF, 10.32 Gy FFF; $p = 0.36$), left parotid (mean dose) (12.38 Gy FF, 12.6 Gy FFF; $p = 0.34$), left cochlea (mean dose) (21.48 Gy FF, 21.95 Gy FFF; $p = 0.26$), right optic nerve (maximum dose) (13.52 Gy FF, 14.1 Gy FFF; $p = 0.32$), left optic nerve (maximum dose) (17.66 Gy FF, 18.1 Gy FFF; $p = 0.35$), optic chiasm (maximum dose) (29.62 Gy FF, 30.08 Gy FFF; $p = 0.35$), and esophagus (mean dose) (11.69 Gy FF, 11.92 Gy FFF; $p = 0.16$).

However, significant differences were observed in the right lung (mean dose) (8.5 Gy FF, 8.85 Gy FFF; $p = 0.04$) and left lung (mean dose) (8.85 Gy FF, 10 Gy FFF; $p = 0.041$). The oral cavity (mean dose) (7.03 Gy FF, 7.53 Gy FFF; $p = 0.09$) did not exhibit a statistically significant difference.

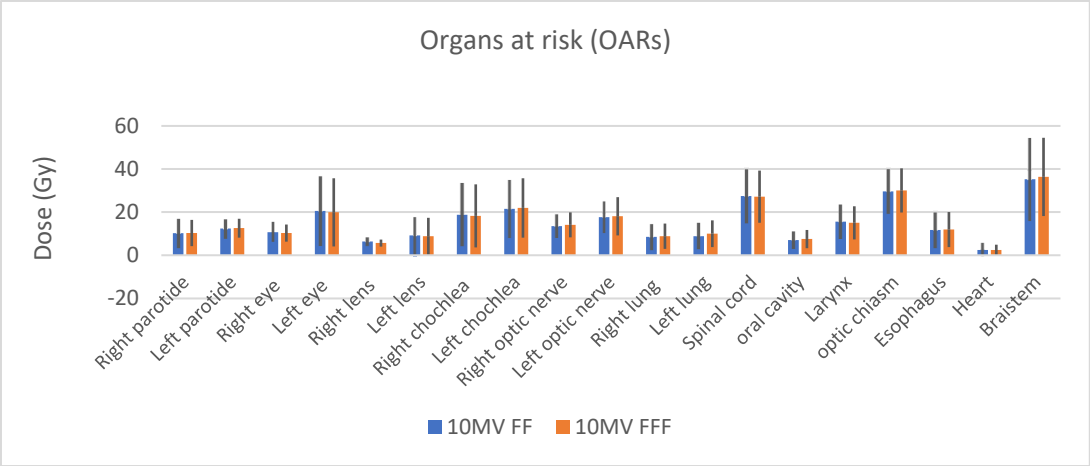

Figure 2. A comparison between the mean doses for the OARs of the H&N patients treated using the VMAT technique of the energy 10 MV in both FF and FFF modes.

3.2.2. Comparison between the planning target volumes for both types at 10 MV

Table 3 compares the average PTV volumes for the patients treated using FF and FFF types for 10 MV. The dose delivered to 95% of the PTV (D95%) was comparable between the two techniques, with no statistically significant difference ($p = 0.11$). The FFF technique delivered a slightly higher dose (33.17 Gy for FF and 33.4 Gy for FFF).

For the dose delivered to 98% of the PTV (D98%), both techniques produced similar results, with no notable difference ($p = 0.17$). The FF technique delivered a slightly higher dose (32.79 Gy for FF and 32.68 Gy for FFF).

The dose to 50% of the PTV (D50%) was slightly higher with the FFF technique (34.97 Gy for FF and 35.21 Gy for FFF and), though the difference was not statistically significant ($p = 0.21$).

The dose received by 2% of the PTV (D2%), representing the highest dose region, was 36.38 Gy for FF and 36.31 Gy for FFF. The difference between the two techniques was minimal and not statistically significant ($p = 0.22$).

Table 3. A comparison between the mean value of the PTV of the H&N patients treated using the VMAT technique with the energy 10 MV in both FF and FFF types.

	10MV			
Planning target volumes	**FF**	**SD**	**FFF**	**SD**
D95%	33.17	±13.18	33.4	±12.96
D98%	32.79	±12.80	32.68	±12.67
D50%	34.97	±13.37	35.21	±13.44
D2%	36.38	±13.89	36.31	±13.81

3.2.3. Comparison between the dosimetric parameters for both types at 10 MV

Table 4 shows that both FF and FFF have the same conformity index (1), which indicates that techniques deliver radiation doses that perfectly match the shape of the target volume.

Regarding the homogeneity index, the FFF technique demonstrates a slightly lower value compared to FF (0.1 for FF vs.0.098 for FFF), though the difference is not statistically significant ($p = 0.36$).

In terms of treatment complexity, the FFF technique requires a greater number of segments (271 for FF vs. 328 for FFF), though the difference is not statistically significant ($p = 0.16$). However, FFF requires a significantly higher number of monitor units (MU) compared to FF (1093.8 MU for FF vs. 1579.4 MU for FFF), with a statistically significant difference ($p = 0.02$).

Table 4. A comparison between the dosimetric parameters using the VMAT technique for the energy 10 MV in both FF and FFF types.

	10MV			
Dosimetric parameters	**FF**	**SD**	**FFF**	**SD**
conformity index (CI)	1	Identical	1	Identical
homogeneity index (HI)	0.1	±0.02	0.098	±0.02
Number of segments	271	±195.45	328	±243.88
Monitor unit	1093.8	±328.24	1579.4	±823.88

3.3. Comparison between the energies 6 and 10 MV for the FF beam type

3.3.1. Comparison between the mean doses of the OARs

Figure 3 compares the mean doses received by the OARs for 20 H&N patients treated using VMAT of 6 MV and 10 MV with FF beams. Among the OARs, the brainstem (maximum dose) received the highest dose (34.53 Gy for 6 MV FF

and 35.26 Gy for 10 MV FF), with no significant difference between the two energies (p = 0.19). Conversely, the heart (mean dose) received the lowest dose (2.6 Gy for 6 MV FF and 2.45 Gy for 10 MV FF), also showing no significant difference (p = 0.25).

While most OARs received slightly higher doses in the 10 MV FF beam type, the differences were not statistically significant. These include the right parotid gland (mean dose) (9.78 Gy for 6MV FF, 10.2 Gy for 10MV FF; p = 0.08), left parotid gland (mean dose) (12.36 Gy for 6MV FF, 12.38 Gy for 10MV FF; p = 0.47), right eye (maximum dose) (10.52 Gy for 6MV FF, 10.7 Gy for 10MV FF; p = 0.35), and left eye (maximum dose) (19.32 Gy for 6MV FF, 20.52 Gy for 10MV FF; p = 0.14). Similarly, the left lens (maximum dose) (8.78 Gy for 6MV FF, 9.16 Gy for 10MV FF; p = 0.29), left cochlea (mean dose) (20.7 Gy for 6MV FF, 21.48 Gy for 10MV FF; p = 0.18), and left optic nerve (maximum dose) (17.32 Gy for 6MV FF, 17.66 Gy for 10MV FF; p = 0.39) showed no significant differences.

Additionally, the spinal cord (maximum dose) (26.68 Gy for 6MV FF, 27.43 Gy for 10MV FF; p = 0.12), larynx (mean dose) (14.52 Gy for 6MV FF, 15.6 Gy for 10MV FF; p = 0.09), and optic chiasm (maximum dose) (27.66 Gy for 6MV FF, 29.62 Gy for 10MV FF; p = 0.18) also exhibited no significant differences. Notably, the right lens (maximum dose) showed a statistically significant difference (5.96 Gy for 6 MV FF, 6.38 Gy for 10 MV FF; p = 0.03).

A few OARs received slightly higher doses in the 6 MV FF beam type, but these differences were not statistically significant: right cochlea (mean dose) (19.1 Gy for 6MV FF, 18.78 Gy for 10MV FF; p = 0.29), right optic nerve (maximum dose) (14.66 Gy for 6MV FF, 13.52 Gy for 10MV FF; p = 0.13), right lung (mean dose) (8.6 Gy for 6MV FF, 8.5 Gy for 10MV FF; p = 0.35), left lung (mean dose) (9.75 Gy for 6MV FF, 8.85 Gy for 10MV FF; p = 0.18), oral cavity (mean dose) (11.87 Gy for 6MV FF, 11.69 Gy for 10MV FF; p = 0.26), and esophagus (mean dose) (11.78 Gy for 6MV FF, 11.69 Gy for 10MV FF; p = 0.11).

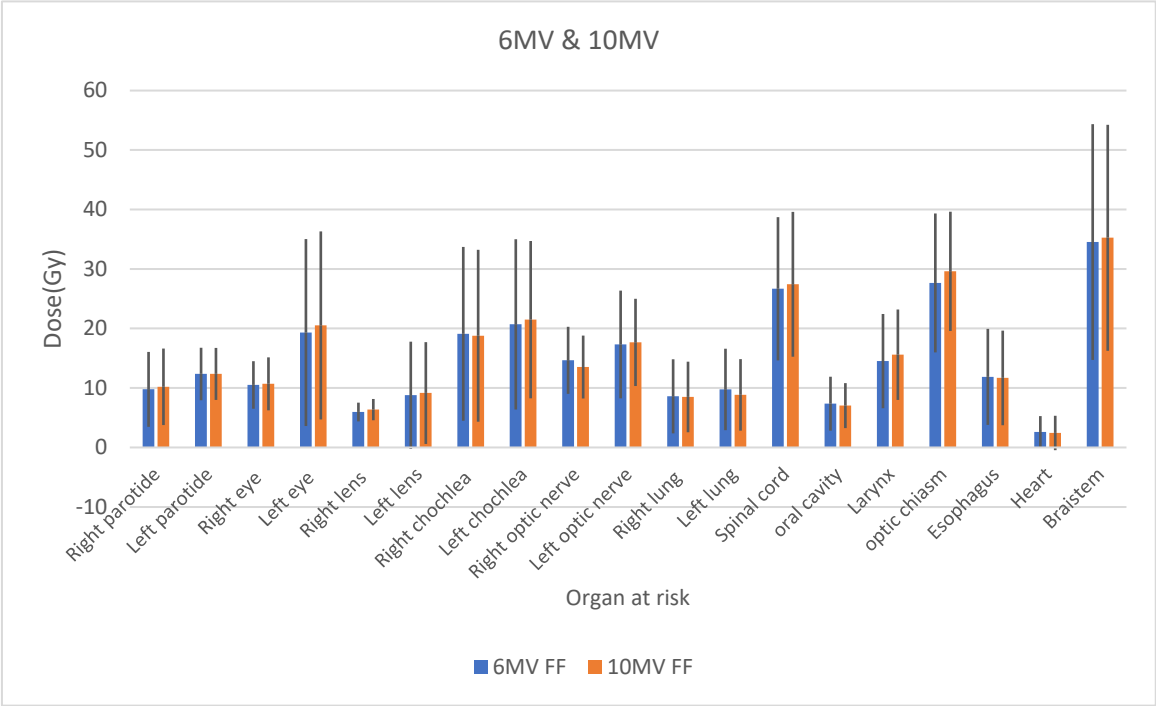

Figure 3. A comparison of the mean doses for the OARs of the H&N patients treated with VMAT technique with the FF beam type in both energies 6 MV and 10 MV.

3.3.2. Comparison between the mean values of the planning target volumes for FF beam type at 6 MV and 10 MV

The planning target volumes (PTV) treated with VMAT flattening filter (FF) beams at both 6 MV and 10 MV energies were analyzed. The dose received by 95% of the PTV (D95%) was nearly the same for both energies, with a significant difference (p = 0.009), as the 10 MV FF beam showed a slight reduction (33.17 Gy) compared to the 6 MV FF beam (33.63 Gy). Similarly, the dose to 98% of the PTV (D98%) was slightly reduced for the 10 MV beam (32.79 Gy) compared to the 6 MV FF beam (33.04 Gy), with a significant difference (p = 0.02).

The dose received by 50% of the PTV (D50%) was very similar between the two energies. The 6MV beam delivered a slightly higher dose (35.3 Gy) compared to the 10 MV FF beam (34.97 Gy), with no significant difference (p = 0.14). The dose received by 2% of the PTV (D2%), representing the highest dose region of the target, was nearly the same for both energy levels, with the 6 MV beam delivering a slightly higher dose (36.43 Gy) compared to the 10 MV FF beam (36.3 Gy), with no significant difference (p = 0.24). Overall, the 6 MV FF beam tends to deliver slightly higher doses to the PTV compared to the 10 MV FF beam.

Table 5. A Comparison between the mean value of the PTV of the H&N patients treated using the VMAT technique in both energies 6 MV and 10 MV with FF beam configuration

Planning target volumes	6MV		10MV	
	FF	SD	FF	SD
D95%	33.63	±12.92	33.17	±13.18
D98%	33.04	±12.67	32.79	±12.80
D50 %	35.3	±13.46	34.97	±13.37
D2 %	36.43	±13.83	36.38	±13.89

3.3.3. Comparison between the dosimetric parameters for the FF beam type at 6 MV and 10 MV

A conformity index value of 1 indicates perfect alignment between the dose and the target volume for both 6MV and 10MV beams. In this case, the 6 MV FF beam demonstrates a slightly better homogeneity index (0.086) compared to the 10 MV FF beam (0.1), with a significant difference ($p = 0.04$) between the two energies.

Regarding the number of segments, the 10 MV FF beam requires slightly more segments (271) compared to the 6 MV FF beam (259.42), with no significant difference ($p = 0.3$). Additionally, the 10 MV FF beam requires more monitor units (1093.8 MU) than the 6 MV FF beam (1028.6 MU), with no significant difference ($p = 0.19$). Overall, while the 6 MV FF beam shows slightly better homogeneity and higher doses to small volumes, both energies exhibit similar dosimetric characteristics.

Table 6. A comparison between the dosimetric parameters using the VMAT technique in both energies 6 MV and 10 MV with FF beam type

Dosimetric parameters	6MV		10MV	
	FF	SD	FF	SD
conformity index	1	Identical	1	Identical
homogeneity index	0.086	±0.01	0.1	±0.02
Number of segments	259.42	±179.03	271	±195.45
Monitor unit	1028.6	±341.04	1093.8	±328.24

3.4. Comparison between the energies 6 and 10 MV for the FFF beam configuration

3.4.1. Comparison between the mean doses of the OARs

Figure 4 compares the OARs for 20 head and neck (H&N) patients treated with 6 MV and 10 MV using the VMAT technique with FFF beams. The brainstem (maximum dose) received the highest dose (35.03 Gy for 6MV FFF, 36.33 Gy for 10MV FFF), with no significant difference between the two energies ($p = 0.18$). The heart (mean dose) received the lowest dose (2.2 Gy for 6MV FFF, 2.45 Gy for 10MV FFF), also showing no significant difference ($p = 0.17$).

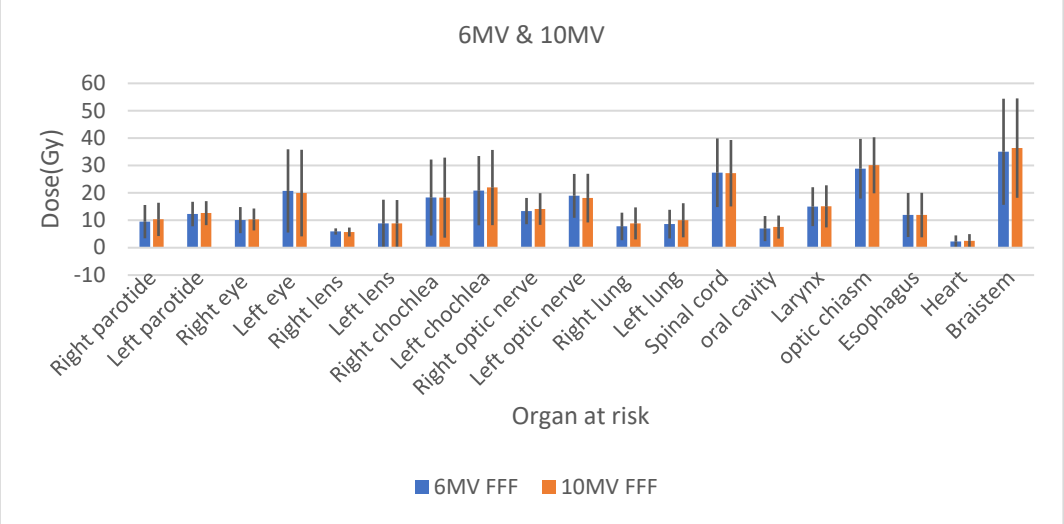

Figure 4. A comparison of the mean doses for the OARs of the H&N patients treated with VMAT technique with the FFF beam type in both energies 6 MV and 10 MV

Most OARs received slightly higher doses in the 10MV FFF beam type. The right parotid gland (mean dose) (9.5 Gy for 6MV FFF, 10.32 Gy for 10MV FFF) showed a significant difference ($p = 0.03$), while the left parotid gland (mean dose) (12.28 Gy for 6MV FFF, 12.6 Gy for 10MV FFF; $p = 0.23$) did not show a significant difference. Other OARs with no significant differences include the right eye (maximum dose) (10.04 Gy for 6MV FFF, 10.3 Gy for 10MV FFF; $p = 0.35$), left cochlea (mean dose) (20.81 Gy for 6MV FFF, 21.95 Gy for 10MV FFF; $p = 0.14$), right optic nerve (maximum dose) (13.34 Gy for 6MV FFF, 14.1 Gy for 10MV FFF; $p = 0.27$), right lung (mean dose) (7.75 Gy for 6MV FFF, 8.85 Gy for 10MV FFF; $p = 0.15$), left lung (mean dose) (8.5 Gy for 6MV FFF, 10 Gy for 10MV FFF; $p = 0.14$), larynx (mean dose)

(14.97 Gy for 6MV FFF, 15.07 Gy for 10MV FFF; p = 0.44), optic chiasm (maximum dose) (28.82 Gy for 6MV FFF, 30.08 Gy for 10MV FFF; p = 0.20), and esophagus (mean dose) (11.91 Gy for 6MV FFF, 11.92 Gy for 10MV FFF; p = 0.46).

A few OARs received slightly higher doses in the 6MV FFF beam type, but these differences were not significant: left eye (maximum dose) (20.72 Gy for 6MV FFF, 19.92 Gy for 10MV FFF; p = 0.28), right lens (maximum dose) (5.9 Gy for 6MV FFF, 5.69 Gy for 10MV FFF; p = 0.29), left lens (maximum dose) (8.82 Gy for 6MV FFF, 8.8 Gy for 10MV FFF; p = 0.48), right cochlea (mean dose) (18.28 Gy for 6MV FFF, 18.26 Gy for 10MV FFF; p = 0.48), left optic nerve (maximum dose) (18.92 Gy for 6MV FFF, 18.1 Gy for 10MV FFF; p = 0.25), and spinal cord (maximum dose) (27.33 Gy for 6MV FFF, 27.18 Gy for 10MV FFF; p = 0.36).

3.4.2. Comparison between the mean values of the planning target volumes for FFF beam configuration at 6 MV and 10 MV

From Table 7, one can notice that the dose to 95% of the PTV (D95%) was slightly lower for the 10 MV FFF beam (33.4 Gy) compared to the 6 MV FFF beam (33.57 Gy), with no significant difference (p = 0.13). Similarly, the dose to 98% of the PTV (D98%) was also slightly lower for the 10 MV FFF beam (32.68 Gy) compared to the 6 MV FFF beam (32.83 Gy), showing no significant difference (p = 0.18). The dose to 50% of the PTV (D50%) was very similar between the two energies, with a marginal difference (35.33 Gy for FFF 6 MV, 33.21 Gy for FFF 10 MV) and no significant difference (p = 0.14).

The dose to the 2% of the PTV (D2%), which represents the highest dose region within the target volume, was slightly lower with the 10 MV FFF beam (36.31 Gy) compared to the 6 MV FFF beam (36.48 Gy). This difference was statistically significant (p = 0.01).

Overall, the results indicate that the 6 MV FFF beam delivers slightly higher doses to the PTV compared to the 10 MV FFF beam, particularly in the highest dose region.

Table 7. A Comparison between the mean value of the PTV of the H&N patients treated using the VMAT technique in both energies 6 MV and 10 MV with FFF beam type.

planning target volume	6MV		10MV	
	FFF	SD	FFF	SD
D95%	33.57	±12.97	33.4	±13.18
D98%	32.84	±12.83	32.68	±12.80
D50%	35.33	±13.54	35.21	±13.37
D2%	36.48	±13.84	36.31	±13.89

3.4.3. Comparison between the dosimetric parameters for the FFF beam type at 6 MV and 10 MV

From Table 8, The conformity index (CI) for both 6 MV and 10 MV with FFF beams is 1, indicating perfect alignment between the dose and the target volume. The 10 MV FFF beam demonstrates a slightly better homogeneity index (HI) of 0.098 compared to 0.104 for the 6MV FFF beam, with no statistically significant difference (p = 0.19).

The 10 MV FFF beam uses slightly more segments (328) compared to the 6 MV FFF beam (290.69), with no statistically significant difference (p = 0.22). Additionally, the 10 MV FFF beam requires more monitor units (1579.4 MU) compared to the 6 MV FFF beam (1390.6 MU), though this difference is not significant (p = 0.09).

In terms of delivery time on the Elekta linac using the VMAT technique for 20 head and neck cases, the FFF beam configuration generally showed reduced delivery times compared to the FF beam type. The FF technique took about 3 minutes to 3 minutes and 20 seconds, while the FFF beam configuration was approximately a minute shorter, ranging from 2 minutes to 2 minutes and 20 seconds.

Table 8. A comparison between the dosimetric parameters using the VMAT technique in both energies 6 MV and 10 MV with FFF beam type.

Dosimetric parameters	6MV		10MV	
	FFF	SD	FFF	SD
conformity index (CI)	1	Identical	1	Identical
homogeneity index (HI)	0.104	±0.02	0.098	±0.02
Number of segments	290.69	±215.97	328	±243.88
Monitor unit	1390.6	±475.58	1579.4	±823.88

3.5. Biological parameters NTCP (%) and EUD (Gy) for the OARs

3.5.1 Comparison between the mean values of biological parameter (NTCP) of the organs at risk for both types at 6 MV.

From Table 9, the spinal cord, esophagus, and heart showed identical values. The NTCP values of the brainstem were higher compared to the other organs in both types. They also in case of using the FFF technique, it was slightly lower than that in case of using FF, and there was a statistically significant difference, where the p-value is 0.0005.

Table 9. A Comparison between the mean value of the NTCP (%) the H&N patients treated using the VMAT technique with the energy 6 MV in both FF and FFF types.

	NTCP	
	6MV FF	6MV FFF
Spinal cord	0	0
esophagus	0	0
Heart	0	0
Brainstem	1.9	1.7

3.5.2 Comparison between the mean values of biological parameter (NTCP) of OARs for both beam types at 10 MV

From Table 10, it can be noticed that the heart and esophagus had identical values, but the spinal cord and brainstem had different values, where in the spinal cord, there was no statistically significant difference (p-value = 0.2), unlike the brainstem, which had slightly higher values. Also, FFF had a lower value. There was a significant difference, where the p-value is 0.

Table 10. Comparison between the mean value of the NTCP (%) of the H&N patients treated using the VMAT technique with the energy 10 MV in both FF and FFF beam types.

	NTCP	
	10MV FF	10MV FFF
Spinal Cord	0.00018	0.00026
esophagus	0	0
Heart	0	0
Brainstem	1.75	0.54

3.5.3 Comparison between the mean values of biological parameter (NTCP) of organ at risk between the energies 6 and 10 MV for the FF beam type

According to Table 11, the heart and esophagus exhibited identical values across both techniques. In contrast, the spinal cord showed slightly higher values with the 10 MV FF technique, although this difference was not statistically significant (p = 0.2). The brainstem presented different values between techniques, with the 10 MV FF technique yielding a slightly lower value, which was statistically significant (p = 0.0005).

Table 11. Comparison between the mean value of the NTCP (%) the H&N patients treated using the VMAT technique in both energies 6 MV and 10 MV with FF beam configuration.

	NTCP	
	6MV FF	10MV FF
S. cord	0	0.00018
esophagus	0	0
Heart	0	0
Brainstem	1.9	1.75

3.5.4 Comparison between the mean values of biological parameter (NTCP) of organ at risk between the energies 6 and 10 MV for the FFF beam type

Table 12 shows that the heart and esophagus demonstrated identical values across both techniques. The spinal cord exhibited a slightly higher value in the 10 MV FFF beam type; however, this difference was not statistically significant (p = 0.2). In contrast, the brainstem showed a lower value in the 10MV FFF beam type, with the difference reaching statistical significance (p = 0.00000332).

Table 12. Comparison between the mean value of the NTCP (%) of H&N patients treated using the VMAT technique in both energies 6 MV and 10 MV with FFF beam configuration.

	NTCP	
	6MV FFF	10MV FFF
S. cord	0	0.00026
esophagus	0	0
Heart	0	0
Brainstem	1.7	0.54

3.5.5 Comparison between the mean values of biological parameter (EUD) of organ at risk for both types at 6 MV

Figure 5 demonstrates that the variations between the FF and FFF techniques were marginal, with the FFF approach producing marginally reduced doses in all examined organs at risk (OARs). Nonetheless, for the spinal cord and esophagus, the observed discrepancies lacked statistical significance (p = 0.07 and p = 0.2, respectively). Conversely,

pronounced differences were noted for the heart and brainstem, both exhibiting statistically significant deviations (p = 0.0 in each case). This hypothesizes that while the two techniques deliver largely similar doses to most OARs**,** the FFF beam type may lead to slightly reduced exposure for certain critical structures**,** particularly the heart and brainstem.

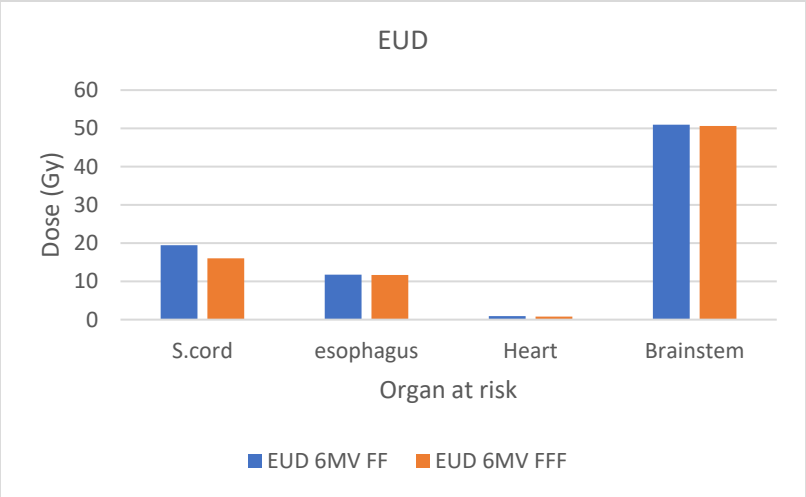

Figure 5. A Comparison between the mean value of the EUD of H&N patients treated using the VMAT technique with the energy 6 MV in both FF and FFF types.

3.5.6 Comparison between the mean values of the biological parameter (EUD) of the organ at risk for both beam configurations at 10 MV

Figure 6 presents the Equivalent Uniform Dose (EUD) delivered to various organs at risk (OARs) using the 10MV FF and 10MV FFF techniques. Overall, the differences in EUD between the two techniques are minimal. For the spinal cord and esophagus, the EUD values are nearly identical, indicating no significant variation between FF and FFF beam configurations (p = 0.4 and p = 0.2, respectively). In contrast, the heart shows a noticeable reduction in EUD with the FF technique, although the absolute dose remains very low for both techniques. The brainstem exhibits the highest EUD among all OARs, with a significantly lower value observed in the FF beam configuration compared to FFF (p = 0.0). This suggests that while both techniques offer comparable protection for most OARs, the FF technique may offer improved sparing of critical structures such as the brainstem and heart.

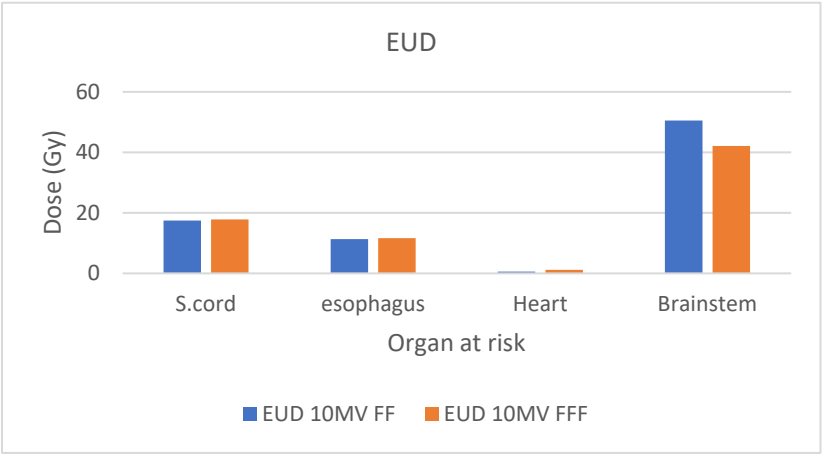

Figure 6. A Comparison between the mean value of the EUD of H&N patients treated using the VMAT technique with the energy 10 MV in both FF and FFF beam types.

3.5.7 Comparison between the mean values of biological parameter (EUD) of organ at risk between the energies 6 and 10 MV for the FF beam type

Figure 7 compares the Equivalent Uniform Dose (EUD) delivered to various organs at risk (OARs) using the 10MV FF and 6MV FF techniques. The the 10MV FF energy yielded slightly lower EUD values than 6MV FF across all OARs. For the spinal cord and esophagus, no significant differences were observed between the two techniques (p = 0.13 and p = 0.24, respectively). In contrast, the heart and brainstem exhibited significant reductions in EUD with the 10MV FF technique, with p-values of 0 and 0, respectively. These findings suggest that while both photon energies provide comparable sparing for certain OARs, the 10MV FF technique may offer improved dose reduction for critical structures such as the heart and brainstem.

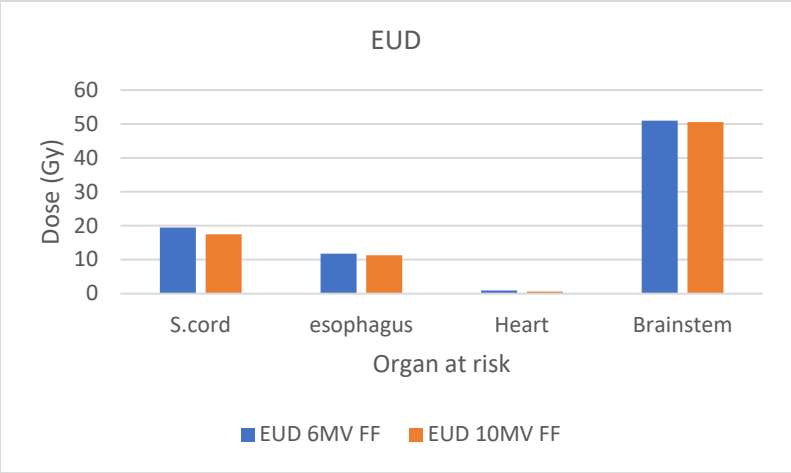

Figure 7. Comparison between the mean value of the EUD of H&N patients treated using the VMAT technique in both energies 6 MV and 10 MV with FF beam type.

3.5.8 Comparison between the mean values of biological parameter (EUD) of organ at risk between the energies 6 and 10 MV for the FFF beam type

Figure 8 evaluates the dose distribution between 10MV FFF and 6MV FFF for selected organs at risk (OARs). The esophagus and brainstem exhibited slightly lower doses with the 10MV FFF technique, whereas the heart and spinal cord received marginally lower doses with 6MV FFF. No significant differences were observed between the two energies for the spinal cord and esophagus ($p = 0.2$ for both). In contrast, statistically significant differences were found for the heart and brainstem, with p-values of 0 and 0, respectively. These results indicate that while the two FFF energies perform similarly for some OARs, the choice of energy may influence dose sparing in critical structures such as the heart and brainstem.

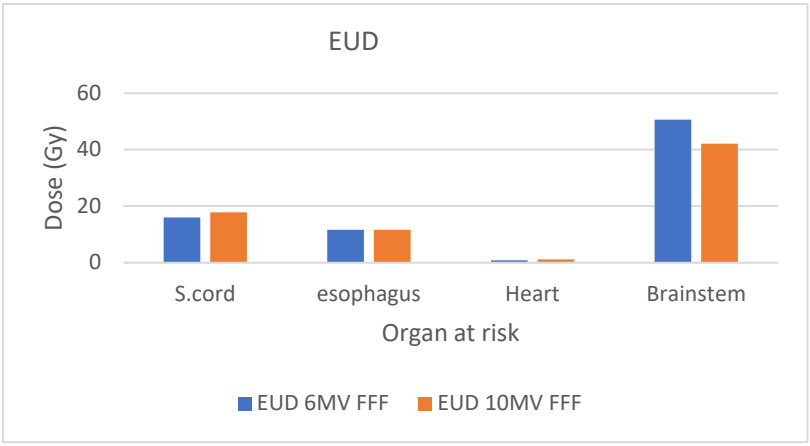

Figure 8. Comparison between the mean value of the EUD of H&N patients treated using the VMAT technique in both energies 6 MV and 10 MV with FFF beam type.

3.6 Second cancer risk estimation (%) for OARs of 20 patients:

3.6.1 Comparison between the mean values of Second cancer risk estimation of organ at risk for both beam types at 6MV.

Table 13 demonstrates subtle but notable differences between the two techniques. Both parotid glands received slightly lower doses in FFF beam type, with statistically significant differences observed (right parotid: $p = 0.00049$; left parotid: $p = 0.0013$). In contrast, the larynx showed reduced dose exposure in FF beam configuration, though this difference was also statistically significant ($p = 0.0005$). These findings suggest that while both techniques achieve clinically acceptable dose distributions, the choice between FF and FFF beam configurations may impact specific anatomical structures differently.

Table 13. Comparison between the mean value of the second cancer risk estimation (%) of H&N patients treated using the VMAT technique in the energy 6MV in both FF and FFF beam types.

OAR	6MV FF	SD	6MV FFF	SD
Right parotid	0.49	±0.31	0.48	±0.30
Left parotid	0.62	±0.22	0.61	±0.22
Larynx	0.73	±0.39	0.75	±0.35

3.6.2 Comparison between the mean values of Second cancer risk estimation of organ at risk for both beam types at 10MV.

Table 14 reveals consistent dose variations between the techniques. Both parotid glands demonstrated slightly higher doses in FFF beam type (right parotid: $p = 0.002$; left parotid: $p = 0.002$), while the larynx received marginally higher doses in FF beam type ($p = 0.0002$). All three comparisons showed statistically significant differences. These findings suggest that while absolute dose differences are modest, they may warrant consideration in clinical applic±ations where these organs are particularly at risk.

Table 14. Comparison between the mean value of the second cancer risk estimation (%) of H&N patients treated using the VMAT technique in the energy 10MV in both FF and FFF beam configurations.

OAR	10MV FF	SD	10MV FFF	SD
Right parotid	0.51	±0.32	0.52	±0.3
Left parotid	0.62	±0.65	0.63	±0.58
Larynx	0.78	±0.38	0.75	±0.38

3.6.3 Comparison between the mean values of Second cancer risk estimation of organ at risk between the energies 6 and 10MV for the FF beam type.

Table 15 demonstrates differential dose distribution patterns between the techniques. While the left parotid showed identical doses for both modalities, the 10MV FF technique yielded slightly higher doses to both the right parotid ($p = 0.0001$) and larynx ($p = 0.0002$), with these differences reaching statistical significance. These findings indicate that while some structures may receive equivalent doses regardless of technique, others exhibit energy-dependent variations that may warrant consideration in treatment planning.

Table 15. Comparison between the mean value of the second cancer risk estimation (%) of H&N treated using the VMAT technique in both energies 6 MV and 10 MV with FF beam configuration.

OAR	6MV FF	SD	10MV FF	SD
Right parotid	0.49	±0.31	0.51	±0.32
Left parotid	0.62	±0.22	0.62	±0.65
Larynx	0.73	±0.39	0.78	±0.38

3.6.4 Comparison between the mean values of Second cancer risk estimation of organ at risk between the energies 6 and 10MV for the FFF beam type

Table 16 reveals distinct dose distribution patterns between the evaluated techniques. While the larynx demonstrated identical dose values for both modalities, both parotid glands exhibited slightly elevated doses with statistically significant differences (right parotid: $p = 0.0001$; left parotid: $p = 0.0005$). This differential effect suggests that while laryngeal dose remains consistent regardless of technique selection, parotid gland doses show technique-dependent variations that may influence clinical decision-making, particularly in cases where parotid sparing is prioritized.

Table 16. Comparison between the mean value of the second cancer risk estimation (%) of H&N treated using the VMAT technique in both energies 6 MV and 10 MV with FFF f.

OAR	6MV FFF	SD	10MV FFF	SD
Right parotid	0.48	±0.30	0.52	±0.3
Left parotid	0.61	±0.22	0.63	±0.58
Larynx	0.75	±0.35	0.75	±0.38

4. DISCUSSION

This study presents the dosimetric and biological differences in treatment plans using flattened (FF) and flattening-filter-free (FFF) beams in the treatment of Head and Neck Cancer, focusing on the influence and impact of energy (6 MV and 10 MV beams) on volumetric modulated arc therapy (VMAT) plans. While extensive research has been conducted on Varian FFF beams (Varian Medical System, Palo Alto, CA, USA), limited literature is available on Elekta FF beams (Elekta Oncology Systems, Crawley, UK) for this specific site.

Previous studies, such as those by Gasic et al. [9] and Ji et al. [10], have explored the potential of using FFF beams for various treatment sites, including the head and neck, brain, prostate, and lung cancer. Our findings align with these studies, demonstrating that the 6 MV FFF beam offers a slightly improved dose-sparing effect for most organs at risk (OARs) compared to the 6 MV FF beam. This improvement means that the 6 MV FFF beam can more efficiently reduce the radiation dose delivered to critical surrounding tissues, as supported by Kumar et al. [1].

According to the results of this study, the planning target volumes (PTV) for both 6 MV FF and FFF beams showed very similar dose distributions, with only minor variations. This indicates that FFF VMAT plans provide comparable results

to FF VMAT plans, as reported by Kumar et al. [5] and Manna et al. [11]. Both techniques exhibited equal conformity index (CI), but the FF beam had a better homogeneity index (HI). Additionally, FFF beams required significantly higher monitor units (MUs) due to their conic shape dose distribution, necessitating compensation through a greater number of smaller segments and MUs, as observed in previous studies (Lechner et al. [13], Vassiliev et al. [14], and Sun et al. [15]).

Regarding the delivery time, the FFF beam type generally showed reduced times compared to the FF beam configuration. This reduction in delivery time leads to less machine operating time, ultimately lowering the treatment cost, and this is agreed with a study by Thomas et al. [16].

For the 10 MV FF beam, a more noticeable advantage in reducing the radiation dose delivered to critical structures was observed, with a statistically significant difference in the dose to the lungs. Both 10 MV FF and FFF beam plans delivered similar dose distributions, with FFF slightly outperforming FF in terms of dose to 95% and 50% of the target volume. However, the differences between the plans were not significant.

Both 6 MV and 10 MV FF plans showed very similar dose distributions and coverage, with slight differences in sparing OARs. The 6 MV FF plan demonstrated better dose homogeneity and a statistically significant difference for the right lens compared to the 10 MV FF plan. The 10 MV FF plan required more segments and higher MUs, leading to increased treatment time and cost.

Therefore, the differences in dose distribution between the 6 MV FFF and 10 MV FFF beams are minor, with the 6 MV FFF beam delivering slightly higher doses at each percentile than the 10 MV FFF beam. Both configurations yield comparable dosimetric results, with the 10 MV FFF beam offering marginally better dose homogeneity but requiring a higher number of segments and MUs.

Previous research has shown that variations in dose can have a substantial impact on radiobiological factors related to NTCP Srivastava et al. [17], potentially influencing the quality of radiotherapy. As a result, assessing NTCP is a critical component when comparing the two technologies, Aly et al. [7], Wu et al. [18].

The biological parameter (NTCP) results were identical for all OARs across techniques and energies except for the spinal cord, though this difference was not statistically significant ($p>0.05$). These findings align with Aras et al. [19] who found FF and FFF beams produced similar results, and Kang et al. [20] who reported minimal radiobiological differences. However, the brainstem showed significant differences ($p<0.05$) across all techniques and energies, with FFF beam type demonstrating reduced values compared to FF, consistent with Wu et al. [18].

For the EUD, no significant difference was observed between FFF (Flattening-Filter-Free) and FF (Flattening-Filter) beam types in the spinal cord and esophagus across all energy levels. However, statistically significant differences were noted for the heart and brainstem in all beam types, as well as when comparing energy levels also the results were lower in FFF but both beam configurations yields comparable results.

For the second cancer risk estimation, statistically significant differences were observed across all comparisons for the left parotid, right parotid, and larynx except for two cases: (1) the left parotid risk was identical between 6MV FF and 10MV FF, and (2) the larynx risk was identical between 6MV FFF and 10MV FFF.

Overall, 6MV FFF beam type slightly reduced the risk to the parotids (supported by Alvarez et al. [21] and Treutwein et al. [22, 23]) but increased the risk to the larynx. Conversely, 10MV FFF beam type increased the parotid risk while reducing the larynx risk. When comparing energies, 10MV exhibited a slightly higher second cancer risk in the parotids than 6MV, particularly in FFF beam configuration. For the larynx, the risk was similar between the two energies in FFF beam type but higher with 10MV in FF beam type.

10MV shows a slightly higher risk in some OARs, but again, the difference is very small, the choice between FF/FFF or 6MV/10MV should prioritize target coverage and normal tissue sparing rather than second cancer risk, given the minimal differences observed

This study contributes valuable insights by comparing both techniques (flattening filter and without the flattening filter) at both energy levels (6 MV and 10 MV) in head and neck cancer treatments using the VMAT technique on the Elekta Versa. However, it is important to note that these findings are based on planning data.

5. CONCLUSIONS

This study provides a comprehensive analysis of the dosimetric and biological and second cancer risk estimation differences between flattened (FF) and flattening-filter-free (FFF) beams and the impact of using both 6 MV and 10 MV energies for Head and Neck Cancer treatment plans using Volumetric Modulated Arc Therapy (VMAT). Our findings indicate that both FF and FFF techniques yield comparable biological and dosimetric outcomes in terms of sparing organs at risk (OARs) and target volume coverage, and second cancer risk estimation.

For the 6 MV FFF beam, there is a slight improvement in dose-sparing for OARs, while the 6 MV FF beam provides a better homogeneity index. The 6 MV FFF configuration required more monitor units and segments (with statistically significant differences) but offered reduced delivery times, leading to more efficient treatment and lower operational costs.

In contrast, the 10 MV FFF beam showed marginally better dose homogeneity and a slight advantage in sparing normal tissue at lower doses. The 10 MV FFF slightly outperformed FF in terms of dose coverage to 95% and 50% of the target volume. The 10 MV FFF plan required additional segments and monitor units (with statistically significant differences), resulting in a slight decrease in treatment time and cost.

It can be concluded that when comparing the impact of the energies, results were very comparable, with a slight advantage for the 6 MV over the 10 MV in sparing OARs and planning target volume coverage, as well as in dosimetric parameters.

Also, this study demonstrates that while radiobiological outcomes between FF and FFF beam types are largely comparable, FFF beams, particularly at 6MV, offer slight advantages in reducing doses to critical structures such as the brainstem and parotids without compromising treatment efficacy. Overall, both FF and FFF beam configurations provided similar outcomes, with minor variations in risk based on energy levels. These results suggest that FFF techniques, particularly at 6MV, offer a feasible approach to reducing dose to critical organs while maintaining treatment efficacy, without significantly altering the overall second cancer risk profile.

ORCID

Reham S. Sherif, https://orcid.org/0009-0009-4374-7212; **Limam A. Neya,** https://orcid.org/0009-0005-1973-6055
Ahmed M. Abdelaal, https://orcid.org/0000-0002-3092-8147; **Ehab M. Attalla,** https://orcid.org/0000-0003-4779-4445
Reem H. El-Gebaly, https://orcid.org/0000-0002-7673-0785

REFERENCES

[1] A. Kumar, K. Sharma, C.P. Bhatt, and A. Garg, "Dosimetric comparison of unmatched flattening filter-free and flattened beams in volumetric arc therapy plans for head-and-neck cancer," J. Med. Phys. **48**, 338-344 (2023). https://doi.org/10.4103/jmp.jmp_68_23
[2] G. Anderson, M. Ebadi, K. Vo, J. Novak, A. Govindarajan, and A. Amini, "An Updated Review on Head and Neck Cancer Treatment with Radiation Therapy," Cancers, **13**, 4912 (2012). https://doi.org/10.3390/cancers13194912
[3] Y. Yan, P. Yadav, M. Bassetti, K. Du, D. Saenz, P. Harari, *et al*., „Dosimetric differences in flattened and flattening filter free beam treatment plans," J. Med. Phys. **41**, 92-99 (2016).
[4] E. Quan, X. Li, Y. Li, X. Wang, R.J. Kudchadker, J.L. Johnson, D. Kuban, *et al*., "A comprehensive comparison of IMRT and VMAT plan quality for prostate cancer treatment," Int. J. Radiat. Oncol. Biol. Phys. **83**(4), 1169–1178 (2012). https://doi.org/10.1016/j.ijrobp.2011.09.015
[5] S.A. Kumar, M.M. Musthafa, C.A. Suja, K.B. Resmi, J. Lisha, G. Muttath, and K.P. Shahirabanu, "Dosimetric comparison of FF and FFF beams in VMAT treatment plans of head and neck cancers," Oncology and Radiotherapy, **15**(7), 1-5 (2021).
[6] D.M. Ghemis, and L.G. Marcu, "Dosimetric Parameters in Hypofractionated Stereotactic Radiotherapy for Brain Metastases: Do Flattening Filter-Free Beams Bring Benefits? A Preliminary Study," Cancers, **15**, 678 (2023). https://doi.org/10.3390/cancers15030678
[7] A. Wagdy, E. Attalla, H. Ashry, T. Eldsoky, "Comparative study between Volumetric Modulated Arc therapy plans using FF and FFF beam in case of head and neck cancer," Journal of Scientific Research in Science, **39**(1), 47-60 (2022).
[8] R.S. Sherif, W.M. Elshemey, and E.M. Attalla, "The risk of secondary cancer in pediatric medulloblastoma patients due to three-dimensional conformal radiotherapy and intensity-modulated radiotherapy," Indian J. Cancer, **55**(4), 372-376 (2018). https://doi.org/10.4103/ijc.IJC_410_18
[9] D. Gasic, L. Ohlhues, N.P. Brodin, L.S. Fog, T. Pommer, J.P. Bangsgaard, and P.M. Rosenschöld, "A treatment planning and delivery comparison of volumetric modulated arc therapy with or without flattening filter for gliomas, brain metastases, prostate, head/neck and early-stage lung cancer," Acta Oncologica, **53**(8), 1005-1011 (2014). https://doi.org/10.3109/0284186X.2014.925578
[10] T. Ji, L. Sun, F. Cai, G. Li, "Comparison between flattening filter-free (FFF) and flattened photon beam VMAT plans for the whole brain radiotherapy (WBRT) with hippocampus sparing," Asia Pac. J. Clin. Oncol. **18**, e263-7 (2022). https://doi.org/10.1111/ajco.13624
[11] S. Manna, S.H. Kombathula, S. Gayen, S. Varshney, and P. Pareek, "Dosimetric impact of FFF over FF beam using VMAT for brain neoplasms treated with radiotherapy," Polish Journal of Medical Physics and Engineering The Journal of Polish Society of Medical Physics, 27, (2021). https://doi.org/10.2478/pjmpe-2021-0023
[12] M. Zhuang, T. Zhang, Z. Chen, Z. Lin, D. Li, *et al*., "Advanced nasopharyngeal carcinoma radiotherapy with volumetric modulated arcs and the potential role of flattening filter-free beams," Radiat Oncol. **8**, 120 (2013). https://doi.org/10.1186/1748-717X-8-120
[13] W. Lechner, G. Kragl, and D. Georg, "Evaluation of treatment plan quality of IMRT and VMAT with and without flattening filter using Pareto optimal fronts," Radiotherapy and Oncology, **109**(3), 437-441 (2013). https://doi.org/10.1016/j.radonc.2013.09.020
[14] O.N.Vassiliev, U. Titt U, F. Pönisch, S.F. Kry, R. Mohan, M.T. Gillin, "Dosimetric properties of photon beams from a flattening filter free clinical accelerator," Phys. Med. Biol. **51**(7), 1907-1917 (2006). https://doi.org/10.1088/0031-9155/51/7/019
[15] W. Sun, L. Chen, X. Yang, B. Wang, X. Deng, and X. Huang, "Comparison of treatment plan quality of VMAT for esophageal carcinoma with: flattening filter beam versus flattening filter free beam," J. Cancer. **9**(18), 3263-3268 (2018). https://doi.org/10.7150/jca.26044
[16] E.M. Thomas, R.A. Popple, B.M. Prendergast, G.M. Clark, M.C. Dobelbower, J.B. Fiveasha, *et al*., "Effects of flattening filter-free and volumetric-modulated arc therapy delivery on treatment efficiency," J. Appl. Clin. Med. Phys. **14**, 155-166 (2013). https://doi.org/10.1120/jacmp.v14i6.4328
[17] S.P. Srivastava, C.W. Cheng, and I.J. Das, "The dosimetric and radiobiological impact of calculation grid size on head and neck IMRT," Practical radiation oncology, **7**(3), 209-217 (2017). https://doi.org/10.1016/j.prro.2016.10.001
[18] J. Wu, H. Song, J. Li, B. Tang, and F. Wu, "Evaluation of flattening-filter-free and flattening filter dosimetric and radiobiological criteria for lung SBRT: A volume-based analysis," Front. Oncol. **13**, 1108142 (2023). https://doi.org/10.3389/fonc.2023.1108142
[19] S. Aras, I.O. Tanzer, N. Sayir, M.S. Keles, and F.B. Ozgeris, "Radiobiological comparison of flattening filter (FF) and flattening filter-free (FFF) beam in rat laryngeal tissue," International journal of radiation Biology, **97**(2), 249-255 (2021). https://doi.org/10.1080/09553002.2021.1857457
[20] S.W. Kang, S. Kang, B. Lee, C. Song, K.Y. Eom, B.S. Jang, *et al*., "Evaluation of the dosimetric and radiobiological parameters in four radiotherapy regimens for synchronous bilateral breast cancer," Journal of Applied Clinical Medical Physics, **23**(8), e13706 (2022). https://doi.org/10.1002/acm2.13706

[21] J.A. Moret, T. Obermeier, F. Pohl, R. Loeschel, O. Koelbl, and B. Dobler, "Second cancer risk after radiation therapy of ependymoma using the flattening filter free irradiation mode of a linear accelerator," Journal of Applied Clinical Medical Physics, **19**(5), 632-639 (2018). https://doi.org/10.1002/acm2.12438
[22] M. Treutwein, F. Steger, R. Loeschel, O. Koelbl, and B. Dobler, "The influence of radiotherapy techniques on the plan quality and on the risk of secondary tumors in patients with pituitary adenoma," BMC Cancer, **20**, 1-13 (2020). https://doi.org/10.1186/s12885-020-6535-y
[23] M. Treutwein, R. Loeschel, M. Hipp, O. Koelbl, and B. Dobler, "Secondary malignancy risk for patients with localized prostate cancer after intensity-modulated radiotherapy with and without flattening filter," Journal of Applied Clinical Medical Physics, **21**(12), 197-205 (2020). https://doi.org/10.1002/acm2.13088

ОПТИМІЗАЦІЯ ПРОМЕНЕВОЇ ТЕРАПІЇ РАКУ ГОЛОВИ ТА ШИЇ: ДОЗИМЕТРИЧНЕ ПОРІВНЯННЯ ПРОМЕНІВ FF ТА FFF У VMAT

Рехам С. Шеріф[1], Лімам А. Нея[2], Ахмед М. Абделаал[2], Ехаб М. Атталла[3], Рім Х. Ель-Гебалі[1]
[1]Кафедра біофізики, Факультет природничих наук, Каїрський університет, Гіза, Єгипет
[2]Інститут Насера, Каїр, Єгипет
[3]Кафедра радіотерапії та ядерної медицини, Національний інститут раку, Каїрський університет, Каїр, Єгипет

Мета: Рак голови та шиї (РГШ) є значною глобальною проблемою охорони здоров'я, зі зростанням захворюваності та високою поширеністю в Південній Азії, особливо в Індії. Променева терапія, включаючи передові методи, такі як об'ємно-модульована дугова терапія (VMAT) та інтенсивно-модульована радіотерапія (IMRT), відіграє вирішальну роль у лікуванні РГШ. Це дослідження має на меті порівняти дозиметричні та біологічні відмінності в оцінці ризику раку, а також вторинної оцінки між сплющеними (FF) та сплющеними пучками без фільтра (FFF) у планах лікування HNC за допомогою VMAT, зосереджуючись на впливі енергій 6 MV та 10 MV. **Методи:** Двадцять пацієнтів з HNC пройшли повторне планування з використанням VMAT на лінійному прискорювачі ELEKTA VERSA HD з пучками потужністю 6 MV FF, 6 MV FFF, 10 MV FF та 10 MV FFF. Оцінювані дозиметричні параметри включали розподіл дози на об'єми планової мішені (PTV) та дозу, що доставляється до 98% мішені (D98), 50% (D50) та 2% (D2), а також дози на органи, що знаходяться в групі ризику (OAR), одиниці моніторингу на сегмент (MU/сегмент), кількість MU/cGy, час проведення лікування, індекс відповідності та індекс однорідності, а також були оцінені біологічні параметри (NTCP та EUD) та вторинна оцінка ризику раку. **Результати:** Результати показали, що 6-мегавольтні пучки FFF забезпечили дещо кращу економність дози для OAR порівняно з 6-мегавольтними FF, без суттєвих відмінностей у покритті цільового об'єму. Як пучки FF, так і FFF продемонстрували порівнянні показники конформності, але пучки FF мали кращі показники однорідності. Пучки FFF вимагали більше моніторних одиниць (MU) та сегментів, але пропонували менший час проведення лікування. Для 10-мегавольтних пучків FFF показав незначні переваги в однорідності дози та щадінні нормальних тканин при нижчих дозах, хоча й вимагав більше MU та сегментів. Це дослідження показало, що NTCP та EUD були значною мірою порівнянні між типами FF та FFF, з незначними, але статистично значущими відмінностями для стовбура мозку (на користь FFF) та серця. Ризики вторинного раку дещо відрізнялися залежно від енергії та техніки. 6-мегавольтний FFF знизив ризики привушних залоз (хоча збільшив ризик гортані). **Висновок:** 6-мегавольтні пучки, особливо FFF, показали незначні переваги у щадінні OAR та покритті цільового об'єму порівняно з 10-мегавольтними пучками. Це дослідження підкреслює дозиметричну порівнянність пучків FF та FFF у лікуванні раку голови та шиї, причому FFF пропонує потенційні переваги в ефективності лікування та скороченні часу проведення опромінення. Це дослідження також показує, що типи FF та FFF дають порівнянні радіобіологічні результати, хоча пучки FFF потужністю 6 MV дещо знижують дози на критичні органи без шкоди для ефективності. Обидва типи працюють подібно, з незначними варіаціями ризику залежно від енергії.

Ключові слова: *рак голови та шиї; об'ємно-модульована дугова терапія (VMAT); фільтр зі сплющенням (FF); безфільтровий фільтр зі сплющенням (FFF); 6 MV; 10 MV*

EAST EUROPEAN JOURNAL OF PHYSICS. 4. 575-581 (2025)
DOI:10.26565/2312-4334-2025-4-60 ISSN 2312-4334

DEVELOPMENT AND EVALUATION OF 3D-PRINTED HOMOGENEOUS AND HETEROGENEOUS PHANTOMS FOR QUALITY ASSURANCE IN RADIATION THERAPY

V. Vashchyshyn[1]*, O. Bezshyyko[2§], L. Golinka-Bezshyyko[2]
[1]Radiotherapy Department, Universal Clinic "Oberig", Kyiv, Ukraine
[2]Taras Shevchenko National University of Kyiv, Kyiv, Ukraine
**Corresponding Author E-mail: v.vashchyshyn@oberig.ua; §obezsh@gmail.com*
Received August 2, 2025; revised September 15, 2025; accepted September 30, 2025

Background: Affordable and locally manufacturable quality assurance (QA) phantoms are critical for maintaining accuracy in radiation therapy, particularly in low-resource settings. This study evaluates the radiological and dosimetric performance of 3D-printed homogeneous and heterogeneous phantoms against commercial standards.

Methods: Two phantom prototypes were developed: a homogeneous model fabricated from PMMA and a heterogeneous model composed of EVA, PLA, MDI-based foam, and gypsum–chalk composite. Radiological properties were assessed using CT imaging with three reconstruction kernels (Hp38, Bf39, Hr32) at slice thicknesses of 1–3 mm. Hounsfield Units (HU) were compared with reference values from the Easy Slab (IBA) and CatPhan 604. Dosimetric validation was performed with Eclipse TPS (v16.1) using 15 3D-CRT and 15 VMAT plans, delivered on Varian TrueBeam (6 MV, 6 MV FFF, 10 MV, 10 MV FFF) and Halcyon (6 MV FFF) accelerators. Point doses were measured with a calibrated Farmer chamber.

Results: The homogeneous PMMA phantom demonstrated HU stability within ±5 HU of the reference values across all kernels, with standard deviations of less than 3 HU. EVA and gypsum–chalk provided tissue-equivalent and bone-equivalent imaging properties (20 ± 3 HU and 1200 ± 15 HU, respectively), while PLA and MDI foam demonstrated excessive variability (>40 HU kernel dependence). Dosimetrically, the homogeneous phantom achieved agreement with TPS calculations within ±2.5% across all energies and techniques. The heterogeneous phantom exhibited deviations of up to 2.8%, remaining within the ±3% tolerance of AAPM TG-119. Variability was most significant for VMAT plans with FFF beams, particularly on the Halcyon platform.

Conclusion: A 3D-printed homogeneous PMMA phantom demonstrated radiological stability and dosimetric accuracy comparable to that of commercial devices, confirming its feasibility for routine QA. The heterogeneous model exhibited acceptable performance but requires material refinement, particularly substitution of PLA and MDI foam, to improve HU stability. These results highlight the potential of additive manufacturing to provide cost-effective, customizable QA solutions for radiation therapy, especially in resource-limited environments.

Keywords: *Quality assurance (QA); 3D printing in medical physics; Imaging phantoms; Computed tomography (CT); HU stability; End-to-end testing; Phantom validation; Affordable QA devices*
PACS: 7.57.Q–

1. INTRODUCTION

Quality assurance (QA) in radiation therapy is critical to ensure accurate dose delivery and patient safety, in line with international recommendations [1]. QA phantoms play a central role in these procedures, providing reproducible conditions for imaging, treatment planning, and end-to-end verification.

In recent years, additive manufacturing (3D printing) has emerged as a promising approach for producing custom QA devices. A growing body of literature has demonstrated the feasibility of 3D-printed phantoms for imaging and dosimetry [2]. For example, Kunert et al. developed realistic 3D-printed body phantoms and compared measured and simulated organ doses in CT of a pregnant woman [3]. Other studies have investigated the impact of material composition and characterized the mechanical and imaging properties of commonly used 3D-printed plastics [4, 5]. Zain et al. reported dosimetric characterization of customized PLA phantoms, showing agreement with solid water within clinically acceptable limits [6].

Systematic reviews confirm that most prior works have focused on thoracic or homogeneous slab models [7]. By contrast, heterogeneous anthropomorphic designs have been evaluated for lung [8], head-and-neck [9, 10], and brain stereotactic radiosurgery applications [11]. Moreover, comprehensive end-to-end tests combining dosimetric and geometric verification have also been reported [12], though such studies remain relatively few.

Despite these advances, the majority of 3D-printed phantoms remain limited in their ability to reproduce heterogeneous tissue properties or to undergo full clinical validation with advanced delivery techniques such as VMAT. This gap is particularly relevant for low- and middle-income countries, including Ukraine, where resource constraints frequently restrict access to advanced QA infrastructure and cost-effective alternatives are urgently needed [13].

2. MATERIALS AND METHODS

2.1. Phantom Design and Fabrication

Two phantom prototypes were designed and fabricated using fused deposition modeling (FDM) 3D printing technology:

Cite as: V. Vashchyshyn, O. Bezshyiko, L. Golinka-Bezshyyko, East Eur. J. Phys. 4, 575 (2025), https://doi.org/10.26565/2312-4334-2025-4-60

1. **Homogeneous phantom** — manufactured entirely from polymethyl methacrylate (PMMA) to provide a uniform electron density.
2. **Heterogeneous phantom** — composed of multiple materials to simulate soft tissue and bone:

- EVA (ethylene-vinyl acetate) — soft tissue surrogate.
- PLA (polylactic acid) — dense soft tissue surrogate.
- MDI-based rigid polyurethane foam — low-density lung-equivalent material.
- Gypsum–chalk composite — cortical bone surrogate.

Design schematics were created in *Autodesk Fusion 360* and exported as STL files for printing. The phantoms were printed using an *Ultimaker S5* 3D printer with 0.4 mm nozzle, 0.2 mm layer height, and 100% infill for PMMA and PLA components. EVA and MDI foams were cut to shape and inserted into designated cavities. The overall dimensions of each phantom matched those of the commercial Easy Slab phantom, allowing for direct performance comparison.

2.2. Reference Phantoms

For benchmarking, two commercially available phantoms were used (Fig. 1):

- **Easy Slab** (IBA Dosimetry, Germany) — a homogeneous PMMA phantom for reference dosimetry and QA.
- **CatPhan 604** (The Phantom Laboratory, USA) — a diagnostic imaging QA phantom.

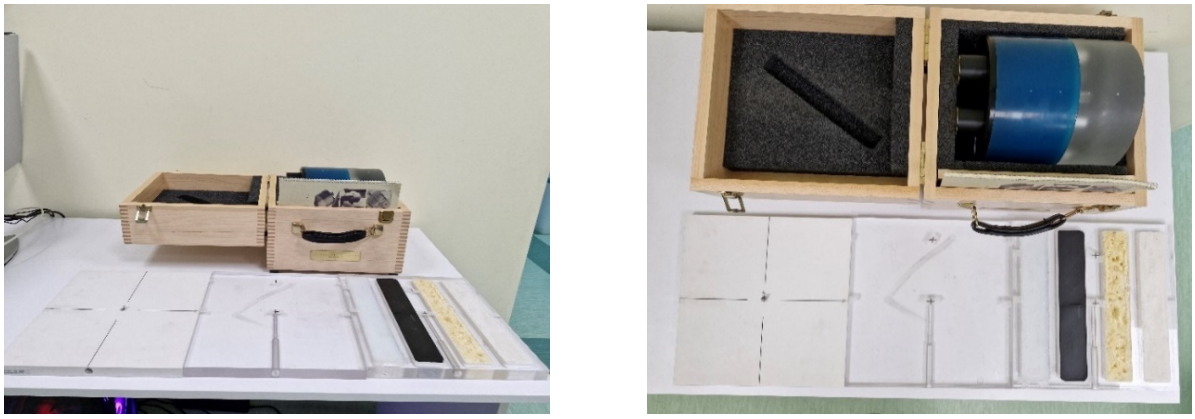

Figure 1. Photograph of the homogeneous and heterogeneous 3D-printed phantoms alongside the IBA Easy Slab and CatPhan 604.

2.3. Radiological Evaluation

2.3.1. CT Acquisition

Radiological properties of all materials were evaluated using a *Siemens SOMATOM Confidence* large-bore CT scanner. Scans were performed at 120 kVp, 250 mAs, with 500 mm field of view (FOV). Slice thicknesses of **1 mm** and **3 mm** were acquired with three reconstruction kernels:

- Hp38 — standard head protocol
- Bf39 — body filter
- Hr32 — high-resolution protocol

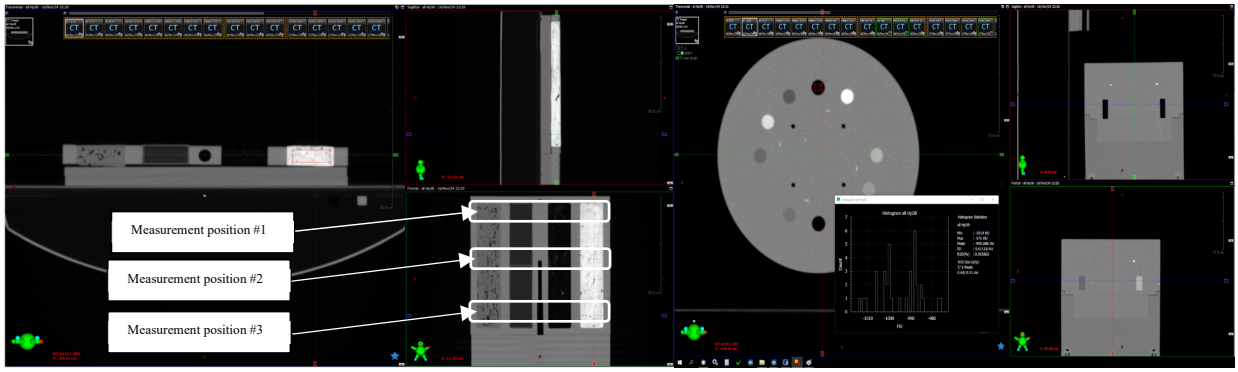

Figure 2. Axial CT slices of phantoms scanned with Hr32 kernel

For each material insert, rectangular regions of interest (ROIs) of 1 cm² were placed in proximal, central, and distal slices using *Eclipse Varian* software (Figure 2). Mean Hounsfield Units (HU) and standard deviations (SD) were recorded.

2.4. Dosimetric Validation

2.4.1. Treatment Planning

End-to-end dosimetric testing was performed using the Eclipse v16.1 treatment planning system (Varian Medical Systems, USA) with AcurosXB dose calculation algorithm on the ARIA oncology platform. For each phantom, 15 three-dimensional conformal radiotherapy (3D-CRT) plans and 15 volumetric modulated arc therapy (VMAT) plans were created. Plans were calculated for the following beam energies:

- Varian TrueBeam 2.7: 6 MV, 6 MV FFF, 10 MV, 10 MV FFF
- Varian Halcyon: 6 MV FFF only

All plans prescribed a dose to isocenter, normalized to 100% at the ion chamber location.

2.4.2 Measurement Setup

Point dose measurements were performed using a calibrated Farmer-type ionization chamber (FC65P, IBA) connected to a DOSE1 electrometer. The chamber was placed in a central cavity of each phantom with a 5 cm water-equivalent buildup upstream (Fig. 3). Temperature and pressure corrections were applied according to IAEA TRS-398 formalism [12].

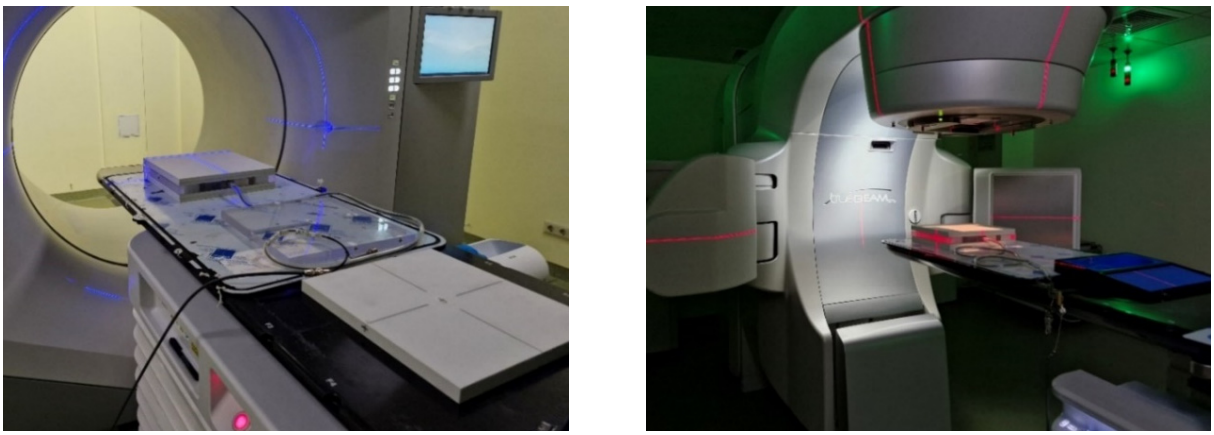

Figure 3. Photograph of measurement setup on TrueBeam with phantom and ionization chamber in position.

2.5 Data Analysis

Measured doses were compared with TPS-calculated doses, and percentage differences were computed:

$$\Delta D(\%) = \frac{D_{meas} - D_{TPS}}{D_{TPS}} \times 100$$

Acceptance criteria followed AAPM TG-119 recommendations, with ±3% considered clinically acceptable [2]. HU variations > 40 HU were considered significant.

3. Results

3.1 Radiological evaluation

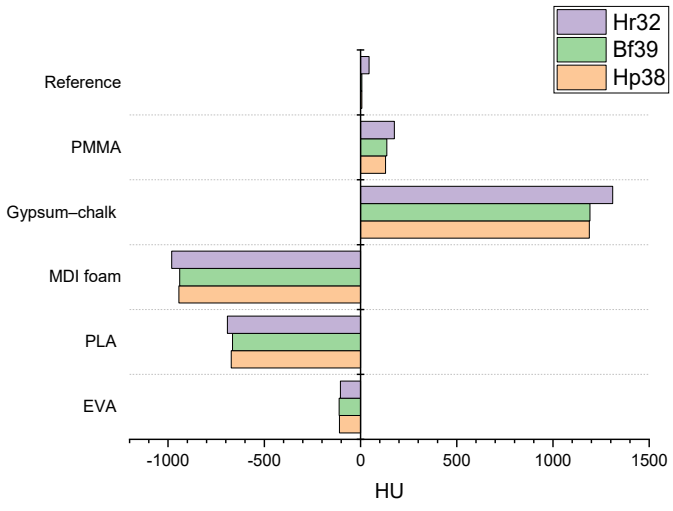

Figure 4. Materials HU variations across different kernels

The homogeneous PMMA phantom demonstrated highly consistent HU values across all three reconstruction kernels, with variations remaining within ±5 HU across different slice positions and acquisition protocols. EVA and the gypsum–chalk composite in the heterogeneous phantom showed stable and reproducible values that align with the expected ranges for soft tissue–like and bone-like surrogates, respectively. In contrast, PLA and MDI-based foam exhibited greater variability, particularly when reconstructed with the Hr32 kernel, where fluctuations exceeded ±40 HU (Figure 4).

Despite these differences, the overall stability of PMMA, EVA, and gypsum–chalk ensured cohesive and clinically interpretable results in subsequent end-to-end testing.

Table 1 summarizes the mean HU values and standard deviations for all materials and kernels, based on measurements in proximal, central, and distal slices.

Table 1. HU mean ± SD for all materials and kernels (Hp38, Bf39 and Hr32)

Hp38	Min HU	Max HU	Mean HU	Average SD, HU	SD/mean in %
air	-1014	-976	-995.1	**9.6**	0.97
PMP	-194	-137	-177.5	**14.6**	8.2
Bone 50%	582	634	608	**12.8**	2.1
LDPE	-111	-55	-84.8	**13.7**	16.1
Polystyrene	-54	-17	-34.6	**9**	26
Acrylic	106	142	125.3	**9.2**	7.4
Bone 20%	167	232	201.4	**16.7**	8.3
Delrin	332	376	350.6	**11.6**	3.3
Teflon	891	957	921.4	**17**	1.8
Heterogeneous 1	-792.3	-13.3	-109.0	**134.1**	124.7
Heterogeneous 2	-739.7	-601.3	-671.9	**32.8**	4.87
Heterogeneous 3	-1007.3	-709.7	-943.7	**39.8**	4.2
Heterogeneous 4	325.7	1402	1188.2	**124.1**	10.5
Homogeneous	98	161	129.9	**10.8**	8.3
Reference	-18.3	41.7	6.7	**7.8**	159.9
Bf39	Min HU	Max HU	Mean HU	Average SD, HU	SD/mean, %
air	-1024	-953	-982.5	**15.1**	1.5
PMP	-206	-137	-171.7	**16**	9.4
Bone 50%	555	631	593.4	**19.5**	3.3
LDPE	-125	-49	-85.7	**18.3**	21.4
Polystyrene	-67	-2	-35.1	**16.9**	48.1
Acrylic	105	145	123.6	**13.1**	10.6
Bone 20%	163	203	186.4	**9.7**	5.2
Delrin	314	374	336.8	**17.4**	5.2
Teflon	880	937	906.5	**15.3**	1.7
Heterogeneous 1	-782	-14.3	-111.2	**127.9**	115.4
Heterogeneous 2	-777	-558	-665.5	**55.6**	8.3
Heterogeneous 3	-1014.7	-753.3	-940.1	**37.8**	4.1
Heterogeneous 4	684	1485	1192.3	**113.0**	9.4
Homogeneous	82.7	178.7	136.7	**13.8**	10.1
Reference	-26	41.7	7.1	**11.2**	180.7
Hr32	Min HU	Max HU	Mean HU	Average SD, HU	SD/mean in %
air	-1024	-1021	-1022	**0.8**	0.1
PMP	-232	-184	-213	**14.7**	6.9
Bone 50%	674	716	693.6	**11.3**	1.6
LDPE	-117	-93	-103.5	**6.9**	6.7
Polystyrene	-56	-32	-45.1	**6.6**	14.6
Acrylic	123	144	136.2	**5.1**	3.8
Bone 20%	211	245	224.4	**10.4**	4.6
Delrin	383	416	401.1	**9**	2.2
Teflon	1051	1093	1064	**12**	1.1
Heterogeneous 1	-830.3	9	-104.6	**145.4**	141.6
Heterogeneous 2	-746.7	-629.3	-691.6	**29.2**	4.2
Heterogeneous 3	-1024	-752	-981.7	**46.5**	4.8
Heterogeneous 4	731.3	1520.7	1310.2	**98.6**	7.5
Homogeneous	151	207.7	175.6	**10.2**	5.8
Reference	24.3	67.3	44.4	**7.7**	17.1

3.1.2 Slice thickness and kernel effects

Reduction of slice thickness from 3 mm to 1 mm had negligible impact on HU values for PMMA and EVA but slightly increased variability in low-density materials such as MDI foam. Kernel selection had the largest influence on high-density materials (gypsum–chalk) and on the unstable components (PLA, MDI), reinforcing the need for material optimization in heterogeneous designs.

3.2 Dosimetric validation

End-to-end dosimetric testing demonstrated strong agreement between TPS-calculated and measured point doses for both phantoms (Table 2). The homogeneous PMMA phantom achieved excellent consistency, with discrepancies across all energies and delivery techniques remaining within ±2.5%. The heterogeneous phantom also performed within the clinically acceptable ±3% TG-119 threshold, with a maximum deviation of 2.8%.

Table 2. Measured vs. TPS dose comparison for all phantoms and energies

TrueBeam		3D CRT			VMAT		
		Meas mean, Gy	TPS, Gy	%, diff	Meas mean, Gy	TPS, Gy	%, diff
Homo	6MV	2.016	2.040	**1.17**	2.041	2.092	**2.50**
	6FFF	2.025	2.042	**0.82**	2.055	2.101	**2.24**
	10MV	1.999	2.014	**0.75**	2.046	2.084	**1.86**
	10FFF	2.038	2.051	**0.65**	2.046	2.097	**2.49**
Hetero	6MV	2.027	2.038	**0.56**	2.049	2.065	**0.78**
	6FFF	2.063	2.039	**-1.18**	2.050	2.042	**-0.38**
	10MV	2.003	2.018	**0.73**	2.055	2.105	**2.45**
	10FFF	2.050	2.043	**-0.34**	2.090	2.081	**-0.43**
Ref	6MV	2.110	2.041	**-3.25**	2.042	2.043	**0.05**
	6FFF	2.032	2.028	**-0.21**	2.059	2.044	**-0.73**
	10MV	2.001	2.043	**2.12**	2.042	2.080	**1.86**
	10FFF	2.041	2.067	**1.29**	2.065	2.057	**-0.39**

Halcyon	3D CRT			VMAT		
	Meas mean, Gy	TPS, Gy	%, diff	Meas mean, Gy	TPS, Gy	%, diff
Homo	2.062	2.069	-0.34	2.029	2.034	-0.25
Hetero	2.068	2.081	-0.62	2.030	2.041	-0.52
Ref	2.060	2.057	0.15	2.035	2.037	-0.11

A clear trend was observed between accelerators: Halcyon measurements showed smaller discrepancies overall compared to TrueBeam, reflecting the stable modeling of the 6 MV FFF beam in Eclipse. On the TrueBeam, slightly larger variations appeared, particularly in cases involving heterogeneous material inserts, likely due to increased sensitivity to density inhomogeneities and geometric setup factors.

No systematic differences were detected between 3D-CRT and VMAT techniques. Both delivery approaches yielded comparable agreement with TPS predictions, indicating that plan complexity did not substantially influence phantom performance. This finding suggests that the observed deviations are primarily attributable to material properties and beam modeling, rather than delivery method.

Figure 5 illustrates these outcomes, showing tight clustering of measured-to-TPS dose ratios around unity for the homogeneous phantom, and somewhat broader but still clinically acceptable distributions for the heterogeneous phantom. Together, these results confirm the suitability of the homogeneous phantom for clinical QA across diverse energies and delivery techniques, while highlighting opportunities for refinement in the heterogeneous design.

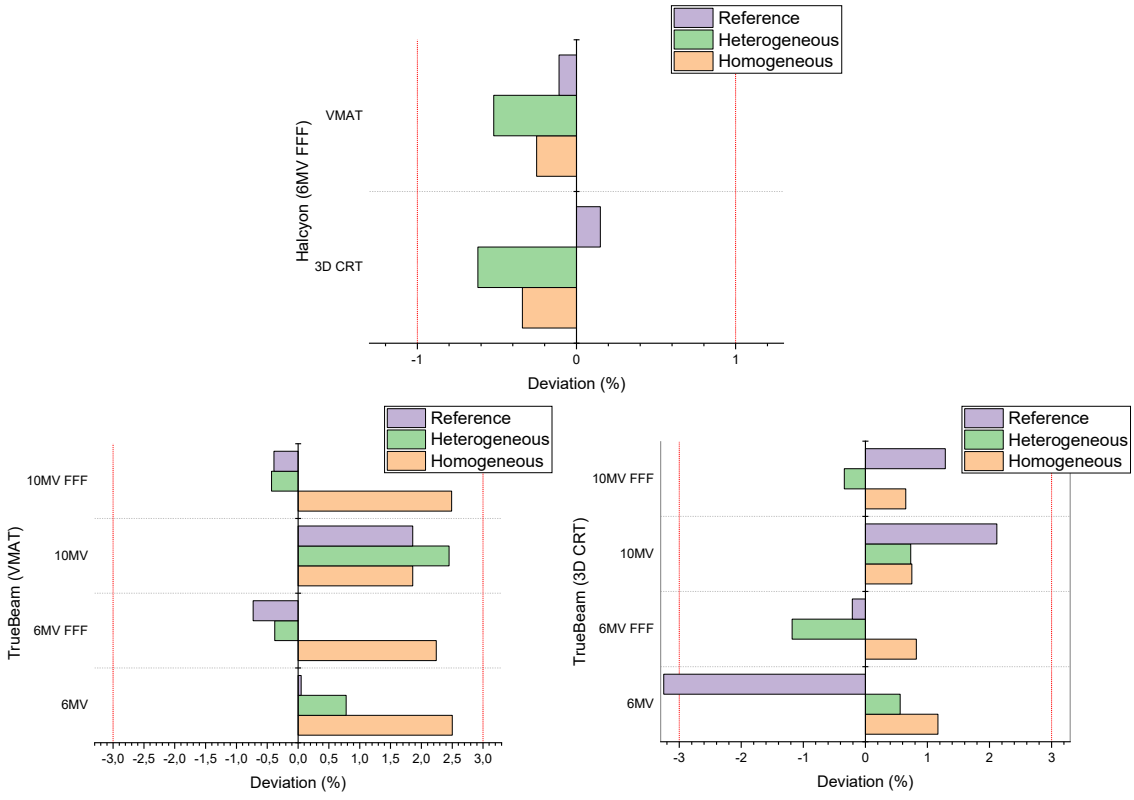

Figure 5. Bar graph of dose deviation by phantom type and beam energy.

3.3 Summary of key findings

The evaluation demonstrated that the 3D-printed homogeneous PMMA phantom provides radiological and dosimetric stability comparable to commercial QA devices. HU values were consistent across kernels with variations within ±5 HU, and dose measurements agreed with TPS calculations within ±2.5% across all energies, delivery techniques, and both accelerators. These results confirm its reliability for clinical end-to-end testing and routine QA.

The heterogeneous phantom showed promising but less stable performance. EVA and gypsum–chalk composites reproduced soft-tissue and bone-like imaging characteristics reliably, whereas PLA and MDI-based foam exhibited excessive HU variability, particularly with high-resolution kernels. Dosimetrically, the heterogeneous phantom-maintained deviations within ±3%, though slightly higher scatter was observed on the TrueBeam compared to the Halcyon.

No systematic differences were identified between 3D-CRT and VMAT deliveries, indicating that phantom performance is robust across both simple and complex treatment techniques. The observed variations are mainly attributable to material selection and, to a lesser extent, accelerator-specific beam modeling and setup factors.

Overall, the findings support the homogeneous phantom as a clinically ready, low-cost QA tool, while the heterogeneous phantom requires further refinement, particularly in material composition, to achieve the same level of stability.

4. DISCUSSION

Our results demonstrate that 3D-printed homogeneous phantoms can achieve HU stability within clinically acceptable ranges and dose agreement with the TPS comparable to commercial standards. This finding aligns with earlier reports that homogeneous 3D-printed materials such as PLA provide reproducible radiological and dosimetric properties suitable for routine QA applications [6, 15, 16].

For heterogeneous phantoms, however, our study confirmed the greater challenges previously described in reproducing tissue-equivalent properties [7, 9, 10]. Variability in HU for bone-equivalent and lung-equivalent regions is consistent with earlier investigations, emphasizing that material selection and printer calibration remain critical factors for accurate tissue simulation. These limitations were also highlighted in end-to-end testing studies, where deviations in HU translated into measurable dose differences in high-gradient regions [8, 10, 11].

At the same time, our approach contributes additional evidence that 3D-printed heterogeneous phantoms are feasible for comprehensive clinical validation. Significantly, our work extends prior evaluations by incorporating end-to-end verification using the VMAT technique, which to date has been rarely investigated in 3D-printed models [10, 12].

Beyond direct phantom performance, our results can also be compared to earlier IMRT commissioning studies [17].

Finally, the broader context of medical physics practice must be considered. The need for accessible, affordable QA solutions is particularly urgent in low- and middle-income countries. Meghzifene et al. highlighted persistent global challenges in medical physics education and training [13], while Zubizarreta et al. documented the critical shortfall in radiotherapy infrastructure in resource-limited settings [18]. Against this background, cost-effective 3D-printed phantoms, as developed in our study, could provide an essential contribution to strengthening QA capacity where it is most urgently needed.

5. CONCLUSIONS

This study demonstrated the feasibility of 3D printing cost-effective phantoms for radiation therapy quality assurance. The homogeneous PMMA phantom demonstrated stable radiological and dosimetric performance comparable to that of commercial devices, whereas the heterogeneous model requires further material refinement to achieve similar reproducibility.

The research was partially supported by the National Research Foundation of Ukraine under the project "Improving Quality and Safety in Radiation Therapy for Cancer and Radiological Diagnostics" with registration number 2021.01/0211 (Science for Safety and Sustainable Development of Ukraine).

ORCID

V. Vashchyshyn, https://orcid.org/0009-0003-0005-1924; **O. Bezshyyko,** https://orcid.org/0000-0001-7106-5213

REFERENCES

[1] IAEA, *Accuracy Requirements and Uncertainties in Radiotherapy.* IAEA Human Health Series No. 31. Vienna: IAEA; 2016.
[2] W. Qiu, H. Sun, Z. Hu, *et al*. "Constructing customized multimodal phantoms through 3D printing. A Preliminary Evaluation," Front Phys. **9**, (2021). https://doi.org/10.3389/fphy.2021.605630
[3] P. Kunert, H. Schlattl, S.S. Trinkl, E. Honorio, D. Reichert, and A.A. Giussani, "3D printing of realistic body phantoms: Comparison of measured and simulated organ doses on the example of a CT scan on a pregnant woman," Med. Phys. **51**(12), 9264-9274 (2024). https://doi.org/10.1002/mp.17420
[4] D. Ma, R. Gao, M. Li, and J. Qiu, "Mechanical and medical imaging properties of 3D-printed materials as tissue-equivalent materials," J. Appl. Clin. Med. Phys. **23**(2), e13495 (2022). https://doi.org/10.1002/acm2.13495
[5] J. Silberstein, and Z. Sun, "Advances and Applications of Three-Dimensional-Printed Patient-Specific Chest Phantoms in Radiology: A Systematic Review," Appl. Sci. **14**(13), 5467 (2024). https://doi.org/10.3390/app14135467
[6] N.E.M. Zain, U. Jais, R. Abdullah, and N.W. Abd Rahman, "Dosimetric characterization of customized PLA phantom for radiotherapy," J. Sains. Nuklear. Malaysia. **31**(2), 1-6 (2019). https://inis.iaea.org/records/7n3ar-vwf37

[7] R. Tino, A. Yeo, M. Leary, M. Brandt, and T. Kron, "A systematic review on 3D-printed imaging and dosimetry phantoms in radiation therapy," Technol. Cancer Res. Treat. (18), (2019). https://doi.org/10.1177/1533033819870208
[8] R.B. Tino, A.U. Yeo, M. Brandt, M. Leary, and T. Kron, "A customizable anthropomorphic phantom for dosimetric verification of 3D-printed lung, tissue, and bone density materials," Med. Phys. **49**(1), 52–69 (2022). https://doi.org/10.1002/mp.15364
[9] N. Kadoya, K. Abe, H. Nemoto, K. Sato, Y. Ieko, K. Ito, S. Dobashi, *et al*. "Evaluation of a 3D-printed heterogeneous anthropomorphic head and neck phantom for patient-specific quality assurance in intensity-modulated radiation therapy," Radiol. Phys. Technol. **12**(3), 351–356 (2019). https://doi.org/10.1007/s12194-019-00527-5
[10] J.W. Yea, J.W. Park, S.K. Kim, D.Y. Kim, J.G. Kim, C.Y. Seo, *et al*. "Feasibility of a 3D-printed anthropomorphic patient-specific head phantom for patient-specific quality assurance of intensity-modulated radiotherapy," PLoS One, **12**(7), e0181560 (2017). https://doi.org/10.1371/journal.pone.0181560
[11] L. Mertens, J. Fleckenstein, V. Steil, and F. Schneider, "A novel end-to-end test for combined dosimetric and geometric treatment verification using a 3D-printed phantom," Med. Dosim. **47**(2), 177–183 (2022). https://doi.org/10.1016/j.meddos.2022.02.002
[12] H. Marshall, T. Selvan, and R. Ahmad, "Evaluation of a novel phantom for the quality assurance of a six-degree-of-freedom couch 3D-printed at multiple centres," Phys. Med. **114**, 103136 (2023). https://doi.org/10.1016/j.ejmp.2023.103136
[13] A. Meghzifene, "Medical physics challenges for the implementation of quality assurance programmes in radiation oncology," Clin. Oncol. (R Coll Radiol), **29**(2), 116–119 (2017). https://doi.org/10.1016/j.clon.2016.10.008
[14] IAEA. Absorbed Dose Determination in External Beam Radiotherapy. Technical Report Series No. 398. Vienna: IAEA; 2000.
[15] Y. Choi, J. Lee, K. Park, R. Park, Y. Cho, J. Kim, and H.H. Lee, "Patient-Specific Quality Assurance Using a 3D-Printed Chest Phantom for Intraoperative Radiotherapy in Breast Cancer," Front Oncol. **11**, 699592 (2021). https://doi.org/10.3389/fonc.2021.699592
[16] A. Chaikh, A. Chaabane, C. Jardin, S. Bassot, T. Beaumont, M. Chea, *et al*. "Modeling and dosimetric characterization of a 3D printed pregnant woman phantom for fetal dosimetry in radiotherapy," Radioprotection. **60**(1), 50–56 (2025). https://doi.org/10.1051/radiopro/2024039
[17] G.A. Ezzell, J.W. Burmeister, N. Dogan, T.J. LoSasso, J.G. Mechalakos, D. Mihailidis, A. Molineu, *et al*. "IMRT commissioning: multiple institution planning and dosimetry comparisons," Med. Phys. **36**(11), 5359–5373 (2009). https://doi.org/10.1118/1.3238104
[18] E.H. Zubizarreta, E. Fidarova, B. Healy, and E. Rosenblatt, "Need for radiotherapy in low and middle income countries – the silent crisis continues," Clin. Oncol. (R Coll Radiol), **27**(2), 107-114 (2015). https://doi.org/10.1016/j.clon.2014.10.006

РОЗРОБКА І ОЦІНКА ГОМОГЕННИХ І ГЕТЕРОГЕННИХ ФАНТОМІВ, НАДРУКОВАНИХ МЕТОДОМ 3D-ДРУКУ, ДЛЯ ЗАБЕЗПЕЧЕННЯ ЯКОСТІ ПРОМЕНЕВОЇ ТЕРАПІЇ

В. Ващишин[1], О. Безшийко[2], Л. Голинка-Безшийко[2]
[1]Відділення променевої терапії, Універсальна клініка «Оберіг», Київ, Україна
[2]Київський національний університет імені Тараса Шевченка, Київ, Україна

Передумови: Доступні та місцеві фантоми контролю якості (QA) мають вирішальне значення для підтримки точності променевої терапії, особливо в умовах обмежених ресурсів. Це дослідження оцінює радіологічні та дозиметричні характеристики 3D-друкованих гомогенних та гетерогенних фантомів порівняно з комерційними стандартами.
Методи: Було розроблено два прототипи фантома: гомогенну модель, виготовлену з PMMA, та гетерогенну модель, що складається з EVA, PLA, піни на основі MDI та гіпсово-крейдяного композиту. Радіологічні властивості оцінювали за допомогою КТ-візуалізації з трьома реконструкційними ядрами (Hp38, Bf39, Hr32) при товщині зрізу 1–3 мм. Одиниці Хаунсфілда (HU) порівнювали з референтними значеннями з Easy Slab (IBA) та CatPhan 604. Дозиметричну валідацію проводили за допомогою Eclipse TPS (v16.1) з використанням 15 3D-CRT та 15 VMAT планів, налаштованих на прискорювачі Varian TrueBeam (6 MV, 6 MV FFF, 10 MV, 10 MV FFF) та Halcyon (6 MV FFF). Точкові дози вимірювали за допомогою каліброваної камери Фармера.
Результати: Гомогенний фантом PMMA продемонстрував стабільність HU в межах ±5 HU від референтних значень для всіх ядер зі стандартними відхиленнями менше 3 HU. EVA та гіпс-крейда забезпечили тканинно-еквівалентні та кістково-еквівалентні властивості візуалізації (20 ± 3 HU та 1200 ± 15 HU відповідно), тоді як PLA та MDI продемонстрували надмірну мінливість (залежність від ядра >40 HU). Дозиметрично, гомогенний фантом досяг узгодженості з розрахунками TPS у межах ±2,5% для всіх енергій та методів. Гетерогенний фантом демонстрував відхилення до 2,8%, залишаючись у межах ±3% допуску AAPM TG-119. Мінливість була найбільш значною для планів VMAT з променями FFF, особливо на платформі Halcyon.
Висновок: Гомогенний фантом з PMMA, надрукований на 3D-принтері, продемонстрував радіологічну стабільність та дозиметричну точність, порівнянну з комерційними пристроями, що підтверджує його доцільність для рутинного контролю якості. Гетерогенна модель продемонструвала прийнятні характеристики, але вимагає вдосконалення матеріалів, зокрема заміни PLA та MDI піни, для покращення стабільності HU. Ці результати підкреслюють потенціал адитивного виробництва для забезпечення економічно ефективних, налаштовуваних рішень контролю якості для променевої терапії, особливо в умовах обмежених ресурсів.
Ключові слова: *забезпечення якості (QA); 3D-друк у медичній фізиці; фантоми візуалізації; комп'ютерна томографія (КТ); стабільність HU; наскрізне тестування; валідація фантома; доступні пристрої для контролю якості*

East European Journal of Physics. 4. 582-589 (2025)
DOI:10.26565/2312-4334-2025-4-61 ISSN 2312-4334

MONTE CARLO CODE FOR CALCULATING THE ELASTIC AND INELASTIC SCATTERING CROSS SECTION ALONG WITH MEAN FREE PATH OF POSITRON SCATTERING IN KIDNEY, LUNG AND THYROID ORGANS

Hawar M. Dlshad[1]*, Jamal M. Rashid[2]
[1]*University of Sulaimani, College of Education, Department of Physics, Sulaymaniyah 46001, Kurdistan Region, Iraq*
[2]*University of Sulaimani, College of Science, Department of Physics, Qlyasan street, Sulaymaniyah 46001, Kurdistan Region, Iraq*
**Corresponding Author email: hawar.dlshad@univsul.edu.iq*
Received August 4, 2025; revised November 8, 2025; accepted November 15, 2025

This research calculated the total cross sections for positron scattering in kidney, lung, and thyroid tissues along an energy range of 100 eV to 1 MeV. Monte Carlo methods were employed to determine both elastic and inelastic integral cross sections, utilizing the Rutherford formula for elastic scattering and the Gryzinski excitation function for inelastic processes. A comparison was made between elastic and Penelope elastic cross sections. The study also examined elastic, inelastic, and total mean free paths as functions of positron energy for all three tissue types. The computational approach is designed to be broadly applicable across different materials. We observed significant differences in cross-section profiles and in the energy dependencies of the mean free path between tissues, attributing these variations to distinct inelastic-scattering characteristics inherent to each material. While the systematic uncertainties in the computational algorithm are challenging to quantify precisely, we believe they are largely systematic.
Keywords: *Cross section; Positron; Mean free path; Human organ; Effective atomic number*
PACS: 34.85.+x, 78.70.Bj, 87.15.-v, 34.80.Gs, 28.41.Ak

1. INTRODUCTION

A positron is defined as the electron antiparticle, having identical properties to an electron except for its positive electrical charge [1]. The interactions between positrons and electrons with solid materials form the foundation of numerous scientific and technological applications. Understanding these interactions is essential for diverse fields including microscopy, materials science, and radiation damage evaluation [2]. While extensive research has focused on electron mean free paths and cross-sections, considerably less information exists for positrons. Theoretical approaches to modeling positron scattering in solid materials can be categorized into three simple models: basic models, Boltzmann transport equation solutions, and Monte Carlo (MC) simulations. The MC technique is regarded as the most fundamental approach since it tracks individual positron paths and records complete scattering event histories. Monte Carlo simulation is a computational method with broad applications across multiple fields, including physics, biology, biophysics, nuclear engineering, biomedical engineering, and medical imaging, etc. [3, 4].

The elastic cross section in physics quantifies the probability that two particles will scatter off each other without any change in their internal states or the production of new particles. That is, the particles remain the same before and after the collision, and only their directions and/or energies may change. This differs from inelastic collisions, where particles may undergo internal transformations or give rise to additional particles [5].

Furthermore, during inelastic collisions, the target atom may be excited to a higher state above its ground level or undergo ionization, depending on the amount of energy transferred by the incident particle. Simultaneously, the incoming particle experiences energy loss and deflects away from its original trajectory. In positron emission tomography (PET) modeling, it is important to consider both positron and electron total cross sections, since high-energy positrons generate secondary electrons via ionization processes [6, 7] .

The inelastic mean free path (IMFP), which represents the mean distance a positron travels before losing energy, is crucial to surface spectroscopy techniques such as photoemission. Additionally, it plays a key role in understanding positron interactions with condensed matter, making it significant for radiotherapy planning and research on radiation effects in human tissues [8]. Ashley developed a theoretical approach to determine both the stopping power (loss of energy per unit distance) and the electrons inelastic mean free path for the range of energies up to 10 keV, based on the optical properties of the medium. This model accounts for exchange interactions between the incoming electron and the electrons of the medium [9].

The study by Tan et al. computed inelastic electron cross sections in DNA by applying the theory of dielectric response and the Penn statistical approximation, with exchange corrections accounted for. To verify their model, their calculations were evaluated by comparison to available experimental and theoretical findings, confirming the validity of their approach [10]. In the same year, they established systematic formulas to calculate both stopping powers and mean free paths of electron for numerous organic compounds, covering the range of energy below 10 keV [11]. Cai et al. determined the elastic cross sections for positrons and electrons using partial wave analysis. The inelastic interactions between positrons and valence electrons were presented by the energy loss function derived from the theory of dielectric.

Cite as: H.M. Dlshad, J.M. Rashid, East Eur. J. Phys. 4, 582 (2025), https://doi.org/10.26565/2312-4334-2025-4-61

Additionally, the interactions between positrons and core electrons were represented using the excitation function of Gryzinski [12]. In this study, we systematically calculated the cross section (σ) and mean free path (λ) within the domain of energy between 100 eV to 1 MeV for three human tissues: kidney, lung, and thyroid. The calculation of total mean free paths (MFPs) for positrons is inversely related to the total scattering cross section. Additionally, the elastic cross section findings were compared with the results obtained from Penelope (2012).

2. METHODOLOGY

2.1 Cross section calculation

The overall cross section consists of two primary components: elastic and inelastic collision cross sections. The inelastic component can be further broken down into cross sections for excitation and ionization processes [10].

2.1.1 Elastic cross section

It represents scattering events where positrons interact with atomic nuclei or bound electrons without losing energy, conserving their kinetic energy while changing direction [13]. The cross section is fundamentally a microscopic parameter derived from quantum mechanical principles. When computing the positron scattering cross sections in human tissues, the model of Rutherford total elastic scattering cross section σ_{el} for atoms is employed, which can be expressed as [2]:

$$\sigma_{el} = \frac{\pi\, e^4 Z^2}{4\,\beta_N(1+\beta_N)E^2}\ , \tag{1}$$

In Eq. (1), E, Z and e are positron energy before collision in electron volts, atomic number of the target, and electronic charge, respectively. β_N is an atomic screening parameter of the Wentzel type due to Nigam et al. and is given by [14, 15]:

$$\beta_N = \frac{5.43\, Z^{2/3}}{E}\ , \tag{2}$$

It can be written as [16]:

$$\sigma_{el} = \frac{6.56\times 10^{-14} Z^2}{4\,\beta_N(1+\beta_N)E^2}\,. \tag{3}$$

In which the value of $\pi\, e^4$ is equal to $6.56\ \times\ 10^{-14}$, if the unit of E in eV and e in units of elementary charge ($1/4\pi\epsilon$). In each compound, an effective atomic number Z_{eff} must be used instead of Z atomic number, therefore Z_{eff} obtained from the Markowicz-Van Grieken expression, which is given by [17 - 19]:

$$Z_{eff} = \frac{\sum_{i=1}^{l} \frac{w_i Z_i^2}{A_i}}{\sum_{i=1}^{l} \frac{w_i Z_i}{A_i}} \tag{4}$$

Where w_i , A_i are the weight fraction given in Table (1), and atomic weight for ith element, respectively.
After each elastic collision, the scattering angle is determined using a uniform random number R, where ($0 < R \leq 1$).

2.1.2 Inelastic cross section

Represents interactions where positrons lose energy to the medium surrounded by coulomb collisions through atomic excitation and ionization mechanisms based on the classical binary-encounter theory [13]. According to Gryzinski's excitation function, the differential cross-section for an energy transfer from a positron with an energy E to an electron of the kth inner shell is [20]:

$$\frac{d\sigma}{d\Delta E} = \frac{6.56\times10^{-14}(cm^2eV^2)Z^2N_S}{(\Delta E)^3}\frac{E_B}{E}\left(1-\frac{\Delta E}{E}\right)^{\left(\frac{E_B}{E_B+\Delta E}\right)}\left(\frac{E_B}{E+E_B}\right)^{\frac{3}{2}}\left\{\frac{\Delta E}{E_B}\left(1-\frac{E_B}{E}\right)+\frac{4}{3}ln\left[2.7+\left(\frac{E-\Delta E}{E_B}\right)^{\frac{1}{2}}\right]\right\}, \tag{5a}$$

The total inelastic scattering cross-section can be calculated from:

$$\sigma_{inel} = \int_0^E \frac{d\sigma(\Delta E)}{d\Delta E}\, d\Delta E, \tag{5b}$$

Therefore

$$\sigma_{inel} = \frac{6.56\times10^{-14}}{E_B^2}\frac{N_s}{U}\left(\frac{U-1}{U+1}\right)^{3/2}\times\left[1+\frac{2}{3}\left(1-\frac{1}{2U}\right)ln\left(2.7+(U-1)^{1/2}\right)\right]. \tag{5c}$$

Here, $U = \frac{E}{E_B}$ (E_B, and ΔE are mean binding energy, and energy loss, respectively). N_s is the electrons number in a particular shell and is given for compounds as follow [2]:

$$N_s = \sum_i (\eta_{si} \times V_i) / \sum_i V_i \ . \tag{5d}$$

Where η_{si} is the electrons number in an atom particular shell of the ith species and V_i is the atoms number in ith species. Now, the total (integrated) cross sections as a function of particle energy E, can be represented as follows:

$$\sigma_{Total}(E) = \sigma_{el}(E) + \sigma_{inel}(E) + \sigma_{br}(E)[\sigma_{an}(E)] \ . \tag{6}$$

Where σ_{el}, σ_{inel}, σ_{br} *and* σ_{an} are elastic, inelastic, bremsstrahlung and positron annihilation cross sections respectively. Since the final term magnitude quantities (Bremsstrahlung and annihilation terms) are very small (in the order of 10^{-16}) compared to others, they can be neglected in the current calculations [21].

2.2 Mean free path calculation

Mean free path is the typical distance between collisions as a positron moves through matter. Positrons, like electrons, have both elastic and inelastic types of mean free path [22, 23]. The mean free path (λ) between interactions of the penetrating particle is expressed with [6]:

$$\lambda = \frac{A}{N_A \rho \sigma} . \tag{7}$$

Where Avogadro number N_A= 6.02214129×10^{23} mol^{-1}, ρ is the mass density (g/cm^3), and A, σ are the molar mass in unit of (g/mol) and the collision cross-section in (cm^2), respectively.

2.2.1 Elastic mean free path

The elastic form of mean free path (λ_{el}) refers to the average distance a positron travels before its direction of motion is significantly altered by an elastic collision (no energy loss) [6, 15].

$$\lambda_{el} = \frac{1}{\mathcal{N} \sigma_{el}} \tag{8}$$

$\mathcal{N}$ is the number density of molecules, given by [21, 24]:

$$\mathcal{N} = \frac{N_A \rho}{A} . \tag{9}$$

2.2.2 Inelastic mean free path

The inelastic mean free path indicates the typical distance a positron passes through before undergoing an inelastic collision, usually through processes like atomic excitation or ionization of surrounding atoms. Whether for an electron or a positron, this mean free path is inversely related to the total inelastic scattering cross section [25].

$$\lambda_{inel} = \frac{1}{\mathcal{N} \sigma_{inel}} \tag{10}$$

For penetrating positron (interaction process), the inverse of total mean free path is [2, 21].

$$\lambda_{int}^{-1} = \mathcal{N} \sigma_{int} \ . \tag{11}$$

Where λ_{int} , σ_{int} are mean free path and cross-section of interaction, respectively.

$$\frac{1}{\lambda_T} = \frac{1}{\lambda_{el}} + \frac{1}{\lambda_{inel}} , \tag{12}$$

Therefore,

$$\frac{1}{\lambda_T} = \frac{N_a \rho}{A} (\sigma_{el} + \sigma_{inel}) . \tag{13}$$

Where λ_{el}, λ_{inel}, λ_T are elastic, inelastic, and total mean free path of positron. Finally, the mean free path is crucial for understanding positron transport in materials and designing experiments using positron beams. It has many applications like: Positron annihilation spectroscopy, material defect analysis, surface studies, and thin film characterization.

3. MONTE CARLO PROCEDURE

This arduous and challenging work relied on the Monte Carlo method of probability, where a comprehensive program was developed in Visual Basic language based on the basic equations of interactions and enhanced the code with Python programming language. Information about the target substance and the energy of the interacting particle was entered as input data, considering all possible interaction probabilities at normal angles perpendicular to the target. Normally one particle trajectory was calculated in the simulation for each compound. The positrons were followed until they slowed down to an energy of 100 eV, depending on the incident energy this required few minutes. We relied on

reliable sources by entering the density value of the material and the Z values for all the compound elements, in addition to their concentrations within that compound, the atomic weight of the elements must be input. In addition to the excitation energy for each core and valence and the number of electrons in both core and valence has been entered, in which these values were taken from international tables. First, the beta values (β_N) mentioned in Eq. (2) must be calculated, and then the elastic cross section σ_{el} values and mean free path elastic λ_{el} must be calculated from Eq. (3) and Eq. (8) for each element in the compound. The inelastic cross section σ_{inel} for both core and valence are then calculated for each element in the compound, in addition to the mean free path λ_{inel} for two states of core and valence. Finally, the total mean free path λ_T is calculated by adding elastic λ_{el} and inelastic λ_{inel} as mentioned before.

4. RESULTS AND DISCUSSIONS

The purpose of this study is to present approximate calculations of cross sections and mean free paths for three types of human tissue: kidney, lung, and thyroid. We applied our method to these tissues as targets because they have wide applications in the field of Nuclear Medicine. The kidney plays a crucial role in positron emission tomography (PET) imaging and radiopharmaceutical metabolism (where (PET) is a nuclear imaging technology that allows imaging of metabolic activities of body tissues or organs) [26, 27]. Lungs are also important in positron scattering research because their low density affects attenuation correction and positron range, influencing PET image resolution and disease diagnostics such as cancer and fibrosis. The thyroid gland is also significant in PET imaging and radiation dosimetry due to its unique physiological and metabolic properties [28]. The composition of materials for each kidney, lung, and thyroid tabulated in Table 1.

Table 1. Material composition of Kidney, Lung and Thyroid [29 - 31]

Fraction by weight			
Element	**Kidney**	**Lung**	**Thyroid**
H	0.103	0.103	0.104
C	0.132	0.105	0.119
N	0.03	0.031	0.024
O	0.724	0.748	0.745
Na	0.002	0.002	0.002
P	0.002	0.002	0.001
S	0.002	0.003	0.001
Cl	0.002	0.003	0.002
K	0.002	0.002	0.001
Ca	0.001	-	-
I	-	-	0.001
Density$\boldsymbol{\rho}$ (g/cm^3)	1.05	1.05	1.05

4.1 Scattering cross sections

These graphs show how positron interaction cross sections vary with energy in kidney, lung, and thyroid tissue from 100 eV to 1 MeV. The semi-logarithmic plots display four interaction mechanisms with cross section (cm²) on the y-axis and positron energy on the x-axis. In all three graphs, the red dashed lines represent the calculated elastic cross section, the blue lines show the calculated inelastic cross section, and the green lines are the total cross sections that calculated by the Monte Carlo (MC) method (current method), which is the sum of the total elastic and total inelastic cross sections. Moreover, the red solid line describes the Penelope elastic cross section.

Figure 1. (a) Shows positron interaction cross sections for kidney tissue, exhibiting a strong inverse relationship with energy, decreasing rapidly from 100 eV to 1 MeV. At low energies (100-1000 eV), elastic scattering (red dashed line) dominates with cross sections around 5×10^{-15} cm². At intermediate to high energies (>1000 eV), inelastic processes (blue line) become dominant. The total cross section (green line) represents the sum of all interactions, reaching 8×10^{-15} cm² at 100 eV. The Penelope elastic cross section (red solid line) appears smaller but shows minimal differences from the calculated elastic cross section due to the logarithmic scale.

Figure 1. (b) shows positron interaction cross sections for lung tissue. At low energies (100-1000 eV), elastic scattering dominates, while at higher energies (>1000 eV), inelastic processes become more significant. All cross sections decrease with increasing positron energy, typical for charged particle interactions with matter.

Figure 1. (c) presents positron interaction cross sections for thyroid tissue. At low energies (100-1000 eV), elastic scattering dominates with values reaching approximately (8×10^{-15} cm²). Although inelastic cross section remains a significant contributor. Above 10 keV, both elastic and inelastic cross sections converge toward negligible values. The total cross section (green line) decreases by approximately four orders of magnitude across the studied energy range. This has important implications for positron transport and dose deposition in thyroid tissue.

For all the above graphs, the comparison between the calculated elastic cross section, and the Penelope elastic cross section shows excellent agreement at higher energies but some divergence appears at lower energies. One can observe that, the largest uncertainties occur at low energies (<1000 eV), while at energies above (10,000 eV), both models agree

very well. Moreover, the greatest discrepancy between models is for thyroid tissue. These differences are most likely due to physical approximations, model assumptions, or parameterizations. And at low energies, the elastic cross section model consistently predicts higher values than Penelope. According to clinical implications the rapid decrease in cross sections with energy means that low-energy positrons interact much more frequently with kidney tissue, leading to higher local energy deposition. This is crucial for: Dosimetry calculations in PET imaging, understanding positron range and annihilation patterns [32], optimizing radiopharmaceutical design for kidney-targeted procedures.

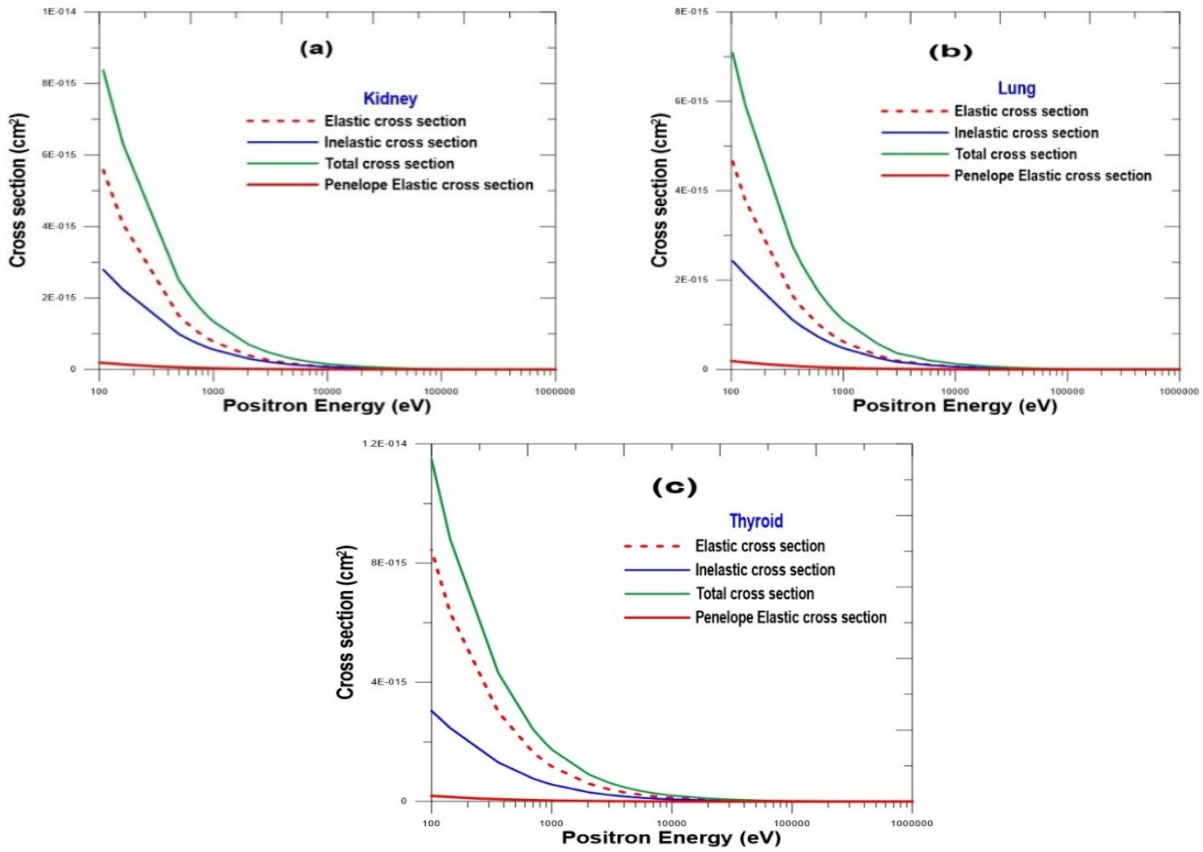

Figure 1. Calculated Elastic, Inelastic, and Total Cross section for (a): Kidney, (b): Lung, and (c): Thyroid organ. Compared with Penelope 2012 Total Elastic cross section

4.2 Positron Mean free path

Figure 2. illustrates the mean free path (in cm) for positrons in kidney, lung, and thyroid tissues plotted against positron energy (in eV). The graphs distinguish between three types of mean free path: elastic, inelastic, and total. The (blue line) represents the elastic mean free path, (red line) shows the inelastic mean free path, and the total mean free paths in (green line).

Figure 2. (a) The mean free path curves for kidney tissue inversely reflect the cross-section data from the previous section, confirming the fundamental relationship in Eq. (10). The mean free path increases dramatically with energy (roughly four orders of magnitude from 1,000 eV to 100,000 eV), explaining why low-energy positrons are effectively contained within small tissue volumes while high-energy positrons can travel much farther before interacting. The nearly identical elastic and inelastic curves indicate both scattering mechanisms are equally probable in kidney tissue. The total mean free path remains below either individual component as it combines both interaction types. This data is valuable for renal PET imaging and therapeutic applications requiring precise positron transport understanding for accurate dose calculations and image reconstruction.

Figure 2. (b) The very short mean free paths at low energies (scale of nanometer) indicate that positrons with low-energy interact very frequently with lung tissue, making them suitable for surface-sensitive applications. Higher-energy positrons penetrate much deeper before interacting. We can say, at lower energies (1,000 to 10,000 eV), the elastic and inelastic scattering have similar magnitudes. But, at energies exceeding (100,000 eV), their difference grows markedly.

Figure 2. (c) Like kidney and lung tissues, all three mean free paths in thyroid tissue increase exponentially with energy of positron, following the same principles of general physics. The one important point is that, the thyroid data shows consistently shorter mean free paths along all energies compared to kidney and lung. At high energies (over 100,000 eV), thyroid values reach about (8×10^{-6} cm) in contrast to lung values of about (1.2×10^{-5} cm). This difference is due to the higher density of thyroid compared to other tissues. Kidney, lung contain significant air spaces, making them less dense than solid thyroid. This shortest mean free paths in thyroid tissue mean positrons interact more frequently and

penetrate less deeply, which is crucial for thyroid imaging and the therapy planning of radioiodine. This data is important for accurate dosimetry in thyroid cancer treatments using radioactive isotopes.

Finally, lung shows the longest mean free paths across all energies, consistent with its lower density. While, thyroid generally shows the shortest mean free paths, reflecting its higher atomic number content (iodine). And kidney falls between lung and thyroid in most energy ranges.

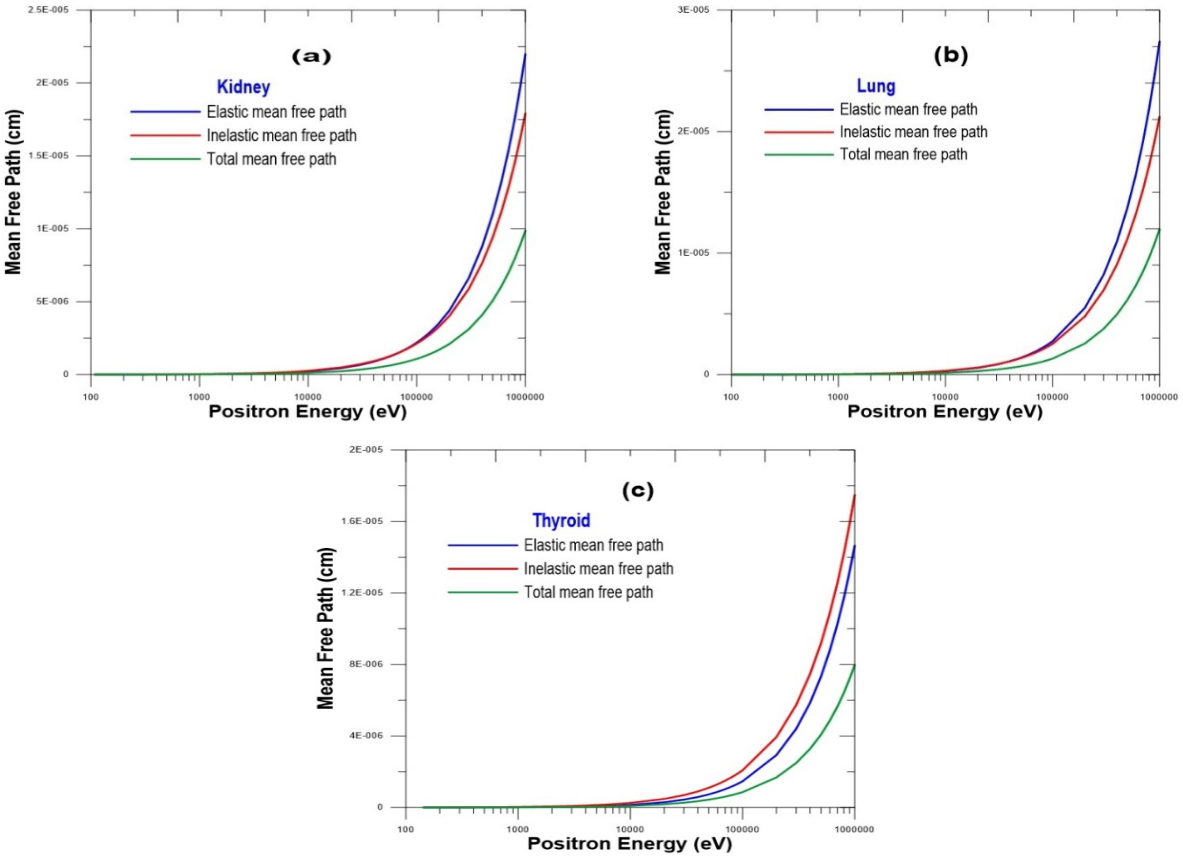

Figure 2. Calculated Elastic, Inelastic, and Total mean free paths for (a): Kidney, (b): Lung, and (c): Thyroid

5. CONCLUSIONS

In this article we presented the elastic, inelastic, total scattering cross sections for (100 eV - 1 MeV) positrons in a group of three human tissues. Also, the mean free paths of positrons are studied for the same energy ranges and human organs by the Monte Carlo method. We noted that as positron energy increases beyond 10,000 eV, all cross sections converge toward similar, very small values approaching zero. This convergence indicates that high-energy positrons interact minimally with tissue, explaining their greater penetration depth and lower stopping power at elevated energies. Conversely, material density and composition play a crucial role in determining mean free path. Higher-density materials containing more atoms and molecules increase collision probability, consequently shortening the positron mean free path, as we see in thyroid tissue [25]. It is observed from the mean free path equations, Eqs. (8) and (10), that it is inversely proportional to both the particle density and the interaction cross section.

In medical applications involving positron emitters in kidney imaging (such as PET scans), these cross sections directly influence image resolution and dose distribution. Higher cross sections at lower energies suggest that low-energy positrons interact more frequently near their emission point, potentially improving spatial resolution while increasing local dose deposition. Although a lot of models for cross section and mean free path have been discussed extensively before, rather less has been available for compound like human tissues like: kidney, lung, and thyroid because they have a complex composition.

ORCID

Hawar M. Dlshad, https://orcid.org/0000-0002-6430-8106

REFERENCES

[1] M. Danch-Wierzchowska, D. Borys, B. Bobek-Bilewicz, M. Jarzab, and A. Swierniak, "Simplification of breast deformation modelling to support breast cancer treatment planning," Biocybern. Biomed. Eng. **36**(4), 531–536 (2016). https://doi.org/10.1016/j.bbe.2016.06.001

[2] I. Adesida, R. Shimizu, and T. E. Everhart, "A study of electron penetration in solids using a direct Monte Carlo approach," J. Appl. Phys. **51**(11), 5962–5969 (1980). https://doi.org/10.1063/1.327515

[3] Y.A. Üncü, G. Sevim, O. Ağar, and H. Özdoğan, "Mass attenuation coefficient, stopping power, and penetrating distance calculations via Monte Carlo simulations for cell membranes," Kuwait J. Sci. 50(1A), 1–12 (2023). https://doi.org/10.48129/kjs.15657
[4] O.N. Vassiliev, *Monte Carlo Methods for Radiation Transport*, (Springer International Publishing, Cham, 2017). https://doi.org/10.1007/978-3-319-44141-2
[5] I. Low, and Z. Yin, "Entanglement Entropy is Elastic Cross Section," J. Med. Phys. **49**, 155–166 (2024). http://arxiv.org/abs/2410.22414
[6] K. Koç, and A. Çetin, "Investigation of Interactions Between Low Energy Positrons and DNA Using the Monte-Carlo method," NeuroQuantology, **13**(2), 160–169 (2015). https://doi.org/10.14704/nq.2015.13.2.852
[7] C.E. Chika, "Estimation of Proton Stopping Power Ratio and Mean Excitation Energy Using Electron Density and Its Applications via Machine Learning Approach," J. Med. Phys. **49**(2), 155–166 (2024). https://doi.org/10.4103/jmp.jmp_157_23
[8] C. Hugenschmidt, "Positrons in surface physics," Surf. Sci. Rep. **71**(4), 547–594 (2016). https://doi.org/10.1016/J.SURFREP.2016.09.002
[9] J.C. Ashley, "Interaction of Low-Energy Electrons with Condensed Matter: Stopping Powers and Inelastic Mean Free Paths from Optical Data," J. Electron. Spectros. Relat. Phenomena, **46**, 199–214 (1988).
[10] Z. Tan, *et al*., "Cross sections of electron inelastic interactions in DNA," Radiat. Environ. Biophys. **43**(3), 173–182 (2004). https://doi.org/10.1007/s00411-004-0249-4
[11] Z. Tan, *et al*., "Electron stopping power and mean free path in organic compounds over the energy range of 20-10,000 eV," Nucl. Instrum. Methods Phys. Res. B, **222**(1-2), 27–43 (2004). https://doi.org/10.1016/j.nimb.2004.02.017
[12] L.H. Cai, B. Yang, C.C. Ling, C.D. Beling, and S. Fung, "Monte carlo simulation of positron induced secondary electrons in thin carbon foils," Journal of Physics: Conference Series, Institute of Physics Publishing, **262**, 012009 (2011). https://doi.org/10.1088/1742-6596/262/1/012009
[13] K. Ratnavelu, M. J. Brunger, and S.J. Buckman, "Recommended Positron Scattering Cross Sections for Atomic Systems," J. Phys. Chem. Ref. Data, **48**(2), (2019). https://doi.org/10.1063/1.5089638
[14] B.P. Nigam, M.K. Sundaresan, and T.-Y. Wu, "Theory of Multiple Scattering: Second Born Approximation and Corrections to Molière's Work," Physical Review, **115**(3), 491–502 (1959). https://doi.org/10.1103/PhysRev.115.491
[15] S. Yalcin, U. Akar Tarim, O. Gurler, O. Gundogdu, and D. A. Bradley, "Screening parameter for elastic scattering of electrons," Radiation Effects and Defects in Solids, **176**(9–10), 919–939 (2021). https://doi.org/10.1080/10420150.2021.1975709
[16] M. Gryzinski, "Two-Particle Collisions. II. Coulomb Collisions in the Laboratory System of Coordinates," Physical Review, **138**(2), 322–335 (1965).
[17] M. V. Manjunatha, and T. K. Umesh, "Effective atomic number of some rare earth compounds determined by the study of external bremsstrahlung," J. Radiat. Res. Appl. Sci. **8**(3), 428–432 (2015). https://doi.org/10.1016/j.jrras.2015.03.005
[18] V. De Smet, R. Labarbe, F. Vander Stappen, B. Macq, and E. Sterpin, "Reassessment of stopping power ratio uncertainties caused by mean excitation energies using a water-based formalism," Med. Phys. **45**(7), 3361–3370 (2018). https://doi.org/10.1002/mp.12949
[19] G.S. Ibbott, "Radiation Dosimetry: Electron Beams with Energies Between 1 and 50 MeV (ICRU Report No. 35)," Med. Phys. **12**(6), 813–813 (1985). https://doi.org/10.1118/1.595780
[20] M. Grvzinski, "Two-Particle Collisions. I. General Relations for Collisions in the Laboratory System," Physical Review, **138**(2), 305–321 (1965).
[21] M. Asai, M.A. Cortés-Giraldo, V. Giménez-Alventosa, V. Giménez Gómez, and F. Salvat, "The PENELOPE Physics Models and Transport Mechanics. Implementation into Geant4," Front. Phys. **9**, 1–20 (2021). https://doi.org/10.3389/fphy.2021.738735
[22] N.J. Carron, *An Introduction to the Passage of Energetic Particles through Matter*, (Taylor & Francis Group, California, USA, 2021). https://doi.org/10.1201/9781420012378
[23] M. Dapor, "Comparison of Electron Compton Scattering with Positron Compton Scattering in Polyethylene," Materials, **18**(7), 1–10 (2025). https://doi.org/10.3390/ma18071609
[24] A. Alshibel, and K. T. Osman, "Mass Stopping Power and Range of Alpha Particles in Biological Human Body Tissues (Blood, Brain, Adipose and Bone)," OAlib, **10**(10), 1–17 (2023). https://doi.org/10.4236/oalib.1110775
[25] A.B. Denison, and H. H. Farrell, "Positron mean free paths between 50 eV and 40 keV," Phys. Rev. B: Condens. Matter. Mater. Phys. **69**(10), 1–8 (2004). https://doi.org/10.1103/PhysRevB.69.104302
[26] S.V. Stepanov, V.M. Byakov, and P.S. Stepanov, "Positronium in Biosystems and Medicine: A New Approach to Tumor Diagnostics Based on Correlation between Oxygenation of Tissues and Lifetime of the Positronium Atom," Physics of Wave Phenomena, **29**(2), 174–179 (2021). https://doi.org/10.3103/S1541308X21020138
[27] E.C. Emond, A.M. Groves, B.F. Hutton, and K. Thielemans, "Effect of positron range on PET quantification in diseased and normal lungs," Phys. Med. Biol. **64**(20), 1–16 (2019). https://doi.org/10.1088/1361-6560/ab469d
[28] H.I. Coerts, B. de Keizer, and F.A. Verburg, "Advances in the Development of Positron Emission Tomography Tracers for Improved Detection of Differentiated Thyroid Cancer," Cancers (Basel), **16**(7), 1–12 (2024). https://doi.org/10.3390/cancers16071401
[29] ICRU, "Tissue substitutes in radiation dosimetry ana measurement ICRU report 44," Bethesda, (1989).
[30] M. Kefalati, S.F. Masoudi, and A. Abbasi, "Effect of human body position on gamma radiation dose rate from granite stones," J. Environ. Health. Sci. Eng. **19**(1), 933–939 (2021). https://doi.org/10.1007/s40201-021-00660-7
[31] A. Arectout, *et al*., "Investigation of photon interaction parameters in Human Body Tissues using GAMOS, FLUKA, and XCOM Studies," Nuclear Analysis, **4**(1), 1–11 (2025). https://doi.org/10.1016/j.nucana.2024.100141
[32] P. Moskal, *et al*., "Positronium image of the human brain in vivo," Sci. Adv. **10**(37), (2024). https://doi.org/10.1126/sciadv.adp2840

КОД МОНТЕ-КАРЛО ДЛЯ РОЗРАХУНКУ ПРУЖНОГО ТА НЕПРУЖНОГО ПЕРЕРІЗУ РОЗСІЯННЯ ТА СЕРЕДНЬОЇ ДОВЖИНИ ВІЛЬНОГО ПРОБІГУ РОЗСІЯННЯ ПОЗИТРОНІВ В ОРГАНАХ НИРОК, ЛЕГЕНЬ ТА ЩИТОВИДНОЇ ЗАЛОЗИ

Хавар М. Длшад[1], Джамал М. Рашид[2]

[1]Університет Сулеймані, Коледж освіти, кафедра фізики, Сулейманія 46001, Регіон Курдистан, Ірак

[2]Університет Сулеймані, Коледж природничих наук, кафедра фізики, вулиця Клясан, Сулейманія 46001, Регіон Курдистан, Ірак

У цьому дослідженні розраховано загальні перерізи розсіювання позитронів у тканинах нирок, легень та щитовидної залози в діапазоні енергій від 100 еВ до 1 МеВ. Методи Монте-Карло були використані для визначення як пружних, так і непружних інтегральних перерізів, використовуючи формулу Резерфорда для пружного розсіювання та функцію збудження Гризінського для непружних процесів. Було проведено порівняння між пружними та пружними перерізами Пенелопи. У дослідженні також розглядалися пружна, непружна та повна довжина вільного пробігу як функції енергії позитронів для всіх трьох типів тканин. Обчислювальний підхід розроблений для широкого застосування до різних матеріалів. Ми спостерігали значні відмінності в профілях поперечного перерізу та в енергетичних залежностях довжини вільного пробігу між тканинами, пояснюючи ці варіації різними характеристиками непружного розсіювання, властивими кожному матеріалу. Хоча систематичні невизначеності в обчислювальному алгоритмі важко точно кількісно визначити, ми вважаємо, що вони значною мірою є систематичними.

Ключові слова: *поперечний переріз; позитрон; середній вільний пробіг; орган людини; ефективний атомний номер*